A Robust Data-Driven Bayesian approach for Complex Nonlinear Aeroelastic System Identification

PhD Thesis

Michael McGurk

Aerospace Centre of Excellence

Department of Mechanical & Aerospace Engineering

University of Strathclyde, Glasgow

January 23, 2026

This thesis is the result of the author's original research. It has been composed by the author and has not been previously submitted for examination which has led to the award of a degree.

Abstract

This thesis presents a computational framework for the analysis of nonlinear aeroelastic phenomena, with particular emphasis on sustained oscillatory behaviour that poses significant challenges in aerospace design. Traditional time-domain methods often prove computationally intensive and limited in scope. To address these challenges, this research introduces innovative frequency-domain and data-driven techniques that substantially reduce computational demands while ensuring robust treatment of uncertainty.

The proposed methodology integrates three core developments: a harmonic balance approach enhanced by operator-based stability analysis, a surrogate modelling strategy informed by probabilistic inference, and a hierarchical learning architecture that leverages models of varying accuracy. These innovations enable the efficient exploration of complex system dynamics without reliance on extensive time-domain simulations, while accurately capturing critical features such as limit cycle oscillations and stability transitions.

A probabilistic framework is employed for the estimation of system parameters and model structures, grounded in statistical evidence. This allows for the construction of bifurcation diagrams augmented with an interval of probability, offering new capabilities for visualising uncertainty in nonlinear dynamic systems.

To overcome the limitations imposed by sparse experimental data, a novel learning architecture is introduced that efficiently synthesises information across models of differing resolution. This approach effectively captures both inherent variability and knowledge-based uncertainty, enabling accurate predictions with significantly reduced data requirements.

The framework is demonstrated on a representative aeroelastic configuration, where it performs robustly under both idealised and noisy conditions. It delivers high predictive fidelity in identifying critical dynamic transitions, while alternative strategies within the framework offer enhanced computational efficiency with controlled trade-offs in accuracy. A notable innovation includes the use of normalised continuation parameters, which facilitate the tracking of intricate nonlinear behaviours across multiple solution branches.

Overall, this work achieves substantial gains in computational efficiency while preserving, and in some cases improving, predictive performance. It supports a wide range of practical applications, from early-stage aeroelastic design to real-time system monitoring, and contributes novel theoretical insights through the integration of advanced continuation methods, hierarchical uncertainty quantification, and Bayesian system identification.

This thesis thus establishes a versatile foundation for the analysis of nonlinear aeroelastic systems, bridging the gap between computational tractability and modelling accuracy. Its modular and extensible architecture positions it for broader application to related phenomena such as flutter and gust response, and provides a pathway towards future innovations in digital twin technologies and certification strategies for next-generation aerospace systems.

Contents

List of Figures

List of Tables

List of Tables

List of Acronyms

- **AFT** - Alternating Frequency Time
- **AUTO** - Automatically (continuation tool)
- **BMU** - Bayesian Model Updating
- **CBC** - Control-Based Continuation
- **COCO** - Continuation Core
- **COV** - Coefficient of Variance
- **DoF** - Degree-of-Freedom
- **eVTOL** — Electric Vertical Take-Off and Landing
- **FFT** - Fast Fourier Transform
- **HBM** - Harmonic Balance Method
- **IDB** - Iterative Data-driven Bayesian Model Updating
- **LCO** - Limit Cycle Oscillations
- **LHS** - Latin Hyper-cube Sampling
- **MATCONT** - MATLAB Continuation
- **MCMC** - Metropolis-Hastings Markov Chain Monte Carlo
- **MCS** - Monte Carlo Simulation

- **NLvib** - NonLinear Vibrations (conmpuational tool)
- **ODE** - Ordinary Differential Equation
- **p-box** - Probability-box
- **PCE** - Polynomial Chaos Expansion
- **PDF** - Probability Density Function
- **PIDB** - Polymorphic Iterative Data-driven Bayesian Model Updating
- **RRMS** - Relative Root Mean Square
- **SDB** - Single-iteration Data-driven Bayesian Model Updating
- **SMC** - Sequential Monte Carlo
- ***std*** - Standard Deviation
- **STOL** — Short Take-Off and Landing
- **TMCMC** - Transitional Markov Chain Monte Carlo
- **UQ** - Uncertainty Quantification

Nomenclature

β_{1C}, β_{1S}, β_0 Orientation of the rotor plane in gimballed hub tiltrotor model.

q_1, q_2 Spanwise and chordwise bending of wing in gimballed hub tiltrotor model.

α Pitch angle of aerofoil system $[rads]$

$\boldsymbol{\phi}$ Matrix of eigenvectors

$\boldsymbol{f}_{nl}$ Vector of nonlinear system force on a mechanical system

$\boldsymbol{J}$ Jacobean matrix.

$\boldsymbol{x}$ Vector of a mechanical system's degrees of freedom

$\boldsymbol{x}_{nl}$ Degrees of freedom of a mechanical system that exhibit nonlinear behaviour

δ Freeplay gap.

ϵ_p Centralisation degree of the posterior distribution in Bayesian process.

η Mode shape for elastic bending.

$\hat{f}$ Data-driven model of function f.

κ Reduced frequency: $(\kappa = \omega b/V)$

λ Continuation parameter of a nonlinear system

$\mathscr{A}$ Convergence criterion of data-driven BMU process.

$\mathscr{B}$ Tempering parameter of TMCMC sampling process.

$\mathscr{P}(t)$ time-dependent projection matrix

μ Mean of a set of data.

Ω Angular velocity of rotor in gimballed hub tiltrotor model.

ω Natural frequency of a system

$\overline{X}_0$, $\overline{X}_{k,s}$, $\overline{X}_{k,c}$ Fourier coefficients of the linear degrees of freedom of a nonlinear system

ψ_{ij} Matrix of size $i \times j$ of eigenvalues

ρ Air density

σ_y Standard deviation of kriging model estimates.

σ_i Variance of kriging model estimates.

σ_p Width parameter in Bayesian process.

Φ_T Monodromy matrix of a mechanical system

A Aerodynamic inertial force matrix of aeroelastic system

B Aerodynamic damping force matrix of aeroelastic system

C Aerodynamic resistive force matrix of aeroelastic system

D Structural damping matrix of a mechanical system

F Vector of external forces applied to a mechanical systems

H Hill's matrix.

K Structural stiffness matrix of a mechanical system

M Structural mass matrix of a mechanical system

Q Linear matrix of an aeroelastic system

$\mathbf{q}_n$ Vector of nonlinear forces of mechanical system, modified for comparability with linear system matrix $\mathbf{Q}$

$\mathbf{x}_L$ Degrees of freedom of a mechanical system that exhibit no nonlinear behaviour related to $\mathbf{x}$

$\mathbf{z}$ Vector of observations $(\hat{x}_{(1,..,i)}, \hat{y}_{(1,..,i)})$.

θ Parameter to be estimated through the Bayesian process.

ϖ Statistical weight function of TMCMC sampling.

ξ Mode shape for torsion.

ζ Damping ratio of a system

ζ_{1C}, ζ_{1S}, ζ_0 Translations in the x-, y-, and z-directions in gimballed hub tiltrotor model.

$C(\kappa)$ Generalised Theodorsen's function

c_1-c_4 Aerodynamic constants

C_β Blade flapping damping.

c_h Heave structural damping.

c_w Chord of wing in gimballed hub tiltrotor model.

c_α Pitch structural damping.

F_0, $F_{k,s}$, $F_{k,c}$ Fourier coefficient of the nonlinear force of a mechanical system

h Heave of aerofoil system $[m]$

h_p Length of pylon in gimballed hub tiltrotor model.

I_α Wing's moment of inertia about the elastic axis.

I_β Blade flapping inertia.

$I_{N\times N}$ Identity matrix of size N

K_β Blade flapping stiffness.

K_h Heave structural stiffness.

K_h Pitch linear structural stiffness.

$K_{\alpha 2}$ Quadratic structural stiffness term.

$K_{\alpha 3}$ Cubic structural stiffness term.

$K_{\beta 1}$ Linear blade flapping stiffness.

$K_{\beta 2}$, $K_{\beta 3}$ Nonlinear blade flapping stiffness.

K_{nl} Freeplay structural stiffness.

L Number of iterations in iterative BMU process

l Number of harmonics in a Fourier series

M_β Aerodynamic moment on blade in gimballed hub tiltrotor model.

m_T Combined mass of the wing and its support structure.

m_w Wing mass.

N Number of degrees of freedom of a mechanical system

p Torsion in spanwise direction in gimballed hub tiltrotor model.

$P(\mathbf{z})$ Posterior distribution of Bayesian process.

$P(\theta)$ Prior distribution in Bayesian process.

R Radius of rotor blades in gimballed hub tiltrotor model.

R_0, $R_{k,s}$, $R_{k,c}$ Residual equation of the HBM continuation scheme.

s Non-dimensional arc-length in continuation scheme.

T Period of an oscillation

Nomenclature

V Free-stream velocity

v Positions in vector $\mathbf{x}$ related to nonlinear degrees of freedom in $\boldsymbol{x}$

V_f Flutter velocity

w Non-dimensional aerodynamic state in aerofoil system

x Single degree of freedom of a mechanical system

X_0, $X_{k,s}$, $X_{k,c}$ Fourier coefficients related to the constant term, the k^{th} sine terms and the k^{th} cosine terms

θ Training data for model $\hat{f}$ inputs.

$\mathbf{U}$ Transformation matrix to convert the Hill's matrix from frequency to time domain

$\mathbf{x}$ Combined vector of mechanical systems position ($\boldsymbol{x}$) and velocity ($\dot{\boldsymbol{x}}$) vector: $[\dot{\boldsymbol{x}}, \boldsymbol{x}]^T$

$\mathbf{y}$ Training data for model $\hat{f}$ outputs.

p Position in vector

y_{Tw} Span of wing in gimballed hub tiltrotor model.

Publication list

This thesis synthesises and extends research outputs published in peer-reviewed venues during the study period. While the core chapters build upon these publications, the material has been substantially revised to ensure coherence across the thesis, with additional analyses incorporated where relevant.

Journal Papers

- Michael McGurk, Olivia Stodieck and Jie Yuan. "Probabilistic aeroelastic analysis of high-fidelity composite aircraft wing with manufacturing variability." *Composite Structures* 329 (2024) [9]
- Michael McGurk, Adolphus Lye, Ludovic Renson and Jie Yuan. "Data-driven Bayesian inference for stochastic model identification of nonlinear aeroelastic systems." *AIAA Journal* 62.5 (2024) [10]
- Michael McGurk and Jie Yuan. "Prediction and validation of aeroelastic limit cycle oscillations using harmonic balance methods and Koopman operator." *Nonlinear Dyn* (2025) [11]

Journal Pre-Prints

- Michael McGurk and Jie Yuan, "A Robust Multi-Level Data-Driven Bayesian Approach for Stochastic Model Identification of Complex Nonlinear systems." (2025) [12]

Conference Papers

- Michael McGurk and Jie Yuan. "Computation of limit cycle oscillations and their stabilities in nonlinear aeroelastic systems using harmonic balance methods." *International Forum on Aeroelasticity and Structural Dynamics (IFASD) 2022*. (2022) [13]

- Michael McGurk, Jie Yuan and Ludovic Renson. "Nonlinear Parameter Estimation using Bayesian Model Updating and Data Driven Surrogate Model." *9th International Conference on Computational Methods in Structural Dynamics and Earthquake Engineering*. (2023) [14]

- Michael McGurk and Jie Yuan. "A multilevel data-driven Bayesian approach for stochastic model updating of nonlinear aeroelastic systems." *AIAA SCITECH 2024 Forum*. (2024) [15]

- Jie Yuan and Michael McGurk. "A multi-level data-driven Bayesian approach to identify probabilistic stability of aeroelastic limit cycle oscillations." *11th European Nonlinear Oscillations Conference*. (2024) [16]

- Michael McGurk and Jie Yuan. "A robust multi-level data-driven Bayesian approach for stochastic model identification of complex nonlinear systems." *Third Physics-Enhancing Machine Learning Workshop: Mechanics & Materials*. (2024) [17]

- Michael McGurk and Jie Yuan. "Multi-level Stochastic Model Identification of Complex Aeroelastic Systems Considering Aerodynamic Nonlinearities." *IMAC-XLIII*. (2025) [18]

- Michael McGurk and Jie Yuan. "Multi-fidelity Data Driven Bayesian Identification of Complex Aeroelastic Systems." *NODYCON 2025*. (2025) [19]

Acknowledgments

To my Nana, Margaret Campbell, and my Mum, Sophia Campbell, whose kindness and love have guided me every step of the way—*happy 60th birthday Mum.*

First and foremost, I would like to express my sincere gratitude to my supervisors, Dr Jie Yuan and Dr JingLang Feng. Their guidance has been fundamental to the success of this project. In particular, I am especially thankful to my primary supervisor, Jie, for his unwavering support and flexibility throughout. I am also grateful to Dr Adolphus Lye and Dr Ludovic Renson for their valuable contributions to the research, and to Tim Allan for his support in the last few months.

My heartfelt thanks go to all my colleagues in the ACE research group for making this chapter of my life so enjoyable. Special mentions to Paul, Simão, Marianna, Lewis, Catarina and Ewan—for tolerating me annoying them in the office and for the amazing night outs and trips we've had over the past four years. A special thank you to my co-council Aurelio who I shared some of the best laughs of my life with at our desk. And of course, cheers to the champs of the MAE five-a-side team and the ACE Swimming Team.

To my close friends and family—especially my Mum, Dad, Rachel and her partner Alice—thank you for your constant encouragement and for putting up with my nonsense over the years. Finally, a deep thank you to my partner, Candy, for her extraordinary patience, love, and support throughout this journey.

This research was made possible through funding from the Engineering and Physical Sciences Research Council (EPSRC), whose support is gratefully acknowledged.

Chapter 0. Acknowledgments

Chapter 1

Introduction

1.1 Research Background & Motivation

A key priority in the aerospace sector is the reduction of carbon dioxide (CO_2) emissions. Without substantial mitigation measures, aviation's contribution to global warming may escalate to approximately 5.2% of total anthropogenic warming under the *Representative Concentration Pathway 2.6* [20]. The industry faces unique decarbonisation challenges due to its reliance on energy-dense liquid fuels, for which viable carbon-neutral alternatives remain limited [21, 22]. Much current research focuses on two primary emission reduction strategies: (1) advanced integration of lightweight materials in airframe design, and (2) development of electric aircraft technologies [23–25]. Both approaches demonstrate potential to significantly decrease the sector's environmental impact while maintaining operational requirements.

Considering the use of lightweight materials, the transition to advanced composite structures in aircraft design is estimated to account for approximately 20–25% of the aviation industry's targeted CO_2 emission reductions [26]. In the context of electric aircraft, many emerging concepts are characterised by compact, lightweight designs optimised for short-range operations. These aircraft often feature unconventional configurations and multiple electric propulsion units. Two representative examples are illustrated in Figure 1.1. The first depicts the Lilium Jet, a novel electric vertical take-off and landing (eVTOL) aircraft [27]. The second example, developed by the

(a)

(b)

Figure 1.1: Sustainable aircraft (a) Liliam [1], (b) Electric Regional Aircraft (ERA) [2]

French manufacturer AURA AERO, is a short take-off and landing (STOL) electric aircraft. As shown, it features eight electric engines and long, slender wings, reflecting design choices aimed at enhancing aerodynamic efficiency and distributed propulsion [28]. While electric aircraft offer substantial reductions in emissions compared to conventional aircraft, all the concepts discussed involve the use of lightweight materials. Consequently, lightweight materials remain a critical consideration in the development and investigation of electric aircraft.

Modelling the dynamic response of lightweight aerospace structures presents significant challenges due to their susceptibility to large geometric deformations, which introduce distributed nonlinearities and complex dynamical behaviour [29,30]. The increasing integration of systems further compounds these challenges, as additional interfaces can generate localised nonlinearities—a phenomenon well-documented in tiltrotor system dynamics [31, 32]. These nonlinear effects can substantially influence system dynamics and control characteristics. In tiltrotor systems, they modify flutter boundaries [31, 33], while in fixed-wing applications, they induce shifts in the aerodynamic centre that impact aircraft controllability [34]. Such nonlinearities are typically categorised into two distinct classes:

- **Geometric nonlinearities**: Distributed throughout the structure, primarily arising from large deflections enabled by lightweight material usage [35]
- **Localised nonlinearities**: Confined to specific regions, often originating from

frictional interfaces in structural joints [36, 37]

The prevalence of localised nonlinearities has increased with the integration of complex modern systems, necessitating careful consideration in both modelling and control strategy development. As such, they will be the primary focus of this work [38, 39].

A prominent manifestation of both geometric and localised nonlinearities is the emergence of self-sustained oscillations, commonly termed Limit Cycle Oscillations (LCOs). These LCOs frequently represent the peak dynamic response of aeroelastic systems, with critical implications for structural fatigue life and operational safety [40]. Experimental observations have consistently verified LCO phenomena across various configurations, particularly in high-aspect-ratio flexible wings [41, 42]. Recent work by Drachinsky and Raveh [43, 44] has further demonstrated subcritical LCO formation in low-speed flutter testing of highly flexible wings, highlighting the prevalence of these nonlinear effects. The stability characteristics of LCOs are of paramount importance: stable LCOs represent physically attainable oscillatory states towards which the system converges, whereas unstable LCOs demarcate boundaries of diverging response, either to a decaying reponse or a divergent oscillation [45]. This distinction fundamentally influences both the prediction of system behaviour and the design of appropriate control strategies.

However, determining LCO behaviour typically requires computationally expensive nonlinear analyses, particularly for generating bifurcation diagrams and assessing stability. This resource-intensive process often leads to the neglect of nonlinear analysis during early design stages, thereby artificially constraining the feasible design space [46]. When performing system identification from experimental data, deterministic approaches that ignore the effects of uncertainties are commonly employed. Additionally, conducting Uncertainty Quantification (UQ) on the identified systems typically requires thousands of model evaluations. On the other hand, while stochastic model updating is gaining popularity, its computational cost remains excessive for nonlinear systems. This computational burden frequently precludes the use of detailed nonlinear models for both parameter estimation and output behaviour analysis. Consequently, this limitation significantly impedes nonlinear aeroelastic analysis using data-driven

approaches, despite their growing prominence in aerospace applications [47, 48]. The resulting gap in capability underscores the critical need for more computationally efficient methods to characterise LCO behaviour in aeroelastic systems.

This work addresses these challenges by developing a robust computational framework for accurate and efficient LCO analysis in complex nonlinear aeroelastic systems. The central research question may be formulated as follows: *To what extent can a unified framework be developed for the nonlinear analysis of complex aeroelastic systems, enabling computationally efficient parameter estimation and uncertainty quantification?*

The framework combines advanced nonlinear dynamics techniques with data-driven approaches to overcome the current limitations in LCO prediction. Section 1.2 details the specific objectives and implementation strategy for achieving these goals. If a framework that ticks all of these boxes is developed and successfully demonstrated, innovative solutions to lightweight sustainable aircraft can be explored with further efficiency and less time and also less computational energy is required for carrying out the simulations required.

1.2 Project Goal & Objectives

The objective of this research is to develop a framework for the efficient and accurate identification of nonlinear aeroelastic systems based on experimental LCO data. Given the inherent noise in experimental measurements, the proposed methodology adopts a probabilistic approach, thereby enabling UQ in the inferred system behaviour.

Such a framework would be highly beneficial in a range of real-world engineering applications, particularly in the design of flexible aircraft wings. By probabilistically identifying the nonlinear parameters of the model, a clearer understanding of the safety margins in the design can be achieved. Furthermore, the data-driven approach using surrogate models significantly reduces the computational time required, thereby accelerating the design process during the early stages. The continued development of advanced tools for nonlinear aeroelastic analysis further enables the industry to push the boundaries of design, facilitating more innovative and efficient solutions.

To address the overarching research question, the primary objective is decomposed into the following four specific research objectives:

1. To develop a computationally efficient method for estimating deterministic LCO behaviour and stability in aeroelastic systems. This work seeks to minimise the computational burden of traditional deterministic methods for LCO characterisation, facilitating their integration with data-driven modelling frameworks.

2. To formulate a probabilistic, data-driven methodology to minimise computational cost while maximising accuracy in the identification of nonlinear models for LCO behaviour in aeroelastic systems. The primary objective is to develop and validate a novel data-driven framework for nonlinear aeroelastic analysis and aleatory UQ.

3. To enhance the computational efficiency of proposed data-driven identification framework through a multi-level and multi-fidelity modelling approach. The aims are to enhance both the data efficiency and predictive accuracy of the framework developed in Objective 2, while incorporating polymorphic UQ.

4. To validate the framework using a high-fidelity aeroelastic test case. This final objective serves to comprehensively validate the full operational capabilities of the framework developed through the preceding objectives.

Each objective will be accomplished by developing appropriate methodologies and conducting both numerical and experimental validation.

1.3 Thesis Organisation

This thesis is structured such that each central chapter addresses one of the research objectives individually. Chapter 2 presents an overall literature review, focusing exclusively on the theoretical foundations relevant to all subsequent chapters. This encompasses an overview of aeroelastic analysis (incorporating both linear and nonlinear approaches), along with a critical review of model updating methodologies and relevant data-driven techniques.

The core chapters (Chapters 3–6) then follow. Each begins by introducing the specific formula required for that section, after which the corresponding methodology is presented in a generalised form. Where applicable, a case study is included to demonstrate the application of the methodology to a test case.

The progression of objectives is as follows:

- Chapter 3 addresses Objective 1. It presents a computationally efficient numerical framework for predicting LCO amplitudes and assessing stability in nonlinear aeroelastic systems. The proposed approach integrates the Harmonic Balance Method (HBM) with the Hill method for stability analysis.

- Chapter 4 addresses Objective 2. It presents a probabilistic, data-driven methodology for minimising computational cost while maximising accuracy in the identification of nonlinear models to capture LCO behaviour in aeroelastic systems. This work builds upon several prior developments.

- Chapter 5 addresses Objective 3. It extends the methods developed in Chapter 4 through an iterative framework whilst integrating hybrid UQ.

These chapters collectively develop the proposed framework and demonstrate its implementation in a simplified test case. Chapter 6 then applies the complete framework to a high-fidelity test case, thereby validating the methodology and addressing the final objective.

Finally, Chapter 7 synthesises how these objectives collectively achieve the overarching aim of the thesis, followed by a discussion of potential improvements and directions for future work.

Chapter 2

Literature Review

This chapter reviews the fundamental theories underpinning the present research. It is structured into three main sections. The first provides an overview of aeroelasticity, with particular emphasis on the challenges posed by nonlinearities in aeroelastic systems—their origins and the key behaviours they can induce. The second section examines standard numerical methods used in the analysis of nonlinear aeroelastic phenomena, highlighting their limitations. The final section explores system identification in nonlinear and data-driven contexts, which serves as the foundation for the computational framework developed in this study.

Core theoretical concepts applicable throughout this work are presented here, while chapter-specific formulations appear in their respective contexts. The analysis employs two key concepts: (1) *data-driven* methods, prioritising empirical data over first-principles modelling, and (2) *robust* approaches maintaining reliability under modelling uncertainties and measurement noise.

2.1 Aeroelastcity

2.1.1 Aeroelatcity Overview

Aeroelasticity fundamentally examines the interaction between aerodynamic, inertial, and elastic forces acting on a structure. The foundational concept is conventionally illustrated by Collar's aeroelastic triangle, shown in Figure 2.1 [49]. This framework

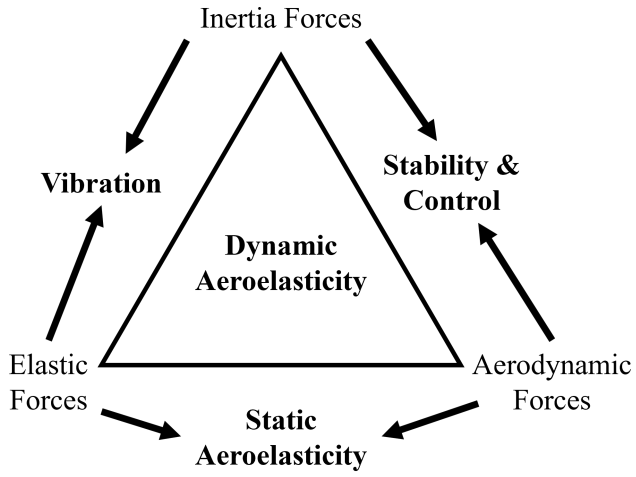

Figure 2.1: Collar's aeroelastic triangle

gives an overview of how the primary disciplines of stability and control, structural dynamics, and static aeroelasticity arise from the coupling of two or three force types. The complete interaction of all three forces leads to dynamic aeroelastic phenomena. For analytical purposes, aeroelastic behaviour is categorised into two distinct regimes: *static aeroelasticity* and *dynamic aeroelasticity*.

Static aeroelasticity examines the non-oscillatory interaction between aerodynamic forces and a flexible aircraft structure [50]. It is referred to as "static" as is is the study of the equilibrium response of a structure to aerodynamic forces, without considering the time-dependent effects or the dynamic oscillations of the structure. A critical consideration in static aeroelasticity is the reduction in control surface effectiveness, potential control reversal, and—most relevant to this work—structural divergence. Divergence occurs when the aerodynamic torsional moment exceeds the structural restoring moment, resulting in unbounded wing twist and, in practice, catastrophic structural failure. For an aircraft, aerodynamic loads increase with airspeed, leading to a critical velocity at which divergence arises, termed the *divergence speed*. Although rarely encountered in operation due to preceding aeroelastic instabilities (discussed later), this speed represents the theoretical upper limit for safe structural design with respect to static aeroelasticity.

Dynamic aeroelasticity investigates the oscillatory coupling between aerodynamic

forces and structural deformation. The most critical phenomenon in this field is *flutter*, which arises from unfavourable energy transfer from the fluid flow to the structure due to coupled inertial, elastic, and aerodynamic interactions (illustrated in Figure 2.1). Beyond a critical threshold known as the *flutter speed*, the structure responds to perturbations with exponentially growing oscillations [51]. In practical applications, this leads to catastrophic structural failure unless mitigated through design or control systems. Flutter is widely regarded as the primary aeroelastic consideration in aircraft design, as its onset typically occurs at lower velocities than static divergence [50]. Consequently, the flutter speed generally defines the upper operational limit for safe flight with respect to aeroelastic effects.

2.1.2 Nonlinear Aeroelastic Phenomenon

The effects discussed thus far pertain to *linear aeroelasticity*, wherein phenomena can be modelled using relatively simple linear mathematical formulations. However, real-world systems frequently exhibit behaviour that violates these linear assumptions, necessitating more sophisticated *nonlinear aeroelastic* models [52].

From a mathematical perspective, this transition introduces significant complexity: unlike linear differential equations (which admit general analytical solutions), nonlinear equations typically require numerical treatment and may exhibit multiple coexisting solutions at identical operating conditions [53]. Moreover, nonlinear systems demonstrate a richer repertoire of dynamic behaviours—including limit cycles, bifurcations, and chaotic responses—that have no counterpart in linear theory [54].

In recent years, nonlinearities have been increasingly tolerated or deliberately incorporated into engineering systems. These nonlinear effects typically originate from three primary sources: structural deformations, aerodynamic interactions, and control system characteristics [52]. As this work focuses on sustainable aircraft design, particular attention is given to *structural nonlinearities*, which dominate in lightweight airframe applications [55].

The most prevalent forms of structural nonlinearity include:

- *Geometric nonlinearities* arising from large deformations (e.g., wing flexure be-

yond small-angle assumptions)

- *Clearance nonlinearities* involving freeplay, intermittent contact, and other non-smooth phenomena
- *Dissipative nonlinearities* from friction or velocity-dependent damping
- *Inertial nonlinearities*, particularly relevant in rotating systems like propellers and turbomachinery [51]

The aviation industry's push toward net-zero emissions has accelerated adoption of lightweight materials and electric propulsion systems. However, these innovations introduce significant modelling challenges: slender composite structures exhibit pronounced geometric nonlinearities under operational loads [56], while non-smooth boundary conditions in articulated control surfaces can trigger complex dynamic responses including bifurcations and LCO [57, 58]. This interplay between sustainability-driven design and nonlinear dynamics forms a critical research area in modern aeroelasticity.

The impact of these nonlinearities can often shift the reliable safety margins in relation to operating velocity in aircraft design and certification. What we are most concerned about in this work being mainly focused on dynamic aeroelatic effects (so oscillatory impacts of fluid structure interaction) is the nonlinear oscillations.

The presence of nonlinearities can significantly alter the conventional safety margins associated with operational velocity in aircraft design and certification processes. Of particular concern in this work are *nonlinear oscillations*, which arise from dynamic aeroelastic effects—specifically, the oscillatory coupling between aerodynamic forces and structural deformation. These nonlinear phenomena can profoundly influence the aircraft's dynamic response and aeroelastic stability boundaries.

2.1.3 Dynamic Nonlinear Aeroelastic Systems

Nonlinearities in aeroelastic systems can lead to subcritical post-flutter responses [59, 60], where self-sustaining oscillations emerge at velocities *below* the linear flutter velocity. These oscillations, known as LCOs, exhibit constant amplitude and frequency

despite the absence of external forcing, and cannot be predicted through conventional linear analysis [61].

The analysis of LCOs necessitates nonlinear modelling approaches, as their amplitude and stability characteristics are governed by the interplay between structural nonlinearities and aerodynamic damping [62]. In certain situations, LCOs can have a beneficial role. For example, LCOs may act as a precursor to more severe instabilities, such as flutter, by manifesting as stable, bounded oscillations with safe amplitudes. These oscillations can provide an operational warning, enabling early detection of impending failure before catastrophic events occur [63]. Furthermore, LCOs are often exploited in applications such as energy harvesting, where the sustained oscillations can be harnessed to convert mechanical energy into usable electrical power. In such cases, the presence of LCOs can enhance the efficiency of energy harvesters by ensuring consistent oscillatory motion, which is critical for optimising energy conversion. [64]

However, subcritical LCOs—those occurring below the linear flutter speed—pose significant design challenges. While linear analysis would indicate a safe operating regime, the presence of LCOs may compromise structural integrity due to their potentially hazardous amplitudes or frequencies [55]. This discrepancy underscores the critical importance of nonlinear aeroelastic analysis in modern aircraft design, particularly for high-aspect-ratio wings and flexible structures where nonlinear effects are pronounced.

The fundamental importance of nonlinear effects in aeroelastic systems can be demonstrated through the classical two Degree-of-Freedom (DoF) pitch-plunge aerofoil system investigated by Liu and Dowell [3]. This system exhibits a linear flutter speed of 31 m/s. When analysed with a linear torsional spring in the pitch DoF and perturbed at 25 m/s (below the flutter speed), the response shows decaying oscillations that asymptotically approach equilibrium, as depicted in Figure 2.2a.

However, introducing cubic nonlinearity in the pitch spring fundamentally alters the system behaviour at the same airspeed. Under identical perturbation conditions, the nonlinear system develops sustained LCOs with a heave amplitude of 0.3 m, as presented in Figure 2.2b. This result carries significant engineering implications: while

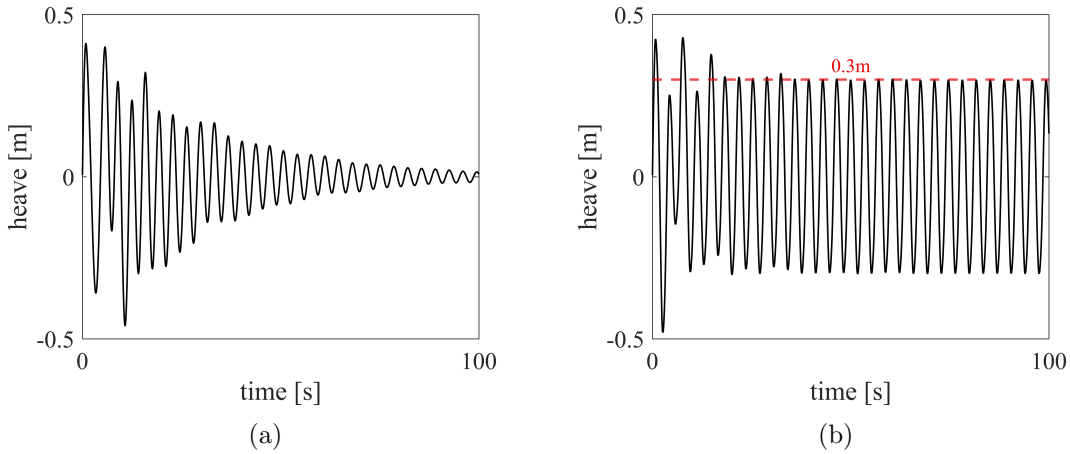

Figure 2.2: Time repose of a simple aerofoil system with and without a nonlinear term under the same perturbation, (a) Linear, (b) Nonlinear

linear analysis would predict safe operation at 25 m/s, the nonlinear system exhibits potentially dangerous oscillations below the nominal flutter speed.

This case demonstrates subcritical LCO behaviour and highlights two critical aspects of aeroelastic design. First, it emphasises the necessity of properly characterising nonlinear stiffness properties in aeroelastic systems. Second, it underscores the importance of comprehensively evaluating LCO behaviour across the operational flight envelope, particularly for systems where nonlinear effects may significantly alter the predicted stability boundaries.

Subcritical LCOs have been extensively documented in experimental studies of high-aspect-ratio flexible wings [41, 42]. Recent work by Drachinsky and Raveh [43, 44] has further demonstrated subcritical LCO formation in highly flexible wing configurations during low-speed flutter testing. These findings corroborate observations of nonlinear aeroelastic phenomena across multiple aerospace applications. For instance, high-altitude long-endurance (HALE) aircraft frequently exhibit persistent LCOs stemming from geometric nonlinearities in their slender wings [55]. Similarly, store separation events can induce transient LCOs due to sudden mass asymmetry [65], while control surface freeplay often generates non-smooth LCOs through hinge nonlinearities [66].

Despite experimental evidence, nonlinear aeroelastic effects are frequently disregarded in computational design processes. This omission primarily stems from the

substantial increase in model complexity, prohibitive computational costs for parametric studies, and convergence challenges inherent to nonlinear solution methods [52]. Such oversights fundamentally constrain the design space for modern aerospace systems, particularly for next-generation composite wings, morphing aircraft configurations, and high-efficiency slender structures where nonlinear effects dominate the aeroelastic response.

2.2 Numerical Methods in Dynamic Aeroelaticity

2.2.1 Nonlinear Aeroelastic Analysis

The onset of LCO typically arises at a specific type of bifurcation known as a Hopf bifurcation [67]. Both theoretical analyses and experimental investigations have demonstrated that Hopf bifurcations coincide with the flutter points of aeroelastic systems [6, 60]. The numerical continuation process leverages previous solutions of the system and the equations of motion to accurately predict subsequent solutions with respect to a chosen continuation parameter.

The fundamental principle of the process is illustrated in Figure 2.3. An initial guess is made for the solution of the system (y in Figure 2.3) at a specified point (x in Figure 2.3). This point is refined by solving a set of residual equations until it lies 'on the branch'. Once a point 'on the branch' is identified, an initial guess close to this point is made, with a small step forward in the continuation parameter (x in Figure 2.3), and the residual equations are solved again to refine the point, which is taken as the next point in the continuation. This iterative process is continued for as long as desired by the user. The resulting branch reveals the nonlinear behaviour of the system and is valuable as it can change direction with respect to the continuation parameter, potentially indicating multiple solutions at the same point in x.

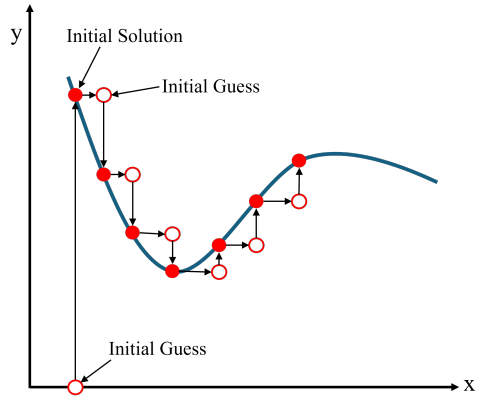

Figure 2.3: Diagram illustrating the numerical continuation method, where a solution branch of a nonlinear system is tracked as a parameter is varied to explore new solutions

Various methods, primarily employing a predictor-corrector approach, have been developed to provide rough estimates followed by refinement for improved accuracy. Among these, methods such as arclength and pseudoarclength continuation have proved effective in tracing solutions beyond turning points, thereby revealing diverse system behaviours.

General nonlinear behaviour of a subcritical aeroelastic system [3] described by a bifurcation diagram is laid out in Figure 2.4. In the bifurcation diagram in Figure 2.4b a stable linear solution exists until a hopf bifurcation is detected at $17.8m/s$. At velocities above this point, the response of the underlying linear system to a perturbation is negatively damped.

The underlying linear dynamics of the systems can typically be determined through eigenvalue analysis. This technique studies how the system's natural vibration modes change with airspeed. The structure's motion equations, which couple its mass, stiffness, damping, and aerodynamic forces (excluding any nonlinear functions), are expressed in matrix form and solved as an eigenvalue problem. Each eigenvalue represents a vibration mode's frequency and damping. As airspeed increases, the aerodynamic forces alter these values—when a pair of complex eigenvalues merge and their real parts become zero (indicating no damping), the system becomes unstable [68].

Taking nonlinear effects into consideration following eigenvalue analysis, numerical continuation is carried out iteratively starting at the bifurcation point. Unstable LCO

are identified at velocities below the bifurcation point and are tracked until a turning point. Following the turning point, stable LCO are tracked. This describes a system where two possible solutions exist between the turning point and the hopf bifurcation point, a stable damped solution and a LCO. Physically, unstable LCO represent a non-converging trajectory that exhibits instability over time. This means following nonlinear areoelastic analysis, the safe operating velocity of the system in Figure 2.4 is shifted from $17.8m/s$ to $13.7m/s$ at the turning point of the bifurcation diagram.

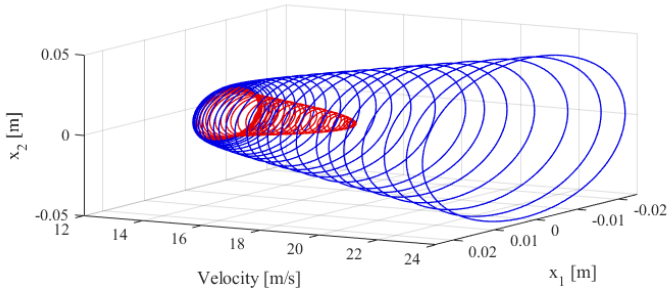

(a) Three-dimensional subcritical bifurcation diagram

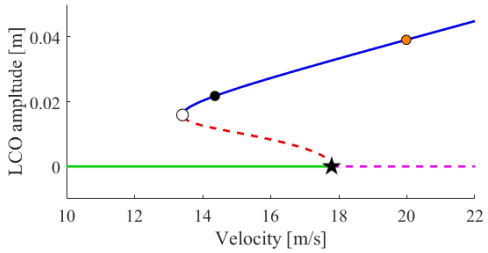

(b) Two-dimensional subcritical bifurcation diagram for 2 DoF aerfoil system [69] (– stable eigenvalues) (- - unstable eigenvalues) (⋆ hopf bifurcation) (◯ turning point)

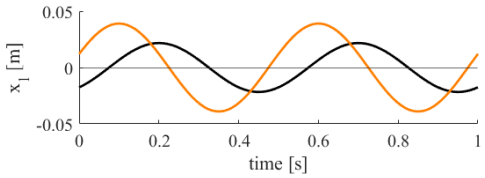

(c) LCO time histories ($14.5m/s$ •) ($20m/s$ •) from (b)

Figure 2.4: Subcritical bifurcation diagram with hopf bifurcation at $17.8m/s$ for 2 DoF aerfoil system [3] (– stable LCO),(- - unstable LCO)

Current state-of-the-art bifurcation analysis software predominantly employs orthogonal collocation methods for LCO tracking and characterisation [70]. This time-domain approach discretises periodic orbits into temporal elements, approximating the solution variables through high-order polynomials on each interval and enforcing the governing equations at Gauss-Legendre collocation points [71]. Such techniques form the computational backbone of widely adopted packages including MAT-

CONT (**MAT**LAB **CONT**inuation) [72], AUTO (**AUTO**matically) [73], and COCO (**CO**ntinuation **CO**re) [74]. While these methods achieve excellent numerical accuracy for low-dimensional systems, their application to large-scale problems remains constrained by memory requirements that scale polynomially with system dimension, leading to prohibitive computational costs for industrial-scale aeroelastic analyses. In a Fourier series approach, the computational load scales linearly with harmonic order. Although time-domain methods may offer slight efficiency advantages for simple low-order systems, the Fourier approach exhibits superior scalability for large, complex systems [75]. The computational challenges persist even when adopting frequency-domain approaches like HBM. High-fidelity systems demand careful consideration of multiple harmonic components, each introducing additional algebraic equations to the nonlinear system.

These computational constraints highlight the critical need for model calibration against experimental data. Accurate nonlinear system identification is crucial for ensuring that mathematical models effectively represent the key characteristics of LCOs. This, in turn, guarantees that the predicted operational envelope of aerospace systems reflects the true behaviour of the system under various operating conditions. Without precise identification, the model may fail to capture critical dynamic phenomena, potentially leading to miscalculations of system performance, stability, and safety margins. Therefore, achieving a high degree of accuracy in nonlinear system identification is fundamental for reliable predictions and the optimal design of aerospace systems. Recent advances in sparse identification of nonlinear dynamics (SINDy) and machine learning-enhanced system identification show particular promise for balancing accuracy with computational tractability in this context [76, 77]. However, both methods can be computationally expensive and can face limitations such as reliance on large, high-quality data sets.

Nonlinear aeroelastic analysis demands sophisticated computational strategies to address the intricate coupling between structural nonlinearities (geometric, freeplay, damping) and unsteady aerodynamic loads. Conventional time-domain methods, such as direct numerical integration via Runge-Kutta schemes, solve the full nonlinear equa-

tions of motion iteratively, making them versatile for transient analyses but prohibitively expensive for parametric studies of periodic responses [52]. While shooting methods can locate LCOs more efficiently by solving boundary value problems, their convergence remains sensitive to initial guesses in high-dimensional systems. Frequency-domain techniques, particularly HBM, offer a compelling alternative by approximating steady-state solutions using truncated Fourier series and transforming the differential equations into nonlinear algebraic systems via the Alternating Frequency Time (AFT) technique—this proves especially effective for systems with smooth, periodic nonlinearities [62]. Bifurcation analysis tools like orthogonal collocation (e.g., MATCONT, AUTO) provide rigorous tracking of solution branches and stability boundaries, but their reliance on polynomial expansions limits scalability for large-scale industrial applications [70].

Recent advances suggest that the future of efficient yet accurate nonlinear aeroelastic analysis lies in hybrid approaches combining data-driven techniques with frequency-domain frameworks. Machine learning-enhanced HBM, for instance, can leverage experimental or high-fidelity simulation data to calibrate reduced-order nonlinear models while preserving the computational efficiency of frequency-domain analysis [78]. Similarly, Koopman operator theory enables the embedding of nonlinear dynamics into linear infinite-dimensional spaces, facilitating the use of frequency-domain tools for strongly nonlinear systems [79]. These hybrid strategies not only mitigate the curse of dimensionality inherent in traditional methods but also bridge the gap between data-rich experimental characterisation and physics-based modelling. As aerospace systems grow more flexible and lightweight, such synergistic combinations of data-driven insights and frequency-domain efficiency may prove indispensable for reliable LCO prediction and flutter boundary estimation in industrial design workflows.

2.2.2 Limit-Cycle-Oscillation Analysis

The characterisation of LCO behaviour typically requires nonlinear analyses that take a not insignificant amount of time compared to linear analysis, particularly through the generation of bifurcation diagrams. Both the construction of these diagrams and subsequent stability assessment involve more complex mathematical techniques compared to

those used in linear systems, often leading to the omission of nonlinear analyses during preliminary design phases. This limitation consequently restricts the available design space [46] and presents challenges for data-driven approaches to nonlinear aeroelastic analysis, which depend on efficient generation of training datasets despite their growing prominence in aerospace applications [47, 48]. These constraints underscore the need for more efficient computational methods for LCO prediction in aeroelastic systems.

HBM present a computationally efficient alternative for determining maximum LCO response amplitudes. The HBM approach approximates periodic LCO motion using Fourier series coefficients in the frequency domain, with the AFT scheme enabling evaluation of diverse nonlinear force types [80]. Compared to conventional time-domain methods that require storage of complete time histories, HBM only necessitates retention of a limited set of coefficients. This methodology proves particularly advantageous for analysing periodic responses in strongly nonlinear systems where time-domain simulations become prohibitively expensive.

However, several challenges persist in HBM implementation:

- Ensuring robust convergence across parameter spaces
- Managing computational costs associated with higher harmonic orders
- Accurate representation of nonsmooth nonlinearities

Existing research demonstrates HBM's superior computational efficiency compared to alternatives like the shooting method while maintaining comparable accuracy [81,82]. Karkar's comparative study [71] further established HBM's robust convergence characteristics for certain nonlinear mechanical systems when contrasted with orthogonal collocation methods. Nevertheless, the literature reveals significant gaps in comprehensive comparisons between HBM and contemporary alternatives, especially within aeroelastic applications [71, 83]. Current investigations remain largely limited to low-harmonic analyses or forced non-autonomous systems [84]. While tools like the NLvib (**N**on**L**inear **vib**rations) package implement HBM, their focus on generic nonlinear mechanical systems and lack of frequency-domain stability analysis capabilities restrict their direct applicability to aeroelastic problems [85]. Despite differences in existing

bifurcation software, the predominant tools rely on orthogonal collocation methods for tracking and modelling LCO [70]. Orthogonal collocation, a time-domain method, segments a periodic orbit into intervals, represents unknown variables using polynomials on each interval, and collocates the governing equations at Gauss points [71]. Orthogonal collocation techniques are integrated into widely used bifurcation software packages such as MATCONT, AUTO, and COCO [72–74]. However, despite their accuracy, these methods are seldom applied to larger systems due to substantial memory requirements, leading to high computational costs.

2.2.3 Limit-Cycle-Oscillation Stability

The stability of LCOs represents a crucial consideration in frequency-domain analyses, particularly when employing HBM. Mathematically, LCOs correspond to periodic solutions of nonlinear dynamical systems, characterised by closed trajectories in phase space [54]. Their stability properties determine the system's response to small perturbations, with stable LCOs acting as attractors that draw in nearby trajectories, while unstable LCOs serve as repellers from which trajectories diverge.

In an engineering context, this distinction carries significant implications. Stable LCOs manifest as bounded oscillatory regimes that may represent acceptable operational conditions, whereas unstable LCOs typically demarcate bifurcation points that often precede dangerous aeroelastic instabilities [61]. Figure 2.5 illustrates this fundamental difference through comparative phase-space portraits and time histories for LCOs of identical amplitude but opposing stability characteristics on a Van der Pol oscillator (where x is a generalised coordinate / degree of freedom). The black line represents a stable LCO. If a stable LCO is identified following a perturbation, the system will converge to that stable shape. In contrast, the other lines illustrate the system's behavior when an unstable LCO of the same amplitude is identified. If a perturbation slightly larger than the amplitude of the unstable LCO is applied, the system's response will increase in amplitude, as shown by the blue line. Conversely, if the perturbation is slightly smaller, the system's response will decrease in amplitude, as indicated by the red line. In both cases, the presence of an unstable LCO means the system will diverge

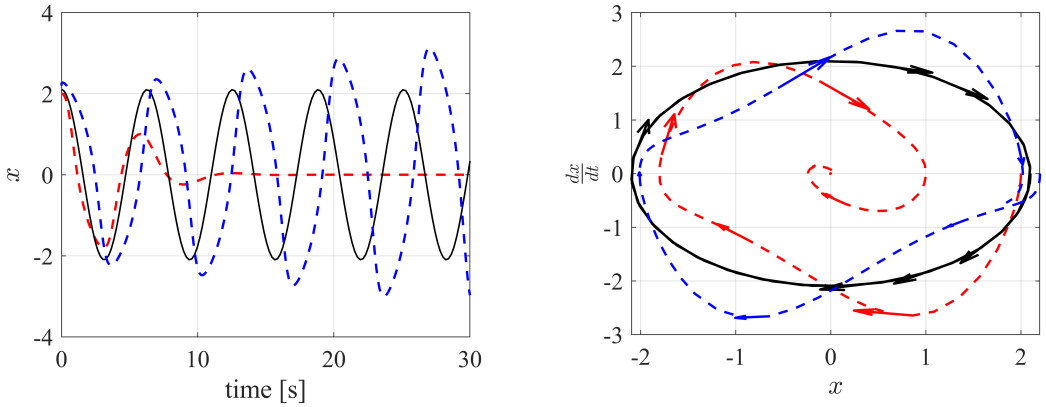

Figure 2.5: LCO stability demonstration on Van der Pol oscillator [4] (– stable), (- - unstable decay), (- - unstable growth) (a) Time history, (b) Phase plot

from it, with the steady-state solution shifting away from the unstable LCO.

A notable challenge emerges when applying HBM to stability assessment, as the method converges to both stable and unstable periodic solutions indiscriminately [86]. When applying the HBM alone, without conducting specific stability analysis of the oscillations, the identified LCO cannot be directly classified as stable or unstable This limitation necessitates the application of complementary stability analysis techniques, such as perturbation analysis of the harmonic balance equations, or numerical continuation methods with stability tracking. The most common method is implementation of Floquet theory, which examines the behavior of small perturbations around a periodic orbit by linearising the system. The stability of the orbit is determined by the Floquet multipliers—the eigenvalues of the linearized system. If all multipliers have magnitudes less than 1, the orbit is stable; if any have a magnitude greater than 1, the orbit is unstable, meaning the system will diverge from the limit cycle [87, 88]. The requirement for such post-processing underscores the importance of rigorous stability verification when employing HBM for practical engineering applications.

The conventional estimation of LCO stability typically involves time domain methods, such as Floquet analysis. However, as frequency domain methods gain prominence in LCO analysis, there is a growing interest in techniques that directly compute stability in the frequency domain. Guillot et al. [89, 90] demonstrated the use of the Hill's

matrix for computing the stability of LCO modeled by Fourier series through eigenvalue analysis. Lazarus and Thomas demonstrated the method's accuracy on a forced Duffing oscillator system [91]. While effective, this method tends to be computationally demanding, especially when dealing with large numbers of harmonic orders necessary for modelling complex nonlinear systems, leading to extended computation times. For large-scale scenarios, stability analysis using the Hill method can be more numerically costly than computing periodic motion [92, 93]. Hill's method determines stability through eigenvalue analysis of the truncated system matrix, but requires full eigensolution and sorting to identify the critical eigenvalues. This process grows computationally prohibitive for high-degree-of-freedom systems, as both the eigenvalue calculation and necessary sorting scale poorly with system size [91].

In recent developments, the Koopman operator has been employed to derive the monodromy matrix directly from Hill's matrix, as elucidated by Bayer and Leine [94]. In the Koopman framework, the dynamical system is characterised by the evolution of functions on the state space over time. This method elevates the problem to a higher-dimensional space where the system demonstrates more predictable behaviour. This innovative approach significantly reduces the number of eigenvalues needed for stability computation, aligning it with the number of degrees of freedom in the system. Consequently, this advancement holds promise for enhancing the efficiency of stability analysis in the frequency domain. However, it has not been applied and validated to nonlinear smooth dynamical systems as well as complex aeroelastic systems.

2.3 System Identification in Nonlinear and Data-Driven Contexts

2.3.1 Nonlinear System Identification and Model Updating

Nonlinear System Identification is very challenging in aeroelasticity. Firstly, the computational expense of nonlinear aeroelastic simulations can be relatively demanding even for low DoF systems, especially using time domain solvers. The duration of nonlinear simulations may not be excessively long—typically only a few seconds on a standard

PC—but compared to linear analysis, which often takes only milliseconds, nonlinear simulations are considerably more time-consuming. This becomes a significant issue when the model needs to be run potentially thousands of times, such as when determining model parameters, quantifying uncertainty, or training a data-driven models. Secondly, experimental testing of nonlinear autonomous systems is challenging due to the limitations of most linear experimental methods [95]. Thirdly, the form of nonlinear functions can be uncertain and usually lacks explicit expressions, which can make it unclear if inaccuracies between the experimental data and numerical data are down to errors in the mathematical model that is selected or errors from experimental results. When using deterministic model updating methods, it is common to face issues with parameter non-identifiability, as certain combinations of nonlinear parameters can lead to comparable results [96, 97]. Recent deterministic approaches [98–100] have shown promise in determining aeroelastic LCO but issues have been highlighted. In using universal approximates to replicate aeroelastic bifurcation diagrams, Beregi et al. [101] found cases of overiftting data. This problem is often encountered when using deterministic approaches with inherently noisy data.

Nonlinear aeroelastic systems present unique challenges, including inherent parameter uncertainties, sensitivity to small variations, and inevitable discrepancies between first-principles models and experimental observations. These factors are particularly critical when predicting phenomena like limit-cycle oscillations, where simplified models and unsteady aerodynamic approximations can lead to significant prediction errors. Furthermore, structural degradation and operational configuration changes progressively erode model fidelity over time. Model updating emerges as an essential methodology to address these challenges, systematically reconciling numerical models with empirical data through parameter calibration, thereby maintaining predictive accuracy throughout the system's operational lifecycle [102].

Model updating has been extensively employed over the past few decades to calibrate the parameters of mathematical and computational models using experimental or operational data [103,104]. It involves the refinement of models—such as finite element, aerodynamic, or control system representations—to better reflect observed system be-

haviour. By systematically adjusting selected parameters, model updating aims to minimise discrepancies between numerical predictions and experimental measurements, thereby bridging the gap between idealised simulations and real-world responses.

Given a set of experimental data, model updating facilitates the identification of an appropriate mathematical model capable of accurately describing the underlying physical system. Common model updating approaches include sensitivity-based methods, which are typically applied to relatively simple, linear systems [105]; Bayesian inference techniques, which are particularly well-suited for handling measurement noise and uncertainty [106]; and data-driven or machine learning methods, which offer greater flexibility and scalability for the analysis of complex, nonlinear systems [107,108]. Each of these approaches offers distinct advantages depending on the structure of the system being modelled, the quality of the data available, and the level of uncertainty present.

A majority of existing techniques provide deterministic estimates of parameters such as Least Squares minimisation, Sensitivity-based model updating and Levenberg-Marquardt algorithm [109–112]. Whilst direct deterministic methods are very effective for linear systems, it is subject to high computational expense for complex and high dimensional dynamical systems, and is very sensitivity to the noise in the experimental data [113]. For nonlinear aeroelastic systems, Beregi employed a classical model update approach estimate nonlinear parameters in a subcritical aerofoil test case using normal form theory. It was concluded that the accuracy of the bifurcation diagram should be improved to account for different uncertainties in the experimental data [101, 114]. Recently, researchers have acknowledged the importance of quantifying uncertainties in the nonlinear behaviour of systems, shifting the deterministic model updating approach to probabilistic ones [57, 113].

Bayesian Model Updating (BMU), originally introduced in [115], has emerged as one of the most robust and versatile probabilistic techniques for nonlinear parameter estimation [116–118]. A key advantage of BMU over alternative probabilistic model updating methods, such as Maximum Likelihood Estimation (MLE), lies in its inherent ability to incorporate prior knowledge in a principled and transparent manner [119].Through Bayesian inference, the posterior Probability Density Function (PDF) of the model pa-

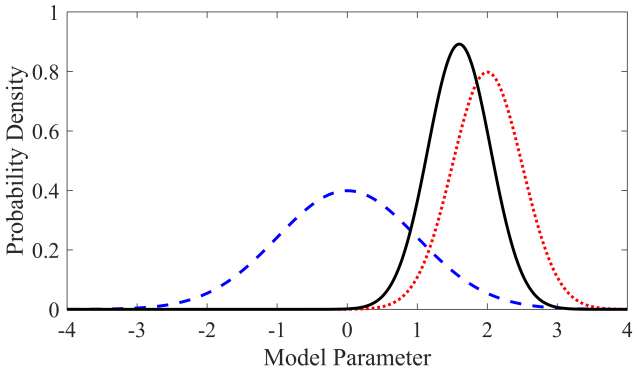

Figure 2.6: Visual representation of Bayesian updating. The prior distribution (–) encodes initial beliefs about a parameter. The likelihood function (- -) reflects the probability of observing new data under various parameter values. The resulting posterior distribution (–) represents updated beliefs after incorporating the evidence, calculated via Bayes' Theorem. Arrows indicate the direction of information flow during the update process.

rameters is computed by conditioning on observed measurement data. These posterior PDFs are critical in quantifying the uncertainty of parameter estimates and enable the derivation of intervals of probability around the predicted values [120].

Figure 2.6 presents a conceptual overview of the Bayesian updating process. The prior distribution encodes initial assumptions about the parameters before data is observed. The likelihood function quantifies the plausibility of the observed data under varying parameter values. By applying Bayes' theorem, these components are combined to form the posterior distribution, which reflects updated beliefs. This posterior not only shifts toward the data but also balances prior information with new evidence, yielding a probabilistic characterisation that fully accounts for uncertainties in both.

The efficiency of the stochastic model updating is highly dependent on the quality of the sampling methods. Iterative sampling techniques are preferred due to their ability to efficiently explore high-dimensional and correlated parameter spaces, handle non-standard posterior shapes, facilitate iterative improvement, support model comparison, and provide reliable UQ. The most common methods are Metropolis-Hastings Markov Chain Monte Carlo (MCMC), Transitional Markov Chain Monte Carlo (TMCMC) and the Sequential Monte Carlo sampler (SMC) [121]. Each method provides case dependent benefits, experiments are often required to select an appropriate sampling

method. Comparisons between sampling methods has been carried out partially in the case of structural health monitoring [122–124]. An advantage to TMCMC is evidence function can be calculated as a byproduct for model selection. Song et.al. utilised TMCMC in successfully selecting a nonlinear model for a wing engine structure [125].

2.3.2 Data-Driven Methods in System Identification

Data-driven modelling encompasses a range of techniques that augment or partially replace first-principles physics with patterns extracted from observed data. The degree of reliance on empirical data versus physical laws varies significantly across methods: from grey-box approaches that combine known physics with learned corrections, to purely statistical models that reconstruct system behaviour without explicit physical constraints. In the context of nonlinear aeroelastic analysis, surrogate modelling offers a compelling solution to the computational bottleneck posed by the thousands of simulations typically required for BMU. Among available data-driven approaches, Polynomial Chaos Expansion (PCE) and neural networks have demonstrated particular efficacy for nonlinear response prediction [126–129]. While PCE methods have shown promise for UQ in aeroelastic applications [130], their practical implementation faces challenges due to the factorial growth in required training data with increasing parameter space dimensionality [131].

These approaches harnesses machine learning, statistical methods, and signal processing techniques to extract underlying relationships and system dynamics directly from experimental or operational measurements. A particularly powerful implementation of this methodology involves surrogate models (alternatively termed metamodels or emulators) - computationally efficient approximations of high-fidelity models that replicate input-output relationships while dramatically reducing computational expense. These models can subsequently serve as computationally efficient substitutes for high-fidelity systems, enabling accurate prediction of complex nonlinear behaviour. This enables rapid design space exploration, optimisation, and UQ in scenarios where conventional simulations would prove prohibitively expensive [132, 133].

For cases with limited training data, kernel-based surrogate models - particularly

Kriging (Gaussian Process regression) - have emerged as a robust alternative. Kriging models excel at capturing complex nonlinear relationships while maintaining computational efficiency, even with sparse datasets (typically time-series) [134–136]. A distinct advantage of Kriging lies in its inherent flexibility to incorporate new observations through sequential updating of the model framework [137, 138]. This capability has proven valuable in uncertainty propagation studies, as demonstrated by Tartaruga's analysis of landing gear bifurcation diagrams [48] and Sun et al.'s investigation of ring damper designs [136].

Recent advances have introduced physics-informed machine learning approaches to enhance predictive accuracy. Lee et al. [5] developed such a framework for aerofoil bifurcation analysis, revealing that conventional deterministic estimation may lead to overfitting when dealing with noisy measurement data. Their work further highlights the importance of employing nonlinear solvers specifically adapted for periodic solutions to improve training algorithm performance.

Data-driven model updating represents an advanced computational methodology that iteratively refines physics-based models through the integration of observational data, effectively combining first-principles modelling with machine learning techniques. This approach addresses the persistent challenge of discrepancies between theoretical models and observed system behaviour.

While the importance of uncertainties in data-driven models for probabilistic response is acknowledged, existing studies often neglect a comprehensive investigation of their effects, primarily due to the high accuracy of data-driven approaches. Current methodologies predominantly focus on aleatory uncertainties stemming from measurement errors in experimental data. Conventional Kriging models, for instance, treat inputs as deterministic while attributing output variability to measurement noise or intrinsic uncertainties [139], modelling epistemic uncertainty through a Gaussian noise term as output variance. However, even in well-trained models with relatively low output variance, the interplay between aleatory and epistemic (polymorphic) uncertainties can substantially influence safety margins [140, 141]. Established techniques for polymorphic uncertainty propagation, such as the probability-box (p-box) method,

are widely adopted in engineering design [142–144].

Data-driven models inherently incorporate uncertainties [145, 146], with Kriging models, for example, providing predictions in the form of a mean estimate accompanied by intervals of probability [147]. Consequently, Kriging has found extensive application in hybrid uncertainty UQ [148, 149] and aeroelastic optimisation [150], where the framework must accommodate both uncertain inputs and outputs, necessitating polymorphic UQ techniques. Diverse methodologies, including p-boxes [151] and possibility theory [152], have been employed in aeroelastic analyses. For instance, Wang and Qiu [153] examined uncertainty propagation in the flutter behaviour of aeroelastic wings using the interval perturbation method, whereas Zheng and Wang [154] applied an interval-based Probability Density Function (PDF) evolution method to assess flutter stability boundaries in aeroelastic systems with polymorphic uncertainties.

Chapter 3

Frequency Based LCO Prediction & Validation

3.1 Introduction

This chapter aims to propose a computationally efficient method for estimating LCO behaviour and determining their stability in aeroelastic systems. By doing so, the first stage of the framework proposed in Section 1.2 will be complete, which will mainly be used for the collection of data to train surrogate models in following chapters.

The objective is to develop a framework for LCO analysis, specifically designed for integration within a data-driven methodology. This is accomplished by conducting LCO analysis solely in the frequency domain, combining HBM continuation with Koopman operator based stability analysis. To validate the proposed method numerically, the comparison is made with state-of-the-art time-domain solvers, namely MATCONT [155] and COCO [156], in both smooth and nonsmooth nonlinear case studies.

First, the methodology for a general aeroelastic frequency domain solver for LCO is pretended. This methodology encompasses a detailed explanation of the HBM continuation scheme and frequency domain stability analysis. A comprehensive outline of the HBM methodology is detailed, incorporating Koopman operator based stability analysis for predicting LCO behaviours. Subsequently, the methodology is applied to a numerical test case, incorporating both smooth and nonsmooth nonlinearities. The

test case results are then validated by comparison with outcomes from MATCONT and COCO software. Ultimately, conclusions are drawn based on the numerical validation of the proposed framework. The main findings of this chapter have been published in [157].

3.2 Methodology

In this section, the computational framework based on HBM and Koopman operator based stability analysis is presented. First, the standard mathematical format is introduced, laying out the basic principles behind HBM continuation based on the work in Ref [54]. The AFT procedure is then outlined, as it is essential to all steps of this methodology. Finally, two methods of determining LCO stability in the frequency domain are described: the standard Hill's method and Koopman operator based analysis. Hill's method is presented as the fundamentals are essential for the Koopman based analysis.

3.2.1 General Equations of Motion

The methods outlined here revolve around mathematical models that can be formulated into the second-order differential equation depicted in Equation 3.1. Nonlinear aeroelastic systems can be organised in this manner under the assumption that structural forces counterbalance aerodynamic forces.

The mathematical model of generic nonlinear dynamical systems for mechanical systems can be expressed in the following form:

$$\mathbf{M}\ddot{\boldsymbol{x}}(t) + \mathbf{D}\dot{\boldsymbol{x}}(t) + \mathbf{K}\boldsymbol{x}(t) + \boldsymbol{f}_{nl}(\ddot{\boldsymbol{x}}, \dot{\boldsymbol{x}}, \boldsymbol{x}) = \mathbf{F}(\ddot{\boldsymbol{x}}, \dot{\boldsymbol{x}}, \boldsymbol{x}, t) \tag{3.1}$$

Where $\ddot{\boldsymbol{x}}, \dot{\boldsymbol{x}}, \boldsymbol{x}$ denotes the vector of system's acceleration, velocity and displacement; $\mathbf{M}$, $\mathbf{D}$ and $\mathbf{K}$ are the structural mass, damping and stiffness matrices respectively. $\boldsymbol{f}_{nl}$ is used to represent different types of structural nonlinearities attached to the system as a nonlinear function of the system's response. $\mathbf{F}$ is the external force applied to the mechanical systems. For the forced response, $\mathbf{F}$ is independent of the system's response

in $\ddot{\boldsymbol{x}}, \dot{\boldsymbol{x}}, \boldsymbol{x}$. For generic aeroelastic systems, the external force will be dependent on the system's response, which can be expressed in the following form [158]:

$$\mathbf{F}(\ddot{\boldsymbol{x}}, \dot{\boldsymbol{x}}, \boldsymbol{x}, t) = \mathbf{A}(\rho, V)\ddot{\boldsymbol{x}}(t) + \mathbf{B}(\rho, V)\dot{\boldsymbol{x}}(t) + \mathbf{C}(\rho, V)\boldsymbol{x}(t) \tag{3.2}$$

Where matrices **A**, **B** and **C** are aerodynamic matrices which are dependent on air density ρ and free-stream velocity V (which acts externally on the system and is not to be confused with velocity of the system's DoF $\dot{\boldsymbol{x}}$). All matrices are size $N \times N$ where N is the number of degrees of freedom of the system. In either forced or aeroelastic systems, the second order differential equation is restructured into a first-order state equation, as shown in Equation 3.3:

$$\dot{\mathbf{x}} = \mathbf{Q}\mathbf{x} + \mathbf{q}_n f_{nl}(\ddot{\boldsymbol{x}}, \dot{\boldsymbol{x}}, \boldsymbol{x}) \tag{3.3}$$

Where $\mathbf{x}$ is $[\dot{\boldsymbol{x}}, \boldsymbol{x}]^T$; q_{nl} is utilised to implement the nonlinear equations in the degrees of freedom they impact and the matrix **Q** is denoted as the linear matrix, as it completely represents the linear dynamics of the system. Where:

$$\mathbf{Q} = \begin{bmatrix} (\mathbf{M}-\mathbf{A})^{-1}(\mathbf{B}-\mathbf{D}) & (\mathbf{M}-\mathbf{A})^{-1}(\mathbf{C}-\mathbf{K}) \\ 0_{N\times N} & I_{N\times N} \end{bmatrix} \mathbf{q_n} = \begin{bmatrix} -(M-A)^{-1} \\ 0_{N\times 1} \end{bmatrix} \tag{3.4}$$

The matrix **Q** will be denoted as the linear matrix, as it completely represents the linear dynamics of the system. Identity matrix of size N is represented by $I_{N\times N}$. This structural arrangement facilitates the conduct of linear analysis to identify the flutter point through the following procedure. By focusing solely on the linear aspect of the system, Equation 3.3 can be expressed as the eigenvalue problem $\dot{\mathbf{x}} - \mathbf{Q}\mathbf{x} = 0$. Assuming an oscillatory response $\boldsymbol{x} = \boldsymbol{x}_o e^{\psi t}$, the eigenvalue problem is formulated as:

$$[\mathbf{Q} - \mathbf{I}\psi_{ij}]\,\boldsymbol{\phi} = 0 \tag{3.5}$$

Where ψ_{ij} are eigenvalues in the conjugate pair

$$\psi_{ij} = -\zeta_{ij}\omega_{ij} \pm i\omega_{ij}\sqrt{1-\zeta_{ij}} \tag{3.6}$$

The undamped natural frequencies are denoted by ω_{ij}, while ζ_{ij} represents the damping ratios. Matrix $\boldsymbol{\phi}$ encompasses the corresponding eigenvectors. Flutter manifests as unstable, negatively damped oscillations. Based on this characterisation, it becomes evident that if any of the real parts of Equation 3.6 are positive, the system exhibits dynamic instability [159].

3.2.2 Harmonic Balance Method

In nonlinear systems, the loss of linear stability typically leads to the emergence of LCO at a hopf bifurcation point. While analysis of the underlying linear system can pinpoint hopf bifurcation points, numerical continuation from such points often reveals the presence of LCO solutions even before the loss of linear stability.

Assuming that the system's dynamic response after a hopf bifurcation is an LCO, we can represent the time response of a single degree of freedom x and it's velocity component $\dot{x}$ using the Fourier series. The system can then be expressed through multi-harmonic response and solved in the frequency domain:

$$x(t) = X_0 + \sum_{k=1}^{l} X_{k,s} \sin k\omega t + X_{k,c} \cos k\omega t \tag{3.7}$$

The variable l denotes the harmonic order of the response, while X_0, $X_{k,s}$, and $X_{k,c}$ represent Fourier coefficients. This assumed response is fundamental to HBM, facilitating the transformation of the system from the time domain to the frequency domain. Instead of necessitating a time integration process spanning potentially hundreds to thousands of time steps, only $N \times (2l+1)$ data points are required to characterise the dynamic behaviour of the system. In total, with N degrees of freedom, there are N values of x, each corresponding to a set of l Fourier coefficients. Thus, for each degree of freedom, there is a distinct set of l Fourier coefficients.

An additional step is necessary to model the nonlinear force component of Equation

3.3. Nonlinear forces are typically depicted as nonlinear time functions. Since they do not adhere to linearity with respect to states or represent explicit functions of time, direct transformation to the frequency domain is impractical [80]. However, the nonlinear force response can be transformed to the frequency domain via the Alternating Frequency Time (AFT) procedure, facilitating the determination of F_0, $F_{k,s}$, and $F_{k,c}$ as (again just looking at a single DoF):

$$f_{nl}(t) = F_0 + \sum_{k=1}^{l} F_{k,s} \sin k\omega t + F_{k,c} \cos k\omega t \tag{3.8}$$

Estimated values of X_0, $X_{k,s}$, $X_{k,c}$, and ω (the estimation will be detailed in Section 3.2.3) are utilised in Equation 3.7 to derive the time domain response over a period. Subsequently, the time domain nonlinear force response $f_{nl}(t)$ is determined. A fast Fourier transform algorithm (FFT) is then applied to estimate Fourier coefficients based on the time domain nonlinear force response. This is commonly known as the AFT procedure, laid out in Figure 3.1. Leveraging these relationships, the equation of motion depicted in Equation 3.3 can be reformulated into a set of algebraic residual equations, which are solved numerically. Accuracy can be assessed through convergence studies and benchmarking against numerical tools such as COCO and MATCONT. A converged HBM result with respect to l can generally be assumed to be reliable for the system under consideration, in the absence of such comparisons.

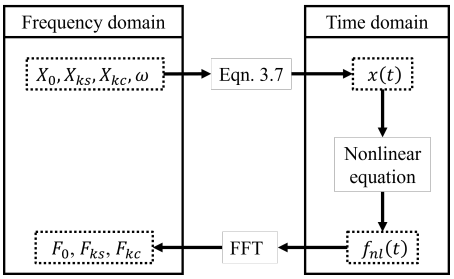

Figure 3.1: Flowchart of the AFT procedure

3.2.3 Continuation Scheme

A continuation scheme is formulated based on the principles of HBM. Its aim is to determine the amplitude and frequency of LCO, along with their corresponding values of a chosen continuation parameter. Given the uncertainty in the shape of the bifurcation diagram, both the continuation parameter λ and LCO frequency ω are treated as unknowns in this scheme. The continuation parameter is an auxiliary variable used to parameterise and trace a continuous family of solutions to a nonlinear system as system conditions or parameters vary. Typically, in an aeroelastic system, velocity is used as the continuation parameter. Residual equations are formulated and solved iteratively throughout the continuation process, considering only the degrees of freedom of the system that exhibit nonlinearities. Consequently, the linear part of the system is solved separately, typically relying on the linear system matrix $\mathbf{Q}$. The setup of these residuals is described in the following, along with the additional constraints required, as both λ and ω are unknown.

Linear Equation

In order to calculate the response of the nonlinear degree of freedom, the response of the linear part of the system $\mathbf{x}_L$ is evaluated. $\mathbf{x}_L$ represents the degrees of freedom of the system with the nonlinear degrees of freedom $\boldsymbol{x}_{nl}$ removed. The linear and nonlinear parts of the system are solved separately so $\mathbf{x}_L$ can be treated as a known when solving the nonlinear part, reducing the number of unknowns in the system. By removing the nonlinear degrees of freedom from Equation 3.3, the system can be rewritten as Equation 3.9. Equation 3.9 is treated as a non-autonomous forced system, with the nonlinear degrees of freedom's impact acting as the forcing term.

$$\dot{\mathbf{x}}_L = (\mathbf{Q})_{p,p}\mathbf{x}_L + (\mathbf{Q})_{p,u}\dot{\boldsymbol{x}}(t) + (\mathbf{Q})_{p,v}\boldsymbol{x}(t) + (\mathbf{q}_n)_p f_{nl}(t) \tag{3.9}$$

It is assumed the linear response of the system is also in the shape described by Equation 3.7. Here, $\overline{X}_0$, $\overline{X}_{k,s}$ and $\overline{X}_{k,c}$ are the linear Fourier coefficients. The subscript p denotes the linear degrees of freedom and v and $u$nomenclature$v$Positions in vector $\mathbf{x}$ related

to nonlinear degrees of freedom in $\dot{\boldsymbol{x}}$ represent the nonlinear degree of freedom and nonlinear differential respectively. Equation 3.7 and and the linear shape function are substituted into Equation 3.9. Performing Harmonic Balance by equating the constant, sine and cosine terms separately allows for System 3.10 to be constructed and hence, the linear Fourier coefficients to be obtained.

$$
\begin{gathered}
(\mathbf{Q})_{p,p} = -(\mathbf{Q})_{p,v}\overline{X}_0 - (\mathbf{q}_n)_p F_0 \\
\begin{bmatrix} -(\mathbf{Q})_{p,p} & -k\omega\mathbf{I} \\ k\omega\mathbf{I} & -(\mathbf{Q})_{p,p} \end{bmatrix} \begin{bmatrix} \overline{X}_{ks} \\ \overline{X}_{kc} \end{bmatrix} = \begin{bmatrix} -(\mathbf{Q})_{p,u}k\omega X_{k,c} + (\mathbf{Q})_{p,v}k\omega X_{k,s} \\ (\mathbf{Q})_{p,u}k\omega X_{k,s} + (\mathbf{Q})_{p,v}k\omega X_{k,c} \end{bmatrix} + \begin{bmatrix} (\mathbf{q}_n)_p F_{k,s} \\ (\mathbf{q}_n)_p F_{k,c} \end{bmatrix}
\end{gathered} \tag{3.10}
$$

Nonlinear equations

Once the Fourier's coefficients of the linear part are obtained, nonlinear section of Equation 3.3 gives the relationship as follows:

$$
\ddot{x}_{nl}(t) = (\mathbf{Q})_{u,p}\mathbf{x}_L + (\mathbf{Q})_{u,u}\dot{x}_{nl}(t) + (\mathbf{Q})_{u,v}x_{nl}(t) + (\mathbf{q}_n)_u f_{nl}(t) \tag{3.11}
$$

Linear Fourier coefficients, denoted by $\mathbf{x}_L = [\overline{X}0, \overline{X}_{k,s}, \overline{X}_{k,c}]$, are obtained by solving only the linear components of the system. Here onve again, the linear degrees of freedom or modes are labeled as p, while the nonlinear degrees of freedom and modes are designated as u and v, respectively. Substituting Equation 3.7 into Equation 3.11 yields the set of $N \times (2l+1)$ residual equations:

$$
\begin{aligned}
R_0 &= (\mathbf{Q})_{u,p}\overline{X}_0 + (\mathbf{Q})_{u,v}X_0 + (\mathbf{q}_n)_u F_0 \\
R_{k,s} &= -k^2\omega^2 X_{k,s} - (\mathbf{Q})_{u,p}\overline{X}_{k,s} - (\mathbf{Q})_{u,u}k\omega X_{k,c} - (\mathbf{Q})_{u,v}X_{k,s} - (\mathbf{q}_n)_u F_{k,s} \\
R_{k,c} &= -k^2\omega^2 X_{k,c} - (\mathbf{Q})_{u,p}\overline{X}_{k,c} + (\mathbf{Q})_{u,u}k\omega X_{k,s} - (\mathbf{Q})_{u,v}X_{k,c} - (\mathbf{q}_n)_u F_{k,c}
\end{aligned} \tag{3.12}
$$

In scenarios involving multiple nonlinear DoF, a set of $N \times (2l+1)$ residual equations are derived for each nonlinear degree of freedom. Incorporating λ and ω as unknowns necessitates formulating two additional residual equations. A common constraint imposed on the scheme is related to pseudo-arclength continuation [160,161]. Using point

j as the reference in the continuation, a prediction for $j+1$ is generated utilising tangential direction vectors. It is assumed that the converged solution for $j+1$ is orthogonal to the initial prediction, imposing the following constraint in the corrector stage during the numerical continuation:

$$R_{2l+2} = (X_{j+1} - X_{j+1,0})\frac{dX}{ds}_j + (\omega_{j+1} - \omega_{j+1,0})\frac{d\omega}{ds}_j + (\lambda_{j+1} - \lambda_{j+1,0})\frac{d\lambda}{ds}_j \tag{3.13}$$

Through this constraint, direction vectors ($\frac{d(X,\omega,\lambda)}{ds}$ where s denotes the non-dimensional arc-length) for the next continuation step are also obtained.

Another widely used constraint is based on the principle of orthogonality between the phase of degrees of freedom and their rates of change [71,162]. This assumption can be used to derive a relationship between j^{th} Fourier coefficients and the $j+1$ points:

$$R_{2l+3} = \sum_{k=1}^{l} -k(X_{k,c})_j(X_{k,s})_{j+1} + k(X_{k,s})_j(X_{k,c})_{j+1} \tag{3.14}$$

Both of these constraints are commonplace in continuation methods and are also employed in time-domain methods. Further details on each can be found in Ref [54,74]. With an equal number of residual equations and unknowns $[X_0, X_{k,s}, X_{k,c}, \omega, \lambda]$ (for $k = 1, \ldots, l$), the system can be numerically solved at each point in the continuation. Full details of how the continuation process is initiated, how each of the additional constraints are derived and how the system is solved is given in full detail in Appendix A.

The system can be solved iteratively typically through the Newton–Raphson procedure [54], shown in Appendix A.4. This involves linking displacements to rates of change through the Jacobian matrix $\boldsymbol{J} = d\dot{\mathbf{x}}/d\mathbf{x}$ via $\dot{\mathbf{x}} = \boldsymbol{J}\mathbf{x}$. While the Jacobian can be numerically evaluated through finite difference methods, this approach can be computationally demanding, particularly for large-scale systems [163]. Alternatively, the analytical Jacobian can be incorporated by defining it via a Fourier transform [83].

$$\boldsymbol{J}(t) = \boldsymbol{J}_0 + \sum_{k=1}^{l} \boldsymbol{J}_{k,s} \sin k\omega t + \boldsymbol{J}_{k,c} \cos k\omega t \tag{3.15}$$

From Equations 3.1 and 3.7 we can derive the Jacobi for each Harmonic order as:

$$\begin{aligned} \mathbf{J}_0 &= \mathbf{Q} + \mathbf{q}_n \left(\frac{\partial F}{\partial X}\right)_0 \\ \mathbf{J}_{k,s} &= \mathbf{Q} + \mathbf{q}_n \left(\frac{\partial F}{\partial X}\right)_{k,s} \\ \mathbf{J}_{k,c} &= \mathbf{Q} + \mathbf{q}_n \left(\frac{\partial F}{\partial X}\right)_{k,c} \end{aligned} \tag{3.16}$$

Approximations for $\left(\frac{\partial F}{\partial X}\right)_0$, $\left(\frac{\partial F}{\partial X}\right)_{k,s}$, and $\left(\frac{\partial F}{\partial X}\right)_{k,c}$ can be achieved by analytically transforming the time-domain derivation $\frac{dfnl}{d\mathbf{x}}(t)$ into the frequency domain using the inverse FFT procedure.

$$\frac{df_{nl}}{d\mathbf{x}}(t) = \left(\frac{\partial F}{\partial X}\right)_0 + \sum_{k=1}^{l} \left(\frac{\partial F}{\partial X}\right)_{k,s} \sin k\omega t + \left(\frac{\partial F}{\partial X}\right)_{k,c} \cos k\omega t \tag{3.17}$$

This necessity arises solely within the nonlinear degrees of freedom. An added advantage is that the Fourier coefficients of the Jacobian can be utilised to directly assess the stability of the response in the frequency domain, as elaborated in the subsequent section.

Additional details of the complete continuation scheme can be found in Appendix A. This includes the process for initiating the scheme and the derivation of the additional residual equations. Furthermore, it describes the application of the Newton-Raphson solver to solve these residual equations. Finally, the procedure for determining the direction vectors, which are used to calculate the subsequent points in the continuation, is also outlined.

3.2.4 Frequency Domain Stability Determination

Once a converged solution including LCO amplitude, frequency, and continuation parameter is achieved in the frequency domain, the stability of the oscillation must be determined. A stable LCO solution describes behavior where, following an initial perturbation, the system's response is drawn towards the LCO. Conversely, with an unstable LCO, the response moves away from the unstable cycle [164].

Time-domain analysis is used as a reference in the study, which relies on the use of monodromy matrix Φ_T (the $(N \times N)$ state transition matrix that describes how small perturbations to a periodic solution of a dynamical system evolve over one full period) to assess the stability of the system through its evolution in state changes over time. The monodromy matrix is illustrated in Equation 3.18 which portrays the evolution of the system's states over a single period T. It can usually be obtained as a byproduct of time-domain continuation processes where the stability of the system can be subsequently assessed based on its eigenvalues known as Floquet multipliers [165]. If the absolute value of any of the N Floquet multipliers exceeds 1, the system is deemed unstable. This approach is herein referred to as time-integration stability analysis.

$$\mathbf{x}_T = \Phi_T \mathbf{x}_0 \tag{3.18}$$

Hill's Method

In the frequency domain, the stability of an oscillation can be computed using Hill's method, which still applies Floquet theory [164]. The stability is determined based on the eigensolution of the truncated Hill's matrix $\mathbf{H}$ as follows:

$$\mathbf{H}_\infty = \begin{pmatrix} \ddots & \vdots & \vdots & \vdots & \iddots \\ \dots & \mathbf{J}_0 + \omega\mathbf{I} & \mathbf{J}_{1,s} & \mathbf{J}_{2,s} & \dots \\ \dots & \mathbf{J}_{1,c} & \mathbf{J}_0 & \mathbf{J}_{1,s} & \dots \\ \dots & \mathbf{J}_{2,c} & \mathbf{J}_{1,c} & \mathbf{J}_0 - \omega\mathbf{I} & \dots \\ \iddots & \vdots & \vdots & \vdots & \ddots \end{pmatrix} \tag{3.19}$$

The Hill's matrix is truncated to size $N(2l+1) \times N(2l+1)$:

$$\mathbf{H} = \begin{pmatrix} \mathbf{J}_0 + l\omega\mathbf{I} & \dots & \mathbf{J}_{-2l} \\ \vdots & \ddots & \vdots \\ \mathbf{J}_{2l} & \dots & \mathbf{J}_0 - l\omega\mathbf{I} \end{pmatrix} \tag{3.20}$$

Assuming $J_{k,s}$ and $J_{k,c}$ for $k > l$ are $N \times N$ zero matrices, as per standard Hill's method. N terms, referred to as Floquet exponents (distinct from Floquet multipliers), are

subsequently selected from the $N(2l+1)$ eigenvalues of the matrix $\mathbf{H}$ [90]. A numerical sorting algorithm is employed to identify eigenvalues corresponding to $k = 0$. The conventional approach involves sorting the eigenvalues based on the amplitude of their imaginary parts. The N eigenvalues with the smallest amplitude of imaginary parts are then selected as the Floquet exponents. Stability is determined by comparing the real parts of the Floquet exponents to zero. For the system to be deemed dynamically stable, all real parts must be below zero; otherwise, the system is unstable.

Koopman Operator Based Stability Analysis

Koopman lift theory can be introduced to reduce the computational cost of frequency domain stability analysis. The Koopman operator stability process operates under two assumptions to derive an approximation of the monodromy matrix. The first assumption is that the higher-dimensional space z can be utilised to estimate the lower-dimensional space $\mathbf{x}$ via:

$$\mathbf{x}(t) \approx \mathbf{x}_z(t) = \mathscr{P}(t)z(t) \tag{3.21}$$

Here, $\mathscr{P}(t)$ represents the time-dependent projection matrix that fulfils the condition $\boldsymbol{C}(t)z(t) = \mathbf{x}_z(t)$, with $z(t)$ composed of monomial terms and Fourier terms of the base frequency [94]. $z(t)$ can be then expressed as:

$$z(t) = \begin{pmatrix} Z_{-l}^1 e^{-il\omega t} \\ \vdots \\ Z_l^1 e^{il\omega t} \\ Z_{-l}^2 e^{-il\omega t} \\ \vdots \\ Z_l^N e^{il\omega t} \end{pmatrix} \tag{3.22}$$

Where l is the maximum frequency order, N is the maximum index of the monomial term and Z_l^N is the l^{th} Fourier coefficient of the N^{th} monomial term. The dimension of this orthogonal basis functions $z(t)$ is $N(2l+1)$. Here, these linear basis functions are ordered by the state at first and then by the frequency in an ascending order. Vector

$\mathbf{Z}_l$ is used to denote the vector containing the Fourier coefficients corresponding to the l^{th} frequency for each monomial term.

A common choice for the projection matrix $\mathscr{P}(t)$ in frequency-based projection is to select the zeroth harmonic, which corresponds to the steady-state or average behavior of the system providing insight into the system's mean behaviour or equilibrium states [94]. To select the components related to the zeroth harmonic of $z(t)$, the frequency domain projection matrix is defined as:

$$\tilde{\mathscr{P}} = (\mathbf{0} \dots \mathbf{0}\ \mathbf{I}_{n\times n}\ \mathbf{0} \dots \mathbf{0}) \tag{3.23}$$

The second assumption of the Koopman operator-based stability method is that the truncated Hill's matrix can be utilised to derive the state transition matrix of the high-dimensional space with [94]:

$$z(t) = \mathbf{U}^{\mathrm{T}} e^{\mathbf{H}t} \mathbf{U} z(0) \tag{3.24}$$

Where $\mathbf{U}$ is the transformation matrix to convert the Hill's matrix from frequency to time domain, satisfying the criteria $\mathbf{U}z(t) = (\mathbf{Z}_{-l}e^{il\omega t} \dots \mathbf{Z}_l e^{-il\omega t})^{\mathrm{T}}$. Substituting Equations 3.21 into 3.24 yields the following expression:

$$\mathbf{x}_z(t) = \mathbf{C}(t)\mathbf{U}^{\mathrm{T}} e^{\mathbf{H}t} \mathbf{U} z(0) \tag{3.25}$$

At $t = 0$, Equation 3.22 simplifies to $z(0) = \tilde{\mathbf{W}}\mathbf{x}(0)$, where:

$$\tilde{\mathbf{W}} = \begin{pmatrix} \mathbf{I}_{n\times n} \\ \vdots \\ \mathbf{I}_{n\times n} \end{pmatrix} \tag{3.26}$$

Utilising both reductions matrices together in Equation 3.25, results in:

$$\mathbf{x}_z = C(t)\mathbf{U}^{\mathrm{T}} e^{\mathbf{H}t} \mathbf{U}\mathbf{W}\mathbf{x}(0) \tag{3.27}$$

Over a full period T this yields:

$$\mathbf{x}_T \approx \tilde{\mathbf{C}} e^{\mathbf{H}t} \tilde{\mathbf{W}} \mathbf{x}_0 \tag{3.28}$$

As per Equation 3.18, this implies that the monodromy matrix can be approximated in the frequency domain by:

$$\Phi_T \approx \tilde{\mathbf{C}} e^{\mathbf{H}T} \tilde{\mathbf{W}} \tag{3.29}$$

This approximation of the monodromy matrix enables the computation of system stability through Floquet multipliers, employing the same method as in standard time-domain stability analysis. Thus, compared to traditional Hill's stability analysis, utilising the Koopman operator reduces the necessary number of eigenvalues from $N(2H+1)$ to just N. This approach will be referred to herein as Koopman operator-based stability analysis. A more detailed derivation of the process is provided in [94].

3.2.5 Implementation

Figure 3.2 provides an overview of the complete HBM continuation process, including stability analysis. The continuation starts with an initial estimate of the LCO frequency from eigenvalue analysis and a small guess for the amplitude. Nonlinear forces are then computed in the frequency domain using the AFT procedure, which estimates the system's linear degrees of freedom. The residual equations 3.12, 3.13 and A.4 are numerically solved. Once a converged solution is achieved, stability analysis is performed using either Hill's method or the Koopman-based procedure. Direction vectors are calculated through finite differences based on previous points in the continuation scheme, and these vectors are used to estimate the next point via the tangent predictor method [54]. This process continues until a user-defined stopping criterion is met, such as the number of points or maximum/minimum continuation parameter.

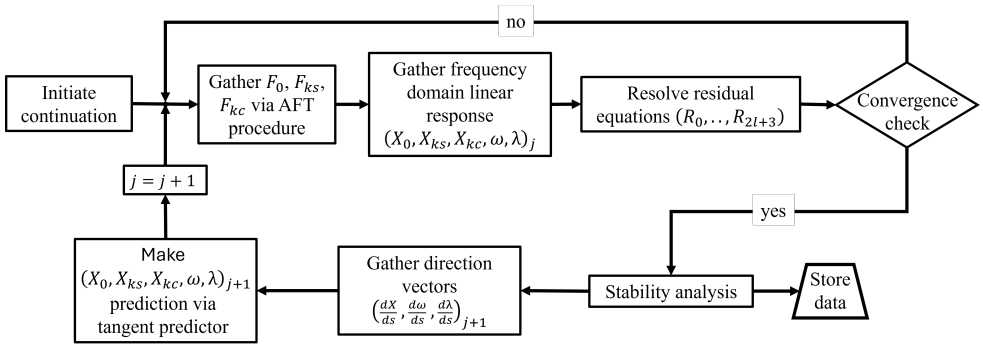

Figure 3.2: HBM continuation process with stability analysis for system exhibiting LCO behaviour.

3.3 Test Case

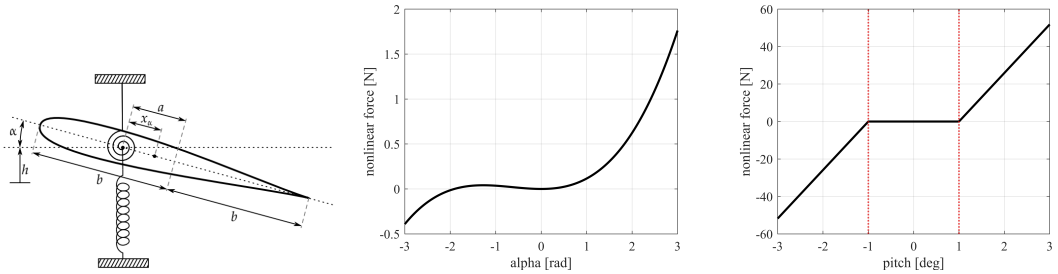

(a) (b) (c)

Figure 3.3: Numerical test case (a) Freebody diagram of 2 DoF aerofoil [5], (b) Quadractic-Cubic nonlinearity, (c) Freeplay nonlinearity with 'freeplay gap' $\delta = 1^o$ (shown by red dotted line)

The model under investigation here is a simplified representation of the system analysed in Ref. [3], focusing on a two DoF aerofoil section depicted in Figure 3.3a. In this model, the degrees of freedom are the pitch angle α and the heave h. The plunge DoF is governed by a spring with stiffness K_h, while a torsional spring K_α resists pitch movement. For the nonlinear flutter rig considered, the state variables are denoted as $\boldsymbol{x} = [h, \alpha, w]$, where h represents heave, α denotes pitch, and w indicates the aerodynamic state. The structural matrices, as shown in Equation 3.1, are configured as

follows:

$$\mathbf{M} = \begin{bmatrix} m_T & m_w x_\alpha b & 0 \\ m_w x_\alpha b & I_\alpha & 0 \\ 0 & 0 & 1 \end{bmatrix}; \ \mathbf{D} = \begin{bmatrix} c_h & 0 & 0 \\ 0 & c_\alpha & 0 \\ -1/b & a-1/2 & 0 \end{bmatrix}; \ \mathbf{K} = \begin{bmatrix} K_h & 0 & 0 \\ 0 & K_\alpha & 0 \\ 0 & 0 & 0 \end{bmatrix} \tag{3.30}$$

Where m_w denotes the wing mass, m_T represents the combined mass of the wing and its support structure, and I_α is the wing's moment of inertia about the elastic axis. The stiffness and damping coefficients are given by K_h and c_h for heave motion, and K_α and c_α for pitch motion, respectively.

Aerodynamic matrices are derived from the unsteady aerodynamic model described by Abdelkef et al. [69]:

$$\mathbf{A} = \begin{bmatrix} -\pi b^2 & a\pi b^3 & 0 \\ a\pi b^3 & -\pi\left(1/8 + a^2\right) b^4 & \\ 0 & 0 & 1 \end{bmatrix}$$

$$\mathbf{B} = \begin{bmatrix} -\pi b C(\kappa) & -\left(1 + (1/2 - a)\right) \pi b^2 C(k)/\rho & -2\pi V b \left(c_1 c_2 + c_3 c_4\right)/\rho \\ \pi \left(a + 1/2\right) b^2/V & -\left(1/4 - a^2\right) \pi b^3 & 2\pi b^2 V \left(a + 1/2\right)\left(c_1 c_2 + c_3 c_4\right) \\ 0 & 0 & -\left(c_2 + c_4\right)/\rho b \end{bmatrix}$$

$$\mathbf{C} = \begin{bmatrix} 0 & -\pi b C(\kappa) & -2\pi V c_2 c_4 \left(c_1 + c_3\right)/\rho \\ 0 & \pi b^2 C(k)\left(1/2 + a\right) & 2\pi b \left(a + 1/2\right) c_2 c_4 \left(c_1 + c_3\right) \\ 0 & 1/\rho V b & c_2 c_4/\rho b^2 \end{bmatrix} \tag{3.31}$$

Where $C(\kappa)$ is the generalised Theodorsen's function detailed in Ref. [166]. Theodrsen's function is related to the model through reduced frequency κ that can be calculated with $\kappa = \omega b/V$. Aerodynamic constants c_1-c_4 are derived with the Sears and Pade approximations [167]. The aerodynamic forces and structural matrices are integrated in the generalised form from Equation 3.3. With nonlinearity present in the pitch DoF

for the case studies under examination, the Boolean matrix allocating the nonlinear function is defined as $q_n = [0, 1, 0]^T$. The specific definition of the nonlinear function f_{nl} varies for each test case. This setup enables linear flutter analysis to precede the detailed numerical continuation method outlined.

To illustrate the nonlinear characteristics of the system under smooth nonlinear conditions, the spring stiffness is modelled using quadratic and cubic terms in the pitch DoF. The shape of the smooth nonlinearity is demonstrated in Figure 3.3b. This method is commonly used to replicate geometrical nonlinear behaviours [5].

$$f_{nl}(t) = K_{\alpha 2}\alpha(t)^2 + K_{\alpha 3}\alpha(t)^3 \tag{3.32}$$

To capture the behaviour of a nonsmooth nonlinearity, the nonlinear function is altered to represent a freeplay nonlinearity on the torsional spring, as depicted in Figure 3.3c. This describes behaviour where the torsional stiffness becomes zero within a range of pitch angles, typically denoted as $-\delta$ to δ (the freeplay gap), resulting in a nonsmooth shape. The segment with zero torsional stiffness is commonly referred to as the freeplay region. Functions of this type are typically employed to model nonlinear impacts arising from localised contact points and friction [168, 169].

$$f_{nl}(t) = \begin{cases} K_{nl}(\alpha(t) + \delta) & \alpha(t) \leqslant -\delta \\ 0 & -\delta < \alpha(t) < \delta \\ K_{nl}(\alpha(t) - \delta) & \alpha(t) \geqslant \delta \end{cases} \tag{3.33}$$

3.4 Numerical Demonstration & Validation

In this section, the outlined methodology will be applied to the specified aeroelastic test case for a purely numerical validation assessment. This will involve comparing the accuracy of bifurcation diagrams to time histories and time-domain continuation tools, namely MATCONT and COCO. The examination will consider both precision and computational cost. Two distinct types of nonlinearity will be explored. Firstly, a smooth nonlinearity, typically employed to model geometric nonlinearities, will be

analysed. Subsequently, a nonsmooth function will be utilised to represent localised nonlinearity.

3.4.1 Smooth Nonlinearity

The results obtained by implementing the smooth nonlinearity described in Equation 3.32 are presented herein. To build the Hill's matrix for frequency domain stability analysis, $\frac{df_{nl}}{d\mathbf{x}}(t)$ is derived from Equation 3.32 as follows:

$$\frac{df_{nl}}{d\mathbf{x}}(t) = 2K_{\alpha 2}\alpha(t) + 3K_{\alpha 3}\alpha(t)^2 \tag{3.34}$$

The parameters outlined in Table B.1 in Appendix B define the test case. For the purely numerical test, a simplified aerodynamic model is utilised, resulting in the neglect of the aerodynamic state w. Consequently, both structural and aerodynamic matrices (Equations 3.30 and 3.31) are reduced from 3×3 to 2×2.

The HBM framework was applied to the test case, and bifurcation diagrams for various harmonic orders are presented in Figure 3.4a. Continuation was initiated from the Hopf bifurcation point (flutter velocity V_f) at 31.45 m/s, identified through linear eigenvalue analysis of the matrix $\mathbf{Q}$. The continuation initially progressed backward with respect to velocity until reaching a turning point, after which the direction reversed. This is subcritcal behaviour, meaning LCO exist at lower velocities than the linear flutter speed.

To establish a reference solution, a high-fidelity run with 100 harmonics was conducted to assess the mean error in velocity for LCO amplitudes ranging from 0 to 0.5 rad. Figure 3.4b indicates that mean error relative to the 100-harmonic solution converges fully by five harmonics. It is observed that the error in the shape of the bifurcation curves for one and two harmonics is nearly identical, with a sharp change occurring at three harmonics. A steep 99.08% reduction in absolute error is observed between two and three harmonics, followed by only marginal decreases up to five harmonics. This trend is validated by Figure 3.4a, which shows a slight change in the bifurcation diagram's shape between two and three harmonics, with negligible differ-

ences beyond three harmonics. This is likely due to the fact that the highest degree of nonlinearity in the nonlinear function is cubic. While this holds true for the convergence of the shape, it may not necessarily apply to the determination of stability.

From a design perspective, the turning point is critical as it represents the minimum velocity at which LCOs are expected. Figure 3.4c reveals a 1.42% change in the turning point location between two and three harmonics, with only minor variations up to five harmonics. While the steep error reduction between two and three harmonics has limited impact on the overall bifurcation diagram shape, full convergence is not achieved until five harmonics with a turning point at $23.91 m/s$.

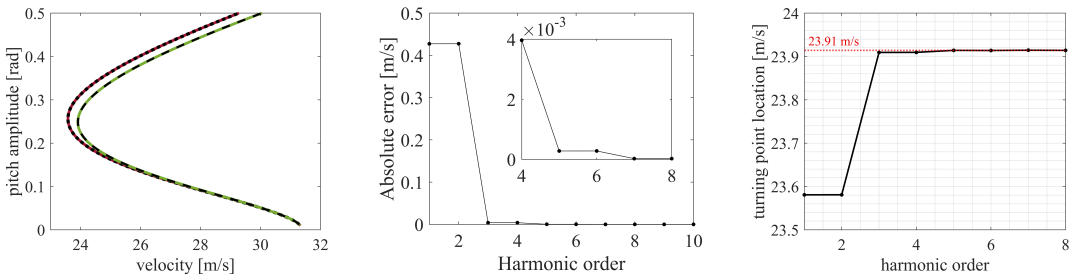

(a) (b) (c)

Figure 3.4: Bifurcation diagram for smooth nonlineaity (a) Shape convergence with harmonic order ($\cdots$ $l = 1$), ($\bullet$ $l = 2$), ($\bullet$ $l = 3$), (-- $l = 100$), (b) Bifurcation diagram mean error with harmonic order, (c) Turning point convergence with harmonic order

The convergence of frequency-domain stability methods is assessed after the bifurcation diagram stabilises. Standard time-domain Floquet analysis, as shown in Figure 3.5a, serves as a reference for stability behaviour. For LCO amplitudes below $0.25 rad$, the Floquet multiplier associated with mode 4 exceeds unity, indicating unstable LCO behaviour. Conversely, for amplitudes exceeding $0.25 rad$, all Floquet multipliers are less than or equal to unity throughout the remainder of the continuation, signifying stable LCO. It is observed that the multiplier for mode 3 remains exactly 1 across the entire continuation. The stability exchange point corresponds to the turning point in the bifurcation diagram, occurring at a velocity of $23.91 m/s$. This indicates the presence of unstable LCOs at low amplitudes, spanning from the turning point to the Hopf bifurcation point. At the turning point, a stability exchange takes place, leading to the

emergence of higher-amplitude stable LCOs.

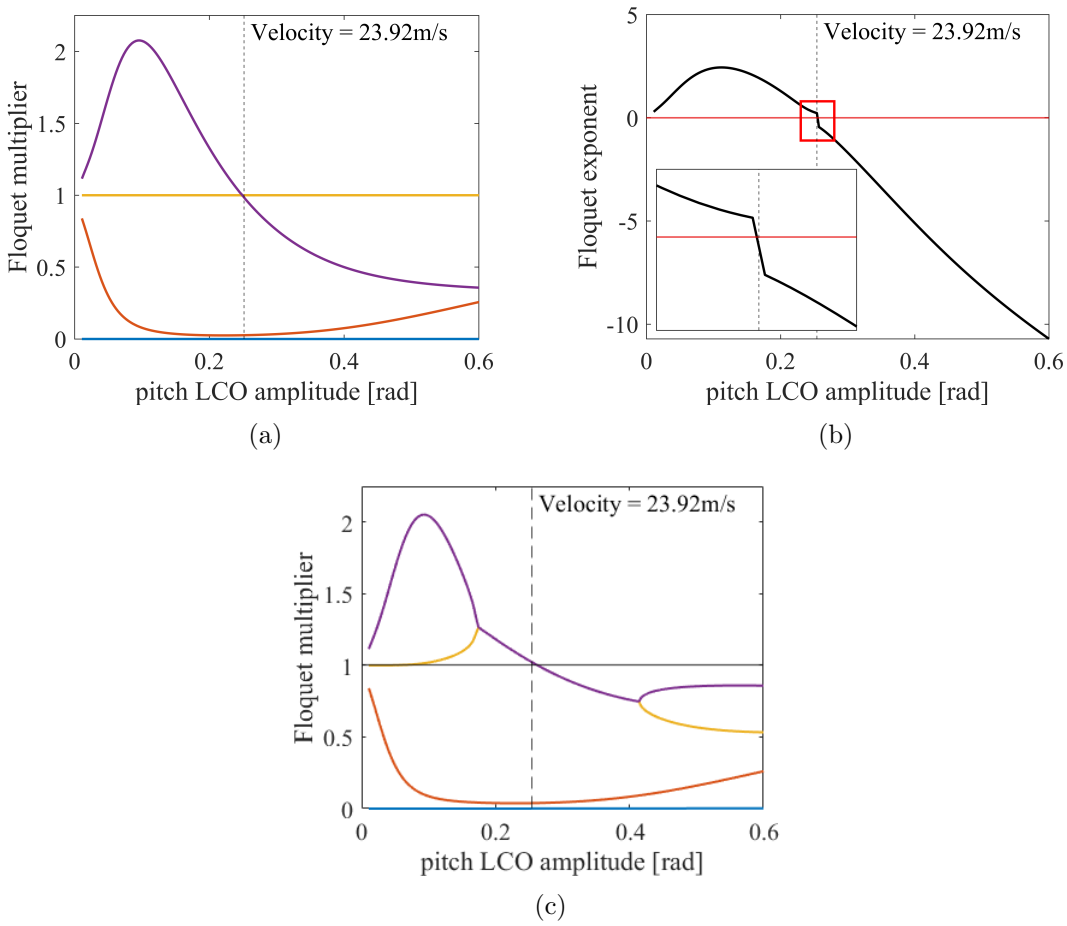

Figure 3.5: Smooth nonlinearity stability eigenvalues a $l = 5$ (• eigenvalue 1), (• eigenvalue 2), (• eigenvalue 3), (• eigenvalue 4) (a) Time integration, (b) Standard Hill's stability method, (c) Koopman based stability method

While time integration provides an exact determination of LCO stability, converting to the time-domain undermines the purpose of employing a frequency domain method for delineating the shape of the bifurcation diagram. Therefore, stability is evaluated using both the standard Hill's method and the Koopman operator-based method to determine the optimal approach in this context, considering accuracy and runtime. Figure 3.5b shows the critical Floquet exponent obtained from the standard Hill's method at 5 Harmonics, indicating where a change of stability occurs. It is observed that the transition from stability to instability occurs within $0.01m/s$ of the prediction

made by the time-integration method. Similarly, in Figure 3.5c, the Koopman operator based method at 5 Harmonics predicts stability exchange at the same point as the standard Hill's method.

It is observed in Figure 3.5b that the Hill's method exhibits an anomalous jump in the Floquet exponent at the point of stability exchange. Furthermore, the Floquet multipliers derived from the Koopman method in Figure 3.5c do not align precisely with those obtained from direct time integration. This discrepancy suggests that modes 3 and 4 are the same value near the stability exchange point but become independent thereafter. While the stability exchange is captured in this instance, further investigation is warranted to determine under what conditions, if any, these results converge to the exact solution.

Focusing initially on the Hill's method, since no exact solution is available for direct comparison, the harmonic order was increased to 100 to achieve fully converged Floquet exponents, as shown in Figure 3.6a. The resulting curve is smooth and exhibits no anomalous jumps near the stability exchange, indicating convergence. This solution is treated as the reference for evaluating the accuracy of Floquet exponents at lower harmonic orders. The mean error over the critical range of LCO amplitudes of interest is presented in Figure 3.6b.

Figure 3.6c presents the Floquet exponents across a range of harmonics, with all exponents corresponding to a given harmonic shown in the same colour. This illustrates the convergence behaviour and overall shape of the Floquet exponents. By six harmonic orders, the error is observed to converge, and this is further confirmed in Figure 3.6c, which demonstrates that for harmonic orders below six, a jump near the stability exchange is evident, whereas at six harmonics, the curve becomes smooth. Despite these jumps, the stability exchange location converges by five harmonic orders. An exception to this is the single harmonic response, where a smooth curve is observed. However, this result underestimates the true stability exchange location by 25%, as reflected in the mean absolute error, making it the second least accurate among the cases considered. A significant increase in error at three harmonics is also observed. Examination of Figure 3.6c reveals that at this harmonic order, the Floquet exponents

fail to predict stability, diverging instead to a large positive value.

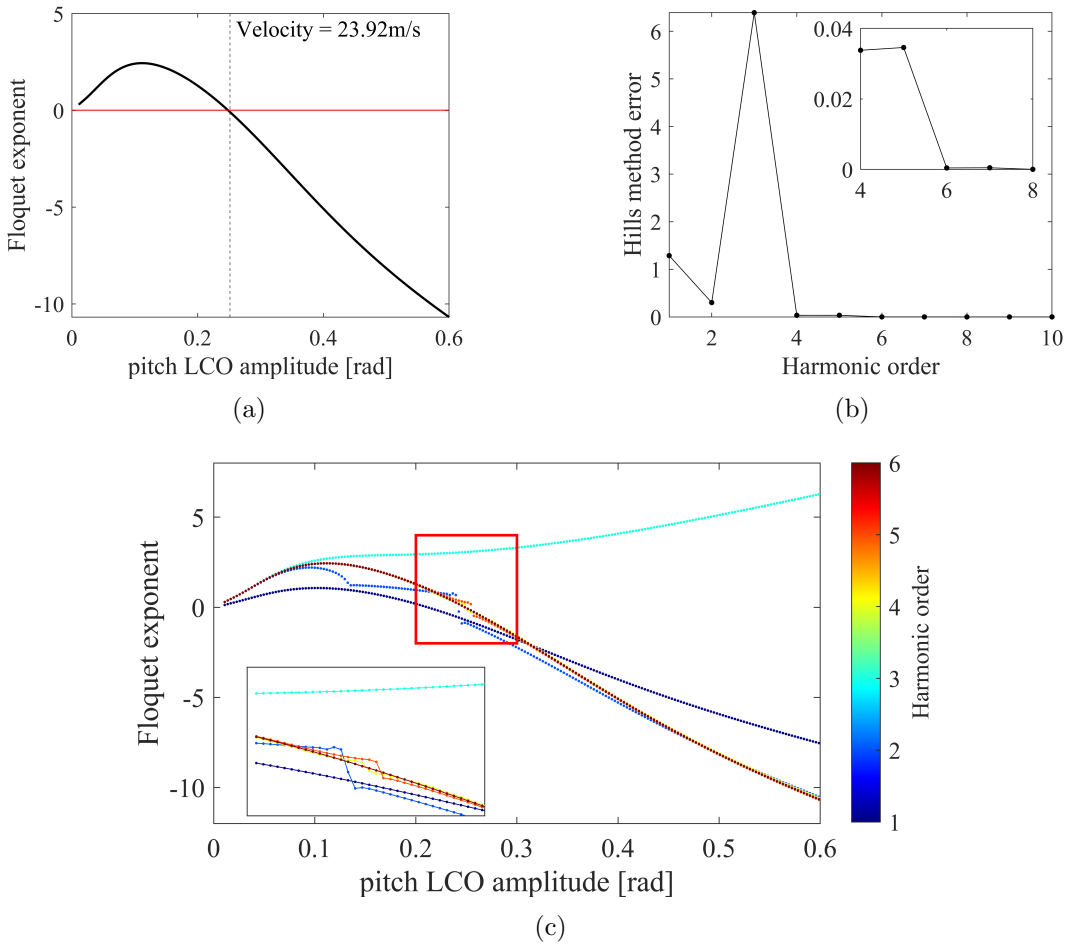

Figure 3.6: Hill's stability method on smooth test case (a) Converged Floquet exponents, (b) Floquet exponent mean error, (c) All Floquet exponents with increasing harmonic order

Using the Koopman method, the exact Floquet multipliers derived from the time integration method serve as a benchmark for assessing its accuracy. Figure 3.7a demonstrates that the mean error in the multipliers converges at eight harmonic orders. It is observed that while modes 1 and 2 converge by six harmonic orders, modes 3 and 4—critical for determining stability—do not converge until eight orders. This is corroborated in Figure 3.7c, which shows that modes 3 and 4 remain the same value prior to eight harmonics. Beyond this point, the Koopman method accurately captures the dynamics of modes 3 and 4, with mode 3 maintaining a multiplier of 1 throughout the

bifurcation diagram, while mode 4 exhibits a smooth transition from stable to unstable. Figure 3.7b highlights the multipliers for modes 3 and 4 at low harmonic orders, with the modes being identical for the full continuation run in the single harmonic result. At harmonic orders between two and four, the stability transition location is underestimated. Notably, at three harmonic orders, the Koopman method predicts that the system becomes unstable again at higher amplitudes in the bifurcation diagram. However, despite discrepancies in the Floquet multiplier shape compared to the exact solution, the stability transition location converges to the value predicted by the time-domain method by five harmonic orders.

Figure 3.7b highlights the multipliers for modes 3 and 4 at low harmonic orders. At harmonic orders between two and four, the stability transition location is underestimated. Notably, at three harmonic orders, the Koopman method predicts that the system becomes unstable again at higher amplitudes in the bifurcation diagram. However, despite discrepancies in the Floquet multiplier shape compared to the exact solution, the stability transition location converges to the value predicted by the time-domain method by five harmonic orders.

The final converged bifurcation diagram, shown in Figure 3.8, is generated using a harmonic order of 5 with Koopman-based stability analysis. The results reveal subcritical behaviour, where unstable LCOs are tracked from the linear flutter velocity up to 23.91 m/s. Beyond this point, a turning point is reached, after which stable LCOs of increasing amplitude are observed with rising velocity.

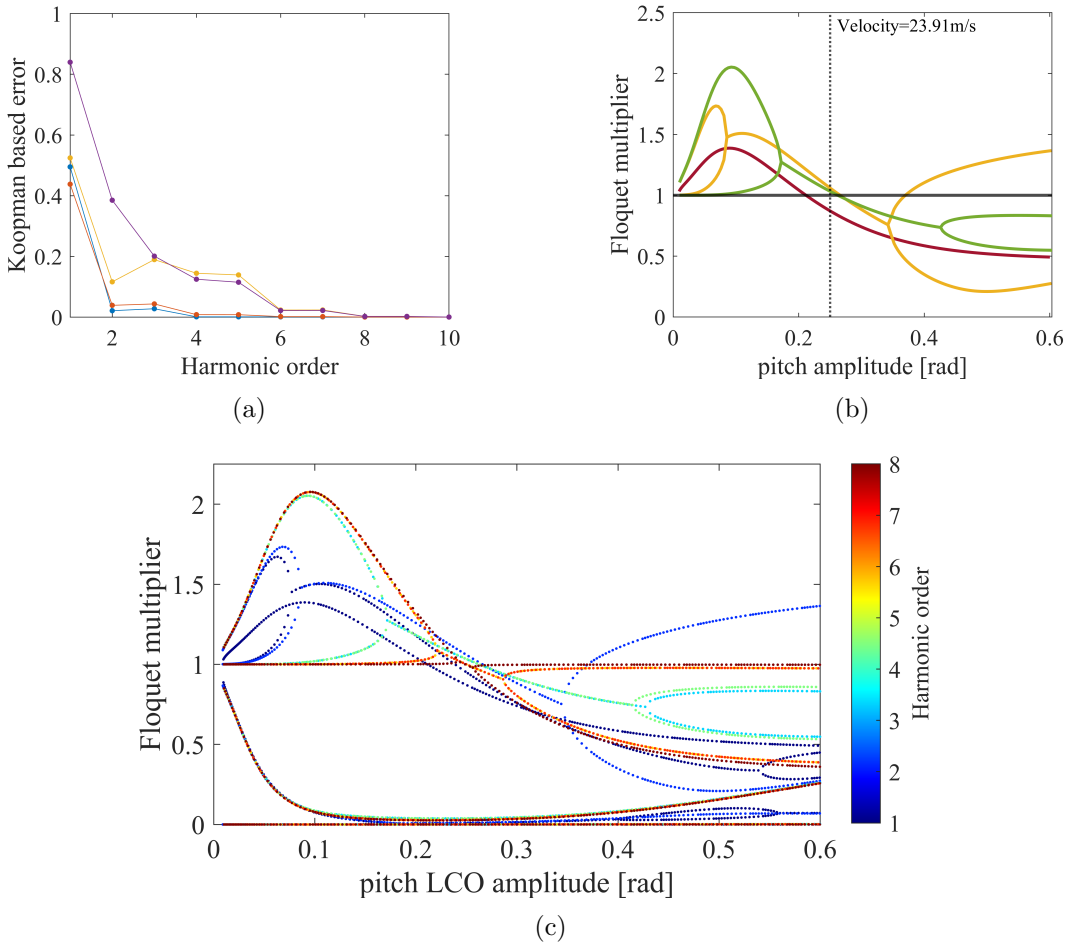

Figure 3.7: Koopman-based stability on smooth test case (a) Floquet multiplier error (colours in line with Figure 3.5a), (b) Mode 3 and 4 at (• $l = 1$), (• $l = 3$), (• $l = 5$), (c) All Floquet multipliers with increasing harmonic order.

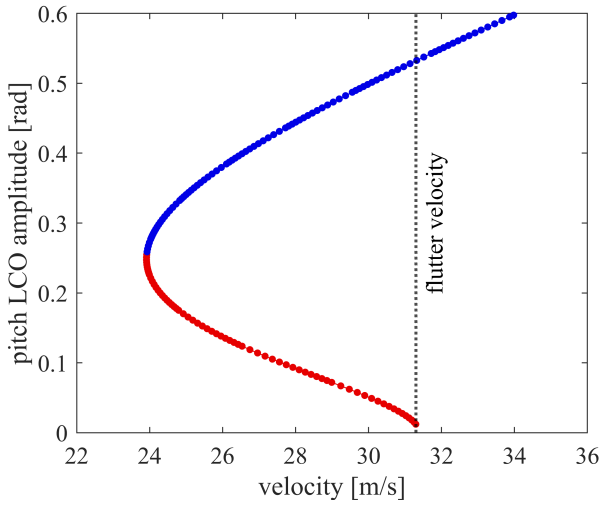

Figure 3.8: Smooth test case converged bifurcation diagram at $l = 5$ (• unstable LCO), (• stable LCO)

3.4.2 Nonsmooth Nonlinearity

The outcomes derived from applying the freeplay nonlinearity outlined in Equation 3.33 are presented in this section. To construct Hill's matrix for frequency domain stability analysis, $\frac{df_{nl}}{d\mathbf{x}}(t)$ is derived from Equation 3.33 as follows:

$$\frac{df_{nl}}{d\mathbf{x}}(t) = \begin{cases} K_{nl} & \alpha(t) \leqslant -\delta \\ 0 & -\delta < \alpha(t) < \delta \\ K_{nl} & \alpha(t) \geqslant \delta \end{cases} \tag{3.35}$$

The parameters are once again outlined in Table B.1, with the primary distinction being the incorporation of nonlinearity in the case of the localised nonlinearity. In the implemented freeplay nonlinearity, two distinct flutter velocities emerge. The first occurs when the absolute value of the pitch is less than δ, resulting in zero torsional stiffness. Under this condition, the flutter velocity remains consistent with the smooth case at $31.45m/s$ (flutter velocity 1). Conversely, in scenarios where $|\alpha| \geqslant \delta$, the flutter velocity is determined by setting $K_\alpha = K_{nl}$ and is calculated to be $29.5m/s$ (flutter velocity 2). Given that flutter velocity 1 corresponds to the hopf bifurcation point, continuation will commence from this point, assuming the aerofoil is perturbed from a state with zero heave and pitch.

Continuation is initiated from flutter velocity 1, and bifurcation diagrams are generated across a range of harmonic orders. The results obtained using 100 harmonic orders are taken as the reference for assessing convergence of the bifurcation diagram's shape. Figure 3.9a illustrates a subcritical pattern, similar to the smooth case, but with a sharper transition. Notably, LCO amplitudes remain negligible before the turning point, beyond which they escalate towards infinity.

Figure 3.9a further shows similarity between the single and two harmonic result and a noticeable change in the shape of the bifurcation curve at the turning point between 2 and 3 harmonics. However, for harmonic orders above 3, even up to 100, the changes are minimal. This observation is validated by the absolute error presented in Figure 3.9b, where a 78.41% drop in error relative to the 100-harmonic result is

observed between 2 and 3 harmonics. An additional 17.26% reduction occurs between 3 and 5 harmonics, but beyond this, only marginal decreases are observed, with full convergence achieved around 10 harmonics.

As in the smooth case study, the turning point location remains the most critical feature of the bifurcation diagram. Figure 3.9c shows that significant jumps in absolute error result in only a 3.25% change in the turning point velocity between 2 and 3 harmonics, with minor differences thereafter. Convergence is reached at 8 harmonics, yielding a turning point velocity of 24.29 m/s. Although the bifurcation shape converges at 10 harmonics, it suggests that the amplitude also requires up to 10 harmonics to achieve full convergence.

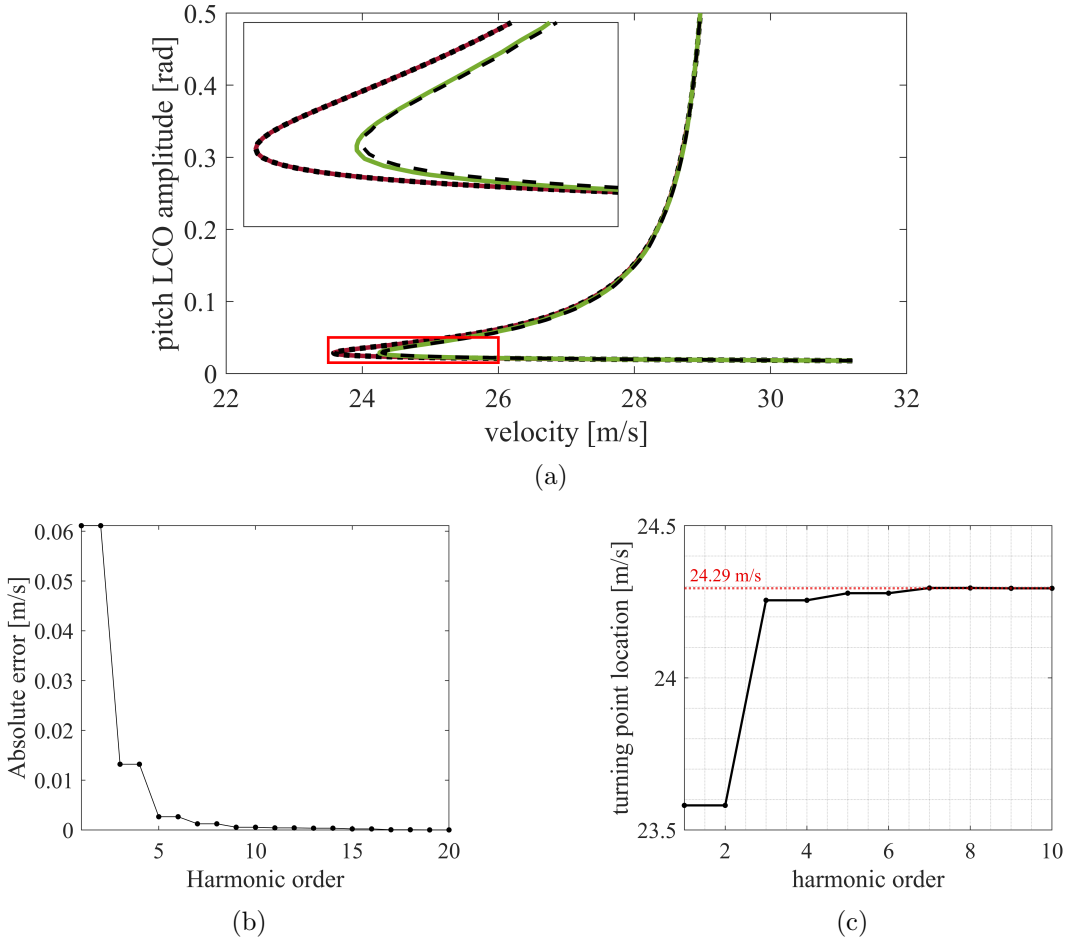

Figure 3.9: Freeplay bifurcation diagram (a) ($\cdots$ $l = 1$), ($\bullet$ $l = 2$), ($\bullet$ $l = 4$), ($\bullet$ $l = 8$), (b) Bifurcation diagram absolute error, (c) Turning point loaction convergence

Once the bifurcation diagram has stabilised with time integration Floquet analysis, as shown in Figure 3.10 as the reference point, the convergence of frequency domain stability methods is assessed. Given the minimal change in amplitude before the turning point in the bifurcation diagram, iteration along the continuation process replaces the LCO amplitude in the stability plots. Time-integration stability indicates an exchange from unstable to stable at iteration 44, corresponding to the turning point of the bifurcation diagram.

Upon examination of the Floquet multipliers and exponents of the frequency domain methods in Figures 3.10b and 3.10c, an erratic pattern is noticeable, with sharp jumps between points. This contrast with the time-domain method suggests discrepancies in depicting the dynamic behaviour. However, in the case of standard Hill's method, such behaviour does not influence the prediction of stability exchange. Despite the erratic nature of the critical Floquet exponent, it still indicates the transition of LCO from unstable to stable at iteration 44, as shown in Figure 3.10b.

As there is no exact solution for the Floquet exponents, the result obtained using 100 harmonic orders, shown in Figure 3.11a, is adopted as the converged solution for accuracy assessment. This plot reveals a generally smooth curve, particularly near the stability exchange point. The mean error in the Floquet exponents over the full continuation run is illustrated in Figure 3.11b. It is observed that the error begins to converge at harmonic orders exceeding 15.

In the outputs from the Hill's method, erratic jumps are consistently observed. However, as shown in Figure 3.11c, for harmonic orders above 4, all Floquet exponents correctly predict an exchange of stability at iteration 44, aligning with the time-domain results. Once again, the single harmonic result exhibits a smooth curve across all iterations but underestimates the turning point location by 12 iterations. Any Floquet multipliers appearing in the top-right or bottom-left quadrants of Figure 3.11c indicate an error. Notably, such erroneous points are confined to results at harmonic orders below 5. This indicates that, despite the chaotic appearance of the results at low harmonic orders, meaningful stability information can still be extracted. Consequently, reliable stability predictions can be obtained even at relatively low harmonic orders,

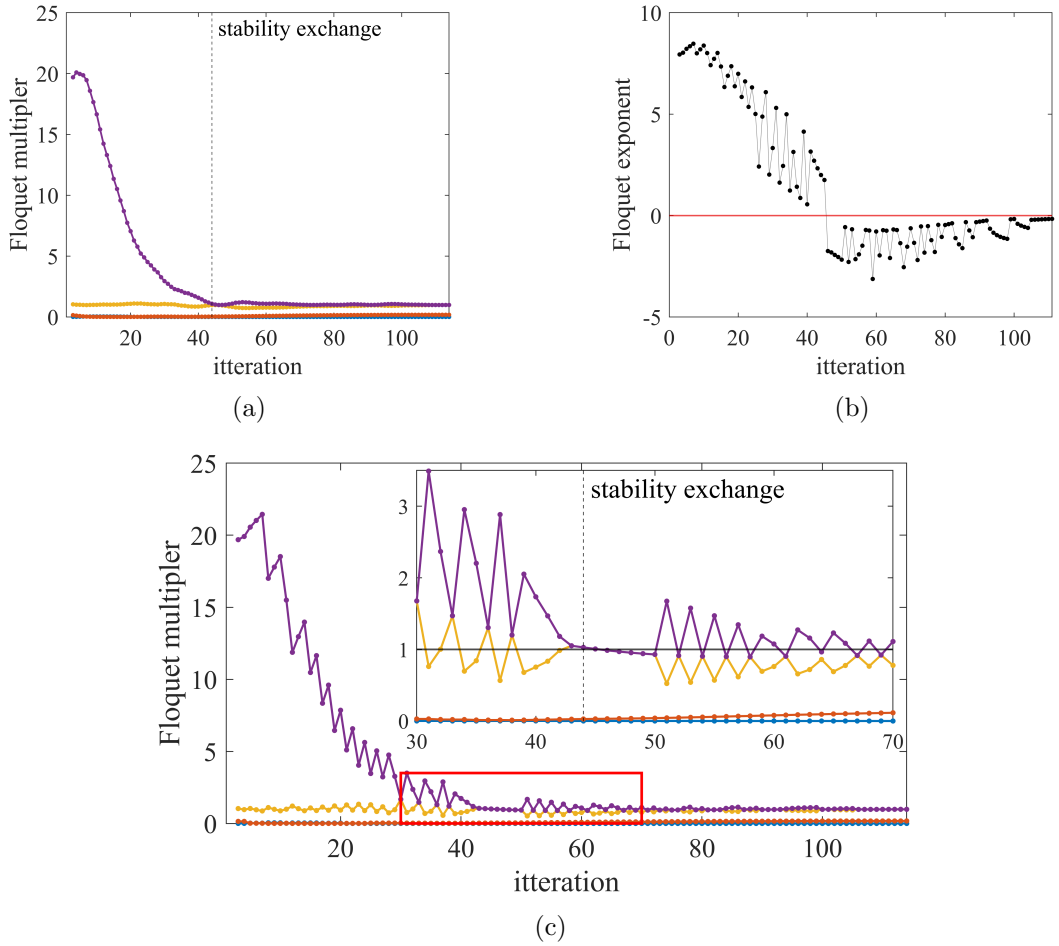

Figure 3.10: Freeplay nonlinearity stability eigenvalues at $l = 8$ (• eigenvalue 1), (• eigenvalue 2), (• eigenvalue 3), (• eigenvalue 4) (a) Time integration, (b) Standard Hill's method, (c) Koopman operator based stability

provided the analysis is carefully interpreted.

Focusing on the results from the Koopman-based method, the apparent errors in the Floquet multipliers obtained through Koopman operator-based stability analysis significantly influence the outcomes. A detailed examination of the critical multipliers in Figure 3.10c reveals that eigenvalues 3 and 4 exhibit chaotic jumps between iterations. Unlike the Floquet exponents, chaotic transitions between stable and unstable states are observed following the exchange of stability indicated by the time-domain results. Additionally, the modes appear to be identical near the stability exchange point, which contrasts with the time-domain results where mode 4 consistently remains at

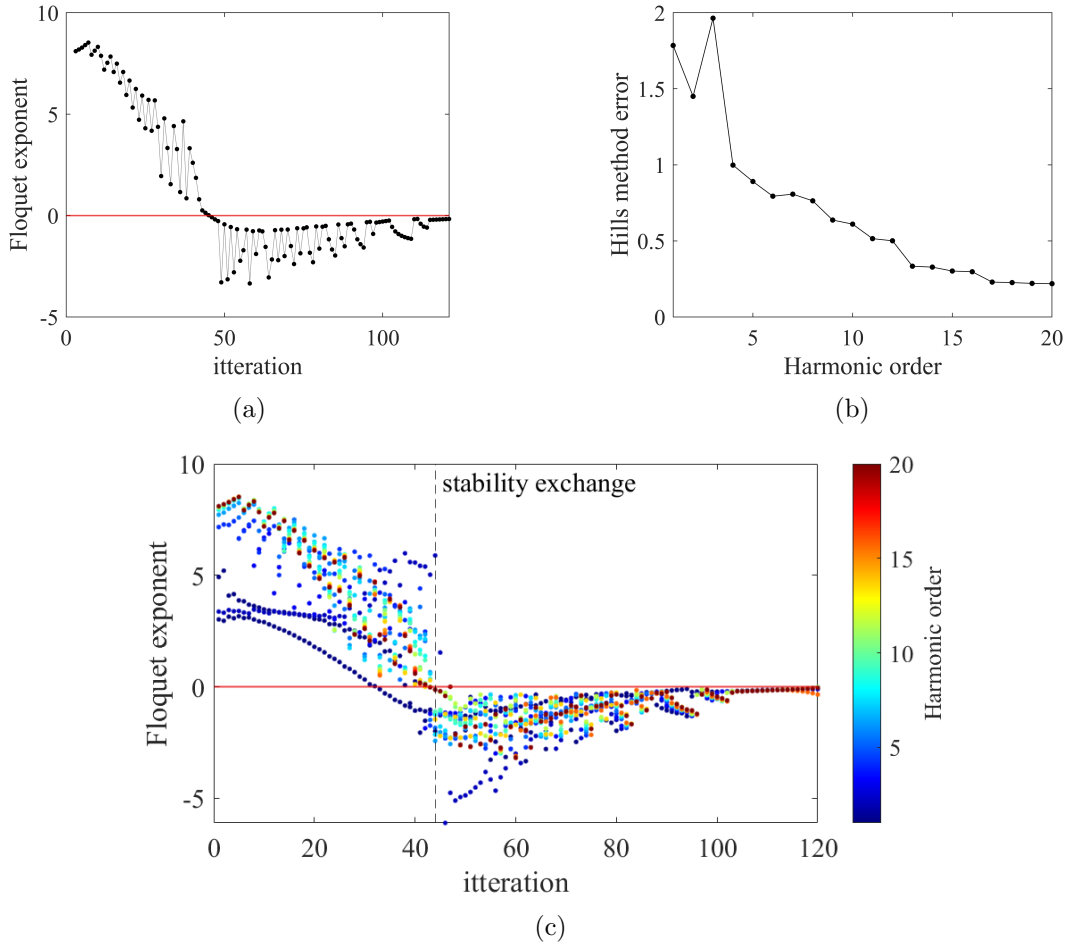

Figure 3.11: Hill's stability method on nonsmooth test case (a) Converged Floquet exponents, (b) Floquet exponent mean error, (c) Convergence study of all Floquet exponents with harmonic order

1 throughout the continuation. This erratic behaviour is illustrated in Figure 3.12a, where the bifurcation diagram shows unpredictable shifts between stability and instability after the turning point. These deviations are inconsistent with the more reliable predictions derived from the time-integration method. An exception is observed in the single harmonic case, where the Floquet multiplier curve remains smooth throughout the continuation, with no chaotic jumps. However, this result yields the largest error compared to the time-domain solution, underestimating the stability exchange by 12 iterations.

The error in the Floquet multipliers from the Koopman method is evaluated against

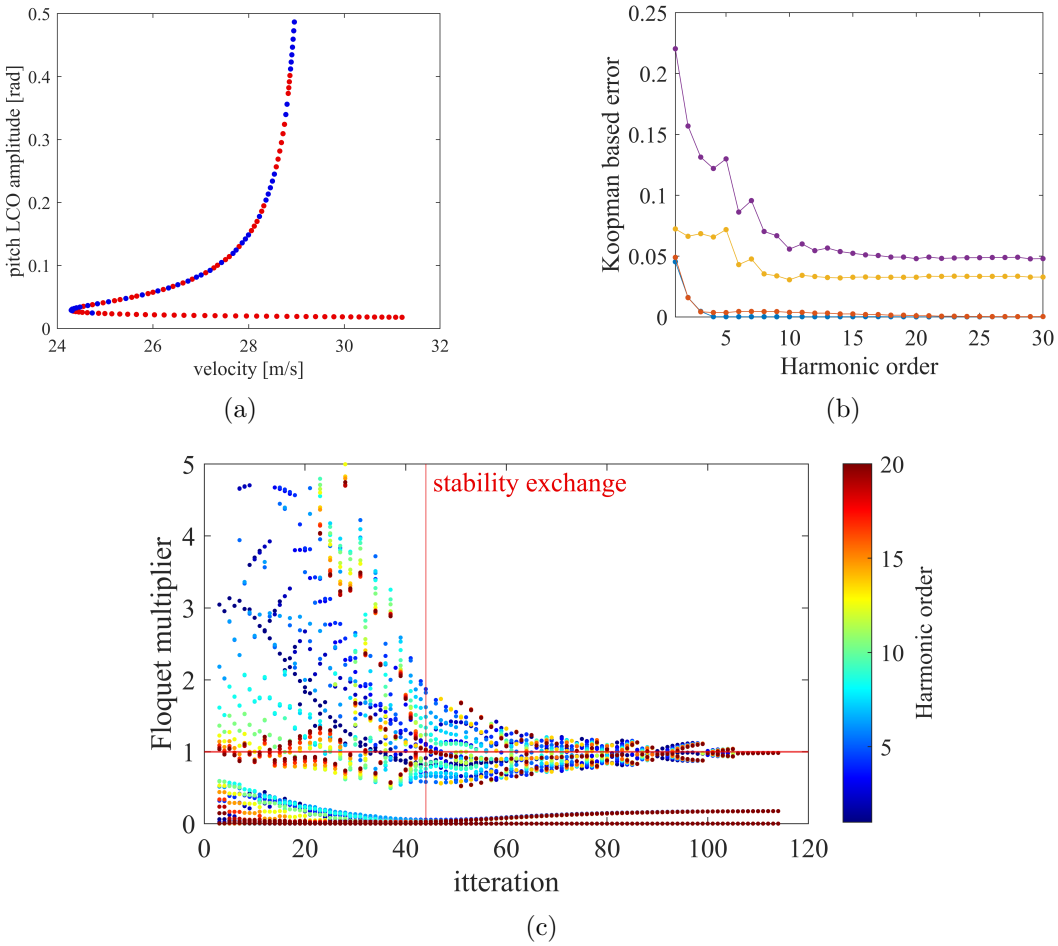

Figure 3.12: Koopman-based stability on smooth test case (a) Bifurcation diagram with stability $l = 8$ (• unstable LCO), (• stable LCO), (b) Floquet multiplier error (colours in line with Figure 3.10c), (c) Convergence study of all Floquet multipliers with harmonic order

the exact solution obtained from the time integration method. Figure 3.12b indicates that while the errors for all modes begin to converge at 20 harmonic orders, they remain relatively high for the critical modes 3 and 4, which govern the stability of the LCO.

Figure 3.12c confirms this observation, demonstrating that although the general shape of the Floquet multipliers converges, chaotic jumps persist between iterations, along with incorrect stability transitions where none should exist. Notably, if any Floquet multipliers fall within the top-right quadrant of Figure 3.12c, this indicates an error. The presence of multiple erroneous points, not limited to regions near the

stability exchange, highlights a broader issue. Even at 100 harmonic orders, chaotic jumps in stability persist, suggesting that the Koopman operator, as applied in this problem, cannot fully capture the stability of the non-smooth case.

The presence of errors in the Hill and Koopman stability methods may be attributed to the inherent approximation nature of the HBM in capturing the dynamic behaviour of a system. In essence, frequency domain methods can only be as effective as their ability to estimate true time histories accurately. This notion is underscored by comparing the true time histories of nonlinear forces with the frequency domain estimates obtained through the AFT procedure, as depicted in Figure 3.13.

An analysis of the error in the case of smooth nonlinearity, presented in Figures 3.13a and 3.13b, reveal that the AFT procedure offers a reasonable approximation of the true nonlinear force at both low and high LCO amplitudes. The relative root mean square error (RRMS) remains below 10^{-3} in both instances, explaining why both frequency domain stability methods exhibit success without chaotic jumps between iterations.

However, when examining the case of a nonsmooth freeplay nonlinearity, as shown in Figures 3.13c and 3.13d, the AFT procedure struggles to accurately capture the behaviour of the nonlinear force. Particularly at low LCO amplitudes, where the freeplay region induces a sharp transition of the nonlinear force to zero, the frequency domain method fails to replicate this flat-line behaviour. Consequently, there is an underestimation in the peak of the force. The RRMS error at low LCO amplitude is 5 orders of magnitude higher than in the smooth case. Although this error diminishes as LCO amplitude increases and the freeplay region becomes less influential, the mean RRMS error remains 2 orders of magnitude larger than in the smooth case. This error source is akin to the Gibbs phenomenon, which states that the error will diminish as the number of harmonics increases but will always be present to some degree [170, 171]. The discrepancy likely elucidates the erratic nature of the frequency domain estimations of stability for the nonsmooth case.

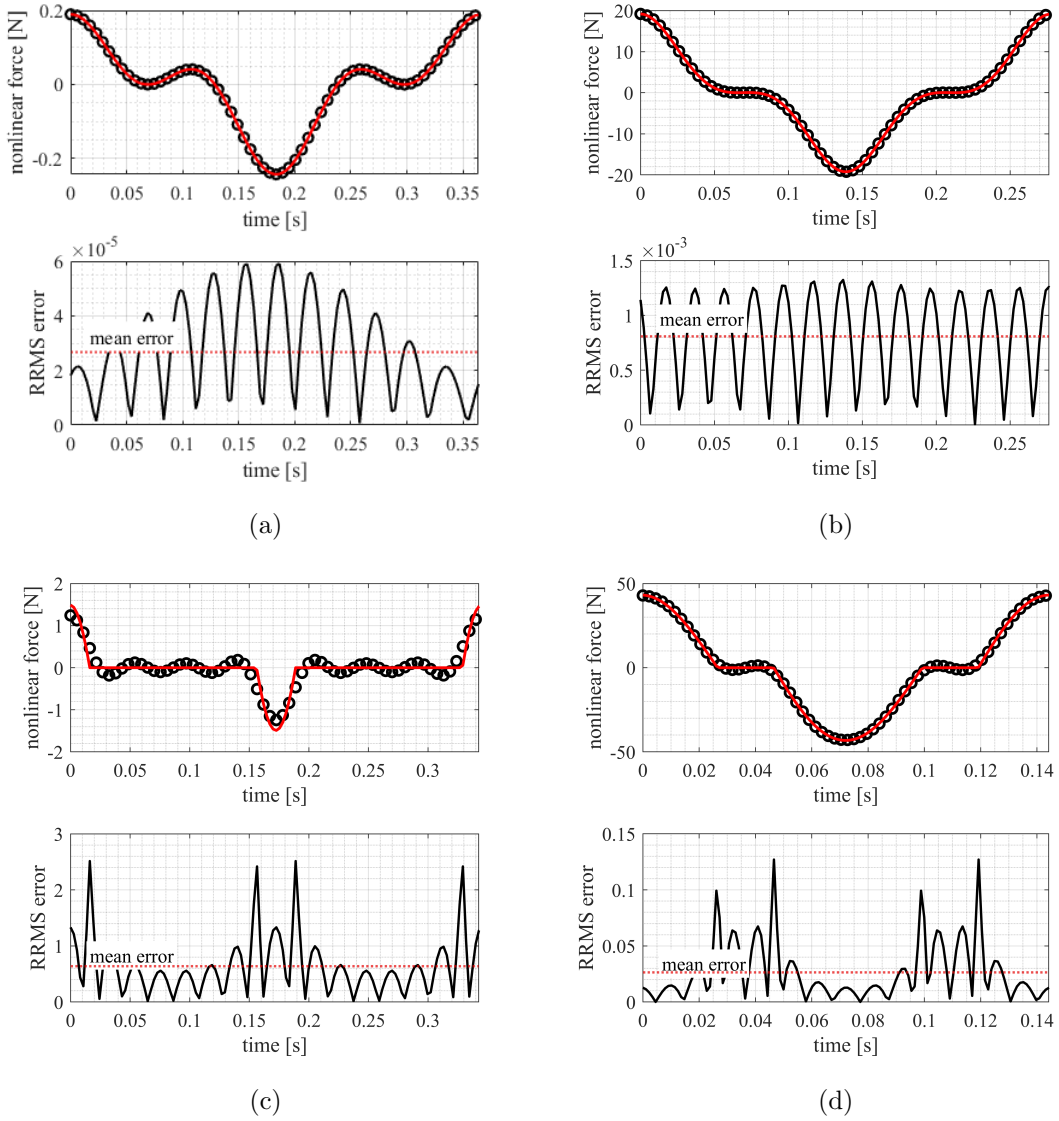

Figure 3.13: Error as a result of AFT procedure in modeling time history of nonlinear forces (– nonlinear force response), (⊖ AFT estimation), Smooth: (a) LCO amplitude = $0.02rad$, (b) LCO amplitude = $0.20rad$, Nonsmooth: (c) LCO amplitude = $0.02rad$, (d) LCO amplitude = $0.20rad$

An alternative explanation for the jumps observed in the Koopman operators may lie in the continuous nature of the oscillatory nonlinear force, f_{nl}, despite its discontinuous slope. The erratic patterns evident in Figures 3.10b and 3.10c could initially be interpreted as reminiscent of the Gibbs phenomenon. However, they are more likely attributable to the jump discontinuities in the Jacobian of f_{nl}. These discontinuities can

induce abrupt variations in the system's response, particularly in regions of heightened sensitivity, resulting in the irregular behaviour observed in the results. This differentiation underscores the necessity of distinguishing numerical artefacts, such as the Gibbs phenomenon, from the inherent physical effects arising from nonlinear system properties, to facilitate a precise interpretation of stability and dynamic behaviour.

The stability information obtained from the standard Hill's method is employed to evaluate the stability of the bifurcation diagram in Figure 3.14b, which is considered the fully converged bifurcation plot for the freeplay study and will be compared to time-domain solvers in Section 3.4.4. Unstable LCOs are initiated at the bifurcation point (flutter velocity 1) and persist in reverse with respect to velocity until reaching $24.3m/s$. Subsequently, a turning point is encountered, resulting in an exchange of stability. Stable LCOs of growing amplitude then emerge between $24.3m/s$ and $29.5m/s$ (flutter velocity 2). At $29.5m/s$, flutter behaviour manifests, characterised by LCO amplitudes tending towards infinity.

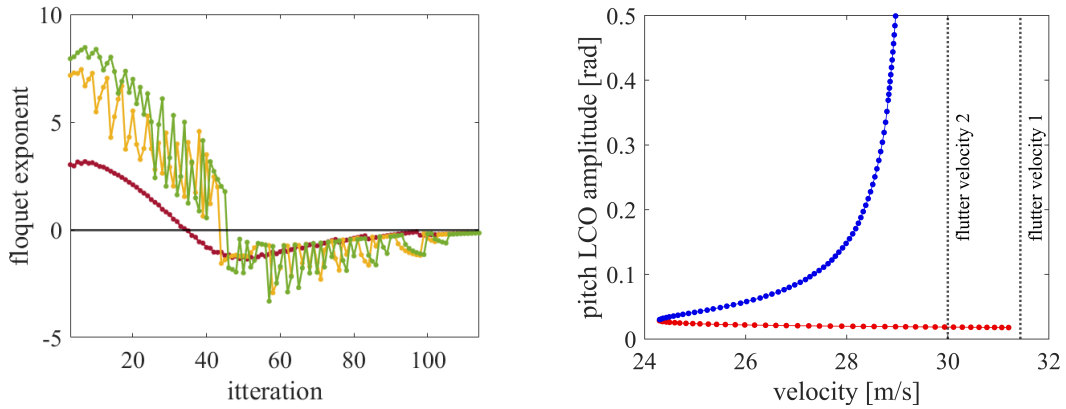

Figure 3.14: Nonsmooth nonlinearity study converged solution (a) Standard Hill's critical Floquet exponent (• $l = 1$), (• $l = 4$), (• $l = 8$), (b) Bifurcation diagram implementing sorted Hill stability (• unstable LCO), (• stable LCO)

3.4.3 Time Domain Comparison

Figure 3.15 compares converged bifurcation diagrams with time histories obtained from the MATLAB *ode*45 differential equation solver for both test cases. The smooth com-

parison in Figure 3.15a, not only clarifies the physical significance of the LCO plot but also validates its accuracy. At velocities below the turning point, the system responds to any initial perturbation in pitch or plunge by oscillating with positive damping before eventually settling to a steady rest state at zero. Responses within the velocity range between the turning point and the linear flutter speed vary depending on the magnitude of the initial perturbation. Small perturbations exhibit behaviour similar to those observed below the turning point, while larger perturbations lead to the generation of LCO. Beyond the linear flutter speed of $31.45m/s$, it is observed that the time response to any perturbation is an LCO with amplitude correlating to the bifurcation diagram.

Similar conclusions can be drawn from the non-smooth comparison in Figure 3.15b. Prior to the turning point, the system responds to any perturbation with a stable rest response. Between the turning point and flutter speed 2 ($24.3 - 29.5m/s$), both stable and unstable LCO branches exist. This implies that under low perturbations, the system responds with a rest solution, while higher perturbations lead to stable LCO and is vaildated by time responses. The amplitude of LCO increases rapidly towards flutter speed 2, as depicted in both the time histories and the bifurcation diagram. Beyond velocities ranging from approximately $29.5m/s$ to $31.45m/s$, the LCO plot indicates unstable LCOs, which either converge to a stable solution or diverge towards infinity. This observation is confirmed by the time responses, where systems settle with low perturbations but exhibit dynamic instability with larger ones (as shown in Figure 3.15). At Velocities above the flutter speed without torsional stiffness, both the LCO plot and the time histories indicate the absence of stable solutions, with the response to any perturbation resulting in binary flutter.

The comparison in Figure 3.15 illustrates that the peak points of the time responses accurately align with the stable curve generated from the HBM results in both test cases. It is worth noting that the amplitude of the unstable section of the LCO plot lacks physical significance. However, the plot clearly indicates that solutions lie on either side of the branch, resulting in either a steady-state rest or a vibrational response (flutter or LCO).

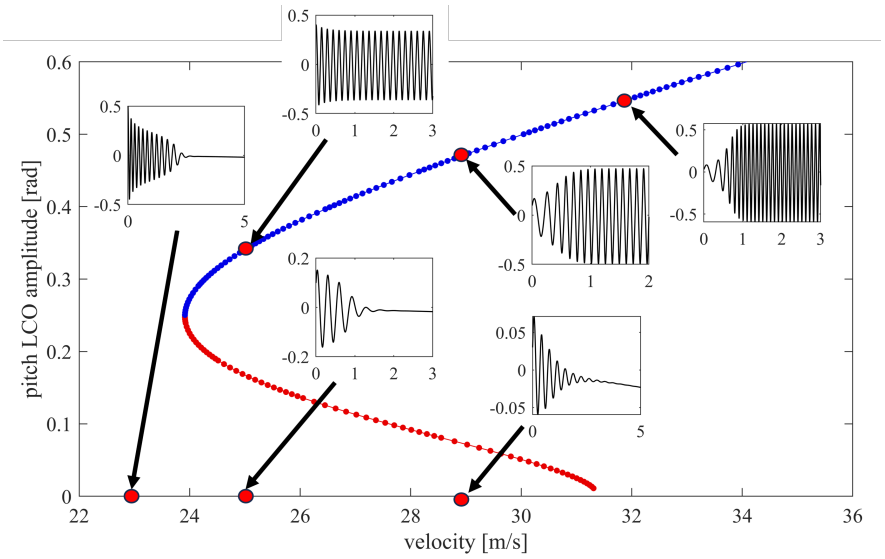

(a)

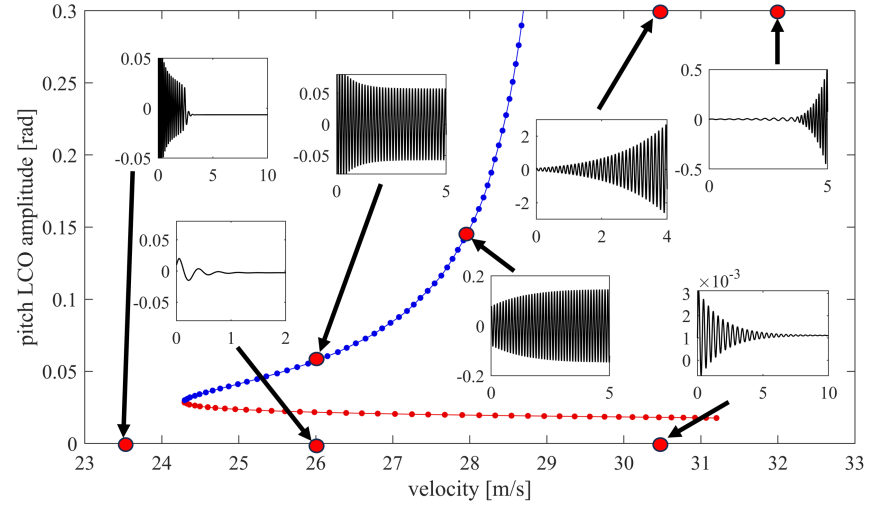

(b)

Figure 3.15: Comparison of bifurcation diagram with time histories obtained from ode solver (• unstable LCO), (• stable LCO), (− pitch time history) (a) Smooth case, (b) Nonsmooth case

3.4.4 Software comparison

In this section, the converged HBM smooth and nonsmooth studies will be compared to time-domain solvers, considering both accuracy and computational cost. Bifurcation diagrams of the same systems are generated using state-of-the-art time-domain solvers, namely MATCONT and COCO. The bifurcation diagrams produced by these time-

domain solvers yield identical results since both utilise time integration to establish their residual equations. The primary distinction between the two lies in their methods for setting up the residual equations: COCO employs orthogonal collocation, whereas MATCONT uses the standard method [72,74]. When comparing the HBM continuation results to those obtained from MATCONT and COCO, a high level of accuracy is evident. Figures 3.16 and 3.17 demonstrate the accurate prediction of stable LCO amplitude. It should also be noted that both MATCONT and COCO predict an exchange in stability in the turning points of both diagrams.

Considering the smooth nonlinearity test case, Figure 3.16 demonstrates almost identical agreement with the MATCONT/COCO bifurcation diagrams. Examining the RRMS error in Figure 3.16b, it is observed that the mean error appears essentially as noise and can be almost neglected. From this, we can assert that in the case of the smooth nonlinearity, the HBM framework provides adequate estimations of LCO behaviour.

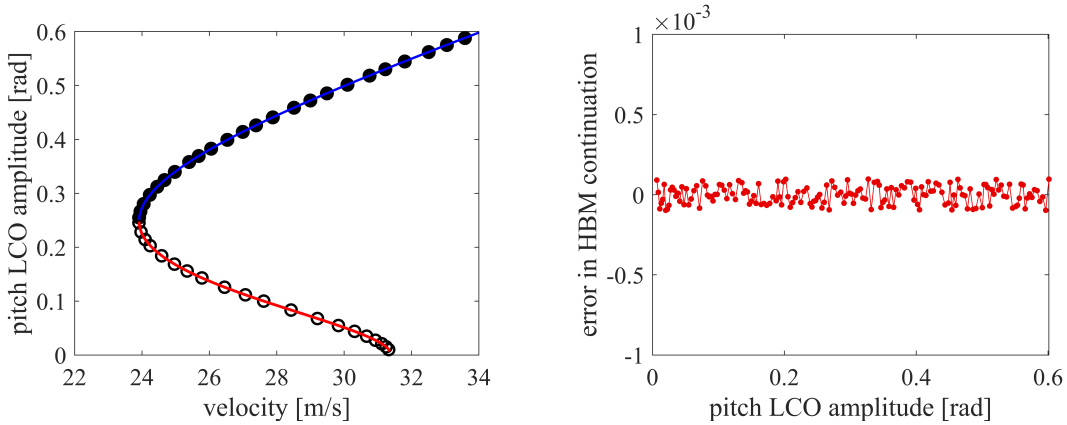

Figure 3.16: HBM continuation compared to time domain ode solver for smooth nonlinearity (a) Bifurcation diagram (HBM continuation: stable •, unstable **o**), (MATCONT/COCO: stable −, unstable −), (b) RMS error of HBM w.r.t MATCONT/COCO

Examining the freeplay comparison in Figure 3.17, inaccuracies in the amplitude of the unstable region are shown, as illustrated in Figure 3.17b. At the hopf point, the amplitude error measures at 45.71%. However, by iteration 30 ($27m/s$), the datasets align. This error may yet again be attributed to the Gibbs phenomenon described in

Figure 3.13. As demonstrated in Figure 3.13d, at pitch LCO amplitudes of 0.10 rad, the mean RRMS error of the nonlinear force response is 27 times less than at 0.02 rad amplitude. This explains why prominent errors are observed at low LCO amplitudes but become less impactful at higher LCO amplitudes. Another potential explanation may relate to the freeplay gap. Specifically, when the LCO amplitude approaches the magnitude of the freeplay gap, the higher harmonic content in the nonlinear force becomes significantly amplified [172]. This phenomenon, as illustrated in Figure 3.13c, can contribute to irregularities in the system response, resulting in the erratic patterns observed in the results.

Regardless of the underlying cause of the error, no quantitative correlation was identified between the magnitude of the unstable LCO and the boundary at which perturbations settle to rest or transition to the stable LCO branch, as is observed in some systems. Instead, the unstable section of the bifurcation diagram offers more of a qualitative insight into the system's behaviour. Specifically, it demonstrated that for small perturbations, the system tends to settle to rest, whereas larger perturbations result in a stable LCO response, with amplitudes aligning with the stable section of the bifurcation diagram. Given that the LCO amplitude is accurately captured within the stable region of the bifurcation diagram, it can be argued that the HBM framework provides an acceptable representation of the dynamic system's physical behaviour in this case.

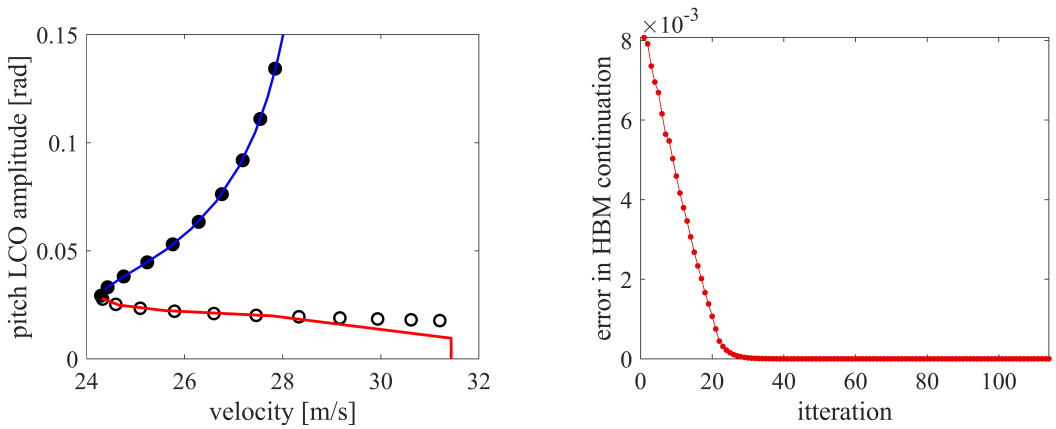

Figure 3.17: HBM continuation compared to time domain solver for nonsmooth nonlinearity (a) Bifurcation diagrm (HBM continuation: stable •, unstable **o**), (MATCONT/COCO: stable –, unstable –), (b) RMS error of HBM w.r.t MATCONT/COCO

Considering the computational costs of the methods, the most computationally demanding aspect of each process involves generating a time series through numerical integration for time-domain methods and employing the AFT procedure for HBM continuation. This difference stands out as the primary distinction between the methods, while other steps remain consistent. In Figure 3.18a, we compare the computation time at an arbitrary point in the continuation for a single run of the AFT procedure with a time-integration solution covering a full period. It becomes evident that at harmonic orders below 9, the HBM continuation scheme is expected to exhibit lower computation times at a fundamental level. However, this assessment does not account for the frequency of iterations required before the convergence of residual equations is achieved, potentially undermining the apparent advantage of a full continuation run.

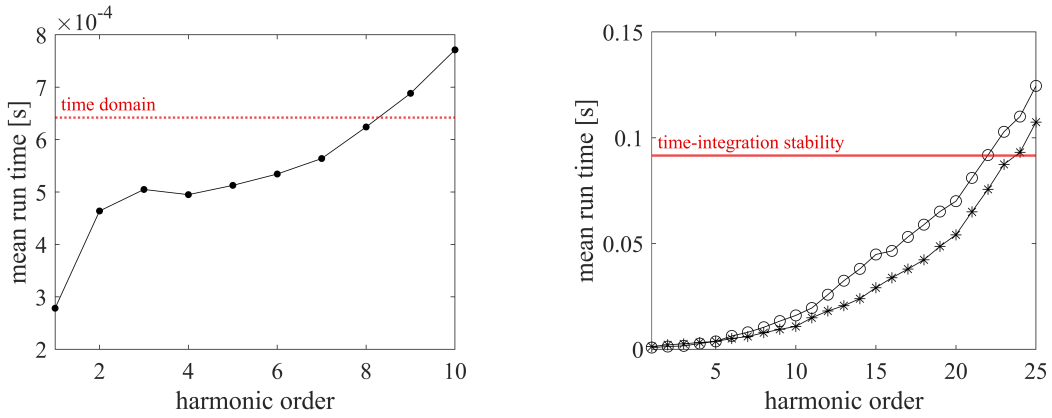

Figure 3.18: (a) Mean AFT method run time for a single LCO with harmonic order, (b) Stability method mean run time for single LCO with harmonic order (⊖ standard Hill's),(∗ Koopman operator based stability)

An essential consideration when evaluating computational efficiency is the choice of stability analysis method. Figure 3.18b presents a comparison of the mean computational time for the three stability methods applied to a two DoF system, representative of both the smooth and nonsmooth cases studied in this work. A key observation is that both frequency-domain methods exhibit lower computational costs than standard time integration up to 22 harmonics. At lower harmonic orders, the computational costs of the two frequency-domain methods are comparable, with the standard Hill's method being slightly more efficient. However, at 5 harmonics, the Koopman operator-based method becomes less computationally expensive and retains this advantage at higher harmonics.

In the smooth test case, the bifurcation curve shape and the absolute error in the Hill's method have converged by 5 harmonics. Similarly, the Koopman method provides accurate stability predictions by this point. Given that stability prediction is the primary goal, and the Koopman method offers a 7% reduction in run time compared to Hill's method and a significant 90% reduction relative to time integration, the Koopman operator-based method emerges as the preferred approach for computational efficiency in smooth cases.

For the nonsmooth study, both the bifurcation diagram shape and error in the

stability methods converge by 15 harmonics, making the Koopman method the optimal choice regarding computational time. However, as previously discussed, the Koopman method was unable to consistently predict the correct stability behaviour even after convergence. Despite the existence of errors relative to the fully converged solution, accurate conclusions about stability can be drawn by 8 harmonics. Therefore, the Hill's method at 8 harmonics is the optimal choice in this scenario, offering an 84.21% reduction in computational time compared to time integration while providing reliable stability predictions for the LCO.

Table 3.1 provides a comparison of the converged HBM solutions for both smooth and nonsmooth case studies to MATCONT and COCO, considering run-time and data storage requirements. This comparison is carried out over a full continuation run with 100 iterations. Regarding run-time, a similar pattern is observed for both the smooth and nonsmooth case studies. MATCONT is the slowest performing of the methods, while the HBM framework is the fastest. The HBM framework offers over a 90% reduction in run-time compared to MATCONT in both cases. For COCO, over a 60% reduction in time was observed in both cases with the converged HBM solutions. For all methods, the smooth case has a lower run-time than the nonsmooth. In the case of MATCONT/COCO, this is likely due to a higher number of time intervals being required to accurately capture the time behavior of the nonlinear force. For the HBM scheme, this is for two reasons: 5 harmonic orders were used in the converged smooth case, but 8 were used in the nonsmooth case, and the standard Hill's method was used over the Koopman operator based method for stability in the nonsmooth case.

Whilst the time reduction between the HBM method and COCO may appear relatively modest—on the order of 15–20 seconds—for a single run this difference is not particularly significant. However, as the intended purpose of this process is to be executed hundreds or even thousands of times, the cumulative time saving could become substantial. Furthermore, as the complexity and number of degrees of freedom of the system increase, it is anticipated that the computational advantage of the HBM method will become more pronounced, since its efficiency is related to the number of harmonics rather than the overall system size.

Data storage refers to the amount of data stored to describe LCO behaviors over the full run. For the time domain methods, this includes the position points of each DoF and time steps obtained through numerical integration. The method of discretion of time steps differs slightly between MATCONT and COCO. In MATCONT, a set tolerance is automatically calculated at each run and used to set a constant time interval over a full period. In COCO, a variable time step is automatically computed as the time-integration is carried out over a period. In the HBM framework, the required data includes the Fourier coefficients describing each DoF's amplitude and natural frequency. Fourier coefficients of the nonlinear force and nonlinear force differential are also required to compute stability. It appears there is a direct relationship between data storage requirements and run time, as more data is required to be handled, resulting in higher run times. The same conclusions are then reached from looking at the data storage and run time comparisons. With the considered test case, below 32 harmonics, HBM is more data efficient than COCO in the smooth case and below 44 in the nonsmooth case.

Table 3.1: HBM time and data storage requirement comparison to generate full bifurcation diagram

	smooth		nonsmooth	
Software	Run Time $[s]$	Data Storage	Run Time $[s]$	Data Storage
MATCONT	105.78	46200	145.31	64600
COCO	29.44	38645	34.16	53250
HBM	10.40	6800	12.68	10400

From the comparisons of both accuracy and computational cost of the HBM framework to MATCONT and COCO, it is evident that the HBM framework is more effective at estimating LCO behaviour via bifurcation diagrams in both the smooth and nonsmooth test cases. However, it should be mentioned that a key reason for this, particularly considering computational cost, is due to the capabilities of each tool. Both MATCONT and COCO have capabilities for searching for other types of bifurcations, and particularly in the case of MATCONT, they provide a more in-depth user interface. In contrast, the proposed HBM framework is only suited for generating bifurcation

diagrams to describe LCO behaviour.

3.5 Conclusions

This study proposed a computationally efficient method for estimating LCO behaviour and determining stability in aeroelastic systems. The methodology involved conducting LCO analysis solely in the frequency domain, integrating the HBM continuation and the Koopman operator.

The Chapter elucidated the methodology for a general aeroelastic frequency domain solver for LCO, providing detailed insights into the HBM continuation scheme and frequency domain stability analysis. Subsequently, this methodology was put into practice through a numerical test case, encompassing both geometric and localised nonlinearities. The results were validated against outcomes from MATCONT and COCO.

In the smooth nonlinear numerical test, successful convergence of bifurcation diagrams and LCO stability estimation was achieved at 5 harmonic orders. The Koopman operator-based method emerged as the preferred choice for stability analysis, offering notable reductions in run-time compared to standard Hill's method and time integration. However, in the nonsmooth nonlinear numerical test, convergence of the bifurcation diagram was achieved at 8 harmonic orders. While the standard Hill's method proved successful compared to time-integration, the Koopman operator-based method exhibited chaotic behavior, rendering it unreliable for LCO stability determination.

Comparisons with MATCONT and COCO underscored the HBM framework's superiority in accuracy and computational efficiency, particularly evident in the smooth test case. Despite some discrepancies in the nonsmooth case, the HBM framework provided a satisfactory description of the system's dynamic behaviour.

From these results, it can be concluded that the proposed framework is well-suited for efficient data acquisition while maintaining an adequate level of accuracy. It exhibits faster computational performance compared to conventional time-domain approaches for LCO analysis and demonstrates satisfactory accuracy, particularly in smooth test cases.

With the HBM framework numerically validated, the subsequent phase of this re-

search will integrate the present methodology into a probabilistic framework for nonlinear system identification of aeroelastic systems. Following numerical validation, the system will be employed to generate training datasets for surrogate modelling. Experimental validation will subsequently be conducted, as detailed in the following chapter.

Chapter 4

Data-driven Bayesian Inference for Stochastic Model Identification

4.1 Introduction

This Chapter will first present the overall probabilistic data-driven model updating methodology for a general nonlinear aeroelastic systems. It will include the process of gathering training data from HBM continuation (building on the work from Chapter 3), the development of Kriging based surrogate models, and the implementation of the Bayesian inference with MCMC, TMCMC and SMC sampling methods. The specific objectives behind the use of different MCMC-based sampling techniques are to provide a comparative study on sampling performance and its robustness towards parameter identification and model updating for a non-linear aeroelastic model under limited data.

In aerospace design, particularly with regard to LCO analysis, probabilistic estimates of system parameters are essential for managing the uncertainty inherent in real-world operating conditions. This approach enhances the ability to predict and mitigate the occurrence of LCOs, which can have significant consequences for both the safety and performance of aerospace systems. By quantifying the uncertainty in parameters, optimising designs, and assessing risks more accurately, engineers can ensure that

aircraft and other aerospace vehicles are robust to LCOs, operate safely within defined limits, and are capable of adapting to varying conditions throughout their operational lifespan.

The three goals for the proposed methodology are (1) to provide distributions that numerically estimate nonlinear parameters (parameters in the nonlinear equation); (2) to produce bifurcation plots with intervals of probability; (3) to rank different forms of nonlinear models. In the following section, the mathematical model and experimentation describing a simplified nonlinear flutter test rig will be described. In the results section, nonlinear parameter estimations using the proposed methodology will first be presented followed by the discussion of the suitability of the nonlinear model and the appropriate choice for the sampling method. This will additionally serve as experimental validation of the framework presented in Chapter 3. Then, the improvement of using alternative nonlinear models through from the Bayesian model selection is described. The foundational elements of this work were originally published in [10, 173].

The framework presented in this chapter would be highly valuable for practical engineering applications, particularly in the design of flexible aircraft wings. Probabilistic identification of nonlinear model parameters enhances understanding of design safety margins, while data-driven surrogate models markedly reduce computational effort, accelerating early-stage design. Continued advances in nonlinear aeroelastic analysis tools will further enable the development of more innovative and efficient designs.

4.2 Proposed Data-Driven Bayesian Approach

The general Methodology is divided into two parts: the development of a surrogate model , and Bayesian model updating with forward UQ. This section presents the theoretical foundations of the proposed framework, followed by its application to a representative nonlinear aeroelastic test case.

4.2.1 Concept of Data-Driven Bayesian Framework

The main concept behind the data-driven Bayesian approach is illustrated in Figure 4.1. A prior parametric space is defined for the parameter θ (typically representing nonlinear aeroelastic parameters in this work), which is characterised as the feasible space within which the parameter values can reasonably exist, based on informed estimates. For example, a quadratic nonlinearity in a typical differential equation would typically fall within the range of 0 to 100. A single data-driven model is then trained to accurately represent the behavior within this parametric space, using training data gathered from sampling the system's equations of motion. After the model is trained, Bayesian inference is applied, which updates the prior parametric space into a posterior distribution. This posterior distribution provides probabilistic estimates for θ.

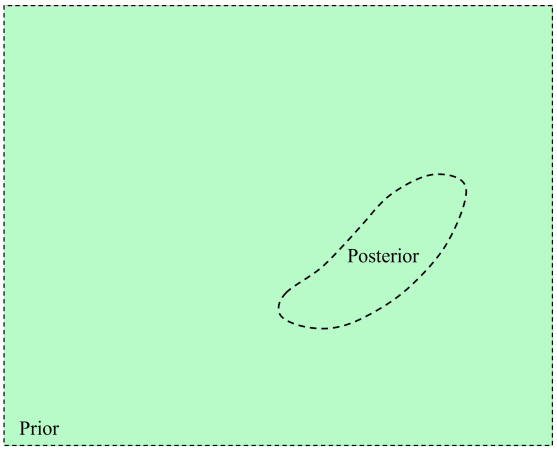

Figure 4.1: Conceptual diagram of data-driven model updating process

4.2.2 The theory of Bayesian inference and sampling techniques

Consider the high-fidelity model f, where

$$y = f(x, \theta) \tag{4.1}$$

where y and x are output and input observations defined over a range of values $x\epsilon\,[x_{min}, x_{max}]$, $y\epsilon\,[y_{min}, y_{max}]$. The goal of this process is to estimate the set of parameters, denoted as θ, based on the observations of x and y using a probabilistic

approach. Once we have these probabilistic estimates for θ, the next step is to derive a probabilistic estimate for y that accurately represents the observations, taking into account both aleatory and epistemic uncertainties. If all observations fall within the probability interval produced by this estimate, it can be assumed that the model with the identified parameters provides an accurate representation of the system. This implies that the model, with these parameters, can then be used for further analysis, enabling a deeper understanding of the system's nonlinear behaviour.

The Bayesian inference process refines a prior distribution of θ into a posterior distribution. Samples are drawn from the prior distribution $P(\theta)$ and a likelihood function is applied to assess how well each sample aligns with the observations. The basic formulation is as follows:

$$P\left(\theta|\mathbf{z}\right) = \frac{P\left(\mathbf{z}|\theta\right).P\left(\theta\right)}{P\left(\mathbf{z}\right)} \tag{4.2}$$

where $\mathbf{z}$ is the vector of observations $(\hat{x}_{(1,..,i)}, \hat{y}_{(1,..,i)})$. The evidence function $P\left(\mathbf{z}\right)$ acts as a normalising constant to ensure the posterior integrates to one. Likelihood function $P\left(\mathbf{z}|\theta\right)$, reflects the degree of agreement between the obtained measurements $\mathbf{z}$ and the model output $f(x, \theta)$. The choice of likelihood function depends on the UQ metric, which is crucial as it can impact the convergence and accuracy of the model updating. Various options exist, such as lognormal distributions [174], inverse error [175], and exponential distributions [176]. The common choice, assuming the error between observations and the model follows a zero-mean normal distribution [121], is to implement a maximum likelihood estimation function as follows:

$$P\left(\mathbf{z}|\theta\right) = \left(\prod_{i=1}^{n} \frac{1}{\sigma_p\sqrt{2\pi}}\right) \exp\left[-\sum_{i=1}^{n} \frac{\left(y_i - f\left(x, \theta_i\right)\right)^2}{2\sigma_p^2}\right] \tag{4.3}$$

Where σ_p is the variance of error ϵ_p which controls the centralisation degree of the posterior distribution. Also referred to as the width parameter, σ_p (as well as ϵ_p) is predetermined and case-dependent. Width parameter is selected based on the resulting acceptance rate of the samples. Acceptance rate shows the trade-off between accepting too many small steps and rejecting too many large proposal steps. Typically an

acceptance rate between 0.15-0.5 ensures the algorithm's efficiency is above 80% so is aimed for [177]. Approximate Bayesian from Equation 5.2.2 (where $P(\mathbf{z})$ is assumed as a constant) is evaluated by drawing samples from prior distributions until converged mean posteriors are reached. As the goal of the sampling is to converge to an unknown stationary distribution, standard methods (such as LHS used for surrogate development) are not suited. This is because standard sampling approaches typically draw samples from the prior parameter space uniformly and do not account for the shape of the posterior distribution. As a result, many samples lie in regions of low posterior probability, making the process inefficient.

Advanced sampling techniques are therefore employed commonly for optimal efficiency [121], the three most common being MCMC, TMCMC and SMC. Each method provides unique benefits in terms of computation time, number of samples required and accuracy. The choice of sampling method is case-dependent and should be considered carefully with the following methods considered:

a Markov-Chain Monte-Carlo

The MCMC (Metropolis-Hastings method) sampler is comprised of two main features, Monte Carlo Simulation (MCS) and Markov chains. Introduced by Markov, a chain is initiated from θ_1 and a transition to θ_2 that is carried out based on a transition probability distribution function [178]. The assumption is that by allowing the chain to extend infinitely, the chain converges to a stationary distribution which corresponds to the posterior. The diagram in Figure 4.2 details how the sampling is carried out. Computation time per sample is the lowest with this method but, often a higher number of samples are required to reach a converged solution. It is common to discard a number of initial samples in what is known as the 'burn-in' to improve the quality of the results. A tuning parameter is also required with MCMC, both tuning parameter and burn-in are predefined with educated trial and error.

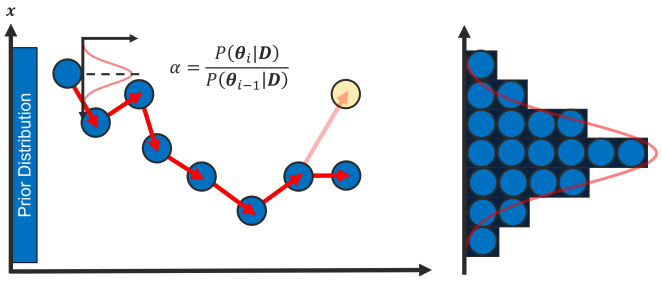

Figure 4.2: MCMC diagram, blue points represent accepted samples and yellow points are not accepted. The term α is acceptance probability of sample i, if it is above a random number between 0 and 1 the sample is accepted.

b Transitional Markov-Chain Monte-Carlo

The TMCMC sampler is an adaptive variation of MCMC [179] and is also a specific variant of the SMC samplers (see Betz et. al [180]). A series of intermediate transitional distributions are used to gradually converge the samples towards the final posterior distribution. In addition, unlike the MCMC, it does not generate samples in a serial manner. Instead, it generates N distinct Markov chains, each initiating from the N samples generated from the previous transition distribution and updates each chain according to its associated statistical weight. Through such approach, the TMCMC sampler is applicable towards sampling from multi-modal posteriors and have also been utilised to sample from high-dimensional posteriors (i.e., 18-dimensions) [121]. The diagram in Figure 4.3 illustrates how the process is carried out. Whilst having a higher computational cost, TMCMC is automatically tuned and converges with fewer samples than MCMC commonly. Parallel computing can also be taken advantage of to improve computational efficiency.

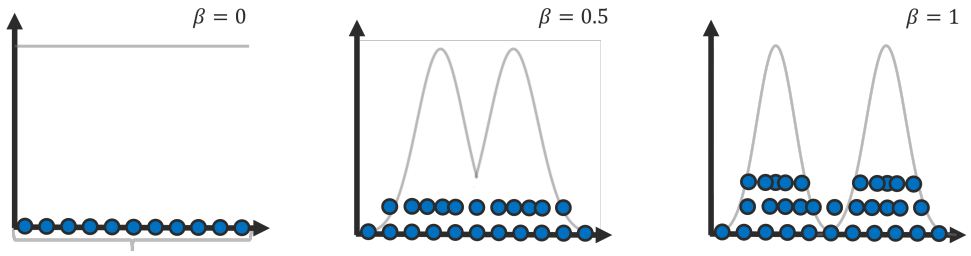

Figure 4.3: TMCMC diagram with three distinct Markov chains of N samples. With each iteration, scaling parameter β is gradually increased from zero to 1 each time refining the prior distribution.

c Sequential Monte-Carlo

The SMC sampler is a subset of the SMC methods that is based the Particle Filter methods typically employed for system identification purposes [181, 182]. The sampler utilises the importance sampling-resampling approach to generate samples sequentially from a dynamical posterior. Like the TMCMC sampler, the sampling procedure involves generating N distinct Markov chains, each initiating from the N samples obtained from the previous transitional distribution. The difference from the TMCMC sampler is that each Markov chain generates a new sample independently from one another (i.e. each Markov chain generates one updated sample from the starting seed sample) which allows the sampling procedure to be easily parallelised. As such, the SMC sampling approach is applicable for on-line Bayesian inference to infer either time-invariant or time-varying parameters, while the MCMC and the TMCMC samplers are only applicable for off-line Bayesian inference to infer time-invariant parameters. In addition, like the TMCMC sampler, it is also able to generate samples from multi-modal and high-dimensional posteriors. The diagram in Figure 4.4 illustrates the SMC sampling process. Computation time per sample is on average less than TMCMC but more than MCMC with convergence usually reached in fewer samples than MCMC.

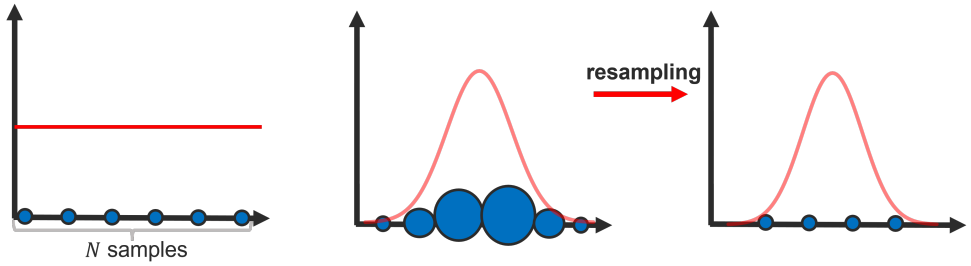

Figure 4.4: SMC diagram. The size of the blue points indicate the statistical weight one the sample with larger points carrying more weight.

Each method will be tested in this study to evaluate which sampling method is suited to the methodology. Further detail into the Bayesian interface and each sampling method are laid out by Lye et al. [121].

4.2.3 TMCMC based class selection

One of the key advantages of Bayesian inference is in model selection. With the evidence term, the validity of models can be ranked. The evidence term is not required in the cases of MCMC but can be numerically estimated [183]. With regards to TMCMC sampling method, the evidence for specific model f, $P(\mathbf{z}|f)$) is a byproduct required for estimation of the statistical weight function ϖ used to describe the importance of each sample [184]. The model selection with TMCMC sampling is formulated in [184]. The TMCMC algorithm draws samples from a series of intermediate distributions, generated iteratively with the capability of converging to complex multi-modal posterior distributions. These PDFs are defined as:

$$P_j \propto P(\theta|f) \cdot P(\mathbf{z}|f,\theta)^{\mathscr{B}_j} \quad j = 0, ..., m \tag{4.4}$$

Where j is the stage number. Tempering parameter $\mathscr{B}$ evolves from $\mathscr{B}_0 = 0$ to $\mathscr{B}_m = 1$ to ensure a smooth transition between the prior and posterior distribution so $P_0 = P(\theta|f)$ to $P_m = P(\theta|f,\mathbf{z})$. The weight of each sample is determined as:

$$\varpi(\theta_{j,k}) = \frac{P(\theta|f) \cdot P(\mathbf{z}|f,\theta)^{\mathscr{B}_{j+1}}}{P(\theta|f) \cdot P(\mathbf{z}|f,\theta)^{\mathscr{B}_j}} = P(\mathbf{z}|f,\theta)^{\mathscr{B}_{j+1}-\mathscr{B}_j} \quad k = 1, ..., N_j \tag{4.5}$$

Where N_j is the number of samples at stage j. Next, compute

$$S_j = \frac{\sum_{k=1}^{N_j} \varpi(\theta_{j,k})}{N_j} \tag{4.6}$$

This process is repeated for each stage. At the end of the algorithm, the evidence of the model can be computed as

$$P\left(\mathbf{z}|f\right) = \prod_{j=0}^{m-1} S_j \tag{4.7}$$

It is common to evaluate $\log\left(P\left(\mathbf{z}|f\right)\right)$ for ease of computation, mainly to avoid numerical problems (e.g. arithmetic underflow) associated with the calculation of the full likelihood function [121]. The less negative $\log\left(P\left(\mathbf{z}|f\right)\right)$ the more evidence there is to suggest the specific model fits the provided data.

4.2.4 Kriging Algorithm

As the model updating process may require thousands of samples to achieve convergence, it is not ideal to run a potentially computationally expensive model f this many times. To address this, data-driven models $\hat{f}$ are trained to replicate the behaviour of the high-fidelity model f. This enables BMU and polymorphic response determination to be carried out without the significant computational cost associated with running the high-fidelity model. The configuration of the model is as follows:

$$[y \pm \sigma_y] \approx \hat{f}(x, \theta) \tag{4.8}$$

Where σ_y is the standard deviation in the estimate of y. Kriging is employed to construct multi-resolution data-driven surrogate models based on input-output pairs $(x, \boldsymbol{\theta}, \mathbf{y})$. Here, x represents the independent variable (typically frequency or amplitude), $\boldsymbol{\theta} = \{\theta_1, \ldots, \theta_n\}$ constitutes the parameter vector for model training, and $\mathbf{y}$ denotes the corresponding system response outputs. The surrogate model is set up as

follows as follows:

$$\hat{f}\left(x,\theta\right)=\mu\left(x,\theta\right)+\mathbf{w}^{T}(x,\theta)\mathbb{S}^{-1}(\mathbf{y}-\mu(x,\boldsymbol{\theta})) \tag{4.9}$$

Here, $\mu(x,\theta)$ is the mean function that represents the expected value or trend of the response variable. It is typically assumed to be constant or defined based on prior knowledge or domain expertise. The covariance matrix $\mathbb{S}$ is an $n\times n$ matrix, where $\mathbb{S}_{ij}=\text{Corr}[(x,\theta_i),(x,\theta_j)]$, representing the covariance or correlation between the i^{th} and j^{th} input points. The weight factor $\mathbf{w}(x,\theta)$ is defined as:

$$\mathbf{w}(x,\theta)=\mathbb{S}^{-1}Corr[(x,\theta),(x,\boldsymbol{\theta}))] \tag{4.10}$$

where $\text{Corr}[(x,\theta),(x,\boldsymbol{\theta})]$ is a vector representing the correlation or covariance between the input (x,θ) and the training point $(x,\boldsymbol{\theta})$. In Kriging, correlation is determined using functions in the spatial domain; here, the Matérn covariance function is employed.

$$Corr[(x,\theta),(x,\boldsymbol{\theta})]=\sigma_i^2\frac{2^{1-\upsilon}}{\Gamma(\upsilon)}\left(\frac{\sqrt{2\upsilon h}}{a}\right)^{\upsilon}K_{\upsilon}\left(\frac{\sqrt{2\upsilon h}}{a}\right) \tag{4.11}$$

where h is a vector representing the separation in multiple dimensions between (x,θ) and $(x,\boldsymbol{\theta})$. The variance σ_i, the smoothness parameter υ, and the range a are determined through the optimisation process described in [185]. The Bessel function is denoted by K_{υ}, and $\Gamma(\upsilon)$ serves as a generalisation of the factorial function for non-integer values [186]. This process continues until the accuracy and variance of $\hat{f}$ converge.

The initial step in training the model involves sampling values of θ from the prior distribution, denoted as $P(\theta)$. This prior distribution covers an extensive but plausible range for the parameters θ (which is also the case for the first iteration of the process that will be laid out in Chapter 5). Posterior distribution, $P\left(\mathbf{z}|\theta\right)$ employed is the same as in the BMU process. LHS is employed with the procedure for drawing samples is as follows:

$$\theta_i = F_P^{-1}\left(\frac{\pi_{ij} - U_{ij}}{N}\right) \tag{4.12}$$

Here, $F_P(\theta)$ represents the cumulative distribution function of $P(\theta)$. The number of samples is denoted by N, and π_{ij} is a random permutation of $1, 2, \ldots, N$ for each i^{th} sample of parameter j. Stratification is applied using U_{ij}, a random number between $[0, 1]$. This yields the training input $\boldsymbol{\theta} = [\theta_1, \theta_2, \ldots, \theta_N]$. The training samples are processed through the high-fidelity model f using $y_i = f(x, \theta_i)$ to obtain the training output $\mathbf{y} = [y_1, y_2, \ldots, y_N]$. The input range x remains constant for each training run.

4.2.5 Algorithm

The formulation presented in this section is implemented to establish the full data-driven Bayesian framework as follows. A data-driven model is built covering a full design space. The accuracy of the model is estimated based on mean comparison with a separate set of comparison data. Once the accuracy of the model has converged to an acceptable degree, BMU is applied with the same prior distribution used to gather training data for the data-driven model. Algorithm 1 gives details on how to compute the probabilistic response of high-fidelity model f with a data-driven model updating framework. Inputs for unknown parameters θ are gathered with LHS and then run through the high-fidelity model.

Output data $\mathbf{y}$ and corresponding input $\boldsymbol{\theta}$ are fed into a training algorithm in Equation 4.9 to produce the main data-driven model. For each training run, an additional run is conducted and stored as comparison data to validate the accuracy of the model. The accuracy is assessed by inputting the data used to generate the comparison plot into the data-driven model and computing the RRMS error between the model's response and the response from the comparison data. Convergence is assessed based on $\mathscr{A}$, percentage difference in accuracy between models with increasing amounts of training data. For instance, if $\mathscr{A}$ is set to 1%, the model is considered to have converged when the accuracy difference between model i and model $i + 1$ is less than 1%. As the single model required in the single-iteration process (as opposed to the multi-iteration process that will be detailed in Chapter 5) is required to have as high as possible the

mean accuracy, the convergence criterion is set high (a low value of $\mathscr{A}$). Once the accuracy of the model has converged BMU is utilised to estimate θ. Finally, the probabilistic estimate of θ is evaluated through the converged surrogate model to obtain a distribution of possible nonlinear system behaviours. This estimate is expected to encompass all experimental observations within its probability interval, defined as the region containing 95% of the data.

Algorithm 1 Data-driven BMU

Input: Experimental observations $\mathbf{z}$, Prior distribution $P(\theta|f)$, Width parameter σ_p, Training data increment N_0, Data-driven model convergence factor $\mathscr{A}$

Output: Polymorphic response $P(y)$, Posterior distribution $P(\theta|\mathbf{z})$, Data-driven model $\hat{f}$

$N = N_0$
$conv = \mathscr{A} + 1$
$i = 0$
while $conv > \mathscr{A}$ **do**
  $i = i + 1$
  $\theta_i = F_P^{-1}\left(\frac{\pi_{ij} - U_{ij}}{N}\right)$
  $y_i = f(x, \theta_i)$
  $\boldsymbol{\theta} = [\boldsymbol{\theta}, \theta_i]$
  $\mathbf{y} = [\mathbf{y}, y_i]$
  $\hat{f}(x,\theta)_i = \mu(x,\theta) + \mathbb{S}^T(x,\theta)\mathrm{K}^{-1}(\mathbf{y} - \mu(x,\boldsymbol{\theta}))$
  $A^i = AccuracyCheck(\hat{f}_i)$
  if $i \geqslant 2$ **then**
    $conv = |A_i - A_{i-1}|$
  end if
  $inc = inc + inc_0$
end while
$\hat{f}(x,\theta)_n = \hat{f}(x,\theta)_i$
$P\left(\theta|\mathbf{z}, \hat{f}\right) \approx P(\mathbf{z}|\theta).P(\theta)$
$\theta = MCS[P(\theta|\mathbf{z})]$ {Monte-Carlo simulations based on posterior distribution}
$P(y) = \hat{f}(x,\theta)_n$ {Monte-Carlo simulations of θ are run through final surrogate mode}

4.3 Experimental Study & Validation

The experimental apparatus and corresponding LCO data employed for framework validation are now described. These datasets, acquired through wind tunnel testing,

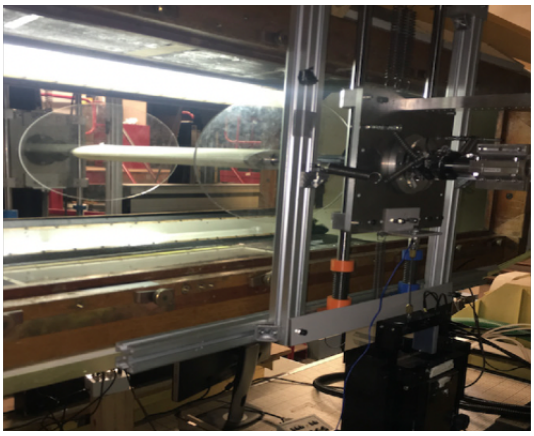

Figure 4.5: University of Bristol's aerofoil flutter rig experimental configuration taken from [6]

will serve two purposes; validation of the HBM framework established in Chapter 3, and verification of the current chapter's methodology. Experimental results for two distinct aerodynamic configurations are included in the validation process.

4.3.1 Experimental Test Rig

Pre-existing experimental data collected at the University of Bristol by Lee et al. [5] has been utilised to validate the methods proposed in this study. Figure 4.5 illustrates the experimental flutter rig, consisting of a NACA-0015 wing profile firmly affixed to a stainless steel shaft. The aerofoil is supported by rotational bearings on each end, enabling rotation, along with a bearing system facilitating vertical displacement. The spring in the heave DoF behaves linearly. Additionally, leaf springs are introduced in the bearings to induce a nonlinear hardening effect in pitch motion. This setup replicates nonlinear effects encountered at interfaces in real aircraft. Further details of the setup can be found in Ref [100]. Heave displacement is measured using an Omron ZX1-LD300 laser displacement sensor, while pitch motion is captured by an RLS AksIM 18-bit absolute magnetic encoder. Wind speed is directly recorded from the wind tunnel control system. Stable and unstable LCO are captured through Control-Based Continuation. The standard linear parameters of the rig were determined through static testing.

Control-Based Continuation (CBC), first introduced by Sieber et al. [187], enables bifurcation analysis to be performed directly within experiments. This is achieved by integrating Newton iterations with feedback control within a continuation framework, which allows for the detection and tracking of unstable LCO [188]. The efficacy of CBC has been demonstrated across a range of mechanical systems. In particular, Lee et al. [189] applied CBC to a two DoF aerofoil, successfully capturing both the amplitude and frequency of unstable LCO (see Ref. [190] for a deeper explanation on CBC and its application in this context).

The raw data undergoes fast Fourier transform analysis to minimise noise, a process repeated for two experimental configurations with different spring constants. The results are displayed in Figure 4.6 where subcritical beahaviour is observed in both configurations. Design rig parameters for each configuration are displayed in Table B.1. In configuration 2, the linear stiffness in both heave and pitch is increased, along with the damping in the pitch DoF. In this case, 11 experimental data points are available, compared to 8 in the previous configuration.

Based on the experimental techniques employed to acquire the data, reasonable assumptions can be made regarding the acceptable level of noise. This noise level is used as the width parameter (σ_p) in the Bayesian model updating process and, subsequently, for data-driven model development in Chapter 5.

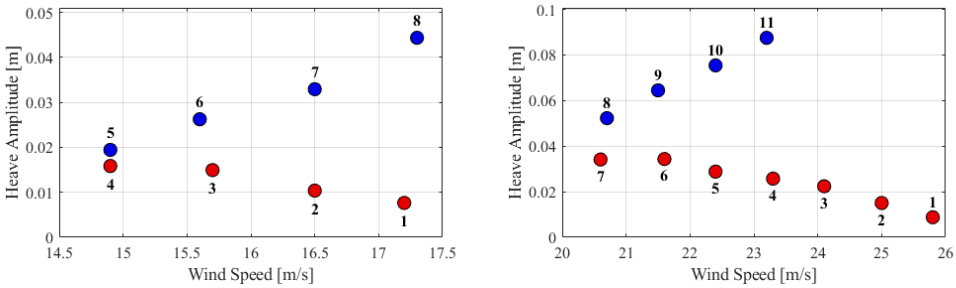

(a) configuration 1 (b) configuration 2

Figure 4.6: Labelled CBC experimental data from University of Bristol flutter rig (• stable LCO) (• unstable LCO)

4.3.2 Numerical Modeling

The linear mathematical model described in Equations 3.30 and 3.31 in Section 3.4.1 is once again utilised. In this test, however, the aerodynamic state w is introduced as a DoF to create a more intricate aerodynamic model. Consequently, the full 3×3 structural and aerodynamic matrices are employed to construct the $\mathbf{Q}$ matrix. As the leaf spring employed in the experimental setup was intended to replicate the behaviour of a geometric nonlinearity, the smooth nonlinearity from Equation 3.32 is again applied to the pitch DoF.

The parameters outlined in Table B.1 in Appendix B are defined for both experimental configurations. Flutter speeds for each setup are obtained through eigenvalue analysis, as also depicted in the table. Estimates for the nonlinear parameters $K_{\alpha 2}$ and $K_{\alpha 3}$ are required. Physically, these parameters characterise the rotational stiffness of the aerofoil as it is deflected. The spring does not exhibit a linear increase in resistance; rather, the resistance grows with increasing rotational displacement, which is what these parameters quantify within the nonlinear equation. Here, deterministic estimates derived from normal theory, as found in the original study [5], as well as updated estimates obtained from a probabilistic Bayesian approach, are separately employed.

4.4 Case Study Implementation

The same two DoF aerofoil system used in the previous chapter is implemented here. The specific goal of the data-driven BMU process here is to provide probabiltic estimates of nonlinear parameters $K_{\alpha 2}$ and $K_{\alpha 3}$ based on the CBC experimental data that was used for validation in the previous test case (Figure 4.6). Along with probabilistic parameter estimates, a probabilistic bifurcation diagram is also required. A bifurcation plot with 95% interval of probability is drawn. In theory, the mean solution should give a close approximation of the true bifurcation plot. It could also be argued, if all input experimental data fall within the interval of probability a reasonable approximation of true uncertainty in the predicted parameters has been captured. If data points lie outside of the interval of probability, it may suggest the mathematical model does not

truly represent dynamic behaviour or there has been errors obtaining the experimental data.

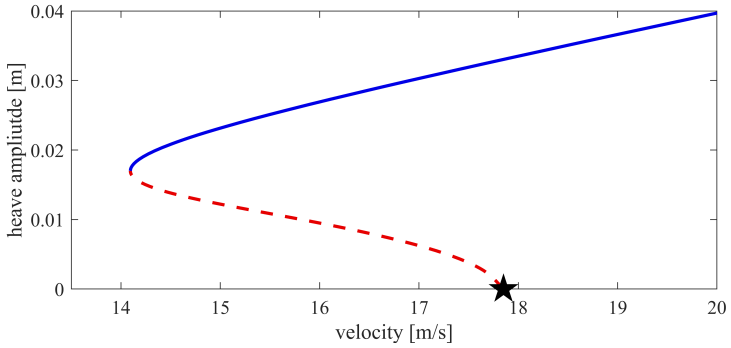

Figure 4.7: Subcritical bifurcation diagram for two DoF aerfoil system with cubic spring nonlinearity, (- stable LCO), (– unstable LCO), ($\star$ hopf bifurcation)

The first factor to consider is the development of the data-driven model for this specific case. Taking the result shown in Fig.4.7 as a generic representation of the expected solution shows that there is a unique velocity V solution for each LCO amplitude point h. It is possible that the Kriging surrogate model $\hat{f}(h, \theta)$ can be set up as $V = \hat{f}(h, \theta)$ where θ represents the vector of nonlinear parameters. The diagram in Fig. 4.8a presents the development of the data-driven model. Training data for the surrogate model is generated from deterministic simulations of nonlinear aeroelastic systems using the HBM based frequency domain solver from the previous chapter. The Kriging algorithm described in Section 4.2.4 is implemented to train the data-driven models. Accuracy is then assessed by comparison with a separate set of data gathered through the frequency domain solver. This is carried out until accuracy of the model has converged.

The BMU process is then considered once a converged data-driven model is produced. Implementation of the procure for this test case is shown in Fig. 4.8b. The same prior distribution used to develop the surrogate model, the CBC data from Section 4.3 and the converged data-driven model is fed into the BMU process from Section 4.2.2. A posterior describing nonlinear parameters $K_{\alpha 2}$ and $K_{\alpha 3}$ are taken as the probabilistic parameter estimates. Monte Carlo samples are subsequently drawn from the posterior distributions and ran through the surrogate model over a range of amplitude values.

Upon obtaining a converged mean bifurcation diagram topology, 95% intervals of probability are computed to yield a probabilistic characterisation of the LCO behaviour. These bounds are expected to encompass all experimental observations.

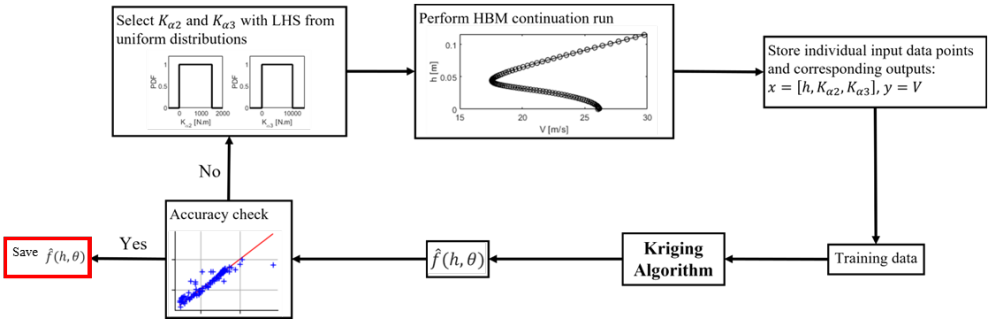

(a) Development of Kriging data-driven models

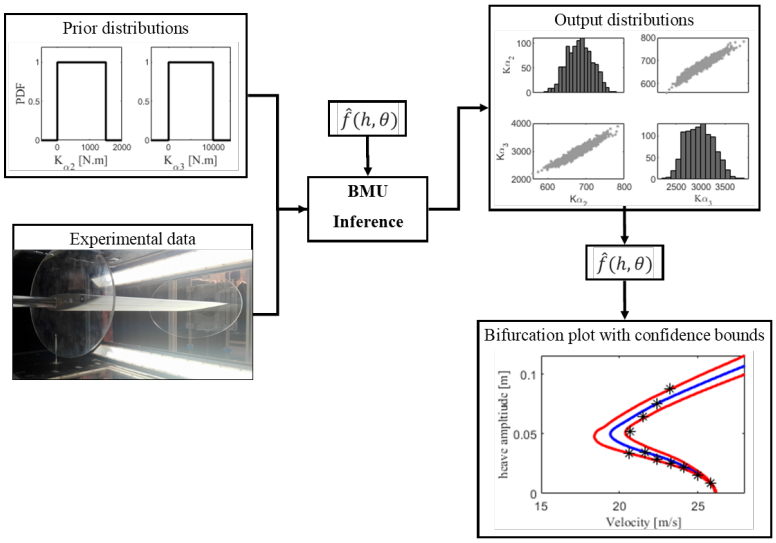

(b) Bayesian model updating with experimental data

Figure 4.8: Methodology of probabilistic identification framework for two degree-of-freedom aerofoil study

Three factors are used to determine the overall quality of results: coefficient of variance, bias and *quality* [180]. Coefficient of variance ($COV = \frac{std}{\mu}$) is used to determine the probability of a prediction where std is the standard deviation and μ is the mean of the prediction from BMU. Bias is calculated with

$$bias = \frac{|\mu - e|}{e} \tag{4.13}$$

Where e is the corresponding true experimental point to μ. This gives a measure of accuracy only considering the mean prediction and not intervals of probability. A completely accurate prediction would give a *bias* of zero. Taking probability of prediction into account, *bias* and COV are used to calculate *quality*.

$$quaility = \sqrt{bias^2 + COV^2} \tag{4.14}$$

Combining both probability and accuracy, *quality* is the main factor used to determine overall accuracy. An ideal prediction would have a *quality* of zero. These factors will be calculated by comparing bifurcation plots using BMU predictions of nonlinear parameters to experimental data for both configurations.

4.5 Results: Comparison of Sampling Methods

In this section, the described probabilistic identification methodology proposed in the section 2 is applied to the two configurations of the above nonlinear flutter test rig. It is assumed that original nonlinear function is in a form shown in Section 3.4.1 as in previous work [5, 100, 101, 189]. Considering the reference data in Ref. [5], we assume that $K_{\alpha 2}$ is in the range of $0 - 1500N/rad^2$ while $K_{\alpha 3}$ is in the range of $0 - 10000N/rad^3$. For each setup, three sampling methods, namely MCMC, TMCMC and SMC sampling methods, are applied and compared in terms of the quality factors of the model identification. These results are also compared to the initial estimates obtained form normal from theory [5] and listed in Table B.1.

Figure 4.9 shows mean accuracy of Kriging surrogate models with respect to the amount of training continuation runs carried out. Here, mean accuracy is estimated based on the difference between predictions from the Kriging model and a separate set of comparison data from continuation runs. Accuracy converges with 400 bifurcation diagrams in training data at 99.8%. The same amount of training data is again required for the second configuration. Figure 4.10 compares the amplitude of LCO obtained from HBM simulation and the Kriging surrogate model. The highlighted area reflects the degree of uncertainty from the predictions using the Kriging model within a 95%

interval of probability. Small discrepancies are observed at turning points as sharpness of the curve is increased which was not improved with increased sampling. The largest overshoot of the turning point observed was 2% (shown in Figure 4.10b which was considered within a reasonable margin of error for this study. Uncertainty in model predictions close to estimated values for nonlinear parameters proved to be less an 1% on average. It was therefore assumed that the mean predictions of the surrogate model were accurate in the subsequent Bayesian parameter estimation process, and the uncertainty associated with the surrogate model was not incorporated into the parameter estimation. With mean predictions, it is observed that the Kriging model is capable of accurately capturing the response of LCO.

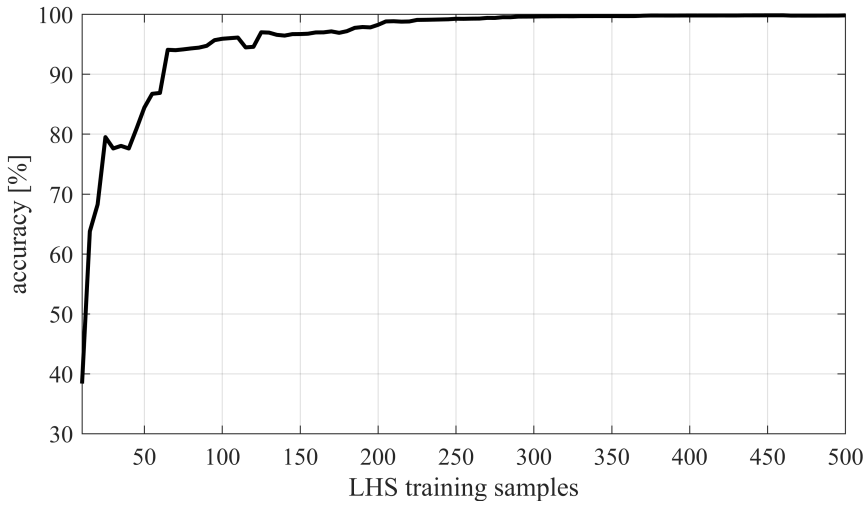

Figure 4.9: Accuracy of surrogate model with respect to sample size for configuration 1

4.5.1 Configuration 1

Bayesian inference framework is firstly applied to the first configuration with the experimental data shown in Figure 4.19. Tuning parameters presented in Table 4.1 are used to ensure an acceptance rate between 0.15-0.5 for each sampling method. Prior distributions are uniform between the stated bounds as low prior knowledge of the parameters is assumed. Figure 4.11 shows the convergence of nonlinear parameters

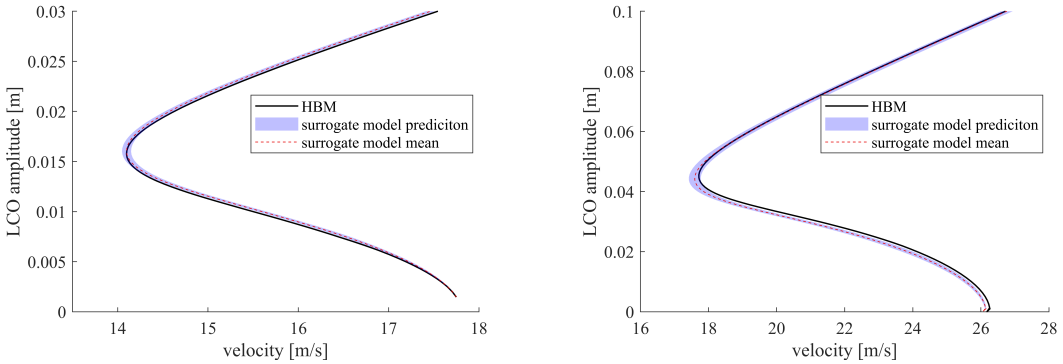

(a) configuration 1 (b) configuration 2

Figure 4.10: Data-driven model output comparison with deterministic model.

Table 4.1: Tuning parameters

Prior distribution bounds	**Width parameter**	**Burn-in**	**Covariance matrix**
K_{α_2}: 0 - 1500	MCMC: 0.6	200	[1000 0]
K_{α_3}: 0 - $1e^4$	TMCMC: 1	0	[0 7000]
	SMC: 0.1	0	

with three sampling methods. The convergence is defined as when the mean and standard deviation of the posterior distribution becomes constant with further sampling. It shows that TMCMC and SMC can converge within 300 samples while MCMC required 2736 samples with additional 200 burn-in samples before the convergence. It is worth noting that SMC converges in the fewest samples with only 153 mainly due to the benefit of using importance sampling. With TMCMC and SMC less samples are required for model updating than in construction of the surrogate model. This seems to suggest there is no need to construct a surrogate model. However, with the goal of using the estimated parameter distributions to quantity the impact of uncertainty on bifurcation diagrams, the surrogate models are again implemented, significantly reducing computation time.

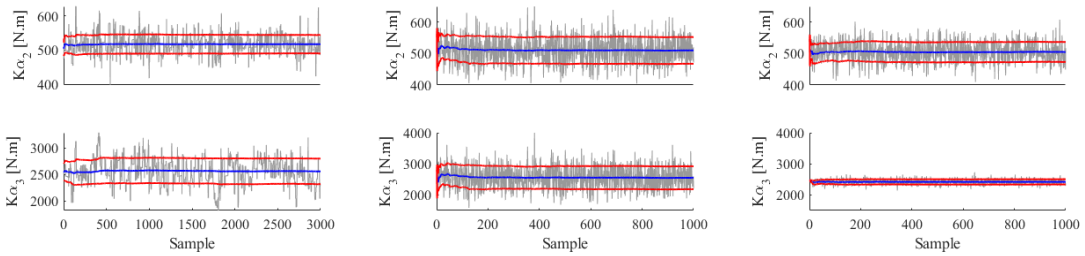

(a) MCMC (acceptance rate = 0.267)

(b) TMCMC (acceptance rate = 0.44)

(c) SMC (acceptance rate = 0.32)

Figure 4.11: configuration 1 trace plots following BMU with each sampling method (– mean),(– mean ± *std*)

Figure 4.12 shows the PDFs and scatter plots using three different sampling methods. It can be observed that each sampling method produces a PDF that resembles a normal distribution. The mean and *COV* of estimated nonlinear parameters are presented in Table 4.2. The estimated mean of the nonlinear parameter between these three sampling methods is within 15%. It is worth noting that the estimation of the mean is around 45% different from the initial estimates shown in Table B.1 in Appendix B. For both parameters, TMCMC provides the smallest interval of probability in parameter prediction. It is also found that the two nonlinear parameters are linearly correlated from MCMC and TMCMC, which however is not observed with the SMC sampling method as no samples are rejected during the sampling process. The correlation between parameters $K_{\alpha 2}$ and $K_{\alpha 3}$ manifests as an elongated likelihood surface, complicating their unique identification and suggesting potential over-parameterisation. This interdependence necessitates specialised sampling methods - the adaptive nature of MCMC and TMCMC proves particularly effective here, as its intermediate distributions naturally handle parameter correlation while maintaining sampling efficiency.

Table 4.2: set up 1 parameter estimation

	MCMC		TMCMC		SMC	
	$K_{\alpha 2}$	$K_{\alpha 3}$	$K_{\alpha 2}$	$K_{\alpha 3}$	$K_{\alpha 2}$	$K_{\alpha 3}$
mean	517.20	2555.8	524.50	2595.9	505.08	2420.6
COV [%]	5.52	9.44	9.72	16.20	6.29	3.47
Convergence (samples)	2736		215		153	

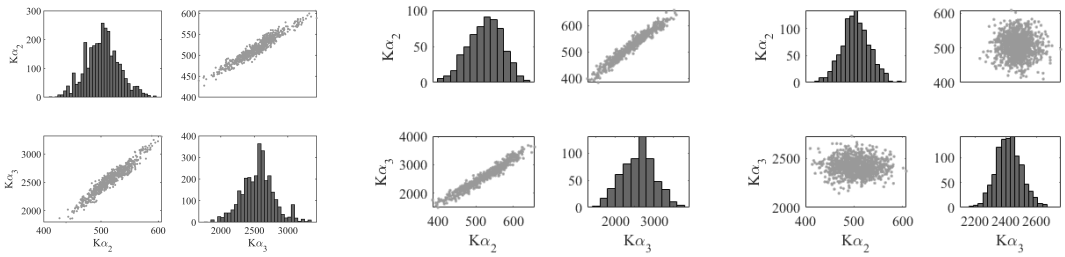

(a) MCMC (b) TMCMC (c) SMC

Figure 4.12: Configuration 1 PDF and scatter plots for $K_{\alpha 2}$ and $K_{\alpha 3}$ with each sampling method

Figure 4.13 shows the distributed bifurcation diagrams using the estimated nonlinear parameters from the BMU. It is observed both TMCMC and SMC results capture all experimental data points within their 95% uncertainty bounds. In the case of MCMC, the interval of probability is much narrower than that using TMCMC and SMC. There are two data points in the upper portion of the diagram falling outside uncertainty bands. It can be also found that the lowest band of the turning point in MCMC and TMCMC spans to $14m/s$ while this point is at $12.20m/s$ for SMC. If we are to assume the mathematical model is correct it indicates that SMC appears to overestimate the uncertainty of LCO.

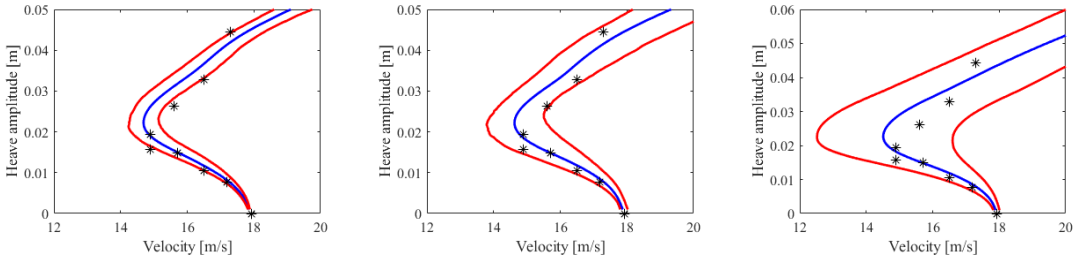

(a) MCMC (b) TMCMC (c) SMC

Figure 4.13: Configuration 1 probabilistic bifurcation plots (* experimental points)(– mean plot), (– 95% interval of probability)

Figure 4.14 shows a comparison of mean lines from three sampling methods, the deterministic estimates from the previous study gathered using normal form theory [5] and experimental data. A clear improvement can be observed with each of the sampling methods compared to the one using the initial estimates. The estimation of the LCO amplitude in each method closely follows the experimental data at the low amplitude points but diverges after the turning point. The mean lines from each method closely follows each other, only overshooting the turning point by $0.3m/s$. Figure 4.14b shows the bias of these four methods in relation to experimental data. Each sampling method is more accurate than the initial estimate for all data points apart from the point 7. The accuracy for all sampling methods remains above 94% without a sharp drop off in accuracy.

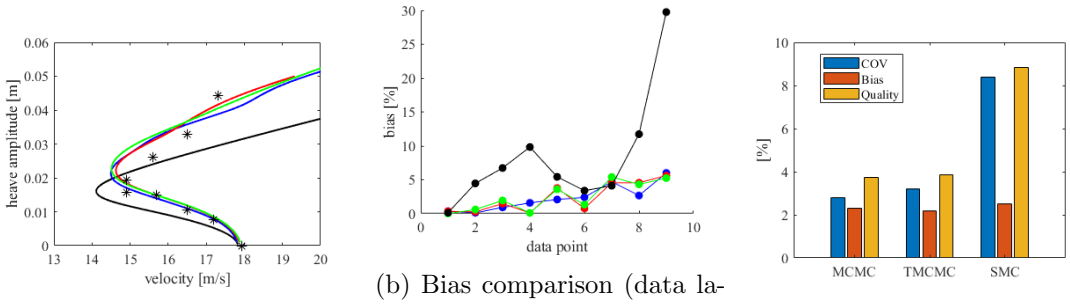

(a) Mean comparison (b) Bias comparison (data labeled in Figure 4.6a) (c) Quality comparison

Figure 4.14: Configuration 1 sampling method comparison (* experimental points),(– initial estimate),(– MCMC),(– TMCMC),(– SMC)

Figure 4.14c shows the quality of the prediction between these three sampling

method. It shows MCMC and TMCMC provide the best overall estimation of physical behaviour in terms of probability and accuracy. The bias of all methods are within 3%. However, the relatively large *COV* in SMC predictions leads to a higher *quality* than the other two sampling methods.

4.5.2 Configuration 2

Using the same method for configuration 1, a surrogate model for configuration 2 is constructed with 386 continuation runs required for training data. The tuning parameters presented in Table 4.1 were implemented for model updating in set up 2. Figure 4.15 shows the convergence of each sampling method where the similar pattern is observed as the first set up. The SMC sampling method remains as the fastest converging one with only 200 samples. Figure 4.16 shows scatter plots and PDFs produced. In this case, each of the sampling methods provide a shape similar to a normal distribution for both parameters. A strong correlation between the parameters is again observed with results from MCMC and TMCMC but not SMC. The mean and *COV* from the estimations are shown in Table 4.3. It can be seen that the mean results from the BMU are closer to the initial estimates shown in Table B.1. The most confident predictions are again achieved with SMC achieving the lowest average COV.

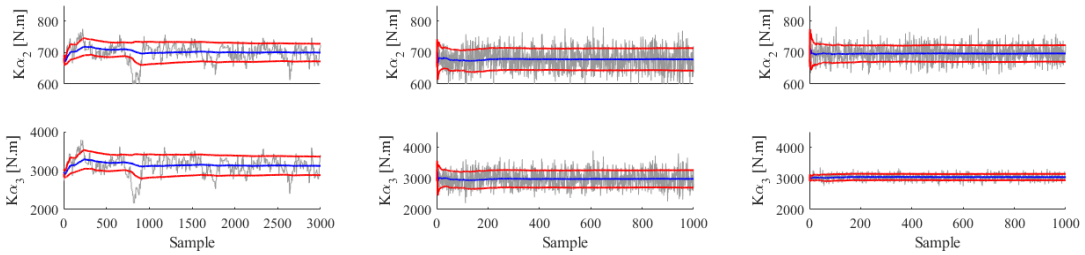

(a) MCMC (acceptance rate = 0.30) (b) TMCMC (acceptance rate = 0.43) (c) SMC (acceptance rate = 0.36)

Figure 4.15: Set up 2 trace plots following BMU with each sampling method (– mean),(– mean ± *std*)

Table 4.3: set up 2 parameter estimation

	MCMC		**TMCMC**		**SMC**	
	$K_{\alpha 2}$	$K_{\alpha 3}$	$K_{\alpha 2}$	$K_{\alpha 3}$	$K_{\alpha 2}$	$K_{\alpha 3}$
mean	700.03	3122.4	678.32	2982.6	697.20	3040.8
COV [%]	4.00	7.66	5.26	9.41	3.76	3.32
Convergence (samples)	2531		207		160	

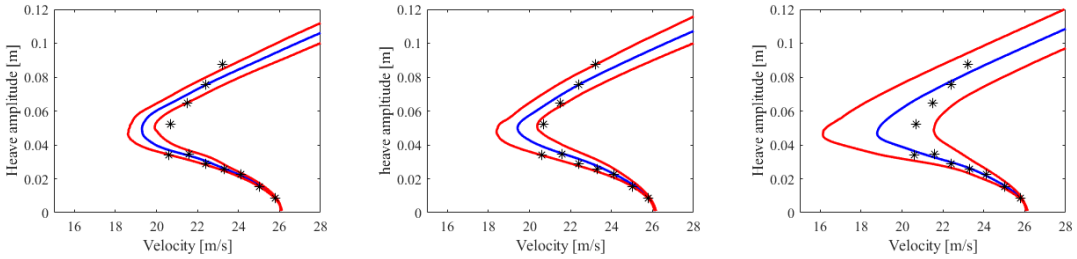

(a) MCMC (b) TMCMC (c) SMC

Figure 4.17: Set up 2 proabilistic bifurcation plots (* experimental points)(– mean plot), (– 95% interval of probability)

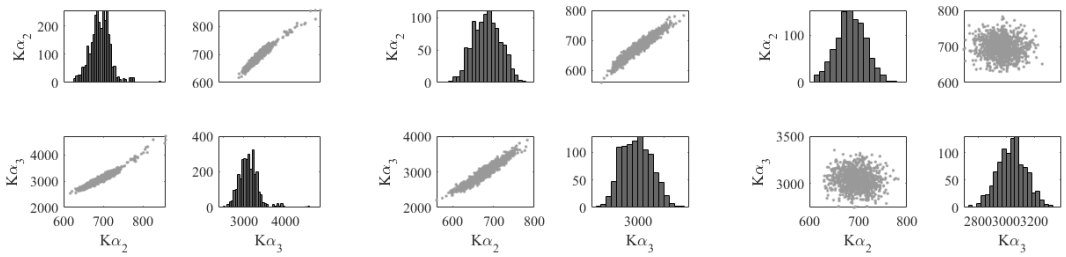

(a) MCMC (b) TMCMC (c) SMC

Figure 4.16: Set up 2 PDF and scatter plots for $K_{\alpha 2}$ and $K_{\alpha 3}$ with each sampling method.

Figure 4.17 shows the bifurcation plot with an interval of probability using the estimated posterior distribution of estimations. Similar results are observed to the first set up, with SMC capturing all data points with a wide interval of probability while MCMC and TMCMC only captures LCO behaviour at low amplitude before the turning point. Again, the MCMC does not capture two data points after the turning point and TMCMC misses only one point. The lower band of SMC significantly overshoots the turning point. As shown in Figure 4.18a, the mean line from each sampling method

is compared to the response generated with the initial estimate. In this case, it is less obvious which prediction is more accurate. At lower amplitudes, the initial estimate matches the behaviour but after the turning point, the accuracy is lost. The mean lines from BMU predictions offer a slight improvement over the initial estimate. The initial estimate overshoots the turning point the most. Figure 4.18b shows a comparison of bias of all the predictions compared to the experimental points. It is observed, the initial estimate is most accurate until the turning point. For the stable LCO, predictions from MCMC and TMCMC provide the most accurate predictions. Figure 4.18c confirms similar conclusions to the Figure 4.14c where MCMC and TMCMC show best overall quality.

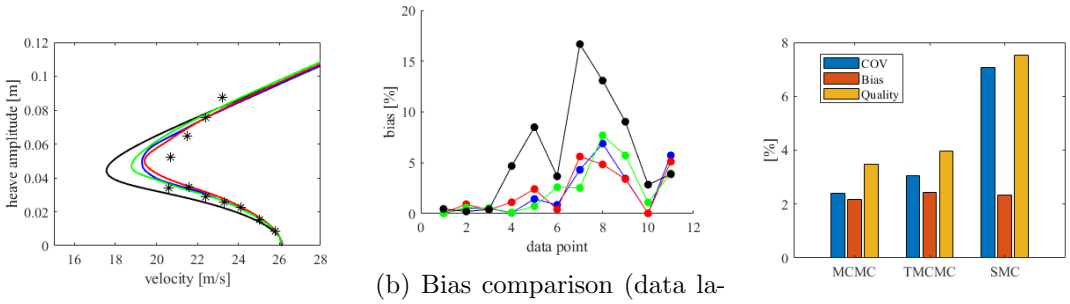

(a) Mean comparison

(b) Bias comparison (data labeled in Figure 4.6b)

(c) Quality comparison

Figure 4.18: Set up 2 sampling method comparison (* experimental points),(– initial estimate),(– MCMC),(– TMCMC),(– SMC)

4.5.3 Conclusions of Sampling Method Comparison

Considering both configurations several conclusions are reached. The experimental data is captured well using BMU leading to better estimations than deterministic results. In the second configuration, the predicted results for both BMU and the initial estimate appear in better agreement than in the first configuration. This could mean the mathematical model holds better for the second set-up or there were fewer errors in gathering the experimental results. Another reason could be the increased number of experimental data points used in the estimation. Considering overall mean accuracy, each sampling method outperformed the initial estimate, particularly at higher amplitudes. Each sampling method can be argued for depending on whether the user prioritises the

accuracy of the mean prediction or a combination of accuracy and probability. If probability and mean prediction is valued MCMC provides the best estimation. In contrast, if capturing all physical behaviour is preferred, TMCMC and SMC may be chosen despite being the overshoot of the turning point especially in the case of SMC. Parameter estimations have the lowest COV with SMC sampling but provide the widest intervals of probability in their bifurcation plots. This is likely due to SMC not rejecting samples and not observing correlations between parameters. Both TMCMC and SMC converge with less samples than training input runs are required, however taking forward UQ into consideration up to 60% less HBM continuation runs are required.

Taking all factors into account, TMCMC provides the best overall compromise in terms of convergence and accuracy for both configurations. In configuration 1 the bifurcation plot produced captures all data points without significantly overshooting the turning point and over 90% of data for configuration 2. The estimations from TMCMC and SMC in configuration 1 capture all physical behaviour within their intervals of probability, which suggests the parameter distributions accurately estimate the true uncertainty of the parameters and the mathematical model hold, particularly in the case of TMCMC. For these reasons, it may be argued the estimated distributions of nonlinear parameters can effectively represent physical behaviour. Alternatively, there is less agreement between all predicted values and experimental data after the turning point. There are two possible reasons: the model only holds for low amplitude results or there was a measurement error in gathering higher amplitude points. For the first case, the form of the model needs to be modified to capture higher amplitude behaviour. Since the errors become larger as amplitude increases, it is more likely the aerodynamic model does not hold for higher amplitude in this scenario, but further investigation is required.

Based on the results from both setups a clear pattern has emerged in that lower amplitude data points are well captured but accuracy is lost in upper sections in both BMU and initial estimates. There may be two reasons the experimental data may not match the results: (1) there was a significant amount of noise or errors in gathering the data; (2) the mathematical model particularly the nonlinear function may not fully

capture the true physical behaviour of the system. In an effort to further improve the accuracy of mathematical models to capture the experimental data, alternative nonlinear models are suggested and ranked in the next section.

4.5.4 Comparisons Between Numerical & Experimental Results

The converged HBM continuation results, employing parameters for both experimental configurations, are now compared with the CBC data to assess the accuracy of both LCO amplitude and stability. The probabilistic parameter estimates correspond to the mean values obtained through TMCMC sampling. The comparison with configuration 1 is depicted in Figure 4.19 for both deterministic and probabilistic parameter estimates. Both the HBM continuation plots and the experimental data exhibit a similar shape, featuring unstable LCO formations preceding a turning point, followed by stable LCO formations. However, discrepancies are evident in the amplitude of the plots, particularly in the deterministic estimate. Figure 4.19c illustrates that errors in amplitude become more pronounced as the amplitude increases in the stable section of the bifurcation diagram, with the highest amplitude point deviating significantly from the bifurcation plot in both estimates. It appears that the gradient of the bifurcation plot aligns with the experimental data before the turning point, but subsequently underestimates the gradient of the experimental data, particularly in the deterministic estimate. Overall, the probabilistic estimate provides a better approximation of the experimental data, with a mean RMS error of 0.13 compared to 0.23 in the deterministic case.

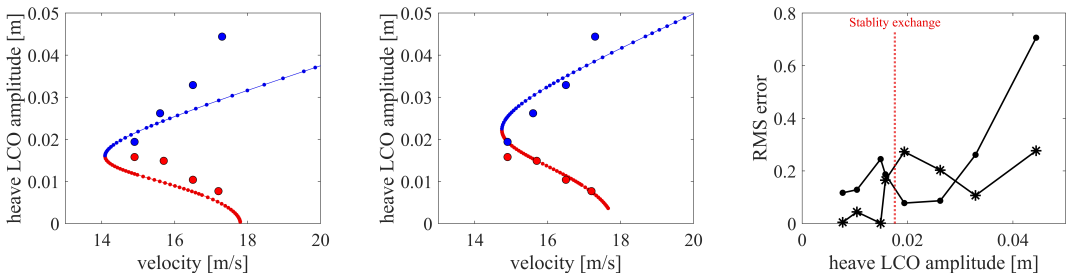

(a) (b) (c)

Figure 4.19: Experimental configuration 1 results: (a) With deterministic parameter estimate at $l = 5$, (b) With probabilistic parameter estimate at $l = 5$, (c) Error w.r.t CBC data [5] (• deterministic), (* probabilistic). Note: • stable LCO; • unstable LCO

The comparison with configuration 2 is illustrated in Figure 4.20. Similar to configuration 1, both the HBM continuation results and the CBC data exhibit unstable LCO at low amplitudes until a turning point is reached, after which stable LCO begin to form. Both sets of HBM results adeptly capture the shape of the unstable section of the bifurcation diagram, showcasing low RRMS errors below 15%, as indicated in Figure 4.20c. However, following the turning point, the shape of the bifurcation diagrams diverges from the CBC data, displaying a shallower gradient than expected, particularly in the deterministic estimate. Additionally, in the deterministic estimate, it appears that the location of the turning point is overestimated, extending back in velocity further than anticipated. This is not the case in the probabilistic estimate, where it appears the location of the turning point has been estimated more accurately. Again, it is observed that the probabilistic estimate captures the behaviour of the data more closely. The probabilistic estimate has a mean RMS error of 0.083 compared to the higher 0.12 in the deterministic case. This is likely due to the probabilistic approach accounting for parameter uncertainties, thereby providing a more robust prediction of system behaviour across varying conditions. This enhances accuracy compared to the deterministic method [10]. In either case, both estimates provide an improvement over the estimated bifurcation diagrams in configuration 1. Consequently, it can be argued that the HBM continuation scheme captures the real behaviour in configuration 2, particularly with the probabilistic estimate.

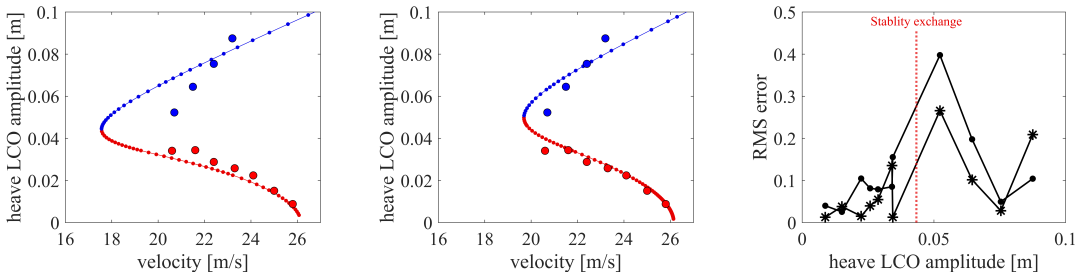

Figure 4.20: Experimental configuration 2 results: (a) With deterministic parameter estimate at $l = 5$, (b) With probabilistic parameter estimate at $l = 5$, (c) Error w.r.t CBC data [5] (• deterministic), (* probabilistic). Note: • stable LCO; • unstable LCO

Overall, the comparison between the HBM continuation scheme and CBC data in this case study presents a mixed outcome. In each configuration, the general shape of the bifurcation diagram is accurate, depicting a subcritical plot with unstable LCO at low amplitudes and stable LCO after the turning point. At low amplitudes, the RRMS errors were relatively low, particularly in the second configuration; however, substantial errors are observed after the turning point. In both configurations, it appears that the gradient of the bifurcation diagram is lower than expected, leading to more pronounced errors at higher LCO amplitudes. This discrepancy suggests a potential issue with either the experimental data, the mathematical model, or the estimated parameters. Improvements in accuracy are, however, observed with the probabilistic parameter estimates over the deterministic ones, especially in configuration 2, where the completed bifurcation diagram has a mean RRMS error under 10%.

4.6 Results: Nonlinear Model Selection

Previously it was assumed both $K_{\alpha 2}$ and $K_{\alpha 3}$ were positive. Prior distributions and LHS for surrogate models for nonlinear parameters could not draw samples from negative design space. In this section, prior distributions that include negative design space are considered. The aim is to improve agreement with results from model updating and experimental data by altering the characteristic of the nonlinear function. Figure 4.21 shows examination of the whole design space. The turning point of all bifurcation plots involving cubic hardening are below $12m/s$ for configuration 1, overshooting what would be expected from the experimental results by over 25%. The same behaviour was observed in configuration 2. For this reason cubic hardening design space is not considered. As seen in [191], the third and fifth-order non-linearity is also considered in sub-critical aerofoil systems. With the same criteria as in Figure 4.21, this nonlinearity's only feasible design space is with third-order softening and fifth-order hardening spring.

$$f_{nl} = \pm K_{\alpha 3}\alpha^3 \pm K_{\alpha 5}\alpha^5 \tag{4.15}$$

Table 4.4: Parameter estimations for model selection

	Model	Parameters[Units]		Mean	COV [%]
1	$K_{\alpha 2} + K_{\alpha 3}$	$K_{\alpha 2}$,$K_{\alpha 3}$	con 1	524.50,2595.9	9.72,16.20
		$[N/rad^2]$,$[N/rad^3]$	con 2	678.32,2982.6	5.26,9.41
2	$-K_{\alpha 2} + K_{\alpha 3}$	$K_{\alpha 2}$,$K_{\alpha 3}$	con 1	-383.78,1442.1	12.20, 22.17
		$[N/rad^2]$,$[N/rad^3]$	con 2	-530.99,1754.2	4.20,7.84
3	$-K_{\alpha 3} + K_{\alpha 5}$	$K_{\alpha 3}$,$K_{\alpha 5}$	con 1	-1822.5,$1.136e^5$	22.01,31.14
		$[N/rad^3]$,$[N/rad^5]$	con 2	-2343.5,$1.061e^5$	19.27,21.55

Table 4.4 shows the three possible nonlinear models to approximate the experimental LCO data. The suitability of the models will be ranked by both the average *quality* of the bifurcation results and the evidence function $\log(P(\mathbf{z}|f))$ from BMU with TMCMC sampling.

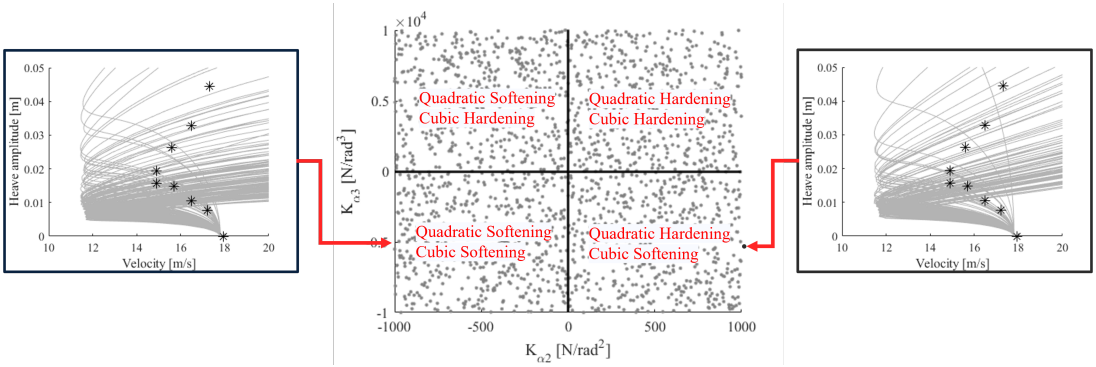

Figure 4.21: Full model selection parameter space. Each point on the scatter plot represents a full bifurcation diagram

The Kriging surrogate models for each nonlinear function are first developed through the same methodology presented in the Section 2. The TMCMC sampling method is selected for BMU since it has proved the most effective method using the original nonlinearity in the previous section. It can also produce the evidence function as a by-product for the model selection. It was found the evaluation of $\log(P(\mathbf{z}|f))$ required additional samples to converge over mean and standard deviation values. Table 4.5 shows that $\log(P(\mathbf{z}|f))$ converges at 10000 samples. For each model with both configurations, 10000 samples are taken to ensure evidence function converged. Tables 4.4 and 4.6 display the estimated parameters for each model and the evidence function

Table 4.5: Convergence of evidence function for configuration 1, model 1 with TMCMC sampling

Samples	100	500	1000	2500	5000	7500	10000	125000
$\log(P(\mathbf{z}\|f))$	-7.83	-7.94	-7.72	-7.35	-7.44	-7.46	-7.45	-7.45

Table 4.6: Evidence function for configuration 1 and 2 from 10000 TMCMC samples

		configuration 1		configuration 2	
	f_{nl}	$\log(P(\mathbf{z}\|f))$	*quality* [%]	$\log(P(\mathbf{z}\|f))$	*quality* [%]
1	$K_{\alpha 2} + K_{\alpha 3}$	-7.45	5.24	-8.86	5.21
2	$-K_{\alpha 2} + K_{\alpha 3}$	-5.30	5.61	-9.74	5.01
3	$-K_{\alpha 3} + K_{\alpha 5}$	-5.68	8.74	-8.77	4.78

compared to the average *quaility* of predictions.

As shown in the Table 4.5, model 3 provided the highest variation in predicted parameters for both configurations. For configuration 1, model 1 has the highest probability in estimations and model 2 has the highest for configuration 2 having the lowest average COV respectively.

Table 4.6 shows the computed evidence of each model for the two configurations. It can be observed that, for configuration 1, the evidence function indicates model 2 is the best choice whereas model 1 has the lowest *quaility* factor. Figure 4.22 shows that nonlinear model 1 and 2 capture all data within intervals of probability. The bifurcation plots produced from all models show plots that closely resemble each other. The model 3 fails to capture one data point from the intervals of probability after the turning point. Figure 4.22 shows a closer examination of the PDFs of nonlinear parameters. It is very clear that multi-modal distributions are produced for the model 2 and 3, suggesting the existence of two possible solutions. The mode with the highest probability density is referred to as peak 1 while peak 2 refers to the lower probability density peak. The model 3 has a single modal solution for $K_{\alpha 3}$ but a multi-modal solution for $K_{\alpha 5}$. Figures 4.24a and 4.24b show the response of LCO using the nonlinear parameters estimated from each peak. For model 2, it can be observed peak 1 fails to capture the highest amplitude point but has a closer overall fit to the experimental data. The response using the nonlinear parameters from the Peak 2 reaches the highest amplitude point

but stays away from the remaining data at amplitudes above the turning point. In model 3, peak 1 captures lower amplitude data and the highest amplitude point. Peak 2 captures data close to the turning point while failing to reach the highest amplitude points.

Considering just average quality, results suggest the model 1 is the optimal choice for configuration 1. This is in line with the bifurcation diagram capturing all experimental points within intervals of probability. Based on the TMCMC class selection, both models 2 and 3 are recommended above model 1. However, the solutions to these models are multi-modal as discussed. Since there are two suggested solutions, it is not valid to just consider the mean and COV of the posterior distribution estimations. This suggests considering a combination of the two different nonlinear functions at different LCO amplitudes might provide a better model than the single solution provided by model 1. Quality measurement assumes there is a single estimated solution whereas evidence function can account for multimodal results. This is why quality and evidence functions recommend alternative solutions in both configurations.

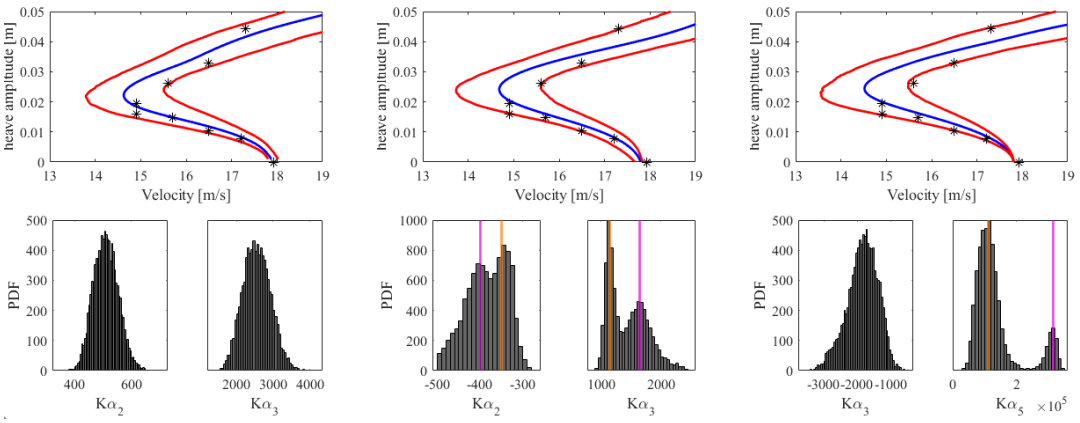

(a) Model 1 (b) Model 2 (c) Model 3

Figure 4.22: Bifurcation diagrams and PDF for configuration 1 with alternative nonlinear models [for multi-modal PDF (– peak 1),(– peak 2)]

In configuration 2 both evidence function and *quaility* suggest model 3 is the optimal choice. The examination of posterior distributions in Figure 4.18 shows that models 1 and 2 converge to a unique solution while model 3 produces a multi-modal

PDF with two possible solutions. Figure 4.24c show the amplitude of LCO with these two possible solutions. It shows peak 1 captures lower amplitude data while peak 2 the higher amplitude points. As was the case with configuration 1, TMCMC model selection favours a combination between these two possible solutions which outperforms a single solution from the original model. Overall suggests that none of the models are perfect, particularly with higher amplitude points an updated model is required.

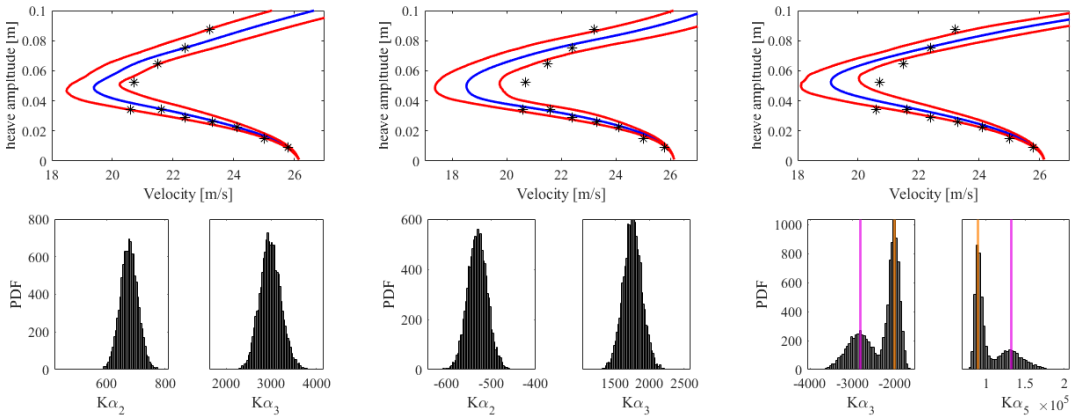

(a) Model 1 (b) Model 2 (c) Model 3

Figure 4.23: Bifurcation diagrams and PDF for configuration 2 with alternative non-linear models [for multi-modal PDF (– peak 1),(– peak 2)]

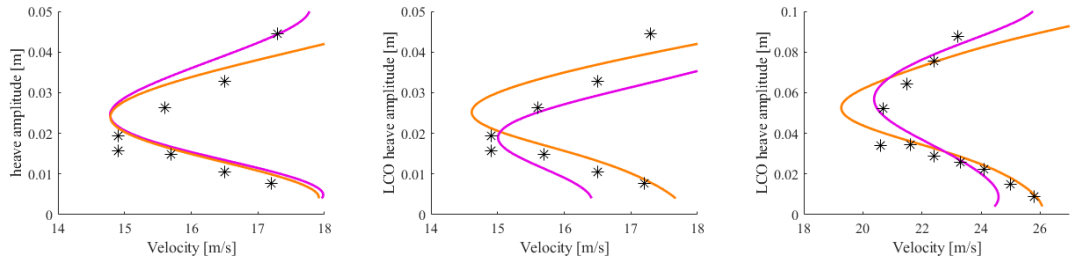

(a) configuration 1, model 2 (b) configuration 1, model 3 (c) configuration 2, model 3

Figure 4.24: Mean response from bifurcation diagrams with multi-modal responses (– peak 1),(– peak 2)

4.7 Conclusions

In this paper, a probabilistic identification methodology for estimating parameters in a nonlinear aeroelastic system is presented. An advanced kriging algorithm is used to develop accurate data-driven surrogate models for LCO behaviour. The surrogate models are employed with BMU to identify the nonlinear parameters and functions. The performance of three advanced sampling methods are compared. Experimental data from the nonlinear flutter rig with two separate configurations was employed with the goal of estimating a nonlinear model to fit the data.

The novelty in this work is the development of a unified framework that integrates Bayesian inference with surrogate modelling to both identify parameters and select among competing nonlinear aeroelastic models. Unlike traditional deterministic approaches, this method is applied to a real experimental rig exhibiting limit-cycle oscillations, enabling more accurate and efficient model updating. Additionally, the approach captures multi-modal posterior distributions, reflecting multiple viable model configurations and providing a more realistic representation of the system's nonlinear behaviour. By combining data-driven model identification, uncertainty quantification, and model selection in a single experimentally validated framework, this work advances the analysis and predictive capability of nonlinear aeroelastic systems.

Probabilistic bifurcation diagrams produced with BMU successfully captured the experimental data was within the computed intervals of probability at low amplitude points. This proved a significant improvement from the initial deterministic approach for each configuration. With higher amplitude points portions of the data were not captured within intervals of probability but made an improvement over the initial estimate. Results from BMU for each sampling method had variations due to the different sampling philosophies associated with each respective approach. In the first configuration, TMCMC and SMC could capture all data points within intervals of probability while SMC overshoots the estimation of the turning point by a large margin. The correlation between nonlinear parameters was also observed in MCMC and TMCMC results. Only SMC could capture all physical behaviour while overshooting the turning

point in the second configuration.

The estimations from the TMCMC is able to capture over 90% of the physical behaviour leading to an average mean accuracy of 98%. Considering the accuracy and convergence, it was determined TMCMC produced the highest quality estimations, capturing all experimental points with much higher convergence than MCMC. All predictions with estimations from BMU were up to 20% more accurate than that from the initial deterministic estimate. Accuracy in prediction of physical behaviour following the turning point dropped. From 5% to 22% of data points are omitted from the interval of probability following the turning point. This suggests the mathematical model does not hold for higher amplitudes of LCO, and a more sophisticated aerodynamic model might be needed. Considering computational efficiency, for purely estimating mean nonlinear parameters more HBM continuation runs are required with TMCMC and SMC with the data-driven approach. In carrying out forward UQ however, the proposed methodology can cut the amount of costly continuation runs by up to 60%.

Two categories of nonlinear models were implemented and evaluated through TMCMC class selection. For the first configuration, the TMCMC process suggested selecting model 2, which includes quadratic softening and cubic hardening. As for the second configuration, model 3 equipped with third-order softening and fifth-order hardening was deemed the most suitable option. After analyzing the quality factor of results obtained from the bifurcation diagrams along with the interval of probability for both scenarios, it can be concluded that model 1 is the most suitable option. An examination of posterior PDFs of nonlinear parameters showed the presence of multi-modal solutions in both configurations. Taking a single mean and standard deviation estimation from either of two estimated solutions did not capture the complete set of data. Upon examining both solutions, it was noted that each solution is capable of capturing a portion of the bifurcation diagram either for lower or upper amplitude data. TMCMC class selection suggests there is no unique solution to represent the nonlinear functions to capture all the physic across a wide range of amplitude, particularly for higher amplitude points.

A further improvement of the mathematical model for the nonlinear aeroelastic

model is required. This could either be achieved with an alternative nonlinear function or implementing nonlinearities in different degrees of freedom. Another area of improvement could be in optimising the amount of training data required for constructing the surrogate models, potentially with an iterative approach. This would integrate the Kriging model with the model updating process. With the fundamental principles of the data-driven framework now validated, the subsequent chapter focuses on enhancing both the training data requirements and UQ aspects.

Chapter 5

Moving Towards an Iterative Data-Driven Bayesian Approach

5.1 Introduction

Building on the methodology presented in the previous two Chapters, this Chapter introduces a novel iterative data-driven Bayesian framework for efficient stochastic identification of complex nonlinear systems. The methodology employs a hierarchical approach where surrogate models of increasing accuracy are systematically constructed across successive refinement iterations, concentrating computational resources on progressively narrower parameter domains. As the framework now permits surrogate models of varying resolution levels, extending beyond the restrictions of the previous chapter, rigorous quantification of the epistemic uncertainties arising from these surrogate approximations becomes essential. Consequently, this uncertainty quantification will be systematically incorporated within the proposed methodology.

The framework makes two key contributions:

1. A unified interface integrating multi-resolution data-driven modelling with iterative BMU, substantially reducing the training data requirements for stochastic system identification. In this context, each *iteration* represents both a specific parameter subspace and its corresponding surrogate model, while *multi-resolution* denotes the concurrent enhancement of model accuracy and domain precision

across itterations.

2. Incorporation of epistemic uncertainties from multi-resolution modelling into the BMU process through adaptive likelihood width parameterisation and generalised p-box methods, enabling robust quantification of polymorphic uncertainties in nonlinear dynamic responses.

These innovations collectively enable simultaneous refinement of data-driven model construction and UQ, advancing the state-of-the-art in nonlinear system identification. This chapter is organised as follows: it will first present the background and formulation of the proposed iterative data-driven Bayesian approach, including iterative Bayesian inference, multi-resolution data-driven models, the interaction interface as well as polymorphic UQ using p-box methods.

The implementation of applying the proposed adaptive Bayesian approach to nonlinear dynamical systems will then be detailed. Results are gathered by applying the proposed framework to the 2DoF aerofoil system from the previous Chapters. Results from the two experimental configurations from Chapter 4 will be then presented and compared with those obtained from a single-iteration approach. Both the amplitude and stability of LCO between the experimental results and numerical simulations are presented. The accuracy and computational cost of each proposed approach against the single-iteration approach will be discussed, including a sensitivity study of interaction parameters.

5.2 Proposed iterative data-driven Bayesian approach

This section presents the concept of iterative, data-driven Bayesian updating, along with a detailed formulation that is essential for understanding the process. First introduced is the theory behind the iterative Bayesian processing. Next, a description of the development of multi-resolution data-driven models is laid out.

5.2.1 Concept of Iterative Data-Driven Bayesian Framework

The main concept behind the iterative adaptive data-driven Bayesian approach is illustrated in Figure 5.1. The iterative approach employs an iterative refinement strategy where:

- The design space is progressively reduced through successive Bayesian model updates
- A *new* surrogate model is trained at each iteration following this reduction
- Initial iterations utilise computationally inexpensive to train, lower-resolution models
- Posterior distributions from each iteration inform the prior distributions for subsequent iterations

This hierarchical strategy achieves two key objectives:

1. Gradual enhancement of both parameter estimation accuracy and surrogate model accuracy (resolution) at each iteration
2. Reduction in overall training data requirements compared to conventional single-iteration approaches

The framework's efficiency stems from its ability to first establish approximate solutions using *coarse* models in broad parameter spaces, before concentrating computational resources on progressively refined domains. This contrasts with single-iteration methods that attempt to construct a single high accuracy model across the entire prior space.

5.2.2 Interaction between data-driven models and Bayesian model updating

The essential aspect of the proposed iterative data-driven BMU is the interaction between the contruction of multi-resolution data-driven models and the iterative model updating process, where each informs and enhances the other. This concept is illustrated in Figure 5.2. A crucial part of this process is updating the prior distribution

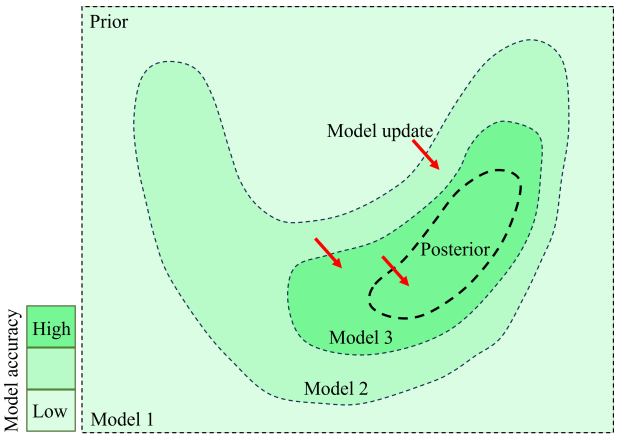

Figure 5.1: Conceptual diagram of iterative data-driven model updating process

based on the posterior distribution from the previous iteration at the start of each stage, and this updated prior distribution is then used to draw samples for constructing a refined data-driven model, which can be expressed as:

$$P(\theta)^{n+1} = P(\theta|\mathbf{z})^{n} \tag{5.1}$$

where n is the current iteration. The surrgoate model $\hat{f}$, developed in Section 4.2.4, is incorporated into Equation 5.2.2 (restated below), where the posterior distribution of θ is estimated through TMCMC sampling.

$$P\left(\theta|\mathbf{z}\right) = \frac{P\left(\mathbf{z}|\theta\right).P\left(\theta\right)}{P\left(\mathbf{z}\right)}$$

The TMCMC sampling method is employed as it was identified as the optimal choice in Chapter 4. Three methods are examined for estimating the width parameter in the log-likelihood function, each representing a different degree of interaction between the data-driven model development phase and the model updating process. It is anticipated that each method will offer distinct benefits depending on the case study; however, experiments must be conducted to identify and quantify these benefits:

a Single-iteration data-driven BMU (**SDB**)

The first and simplest approach is a single-iteration process where σ_p is set as an

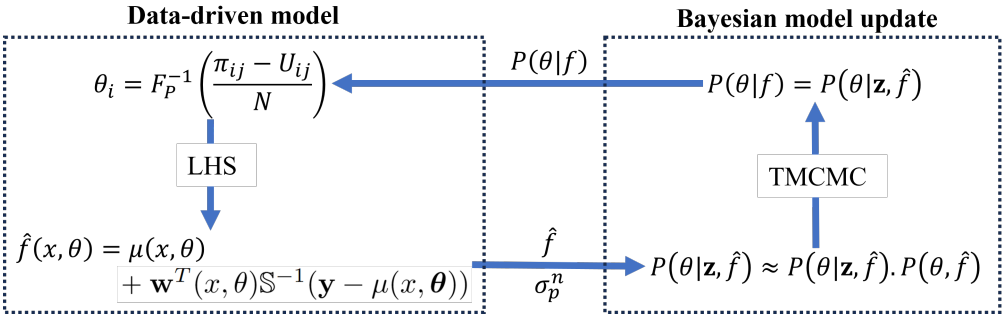

Figure 5.2: Interaction between data-driven model development and BMU in iterative process.

estimate of the noise in the observations **z**, and the entire procedure is carried out in a single iteration. The results from this method will be used as a reference method in the study. This implementation represents the most elementary form of the iterative approach, designed to validate the fundamental concept through a simplified test case. Essentially the same method laid out in Chapter 4.

b Iterative Data-driven BMU (**IDB**)

In the second method, the width parameter σ_p^n is progressively reduced at each iteration by a factor determined by the total number of iterations and the current iteration, decreasing linearly and converging to σ_p at the final iteration. This methodology establishes a direct coupling between data-driven model construction and the BMU process. This methodology represents a minimal implementation of the iterative framework, designed to validate its fundamental principles under simplified conditions.

$$\sigma_p^n = (N + 1 - n) \times \sigma_p \tag{5.2}$$

c Polymorphic Iterative Data-driven BMU (**PIDB**)

In this method, the epistemic uncertainties from the data-driven model are quantified to define σ_p^n at each iteration. During the training of surrogate models, the mean standard deviation of model estimates, denoted as σ_i, can be directly obtained from the data-driven model at each iteration as shown in Equation 5.3

(restated from the Section 4.2.4). It exhibits the highest level of interaction between the data-driven model development and the model updating process.

$$Corr[(x,\theta),(x,\boldsymbol{\theta})] = \sigma_i^2 \frac{2^{1-\upsilon}}{\Gamma(\upsilon)} \left(\frac{\sqrt{2\upsilon h}}{a} \right)^{\upsilon} K_{\upsilon} \left(\frac{\sqrt{2\upsilon h}}{a} \right) \tag{5.3}$$

$$\sigma_p^n = \sigma_i \tag{5.4}$$

This process yields an estimate of the epistemic uncertainties inherent in the data-driven model.

5.2.3 Polymorphic Uncertainty Quantification

The intentional tolerance for lower-accuracy surrogate models at initial iterations introduces measurable modelling uncertainties. These uncertainties may significantly affect the predicted system response, in contrast to the negligible effects demonstrated in Chapter 3. For these reasons, a p-box approach is developed to obtain a combined probabilistic response that accounts for both aleatory uncertainties in the experimental data and epistemic uncertainties arising from surrogate model approximations.

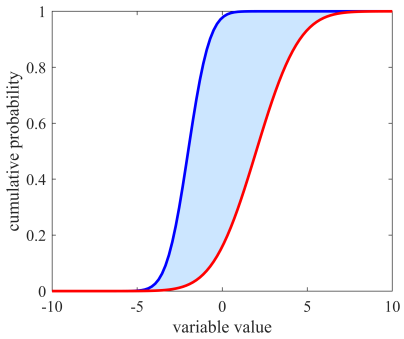

Figure 5.3: Probability-box illustrative example, (- lower boundary), (- upper boundary)

Once a converged (or stabilised) estimate for the posterior distribution is attained, probabilistic estimate of the parameters θ can is taken as $P(\theta)$. The final step of the process is to obtain the polymorphic probabilistic response of y over the range x, based on the stochastic estimates of θ. This estimate must account for uncertainties arising

from both the parameter estimate and the predictions of the data-driven model. This is where the p-box method is applied, as is standard in combined UQ [192, 193]. The fundamental principle behind this method is shown in the following:

$$\underline{P}(y) \leqslant P(y) \leqslant \overline{P}(y) \tag{5.5}$$

where $P(y)$ represents the distribution at observation y, and $\underline{P}(y)$ and $\overline{P}(y)$ denote the upper and lower boundaries of the predicted values of y from the model $\hat{f}$. The distribution $P(y)$ is obtained by drawing Monte-Carlo samples of θ from the final posterior distribution $P(\theta|\mathbf{z})$ and calculating a mean estimate of y using $y = \hat{f}(x, \theta)$. This process is repeated until a converged mean estimate for y is achieved, and the total scatter is used to estimate the distribution $P(y)$, providing the purely aleatory estimate. Each estimate of y is accompanied by an epistemic uncertainty or p-box as shown in Figure 5.3, quantified by σ as described in Equation 5.3. This allows for the upper and lower bounds for each estimate to be stored, which are then used to compute the distributions $\underline{P}(y)$ and $\overline{P}(y)$, in essence rewriting Equation 5.5 as

$$P(y - \sigma) \leqslant P(y) \leqslant P(y + \sigma) \tag{5.6}$$

Using these distributions in Equation 5.5, the mean of $P(y)$ is taken as the polymorphic mean. The lower 5^{th} and upper 95^{th} percentiles of $\underline{P}(y)$ and $\overline{P}(y)$ are used to define the polymorphic intervals of probability.

The detailed implementation of these three methods for nonlinear systems will be elaborated upon in the following Section.

5.3 Algorithm

This section will discuss how the formulation presented in the previous section is implemented to establish both single- and multi-iteration data-driven BMU approaches. Two distinct versions of the iterative approach will be presented. The first method, referred to as IDB, determines the number of iterations solely based on user input. The

second iterative methodology, known as PIDB, takes into account uncertainty from the data-driven models and utilises this information to determine the number of iterations.

The key difference of the multi-iteration approach from single-iteration updating is the presence of a feedback loop over a number of iterations. Stochastic model updating is carried out with coarse models via Bayesian inference and the resulting posterior distribution is used to gather training data for a less coarse data-driven model specialised to a reduced design space. The width parameter σ_n of the proposal distribution is reduced at each iteration converging with the estimate that would be used in the single-iteration process σ_p in the likelihood function. A detailed description of the process is presented in Algorithm 2. A larger width parameter will be used at initial iterations to allow the exploration of the wider parametric space using relatively coarse models.

In the IDB approach whereby number of iterations L is predefined. The width parameter is reduced at each iteration by a factor based on the total number of iterations and the current iteration in a linear fashion, converging to σ_p at iteration L as described in Equation 5.2. As the number of iterations is set by the user in this method, $IterationConvergence$ is true when $n = L$. In this context, convergence refers to the point at which the accuracy of the data-driven model satisfies the specified criterion. The effectiveness of this method is dependent on the input of the user for a number of iterations.

In the PIDB approach, the epistemic uncertainties derived from the data-driven model are quantified to define σ_n at each iteration. During the training of these models, the mean standard deviation of model estimates, denoted as σ_i, can be directly obtained from Equation 5.3. The $IterationConvergence$ criterion is satisfied when the mean variation from the data-driven model is less than the noise estimate derived from the observations ($\sigma_p^n < \sigma_p$). At this stage, it can be argued that the epistemic uncertainties exert a lesser influence on the outputs than the aleatory uncertainties stemming from the observations, meaning that the uncertainties which can be controlled are less significant than those which cannot.

In the multi-iteration process, the parameter $\mathscr{A}$ is defined identically to its definition

in the single-iteration process and remains constant across all iterations. However, it is crucial to select an appropriate value of $\mathscr{A}$ specifically for the iterative process, typically higher than that used in the single-iteration process. This approach enables the acceptance of less accurate data-driven models at initial iterations while ensuring that accuracy improves as the data becomes more refined upon further iterations. Once the mean accuracy of the model has converged concerning $\mathscr{A}$, σ_i is preserved as σ_p^n and utilised as the width parameter at iteration n in the BMU. Subsequently, the posterior distribution of the current iteration is employed to generate more samples to train the subsequent data-driven model on further iterations.

Algorithm 2 Iterative data-driven BMU (IDB and PIDB)

Input: Experimental data $\mathbf{z}$, Initial prior distribution $P(\theta)^0$, Width parameter σ_p, Training data increment N_0, Surrogate model convergence factor $\mathscr{A}$

Output: Polymorphic response data $P(y)$, Final posterior distribution $P(\theta|\mathbf{z})$, Final surrogate model $\hat{f}$

Initialisation $P(\theta)^1 = P(\theta)^0$
$n = 0$
while $L_{conv} = 0$ **do** {Iteration convergence}
  $n = n + 1$
  $N = N_0$
  $conv = \mathscr{A} + 1$
  $i = 0$
  while $conv > \mathscr{A}$ **do** {Surrogate model convergence}
    $i = i + 1$
    $\theta_i = F_P^{-1}\left(\frac{\pi_{ij} - U_{ij}}{N}\right)$
    $y_i = f(x, \theta_i)$ {Samples already in data base are not rerun}
    $\boldsymbol{\theta} = [\boldsymbol{\theta}, \theta_i]$
    $\mathbf{y} = [\mathbf{y}, y_i]$
    $[\hat{f}(x,\theta)_i, \sigma_i] = \mu(x,\theta) + \mathbf{w}^T(x,\theta)\mathbb{S}^{-1}(\mathbf{y} - \mu(x,\boldsymbol{\theta}))$
    $A^i = AccuracyCheck[\hat{f}(x,\theta)_i, \sigma_i]$
    if $i \geqslant 2$ **then**
      $conv = |A_i - A_{i-1}|$
    end if
    $N = N + N_0$
  end while
  $\hat{f}(x,\theta) = \hat{f}(x,\theta)_i$ {Converged surrogate model at n^{th} layer}
  $\sigma_p^n = WidthParmeter(n, \sigma_i)$ {Set width parameter σ_n}
  if $IterationConvergence = False$ **then**
    $P(\theta|\mathbf{z}) \approx P(\mathbf{z}|\theta).P(\theta)$ {Utilising σ_n in Likelihood function}
    $P(\theta)_{n+1} = P(\theta|\mathbf{z})_n$ {Update prior for next iteration}
    $[\mathbf{y}, \boldsymbol{\theta}] = DiscardData(P(\theta|\mathbf{z})_n, [\mathbf{y}, \boldsymbol{\theta}])$ {Discard training data not within posterior distribution (3σ rule)}
  else
    $P(\theta|\mathbf{z}) \approx P(\mathbf{z}|\theta).P(\theta)$ {Utilising σ_p in Likelihood function}
    $N_{conv} = 1$
  end if
end while
$P(\theta|\mathbf{z}) = P(\theta|\mathbf{z})^n$
$\hat{f}(x,\theta) = \hat{f}(x,\theta)^n$
$\theta = MCS[P(\theta|\mathbf{z})]$ {Monte-Carlo simulations based on posterior distribution}
$P(y - \sigma) \leqslant P(y) \leqslant P(y + \sigma)$ {Polymorphic UQ}

5.3.1 Case Study

The same case study is used as in the previous two chapters. Again, nonlinear parameters $K_{\alpha 2}$ and $K_{\alpha 3}$ are treated as uncertain aleatory parameters. The methodology described in the last section will be applied to estimate these two nonlinear parameters.

The flowchart in Figure 5.4 details the application of the iterative data-driven Bayesian approach to the nonlinear aeroelastic test case. Inputs for the IDB or PIDB approach are initially defined and fed into the framework, including prior uniform distributions for nonlinear parameters $P(K_{\alpha 2}, K_{\alpha 3})$. This region specifies a general area where there is a reasonable degree of belief the parameters can exist, applicable to both single- and multi-iteration frameworks. The estimated width parameter, denoted as σ_p, is determined based on the expected level of noise in the experimental data, specifically the average standard deviation of the observations. This input remains consistent across both single- and multi-iteration processes. The initial increment of training data collected, represented as N_o, is uniformly set for all processes.

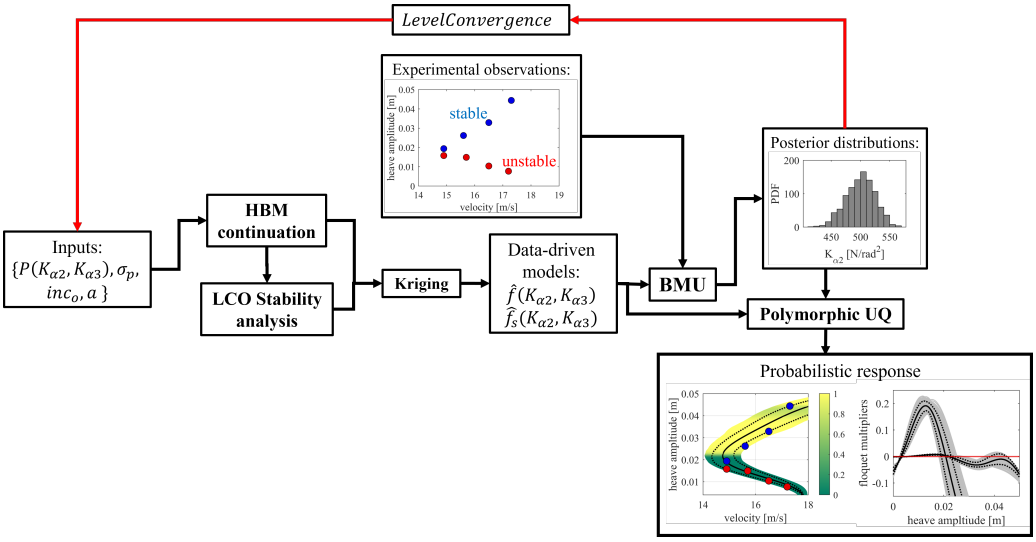

Figure 5.4: Flowchart of iterative Data-driven BMU applied to the nonlinear aeroelastic case

The accuracy convergence criterion $\mathscr{A}$ is set at a high level for the single-iteration process to develop the most accurate data-driven model possible, covering the full parametric space defined in the prior distributions. For the iterative process, a lower convergence criterion is set to allow coarser models to be accepted at initial iterations. It is important to emphasise that convergence is determined by the accuracy of the data-driven models at each iteration, and is influenced by both user inputs and the width parameter. Since convergence is relative to the accuracy of the previously trained

model, this should enable the accuracy of the models to improve as the design space is refined across iterations. Only in the IDB framework would the number of iterations be set as an input.

Samples of $K_{\alpha 2}$ and $K_{\alpha 3}$ are drawn from the prior distribution and fed through the high fidelity HBM framework giving output of LCO amplitude and corresponding velocity. This is referred to as the high (or full) fidelity process f. Data is drawn from f and fed into the Kriging algorithm to train the data-driven model $\hat{f}$ in increments of N_o [136]. Surrogate model $\hat{f}$ is set up in the same manner pretended in Section 4.4. Once the accuracy of $\hat{f}$ has converged relative to $\mathscr{A}$, it is used within the Bayesian framework to estimate $K_{\alpha 2}$ and $K_{\alpha 3}$.

For the single-iteration process, the width parameter is set at σ_p. In the IDB, it is estimated based on the current iteration the framework is on (Eqn. 5.2), and in the PIDB, it is based on the mean variation in data-driven model predictions obtained directly from the Kriging algorithm. The presence of the red highlighted feedback loop is the key difference between the single- and both multi-iteration processes. The ***IterationConvergence*** step differs in the IDB and PIDB approaches. In the IDB, the process has converged when $n = L$, while for the PIDB, it is when $\sigma_p > \sigma_p^n$. At this stage, the epistemic uncertainty within the data-driven model is found to be less than the estimated noise in the experimental data (aleatory uncertainty). Consequently, we can reasonably assert that the primary source of uncertainty lies within the experimental data rather than the data-driven model.

For each process, once it has converged, the final probabilistic estimates of $K_{\alpha 2}$ and $K_{\alpha 3}$ are used to obtain bifurcation diagrams with polymorphic intervals of probability. The data-driven model describing the bifurcation diagram shape from the final iteration, $\hat{f}(h, K_{\alpha 2}, K_{\alpha 3})$, is saved as the converged data-driven model. On the final iteration, data-driven models are also trained through Kriging to estimate Floquet multipliers based on inputs of $K_{\alpha 2}$, $K_{\alpha 3}$, and LCO amplitude. The training data is obtained through the previously described Koopman-based stability analysis.

Monte-Carlo samples of $K_{\alpha 2}$ and $K_{\alpha 3}$ are run through $\hat{f}$ with the p-box method for a range of amplitudes, providing the shape of the probabilistic bifurcation diagram.

Table 5.1: Data-driven model updating inputs and outputs

	inputs					**outputs**				
	$P(\theta)^0$	N	σ_p	inc_0	$\mathscr{A}$	mean	COV	$\hat{f}$ accuracy	f runs	$\hat{f}$ runs
SDB	$K_{\alpha 2}$: Uniform(-$1e^3, 1e^3$) $K_{\alpha 3}$: Uniform(-$1e^4, 1e^4$)	1	$0.6m/s$	10	0.5%	$K_{\alpha 2}$: $508.6N/rad^2$ $K_{\alpha 3}$: $2549.9N/rad^3$	6.4% 11.7%	96.7%	1200	2000
IDB	$K_{\alpha 2}$: Uniform(-$1e^3, 1e^3$) $K_{\alpha 3}$: Uniform(-$1e^4, 1e^4$)	3	$0.6m/s$	10	2%	$K_{\alpha 2}$: $499.9N/rad^2$ $K_{\alpha 3}$: $2356.6N/rad^3$	5.0% 8.3%	99.8%	309	4000
PIDB	$K_{\alpha 2}$: Uniform(-$1e^3, 1e^3$) $K_{\alpha 3}$: Uniform(-$1e^4, 1e^4$)	-	$0.6m/s$	10	2%	$K_{\alpha 2}$: $506.1N/rad^2$ $K_{\alpha 3}$: $2428.2N/rad^3$	4.0% 7.0%	99.6%	290	4000

This data is then processed through the model $\hat{f}_s(h, K_{\alpha 2}, K_{\alpha 3})$ to derive a probabilistic estimate of LCO stability. The likelihood of stability is assessed based on the percentage of samples indicating LCO stability.

5.4 Model Updating Results

In this section, the results from experimental configuration 1 (shown in Figure 4.6a) are presented and discussed in detail. First, the single-iteration results are outlined, followed by the results of both iterative procedures. A comprehensive comparison is then made between the three methods. Subsequently, the key results from applying all three methods to configuration 2 are briefly presented and discussed. Finally, a sensitivity analysis is performed and discussed on the width parameter with both experimental configurations.

5.4.1 Single-Iteration Updating: Configuration 1

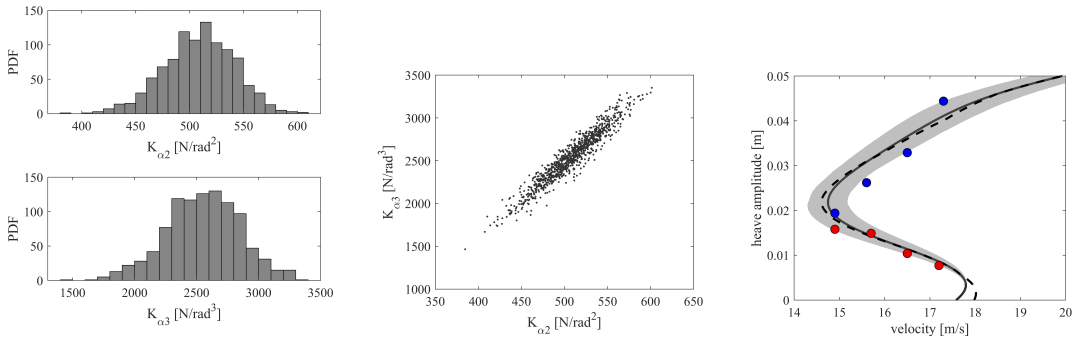

(a) (b) (c)

Figure 5.5: Single-iteration data-driven BMU probabilistic results: a)Nonlinear parameter histograms, b)TMCMC scatter plot, c) Probabilistic response (− data-driven mean), (■ 95% aleatory interval of probability),(−− HBM continuation), (• stable CBC data), (• unstable CBC data)

Table 5.1 shows the inputs of the single-iteration data-driven BMU applied to the case study, which is used a reference case for the iterative updating framework. Prior distributions $P(\theta)$ for each parameter is taken to be uniform within the defined boundaries. Based on prior knowledge and experiments, the magnitude of stiffness should not exceed $1e^3[N/rad^2]$ for the quadratic term and for $1e^4[N/rad^3]$ for the cubic term. It is possible however for parameters to be both positive and negative. Width parameter was determined based on experiments with the converged surrogate model. BMU with TMCMC sampling is carried out until acceptance rate is as close to the idea value of 0.234 as possible.

A single data-driven model is trained across the entire design space, in contrast to the approach in Section 4.6 where four distinct nonlinear models were constructed, each covering a quarter of the design space. This unified approach provides a benchmark for comparing method performance, as alternative techniques must identify the correct model without prior knowledge of nonlinear parameter distributions. Consequently, the single-iteration results presented here differ from those in Chapter 4, where model selection was performed under more constrained conditions. The unified model achieved a convergence accuracy of 96.7% using 1200 training samples.

With TMCMC, 1000 samples are drawn from the data-driven model to ensure a stationary solution was reached. A further 1000 samples are drawn via MCS from $\hat{f}$ to determine probabilistic behaviour. The data-driven model takes on average 0.0012 seconds to run. Figure 5.5 a shows the histograms with normal shapes with relatively low COV suggesting a single-modal solution. Table 5.1 also shows the mean and COV of the stiffness estimates.

The bifurcation diagram shown in Figure 5.5 c captures the majority of experimental CBC points within the interval of probability. Using mean parameter estimates directly with HBM continuation produces results in slightly deviation from the surrogate model mean due to the accuracy of the data driven model, particularly at low amplitude points close to the hopf bifurcation.

Figure 5.6 shows both probabilistic stability including the epistemic uncertainty from the data-driven model are considered. It is evident that incorporating epistemic uncertainties results in an average expansion of the 95% interval of probability of the bifurcation plot shown in shaded area by $0.44m/s$, equivalent to a 53% increase comparing to the one without including epistemic uncertainty shown in dotted line. It is found that all experimental data falls within the expanded 95% interval of probability indicating the importance of adding epistemic model uncertainties.

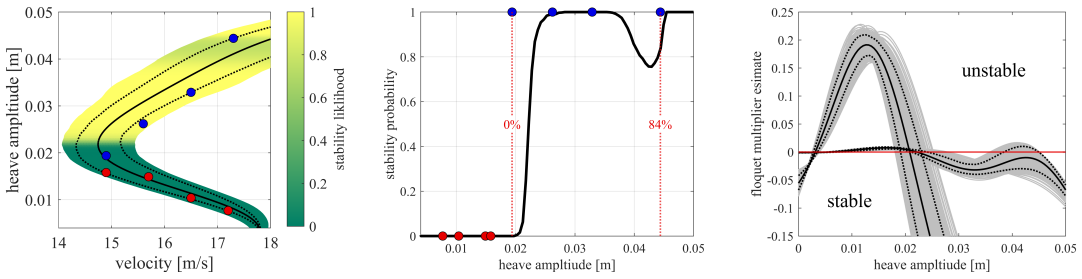

(a) (b) (c)

Figure 5.6: SDB polymorphic UQ results with stability (• stable CBC data), (• unstable CBC data): a) Probabilistic bifurcation diagram (shaded area = polymorphic interval of probability), (- mean plot),(. . . aleatory interval of probability), b) Stability likelihood, c) Floquet multipliers

Figure 5.6 shows a smooth transition from unstable to stable LCO is evident at the turning point, consistent with expectations based on CBC data. However, the

lowest amplitude stable LCO experimental point was not accurately predicted, with 0% of the data indicating stability at this point (see dotted red line in Figure 5.6b). At heave amplitudes ranging between $0.036m$ and $0.046m$, the portion of data suggesting stability unexpectedly drops from 1 to as low as 0.75 before returning to 1. From an engineering context, this implies that there is limited evidence to suggest whether the model will respond with a stable LCO or diverge following a perturbation at this airspeed. Figure 5.6c shows estimations of Floquet multipliers from the data-driven model $\hat{f}_s(h, K_{\alpha 2}, K_{\alpha 3})$. It is observed that a portion of the mode 2 Floquet multipliers becomes positive within the range of $0.036m$ to $0.046m$. This contradicts the conclusion reached from both CBC data and training data where following the turning point in a subcritical bifurcation diagram as there is a permanent change in stability. The discrepancy suggests that either a larger experimental dataset or more refined training data is required to accurately depict stability behavior in the single-iteration study. Full conclusions will be provided once the other methods have been tested.

5.4.2 Iterative Updating: Configuration 1

Table 5.1 shows the inputs into the algorithm for both IDB and PIDB approaches. Initial prior distributions mirror those utilised in the single-iteration study, while the final width parameter remains consistent to facilitate effective comparison of results. To accommodate coarser models at initial iterations, the convergence criterion for the data-driven model is adjusted from 0.5% to 2% for both iterative studies. In the IDB study, the number of iterations is set to three as an initial estimate. Conversely, for the PIDB study, the number of iterations will be determined automatically. Nevertheless, the convergence criterion for the number of iterations is also satisfied at three iterations.

Table 5.1 also presents the probabilistic parameter estimates for each study, alongside corresponding histograms and bifurcation diagrams displayed in Figures 5.7 and 5.8. These bifurcation diagrams do not incorporate epistemic uncertainties in the data-driven models at this stage. Each histogram demonstrates a normal distribution shape, indicating a consistent pattern. The mean parameter estimates for the single-iteration process and both iterative approaches exhibit close agreement, differing by less than

3%. The iterative approaches offer enhanced predictive probability, evidenced by lower COV for each parameter estimate. Specifically, the PIDB results show the highest probability of predictions, with the lowest COV observed for both $K_{\alpha 2}$ and $K_{\alpha 3}$ estimates.

Furthermore, the probabilistic bifurcation diagrams for the iterative approaches yield nearly identical outcomes, as illustrated in Figures 5.7c and 5.8c. However, only three CBC data points (1, 3, and 5) out of eight fall within the aleatory 95% interval of probability. Mean predictions from the data-driven models closely mirror those from the high-fidelity HBM model across all points on the bifurcation diagram.

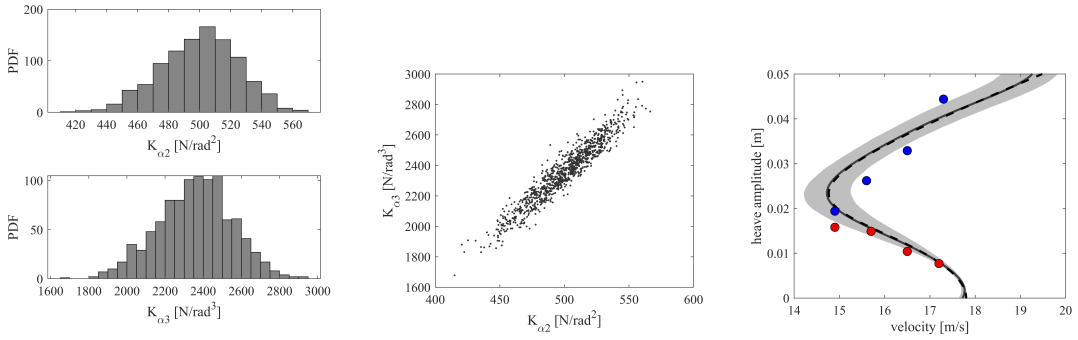

(a) (b) (c)

Figure 5.7: IDB results: a) Nonlinear parameter histograms, b) TMCMC scatter plot, c) Aleatory probabilistic response (− data-driven mean), (■ 95% aleatory interval of probability),(−− HBM continuation), (• stable CBC data), (• unstable CBC data)

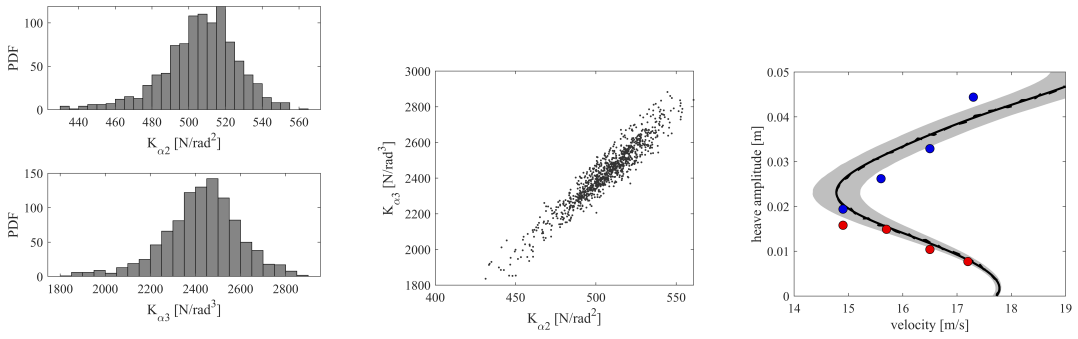

(a) (b) (c)

Figure 5.8: PIDB results: a) Nonlinear parameter histograms, b) TMCMC scatter plot, c) Aleatory probabilistic response (− data-driven mean), (■ 95% aleatory interval of probability),(−− HBM continuation), (• stable CBC data), (• unstable CBC data)

Table 5.1 shows that the comparison of the accuracy of the final data-driven model between the single-iteration process and two iterative studies. The IDB approach demonstrates the most significant enhancement, with a 3.1% increase in accuracy, while the PIDB approach shows a 2.9% improvement. The most notable change from single- to iterative updating is observed in the total amount of required training data (f runs). With only 290 high-fidelity runs, the PIDB approach necessitates the least amount of training data, resulting in a substantial 76% reduction compared to the single-iteration study. Similarly, IDB also leads to a significant reduction in training data, achieving a 74% decrease. The data-driven model is executed 1000 times at each iteration and an additional 1000 times to determine probabilistic behavior. The average time to execute f is 6.5 seconds, while $\hat{f}$ takes 0.0012 seconds. This translates to a total runtime of 2.17 hours for the single-iteration approach, 33.5 minutes for IDB, and 31.4 minutes for PIDB.

Table 5.2 provides an overview of the results at each iteration including all training data at each iteration. Figures 5.9 and 5.10 visually illustrate the evolution of the iterative processes along with the TMCMC scatter plots generated using the resultant data-driven models. It is apparent that the iterative algorithm adeptly updates the design space based on the current model and utilises the updated priors to gather refined training data. The process converges to a single modal solution in both cases by the second iteration. The mean data-driven model standard deviation in prediction ($\hat{f}$ std) takes three iterations in both iterative processes to fall below σ_p. The PIDB process yields the data-driven model with the highest level of probability. In each iterative study, a significant change in data-driven model accuracy and mean nonlinear parameter estimates occurs between iterations 1 and 2. This phenomenon is likely attributable to the design space transitioning from a multi-modal to a single modal space, which is further illustrated in Figure 5.11 with prior distributions from the IDB process.

Table 5.2: Configuration 1 iterative results

	Iteration	f runs / held	$\hat{f}$ accuracy	$\hat{f}$ std	σ_p^n	$K_{\alpha 2}$ $[N/rad^2]$	$K_{\alpha 3}$ $[N/rad^3]$
SDB	1	1200 / 0	96.7%	$0.22m/s$	$0.60m/s$	508.6 ± 32.6	2549.9 ± 298.3
IDB	1	180 / 0	74.9%	$3.50m/s$	$1.80m/s$	235.6 ± 188.3	345.7 ± 1171.5
	2	29 / 11	97.1%	$0.63m/s$	$1.20m/s$	497.3 ± 57.6	2356.9 ± 486.0
	3	95 / 5	99.8%	$0.12m/s$	$0.60m/s$	499.9 ± 25.0	2356.6 ± 195.1
PIDB	1	180 / 0	74.9%	$3.50m/s$	$3.50m/s$	291.5 ± 261.2	630.1 ± 2057.6
	2	56 / 24	96.2%	$0.75m/s$	$0.75m/s$	498.2 ± 53.0	2460.7 ± 498.2
	3	54 / 6	99.6%	$0.08m/s$	$0.60m/s$	506.1 ± 20.2	2428.2 ± 169.1

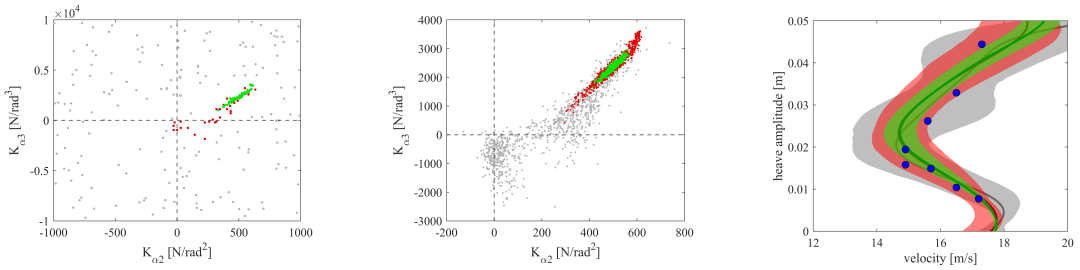

(a) (b) (c)

Figure 5.9: IDB comparison over iterations (• iteration 1),(• iteration 2),(• iteration 3): a) training data, b) TMCMC scatter plot, c) Purely aleatory probabilistic response

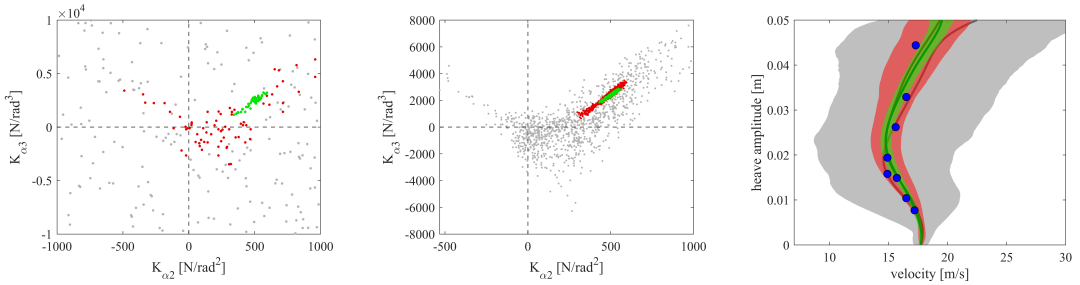

(a) (b) (c)

Figure 5.10: PIDB comparison over iterations (• iteration 1),(• iteration 2),(• iteration 3): a) training data, b) TMCMC scatter plot, c) Polymorphic probabilistic bifurcation diagrams

The evolution of the probabilistic response in the IDB study is depicted in Figure 5.9c, where shaded areas represent the 95% aleatory intervals of probability. Notably, the response at iteration 1 appears chaotic. However, the mean response at iterations 2 and 3 is nearly identical, albeit with a noticeable increase in probability between the iterations. In Figure 5.10c, the impact of epistemic uncertainties from the data

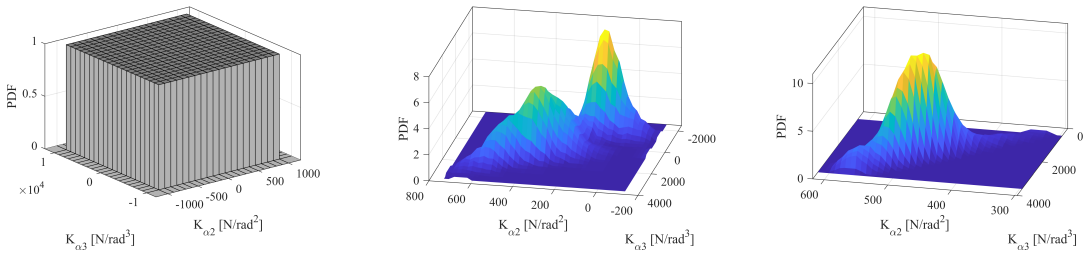

Figure 5.11: Prior distributions over iterations for IDB study: a) iteration 1, b) iteration 2, c) iteration 3

driven model is incorporated into the bifurcation diagrams. The changes in response between iterations 2 and 3 follow a similar pattern as observed in the IDB study. Epistemic uncertainties exert a significant impact on the probabilistic response at the first iteration, resulting in an interval of probability up to 300% wider than purely aleatory bounds. With the accuracy improvement of data driven models in iteration 2 and 3, the interval of probability is reduced significantly.

Figure 5.12 illustrates the process of retaining data from previous layers. Table 5.2 also show the number of training runs from the previous layer (the term "$\hat{f}$ held") that persist within the design space of the updated prior. With IDB approach, although the model construction entails 40 input runs at iteration 2, 11 points from the 180 collected on iteration 1 fall within the shaded area in Figure 5.12a. Consequently, only 29 additional training points are needed. Similarly, at iteration 3, 5 points from the previous iteration's data collection remain within the design space, resulting in a total training data requirement of 309 high fidelity model runs. The PIDB process preserves the most significant amount of data overall, saving a total of 30 training runs. Figure 5.12c also provides insights into the accuracy of the data-driven models concerning comparison data. The previously discussed increase in accuracy between iterations 1 and 2 is further highlighted here.

5.4.3 Probabilistic stability response

Figures 5.13 and 5.14 shows probabilistic stability response using IDB and PIDB approaches, and the impact of epistemic uncertainties on the stability. The probabilistic

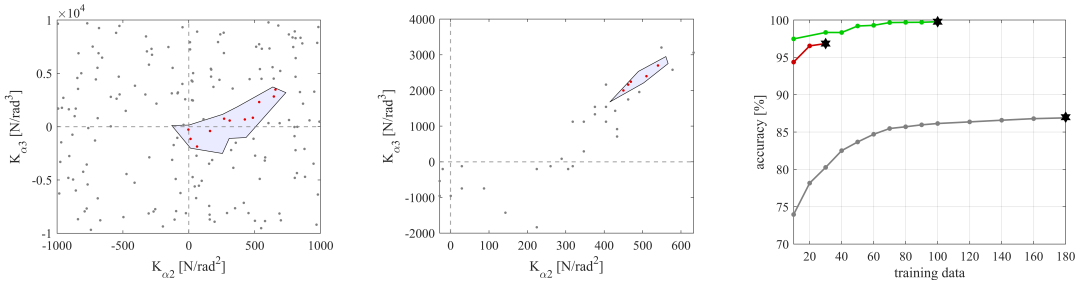

(a) (b) (c)

Figure 5.12: IDB training data over iterations (• discarded data),(• held data): a) iteration 1 to 2, b) iteration 2 to 3, c) model accuracy (- iteration 1), (- iteration 2), (- iteration 3), (⋆ convergence point)

response shape and stability yield nearly identical results using these two approaches, depicting a smooth transition from unstable LCO at low amplitudes to stable LCO at high amplitudes. Interestingly, the majority of stability information suggests that the lowest amplitude stable LCO (point 5 as labeled in Figure 4.6a) is unstable. However, in the PIDB study, more data indicates stability at this point, with 2.5% suggesting stability compared to only 0.2% in the IDB study.

The overall impact of epistemic uncertainties on the intervals of probability at the final iteration is relatively low. Notably, the interval of probability of the IDB is most affected, with a mean increase of 18.2% in the width of the interval of probability. This observation is expected, as the data-driven model for iteration 3 exhibits a higher mean standard deviation in predictions than the PIDB process. In contrast, combined polymorphic intervals of probability for the PIDB study expand by a mean of 6.8% compared to purely aleatory bounds. However, even with combined UQ, only 3 out of the 8 CBC points fall within the interval of probability. The only probabilistic bifurcation diagram that encompasses all CBC data is the combined single-iteration study. This discrepancy suggests a high level of noise in the experimental data is being underestimated or that the mathematical model does not accurately represent the data.

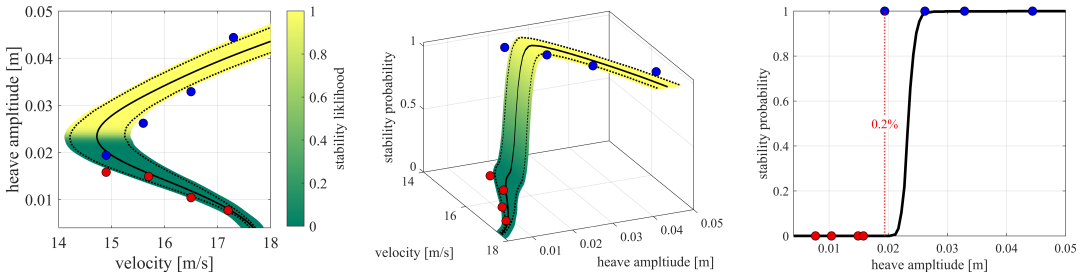

(a) (b) (c)

Figure 5.13: IDB polymorphic UQ results including stability information (shaded area = polymorphic interval of probability), (- mean plot),(. . . aleatory interval of probability), (• stable CBC data), (• unstable CBC data): a) Polymorphic response, b) Polymorphic surf plot, c) Stability likelihood

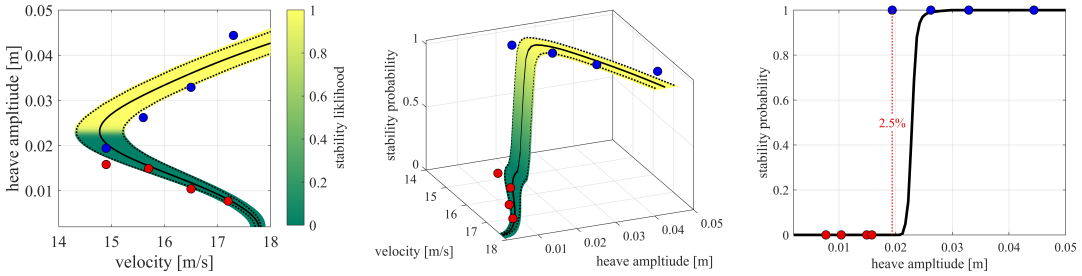

(a) (b) (c)

Figure 5.14: PIDB polymorphic UQ including stability information (shaded area = polymorphic interval of probability), (- mean plot),(. . . aleatory interval of probability), (• stable CBC data), (• unstable CBC data): a) Polymorphic response, b) Polymorphic surf plot, c) Stability likelihood

5.4.4 Overall comparison

Figure 5.15 provides a direct comparison of the results obtained from the three data-driven BMU processes discussed. PDF diagrams for parameter estimations shown in Figure 5.15 (a) exhibit similar Gaussian shapes, with mean predictions differing by no more than 2% across all methods. Notably, PIDB updating yields the lowest COV and maximum probability density at the mean point. Combined polymorphic probabilistic bifurcation diagrams reveal that the single-iteration process exhibits the widest intervals of probability. This observation is likely attributed not only to the single-iteration parameter estimations having the largest COV, but also to the impact of epistemic uncertainties within the data-driven model which has lower convergence

than the other two approaches. Conversely, the PIDB study exhibits the most narrow interval of probability.

Evaluation of stability information shown in Figure 5.15c highlights a noticeable change between the single-iteration and both iterative approaches. Specifically, the region where stability probability drops to 0.75 in the single-iteration study, between $0.036m$ and $0.046m$, does not exist in the iterative results. Instead, stability probability remains at 1 for all points following the turning point in both iterative studies. This observation aligns more closely with the CBC data, indicating the existence of a stable LCO in this region. Unlike the single-iteration study, this suggests that sufficient training data is gathered in the final iteration to accurately describe LCO stability information with the iterative approaches.

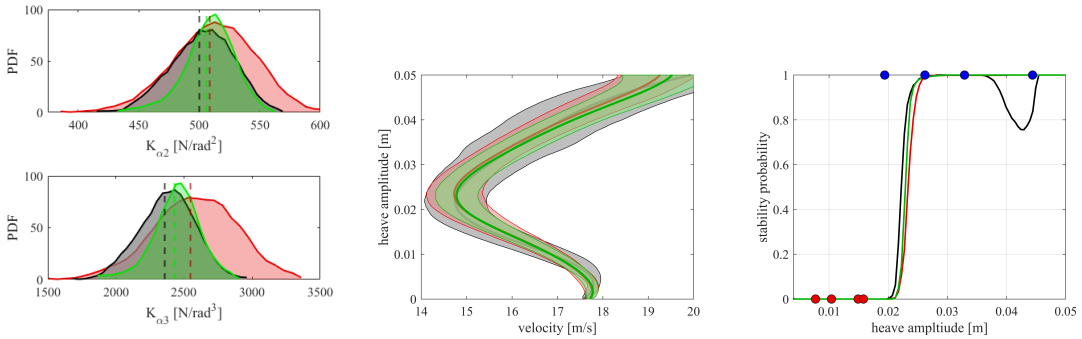

(a) (b) (c)

Figure 5.15: Method comparison of final results for configuration 1 (■ SDB), (■ IDB), (■ PIDB): a) Nonlinear parameter PDF, b) Polymorphic probabilistic response, c) Stability likelihood (• stable LCO) (• unstable LCO)

5.4.5 Overall comparison for configuration 2

Similarly, the three data-driven BMU methods are applied to a second set of experimental data, as shown in Figure 4.6b. The inputs to each algorithm are consistent with those presented in Table 5.1, except for the modification of σ_p, which is set to $0.85m/s$.

Key results for each process are summarised in Table 5.3. In the single-iteration study, the amount of training data remains consistent with the first configuration, with the data-driven model achieving accuracy within 1% of the initial results. For

Table 5.3: Configuration 2: Iterative results

	Iteration	f runs / held	$\hat{f}$ accuracy	$\hat{f}$ std	σ_p^n	$K_{\alpha 2}$ $[N/rad^2]$	$K_{\alpha 3}$ $[N/rad^3]$
SDB	1	1200 / 0	97.6%	$0.60m/s$	$0.80m/s$	720.9 ± 24.6	3382.8 ± 183.8
IDB	1	150 / 0	88.1%	$2.70m/s$	$2.40m/s$	206.7 ± 448.0	463.4 ± 2273.5
	2	77 / 23	94.5%	$1.19m/s$	$1.60m/s$	494.0 ± 450.4	2523.5 ± 1710.0
	3	47 / 53	98.3%	$0.62m/s$	$0.80m/s$	707.0 ± 24.7	3173.9 ± 196.1
PIDB	1	150 / 0	88.1%	$2.70m/s$	$2.70m/s$	123.8 ± 439.2	-44.4 ± 2421.9
	2	65 / 35	92.5%	$1.63m/s$	$1.63m/s$	455.7 ± 418.6	1855.3 ± 2132.5
	3	39 / 61	98.8%	$0.64m/s$	$0.80m/s$	709.4 ± 19.9	3203.6 ± 153.3

the IDB approach, a significant reduction in training data is observed, requiring only 274 training runs in total. The parameter estimates for $K_{\alpha 2}$ and $K_{\alpha 3}$ differ by 2% and 6% from the single-iteration results, respectively. However, the probability in the predictions is marginally lower in the IDB results. Notably, the iteration 3 data-driven model in the IDB study demonstrates superior accuracy compared to the single-iteration model.

An examination of the PIDB results reveals a marginal improvement across nearly all metrics compared to the other approaches. The process converged over three iterations, as was the case in configuration 1. Only 254 training runs were required, representing a 3.5% reduction compared to the IDB study and a 79% reduction compared to the single-iteration study. The parameter estimates are within 2% of those from the IDB study, with slightly higher probability. On average, the third-iteration data-driven model is 0.5% more accurate than the final IDB model, although it exhibits slightly higher variation in model predictions. Figures comparing the outputs from each process are presented in Figure 5.16. It can be seen that the PDFs for each of the predicted parameters exhibit similar behaviour, following normal distributions. The probabilistic response, shown in Figure 5.16b, indicates that the results from both the IDB and PIDB approaches are nearly identical. The single-iteration response, however, displays significant uncertainty at low and high heave amplitude points. As the parameter estimates are close to those of the other two methods, this suggests that the uncertainty arises from the data-driven model and that additional training is required in these regions. The LCO stability results in Figure 5.16c demonstrate that each method accurately predicts the stability of the observations. The only discrepancy

is found in the single-iteration results at low heave amplitudes, where the data-driven model suggests that LCO in this region are stable, although we know this is incorrect based on the results from the other two methods and the training data. This discrepancy is likely due to the aforementioned high uncertainty in the data-driven models for this region.

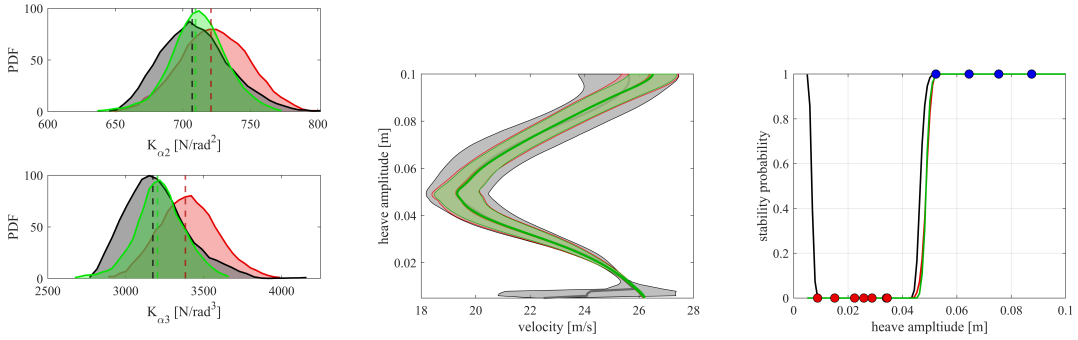

(a) (b) (c)

Figure 5.16: Configuration 2 method comparison of final results (■ SDB), (■ IDB), (■ PIDB): a) Nonlinear parameter PDF, b) Polymorphic probabilistic response, c) Stability likelihood (• stable LCO) (• unstable LCO)

The final results from the PIDB approach are presented in Figure 5.17. From the iterative scatter plots, it can be observed that a single modal solution is not identified until the final iteration, with a significant refinement occurring between iteration 2 and 3. This suggests that tuning the width parameter at each iteration could potentially provide a smoother transition from the full design space to a single modal solution. Examination of the probabilistic bifurcation curve shows that the majority of experimental observations are captured within the 95% interval of probability. However, three points remain outside these bounds, and, as observed in the previous configuration, the gradient of the stable region in the diagram does not fully align with the experimental observations. This provides further evidence that the mathematical model employed in this study does not fully capture the behaviour exhibited in the experimental data.

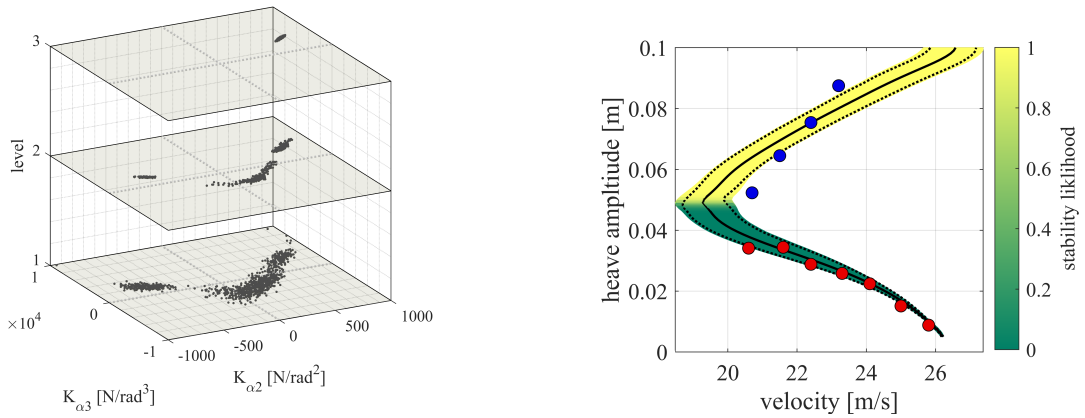

(a) (b)

Figure 5.17: Configuration 2 PIDB polymorphic UQ including stability information: a) Iterative scatter plot, b) Polymorphic surf plot (shaded area = polymorphic interval of probability), (- mean plot),(. . . aleatory interval of probability), (• stable CBC data), (• unstable CBC data)

5.5 Sensitivity Study of Interaction Parameters

A sensitivity analysis was conducted with both configurations to verify the assumption that the variance in the data-driven model σ_i can provide an accurate estimation of the width parameter σ_p^n in the iterative BMU process. The parameter estimations Chapter 4 will be used as the reference to benchmark the effectiveness of interaction parameter selection.

5.5.1 Configuration 1

Figure 5.18 (a) and (b) illustrates the outcome of applying various width parameters σ_p in configuration 1 using the data-driven model used for the first iteration. MBD and PMBD approaches employ the width parameters from Equation 5.2 and 5.4 separately, which are the dashed lines in Figure 5.18 (a) and (b). It is observed that high values of σ_p result in a minimal reduction in the width of distributions of the targeted nonlinear parameters. For both parameters, when σ_p drops below 2 m/s such as using IDB approaches, the 95% interval of probability falls outside the parameter estimate from the single-iteration study. This suggests that choosing such a low-width param-

eter may hinder the collection of training data where the solution exists at the next iteration. An examination of the width parameters from IDB and PIDB reveals an interesting result for both parameter estimates, as shown in Figure 5.18 (a) and (b). It is observed that, with the IDB estimate at 1.8 m/s, part of the single-iteration solution lies outside the 95% interval of probability of the updated posterior distribution. In contrast, at the PIDB estimate of 3.5 m/s, the full probabilistic estimate for each parameter is contained within the updated design space. While the IDB method results in a greater reduction of approximately 75% in width of parameter distribution for the next iteration, the PIDB approach successfully captures the final targeted parameter distribution from the single-iteration solution, while still achieving a 65% reduction.

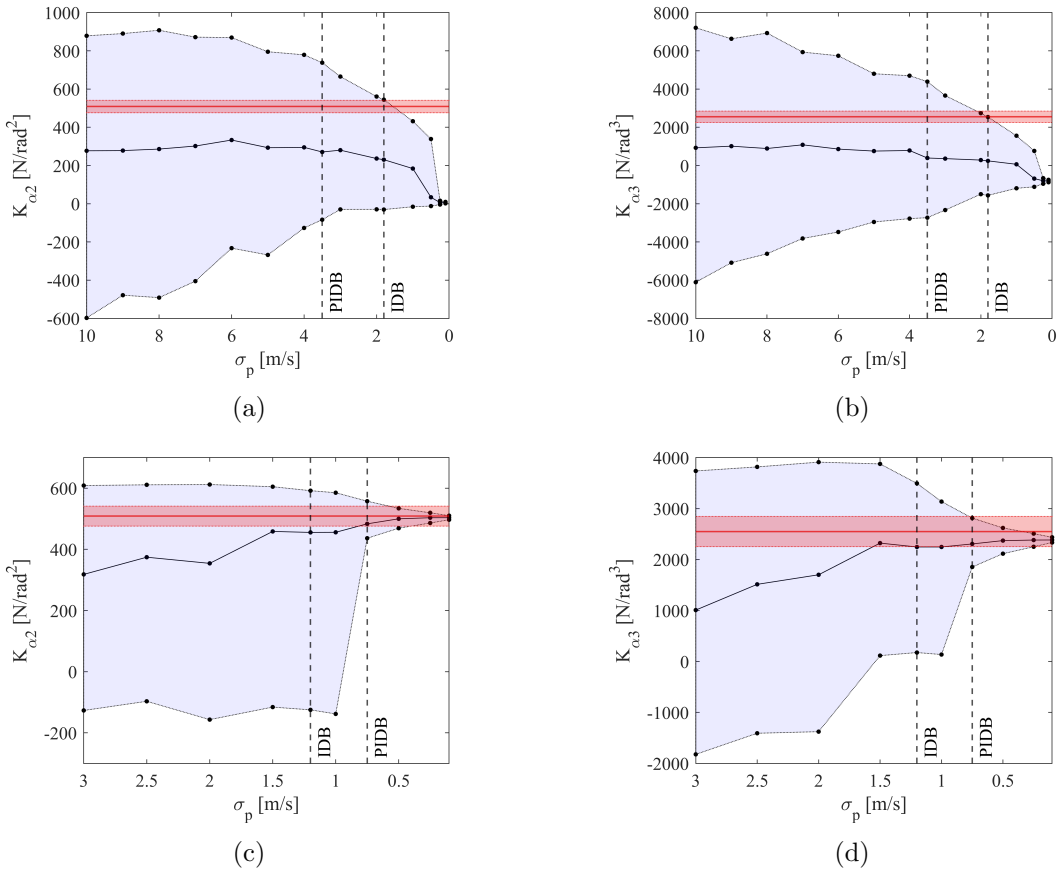

Figure 5.18: Configuration 1 sensitivity study of reducing width parameter with $K_{\alpha 2}$ and $K_{\alpha 3}$ probabilistic parameter estimates over iterations (■ 95% interval of probability), (■ single-iteration 95% interval of probability): a) $K_{\alpha 2}$ iteration 1, b) $K_{\alpha 3}$ iteration 1, c) $K_{\alpha 2}$ iteration 2, d) $K_{\alpha 3}$ iteration 2

The results of varying the width parameter in the second iteration are presented in Figure 5.18 (c) and (d). For both width parameter estimates using PIDB and IDB approaches, the posterior estimates of $K_{\alpha 2}$ and $K_{\alpha 3}$ include an interval of probability from the targeted estimates from the single-iteration updating. With the IDB estimate, the design space is reduced by only 23%, whereas with the PIDB estimate, a 70% reduction is achieved. This significant difference arises due to the large change in the posterior distribution for $K_{\alpha 2}$ between the σ_p values of 0.8 m/s and 1 m/s. It is because, for the higher value over 1 m/s, a multi-modal solution is still considered, but by less than 0.8 m/s, the process has converged to a single-modal estimate for $K_{\alpha 2}$.

From the variation of width parameters across both iterations in configuration 1, it is evident that the PIDB method is the most effective in this case. It excels both in capturing the solution within the design space on initial iterations and in narrowing the design space to a single-modal solution on further iterations. There is still room for improvement, however. Ideally, the design space should be reduced as much as possible without excluding the desired solution. In the first iteration, the PIDB method could reduce the design space by an additional 8% while keeping the solution within its boundaries. Achieving this, however, is challenging without prior knowledge of the solution. In this configuration, it can be concluded that the PIDB method is effective in reducing the design space without excluding the desired solution.

5.5.2 Configuration 2

Figure 5.19 presents the results of the sensitivity study for configuration 2 over the first two iterations. In this configuration, the estimates for σ_p are much closer than those in configuration 1. At iteration 1 shown in Figure 5.19 (a) and (b) , both estimates of σ_p are near the interval of probability, but in the IDB estimate, part of the single-iteration solution lies outside the interval of probability, whereas the PIDB estimate just captures the full solution for both parameters. At iteration 2 shown in Figure 5.19 (c) and (d), both estimates of σ_p encompass the entire single-iteration solution within their intervals of probability. There is potential for further refinement of the design space. In this configuration, it is less clear which method provides the best estimate

of σ_p, as the estimates are very close at both iterations. The evidence from iteration 1 suggests that the PIDB offers a slightly better estimate, as it does not exclude any of the single-iteration solutions from its interval of probability. The iteration 2 study shows that neither estimate is perfect as the targeted solution from the single-iteration update at the boundary of the posterior distribution from both approaches.

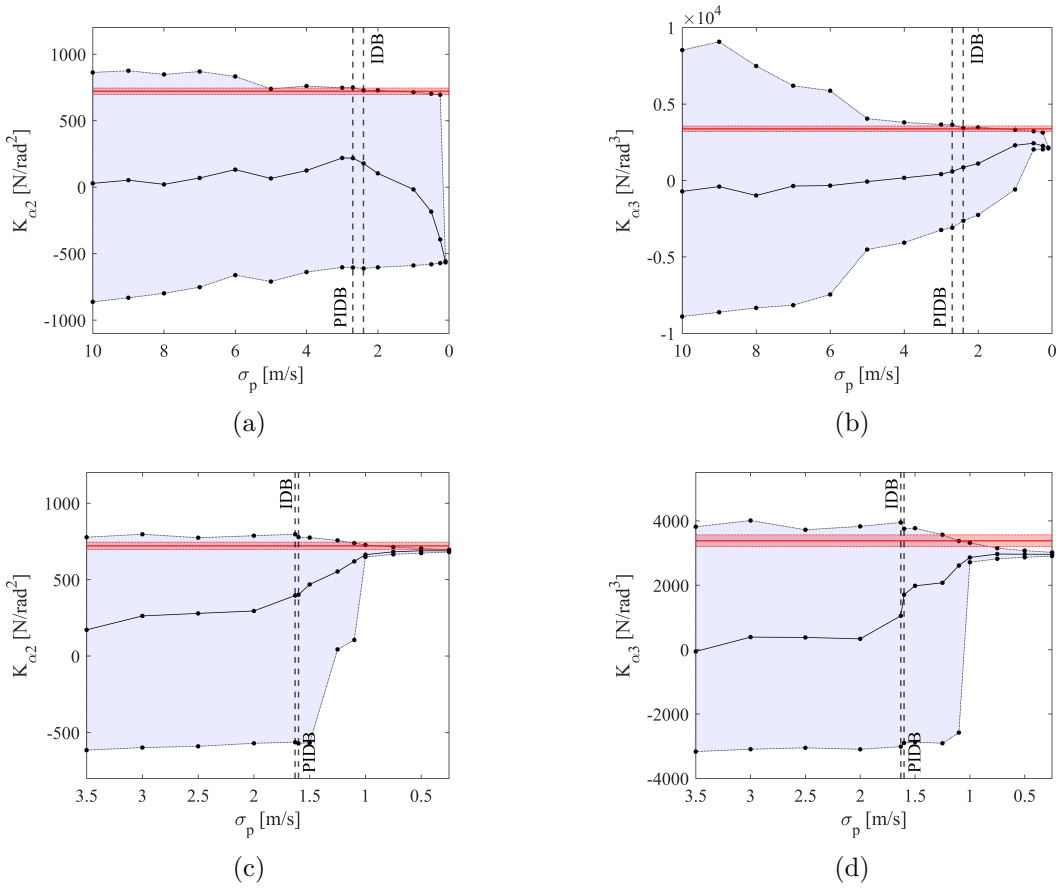

Figure 5.19: Configuration 2 sensitivity study of reducing width parameter with $K_{\alpha 2}$ and $K_{\alpha 3}$ probabilistic parameter estimates over iterations (■ 95% interval of probability), (■ single-iteration result): a) $K_{\alpha 2}$ iteration 1, b) $K_{\alpha 3}$ iteration 1, c) $K_{\alpha 2}$ iteration 2, d) $K_{\alpha 3}$ iteration 2

5.5.3 Discussion

The study on configuration 1 demonstrates that the proposed IDB approach achieved a 74% reduction in training data requirements and runtime, along with a 3.1% improvement in data-driven model accuracy. Notably, parameter estimates deviated by

no more than 2% compared to the single-iteration study. Similarly, the PIDB approach resulted in a substantial 76% reduction in training data and runtime, while maintaining parameter estimates within 2% of the single-iteration method and yielding a 2.9% increase in model accuracy. Furthermore, the PIDB approach exhibited the highest probability in predictions, producing estimates with the lowest variation. Results from the second configuration align with those from the first. The PIDB approach achieved a 79% reduction in training data requirements compared to the single-iteration study and a 3.5% reduction compared to the IDB method. The final data-driven model from the PIDB approach also demonstrated a 1.2% increase in accuracy over the single-iteration approach and a 0.5% improvement over the IDB method.

Considering epistemic uncertainties in the probabilistic response for configuration 1, both iterative approaches exhibited reduced susceptibility to model uncertainty compared to the single-iteration approach. The PIDB approach resulted in the smallest increase the interval of probability, with only a 6.8% rise relative to the purely aleatory bounds. The IDB approach also demonstrated improvement over the single-iteration method, showing an 18.2% increase in the interval of probability, compared to the 53% observed in the single-iteration study. This suggests that the probabilistic results derived from data-driven models in the iterative studies can be regarded with higher probability. The findings from configuration 2 align with these conclusions, with epistemic uncertainties widening the stability boundaries in the single-iteration approach by an average of 40%, while both iterative approaches experienced only a 7% increase, displaying almost identical probabilistic response results. Probabilistic LCO stability results from both iterative studies depicted a smooth transition from unstable LCO at low heave amplitudes to stable LCO at high amplitudes for both configurations. Notably, the period of instability observed post-turning point in the single-iteration study for configuration 1 was absent in either iterative study, suggesting closer agreement with CBC data.

A sensitivity analysis was conducted on both configurations to validate the assumption that variance in the data-driven model can accurately estimate the width parameter in the model updating process, using single-iteration study parameter esti-

mates as reference results. In configuration 1, high values of σ_p resulted in minimal reduction in design space, but values below 2 m/s caused the 95% parameter estimate to fall outside the updated design space, suggesting exclusion of necessary training data. While the IDB method achieved a 75% reduction in design space, the PIDB method effectively captured the single-iteration solution within a 65% reduction. In the second iteration, PIDB narrowed the design space by 70%, compared to only 23% for IDB. Across both iterations, the PIDB method proved more effective by converging to a single-modal estimate while maintaining the solution. In configuration 2, σ_p estimates were closer than in configuration 1. At iteration 1, the IDB estimate excluded part of the single-iteration solution from the interval of probability, while the PIDB captured the full solution. At iteration 2, both methods encompassed the entire single-iteration solution, with PIDB showing slightly better accuracy. Although neither estimate is perfect, the PIDB method consistently demonstrated greater reliability across configurations.

5.6 Conclusions

This Chapter proposed a iterative data-driven Bayesian framework for stochastic model identification of complex nonlinear dynamical systems to significantly reduce computational expense of high fidelity simulations. It will build upon the contributions of the previous chapter, further enhancing it by demonstrating that training costs can be reduced and that uncertainty in the data-driven models can also be incorporated. Multi-resolution data-driven models were constructed using the iterative BMU process with limited experimental data. One of the major contributions was that epistemic data-driven model uncertainties was effectively included in the proposed iterative framework through p-box for the first time. Through a nonlinear aerofoil aeroelastic case study aimed at stochastically identifying nonlinear parameters, the findings of this study highlight the efficacy of the two proposed iterative data-driven approaches in significantly reducing training data requirements by 76% and further improving data-driven model accuracy compared to the single-iteration approach.

Experimental observations from two configurations were tested, with each study

also undergoing polymorphic uncertainty propagation to assess the probabilistic response, alongside probabilistic data-driven stability analysis of LCO. Notably, in the single-iteration study, quantifying the impact of epistemic uncertainties in the data-driven model led to a 53% increase in the 95% interval of probability for configuration 1. In configuration 2, the epistemic uncertainties in the data-driven model resulted in substantial variation in model estimations at low and high LCO amplitudes, leading to inaccuracies in the stability predictions. This significant expansion reflects a considerable level of epistemic uncertainty, indicating the necessity to include it in the robust predictions. Additionally, probabilistic stability analysis in the single-iteration study revealed a period of instability in LCO amplitude between $0.036m$ and $0.046m$, contradicting CBC data. This discrepancy suggests an insufficiency in stability training data for this range, which can be addressed using the iterative data-driven framework.

With the primary focus of this study being the reduction of high fidelity simulation requirements and addressing epistemic uncertainties from multi-resolution data driven models, it can be concluded that PIDB emerges as the optimal choice by comparing the results to IDB approach as well as from the following sensitivity study. This method exhibited the lowest training data requirements among the three considered while maintaining parameter estimations within a 2% deviation compared to other methods. While the IDB approach produced the most accurate surrogate models by 0.2% more accurate than PIDB, it requires up to 6% more training data. Moreover, the PIDB approach offers the additional advantage of requiring fewer inputs from the user, with the automated iteration convergence operating successfully.

Although iterative approaches effectively reduced computational costs and epistemic uncertainty, none of the probabilistic responses fully aligned with the experimental CBC data. This discrepancy also applies to the probabilistic stability results, particularly regarding the stability of CBC point 5 in configuration 1, which none of the proposed methods accurately predicted. These findings indicate that there may either be considerable noise in the data or an insufficient representation of the underlying physics in the mathematical model s was also observed in Chapter 3. Given the probabilistic nature of this approach and the minimised impact of epistemic uncertainties, the most

likely conclusion is that the mathematical model needs to be updated.

With the iterative framework now validated against experimental data, the natural progression is to demonstrate its full capabilities through an advanced test case. An ideal case study would exhibit three key characteristics; high-fidelity nonlinear aeroelastic behaviour representative of real-world systems, increased DoF compared to the current implementation, and more complex dynamic responses than the subcritical behaviour analysed in this chapter.

Chapter 6

Gimballed Hub Tiltrotor Case Study

6.1 Introduction

With the iterative data-driven Bayesian framework validated as well as HBM based computational framework has demonstrated on a simple test case, the focus of this chapter is to evaluate the frameworks' capabilities using a complex and high-fidelity aeroelastic test case. The work should evaluate the computational framework as well as the system identification aspects as well. It aims to assess the robustness of the proposed frameworks in chapter 2 and 4, which is able to deal with a more complex and realistic aeroelastic system including:

1. More complex nonlinear dynamical behaviour

   The introduction of nonlinearities into the system should lead to the formation of LCO, ideally resulting in a subcritical shape in the bifurcation diagram. While the presence of LCOs is critical, the realistic nonlinear aeroelastic system may produce a bifurcation diagram with a more intricate shape than the relatively simple subcritical form observed in previous sections. It provides a more rigorous assessment of the proposed framework's capabilities.

2. Higher fidelity system with more nonlinear DoFs

A simplified low fidelity nonlinear aeroelastic systems was studied in the previous sections using 2DoF aerofoil model. However, it is far away from the real-world nonlinear systems. A high-fidelity test case is necessary to ensure that the framework is tested under conditions that reflect real engineering systems, as would be encountered in industry-standard analysis.

3. Higher computational expense

   Conducting both time-domain and frequency-domain analyses of the system is expected to incur significantly higher computational costs compared to the previous study. Since the framework is designed to reduce computation time, its advantages will be most evident when applied to a computationally expensive system. This approach also aligns with the complexity of real-world systems used in industry, thereby demonstrating the framework's practical relevance.

The gimballed hub model, developed by Johnson and his contemporaries in Ref. [194] to describe the behaviour of a tiltrotor wing, was identified as a representative test case.

The sections in this Chapter are organised as follows: gimballed hub model is first introduced, including a justification for the high fidelity test case. It is followed by a detailed presentation of the mathematical model, including linearised and nonlinear analysis using HBM framework. The results will be validated using time domain solutions. Subsequently, an improved generalised data-driven model is presented that is necessitated by the increased complexity of the case study. After that, the stochastic identification framework is then applied to two sets of pseudo-data, designed to emulate real experimental data where the results are analysed and discussed. Finally, conclusions are drawn regarding the process for conducting a high-fidelity case study.

6.2 Gimballed Hub Model

Tiltrotor aircraft are a unique class of fixed-wing aircraft powered by rotors that can be tilted by the pilot to vector their thrust. Their flight envelope combines the VTOL capabilities of helicopters with the range and speed of turboprop aircraft. In military

(a) (b)

Figure 6.1: VTOL aircraft (a) VX4 [7], (b) Transwing VTOL drone [8]

applications, this versatility enhances operational agility and lifting capacity, while in civilian contexts, tiltrotors offer a promising solution to global airport congestion. From a civilian perspective, the VX4 electric aircraft, shown in Figure 6.1a, exemplifies advanced VTOL technology. Developed by Vertical Aerospace, it is designed for urban air mobility and features four pairs of tilting rotors, enabling seamless transitions between vertical take-off, landing, and forward flight. Significant UK funding has been invested in this technology, as highlighted in recent research [195]. From a military standpoint, the Transwing VTOL unmanned aircraft system, illustrated in Figure 6.1b, represents a cutting-edge application of VTOL technology. Developed by PteroDynamics, it has garnered considerable interest for its potential in military logistics and operations, as discussed in recent studies [196].

Tiltrotor aircraft exhibit nonlinear LCO behaviour known as whirl flutter, an aeroelastic instability. This phenomenon is sensitive to various parameters, but a well-established triggering mechanism is the exceedance of a critical onset airspeed. Consequently, whirl flutter is primarily a concern during the cruise flight regime. It arises due to the interaction of aerodynamic and gyroscopic forces acting on the rotor with the elastic structural modes of the rotor, nacelle, and wing. Historical incidents have demonstrated that whirl flutter can rapidly lead to catastrophic structural failure. Whirl flutter imposes significant performance limitations on tiltrotor aircraft. Directly, it necessitates operating below the critical onset airspeed, while indirectly, it requires

the addition of aerodynamically detrimental stiffness (and increased wing thickness) to ensure aeroelastic stability up to the design speed [197]. Notably, observations of cases where oscillation amplitudes remained constant [198] suggest that whirl flutter may manifest as a LCO rather than merely the divergence of a linear system. Furthermore, studies incorporating cubic stiffness nonlinearities in wing and control surface models have demonstrated the influence of these nonlinearities on flutter onset speeds. Wind tunnel tests have shown good agreement with theoretical predictions, validating these findings [199–201].

A critical feature of a dedicated tiltrotor rotor-nacelle model is the incorporation of a gimballed rotor hub, which allows the rotor to rotate elastically about the end of the shaft. This shaft, in turn, can rotate in space due to wing flexure. The model employed in this chapter was originally developed by Johnson in 1974 [194] and has been widely used in recent studies, such as [202–204]. Published as a NASA technical note, this model, like the earlier investigations by Reed, formed part of a comprehensive theoretical and experimental study. The inclusion of the gimballed hub, along with multiple additional degrees of freedom—primarily in the rotor but also in the wing—results in a system with significantly more complex dynamics than those captured by classical modelling techniques. This complexity makes the model far more representative of real-world tiltrotor aircraft systems [205]. The work of Mair and colleagues [32, 46] demonstrated that the model exhibits intricate nonlinear behaviour when cubic stiffness is introduced, producing highly complex bifurcation diagrams.

This model aligns with the three criteria established for this study: it is high-fidelity and complex, accurately captures the behaviour of real-world systems, and demonstrates complex nonlinear dynamics. As such, it serves as an ideal candidate for the high-fidelity case study to validate the proposed methodologies.

6.2.1 Mathematical Model

The gimballed hub model can be represented by the free-body diagram shown in Figure 6.2. It depicts a wing fixed at the root, with a rotor-nacelle assembly mounted at the wing tip in cruise configuration. The rotor-nacelle generates thrust and consists of a

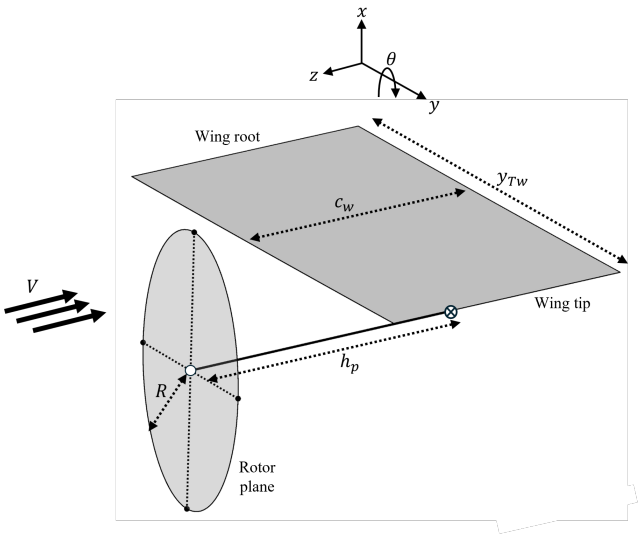

Figure 6.2: Gimballed hub model free body diagram

rigid pylon of length h_p, connected to a rotor with blades of radius R, rotating at an angular velocity Ω. The wing is modelled as a cantilever plate, free to bend in the x- and z-directions and to twist under the influence of forces exerted by the pylon or aerodynamic loads resulting from airflow of velocity V. For the wing, a high-aspect-ratio configuration is assumed, allowing the application of aerodynamic strip theory. The wing structure is modelled using beam theory, with chordwise and flapwise bending represented in the following form:

$$\begin{aligned} x_w(t, y_w) &= \sum_i q_i(t)\eta_w(y_w) \\ z_w(t, y_w) &= \sum_i q_i(t)\eta_w(y_w) \\ \theta_w(t, y_w) &= \sum_i p_i(t)\xi_w(y_w) \end{aligned} \tag{6.1}$$

Here the subscript w represent wing, ξ_w represents the mode shape for torsion, η_w denotes the mode shape for the elastic bending of the wing, and i indicates the number of modes. The assumed mode shapes are $\eta_w(y) = \frac{y^2}{y_{tw}}$ for bending and $\xi_w(y) = \frac{y}{y_{Tw}}$ for torsion. These expressions capture the fundamental characteristics of the respec-

Table 6.1: Whirl flutter model degrees of freedom

Symbol	DoF
β_{1C}	longitudinal tip path plane pitch
β_{1S}	lateral tip path plane tilt/yaw
ζ_{1C}	lateral rotor centre-of-gravity offset
ζ_{1S}	longitudinal rotor centre-of-gravity offset
β_0	collective flap
ζ_0	collective lag
q_1	wing beamwise bending
q_2	wing chordwise bending
p	wing torsion

tive deflections observed in real-world systems while satisfying the essential boundary conditions of zero deflection and zero slope at the root [206]. Only the first mode for each wing DoF is considered, as higher-frequency modes are less likely to couple with the rotor dynamics [202].

To model the interactions between the rotor-nacelle system and the wing, the system is mathematically described by a set of coupled differential equations derived from Lagrangian mechanics or Newton-Euler formulations. For example, the flapping motion of the rotor is governed by:

$$I_\beta \ddot{\beta} + C_\beta \dot{\beta} + K_\beta \beta = M_\beta \tag{6.2}$$

where I_β, C_β, and K_β represent the flapping inertia, damping, and stiffness, respectively, and M_β denotes the aerodynamic moment. Similarly, the wing bending and gimbal tilt dynamics are modelled using analogous equations. These coupled degrees of freedom enable the system to accurately capture complex aeroelastic phenomena.

Detailed derivations of the model, including the coupling between wing and rotor forces, are provided in [194]. The degrees of freedom are summarised in Table 6.1 and illustrated in Figure 6.3. The model includes three rotor-related degrees of freedom: β_{1C}, β_{1S}, and β_0, which describe the orientation of the rotor plane, accounting for pitch, yaw, and coning effects. The motion of the rotor plane's centre is described by ζ_{1C}, ζ_{1S}, and ζ_0, representing translations in the x-, y-, and z-directions, respectively.

For the wing, q_1 and q_2 represent spanwise (x-direction) and chordwise (z-direction) bending, while p denotes torsion about the spanwise (y-direction) axis. These degrees of freedom are coupled, and their mutual excitation leads to the onset of whirl flutter phenomena.

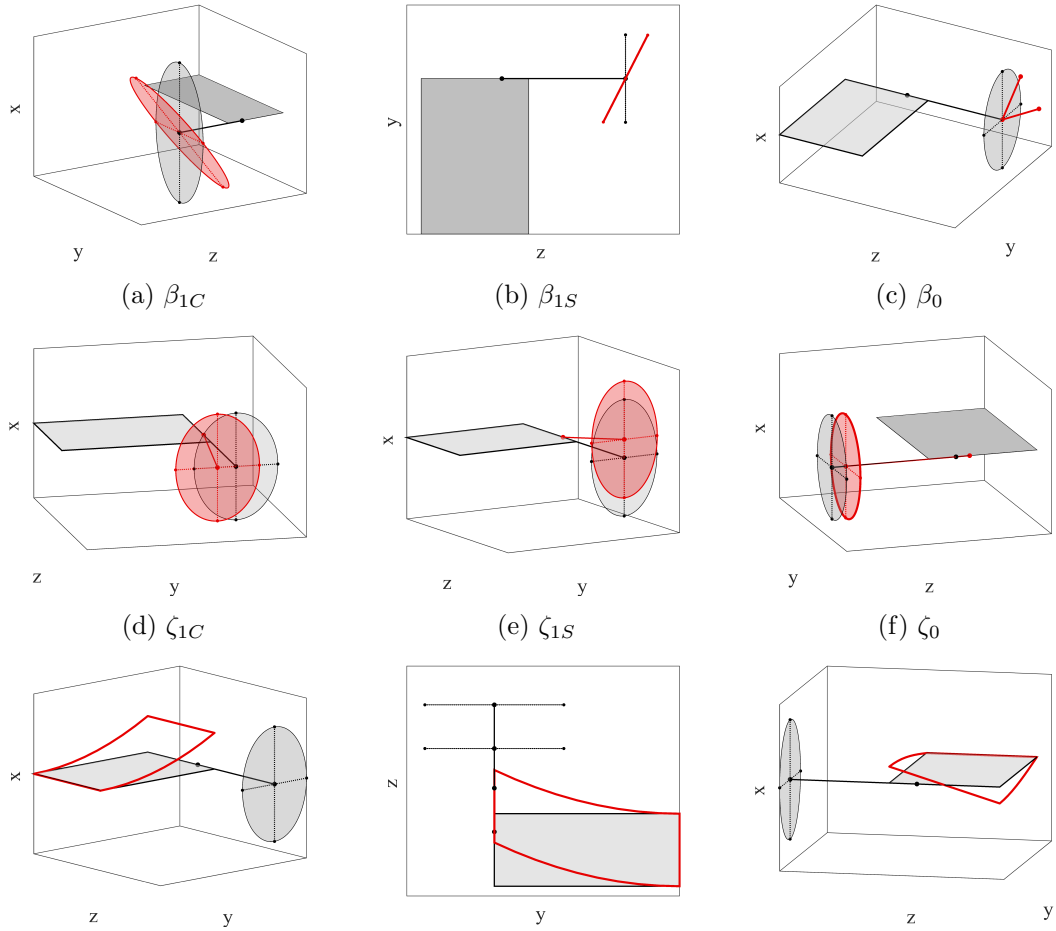

Figure 6.3: Gimballed hub model degrees of freedom illustrated illustrated (■ undeformed mode), (■ deformed mode)

Following the derivation presented in [194], the full equations of motion can be expressed in the form of Equation 3.3 from Section 3.2.1 (restated below) by defining $\boldsymbol{x}$ as:

$$\dot{\mathbf{x}} = \mathbf{Q}\mathbf{x} + \mathbf{q}_n f_{nl} \tag{6.3}$$

$$\boldsymbol{x} = [\beta_{1C} \quad \beta_{1S} \quad \zeta_{1C} \quad \zeta_{1S} \quad \beta_0 \quad \zeta_0 \quad q_1 \quad q_2 \quad p]^T \tag{6.4}$$

The combined mass, damping, and stiffness matrices for the system are detailed in Appendix C following Ref [46,194]. To introduce nonlinear effects into the system, the blade flapping stiffness profile is replaced with a polynomial expression, similar to the approach used in the previous case study. However, adapting this model requires careful consideration. The nonlinear blade flapping stiffness must first be applied to each blade within the rotating frame of reference. Subsequently, the multi-blade coordinate transformation is reapplied to derive the full system equations. The nonlinear blade flapping stiffness for the m^{th} blade, denoted as $K_{\beta,\text{nl}}$, within the rotating frame of reference, is expressed as:

$$K_{\beta,nl}\beta_m = K_{\beta 1}\beta_m + K_{\beta 2}\beta_m^3 + K_{\beta 3}\beta_m^5 \tag{6.5}$$

The K_β terms characterise the influence of nonlinear stiffness on the motion of the blade's tilt plane. Similar to the K_α terms discussed in the previous chapter, the K_β terms describe the rotation of the blade plane. Following the comprehensive derivation provided by Mair and colleagues [46, 202], Equation 6.5 is expanded to yield three complex nonlinear equations associated with the β_{1C}, β_{1S}, and β_0 degrees of freedom. This results in the vector shown in Equation C.8 in Appendix C, which serves as the nonlinear component in Equation 6.3.

For simplicity and to facilitate comparison, the parameters from the original study are adopted for this case study and are presented in Table C.1 in Appendix C.

6.3 Aeroelastic analysis

Conventional deterministic analysis must precede application of the developed framework to the test case. This foundational analysis involves identifying the system's linear flutter speeds and characterising the expected bifurcation diagram topology, establishing essential baseline behaviour for subsequent probabilistic evaluation.

6.3.1 Linear Analysis

Using the parameters from Table C.1, linear eigenvalue analysis was conducted. The results, presented in Figure 6.4 showing real parts of the eigenvalues of $\mathbf{Q}$, indicate that linear whirl flutter occurs at 307 m/s in the collective flap mode. The eigenvalue analysis is validated by the pre- and post-flutter time histories obtained through standard Ordinary Differential Equation (ODE) methods, as shown in Figures 6.4a and 6.4b. Below the flutter speed, a decaying oscillation is observed, while a rising oscillation occurs just above the flutter speed. The divergence speed of the model was found to be 350 m/s. These linear results align with those presented in Ref. [46], confirming a system with a relatively high flutter speed and a divergence speed shortly thereafter.

6.3.2 Nonlinear Analysis

With the linear analysis complete, the next step is to perform nonlinear analysis and validate the results. Two nonlinear parameters, $K_{\beta 2}$ and $K_{\beta 3}$, are considered here. By setting these to arbitrary values from Ref. [202] and applying the framework outlined in Chapter 3, the bifurcation diagrams presented in Figure 6.5 are generated with 20 harmonic orders to ensure convergence.

The first key observation is the presence of subcritical behaviour, with LCO emerging at speeds as low as 80 m/s. This underscores the importance of nonlinear analysis, as the linear analysis erroneously suggests safe operation up to 350 m/s where aeroelatic divergence occurs. The second key observation is the increased complexity of the bifurcation curves compared to the simple subcritical shapes observed in previous chapters. For each DoF, multiple LCO amplitudes exist across sections of the velocity range, a phenomenon not seen in prior studies. Notably, the curve for β_{1C} exhibits a self-intersecting pattern, indicating a highly complex dynamic response. Even for relatively simple response as the behaviour observed for the β_0 DoF in the upper branch of the bifurcation diagram—regions exist where multiple stable LCO amplitudes coexist at identical freestream velocities.

Referring to Section 4.4, the surrogate model was initially formulated as $V = \hat{f}(h, \theta)$, which assumes a unique velocity value for each LCO amplitude. However, as demon-

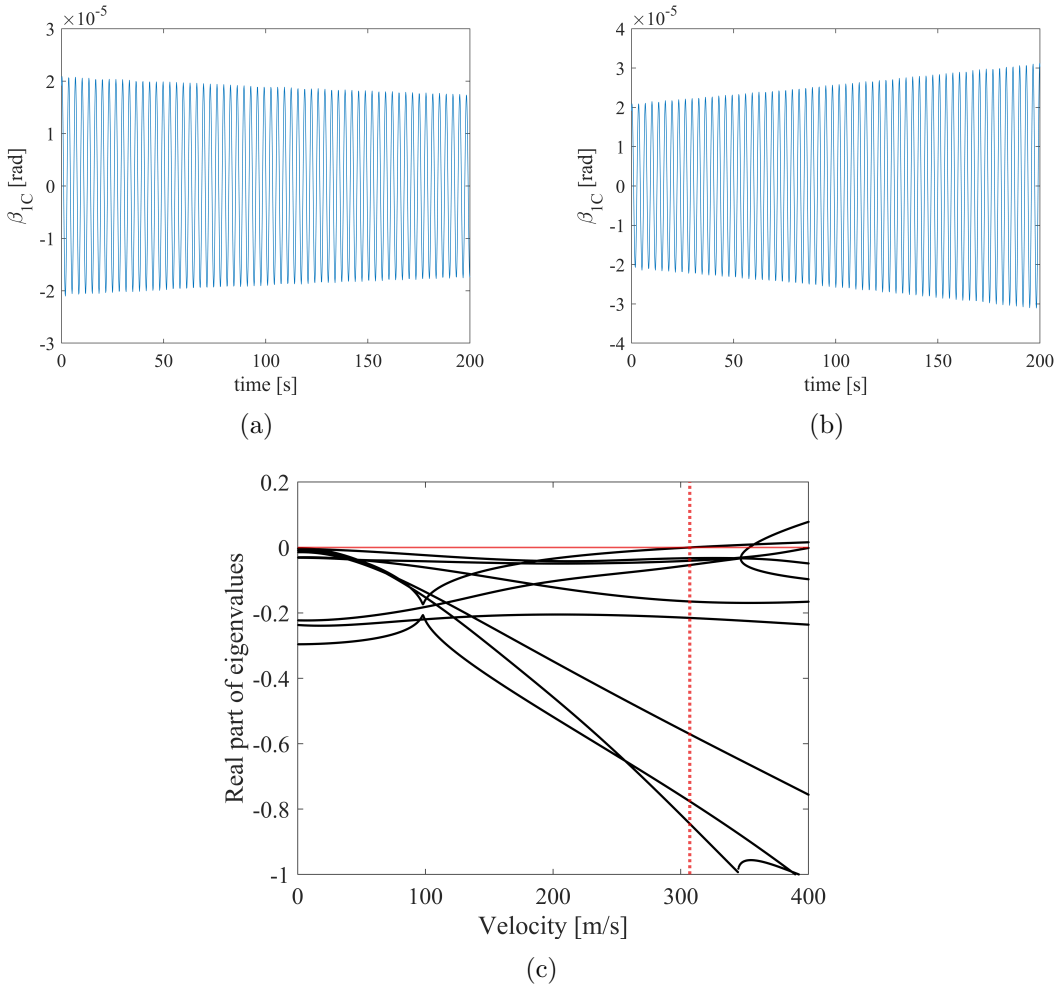

Figure 6.4: Linear analysis of gimballed hub model (a) Pre flutter time history at $V = 306m/s$, (b) Post flutter time history at $V = 308m/s$, (c) Eigenvalue analysis ($\cdots$ flutter point)

strated in this case study, this one-to-one correspondence does not hold for any of the system variables. These results indicate that the surrogate model development methodology presented in Chapter 4 requires modification to accommodate the complex nonlinear behaviour exhibited by the system.

The complex bifurcation curve for β_{1C} is further examined in Figure 6.6. It is observed that the amplitudes obtained from time histories, computed using standard ODE methods, align closely with the predictions from the bifurcation diagram, despite the curve's intricate shape. This agreement validates the bifurcation diagram's predic-

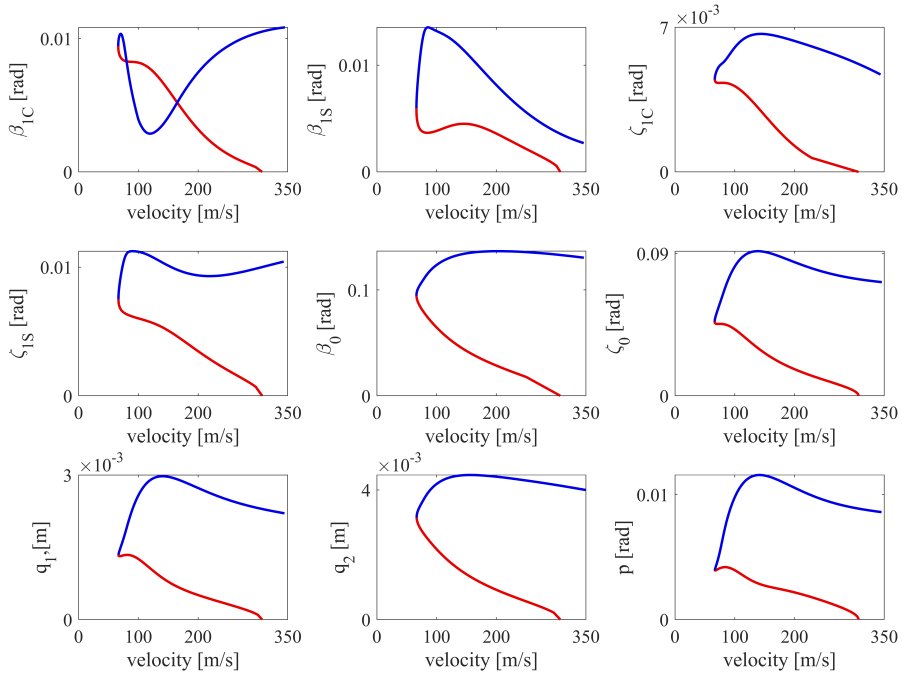

Figure 6.5: Gimballed hub model bifurcation diagrams for all degrees of freedom with random $K_{\beta 2}$ and $K_{\beta 3}$ values (• unstable LCO), (• stable LCO)

tions and establishes that they can be relied upon with the same probability as the time-domain results.

A detailed comparison is presented in Figure 6.7, examining the relationship between harmonic order and the stable portion of the time-domain solution from Figure 6.6. Only the stable section was analysed, as ODE methods can only capture stable LCO. Figure 6.7a demonstrates that while shape discrepancies are evident at low harmonic orders, convergence improves rapidly for orders $l \geqslant 2$. This convergence is further supported by the amplitude error analysis in Figure 6.7b, which shows the HBM continuation error decreasing from initial values exceeding 5% to below 1% by $l = 5$, with full convergence achieved by $l = 8$. The stability comparison in Figure 6.7c reveals that Koopman and Floquet methods achieve complete agreement by $l = 8$. The marginally higher mean error in Koopman analysis stems from evaluating 18 Floquet multipliers compared to a single amplitude measurement, with the reported error representing the mean across all multipliers.

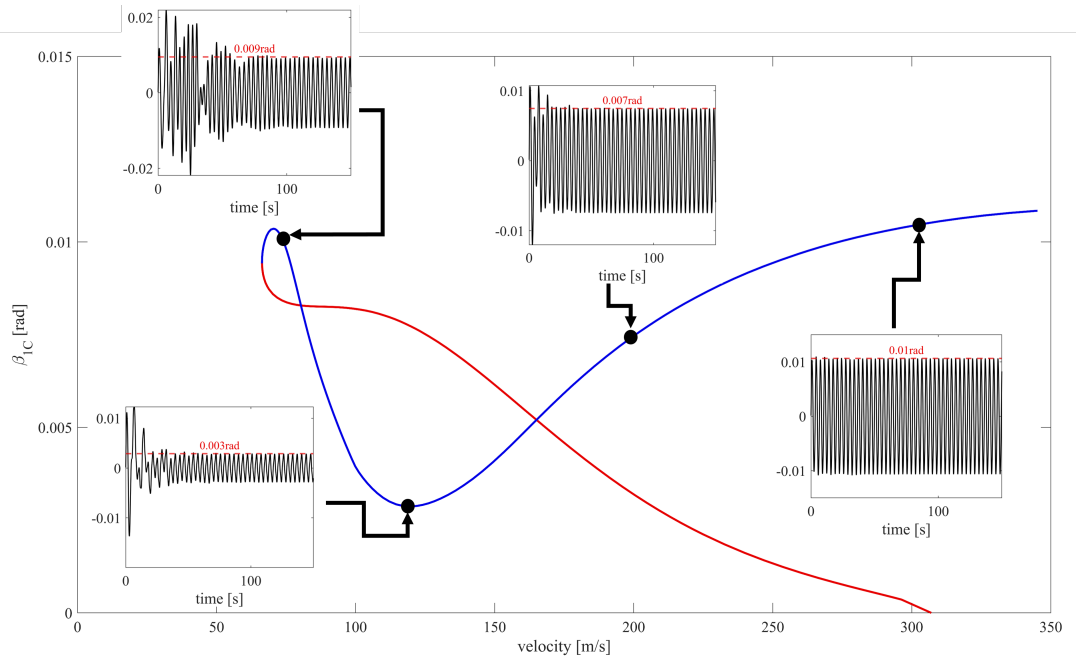

Figure 6.6: Comparison of bifurcation from Figure 6.5 diagram with time histories (• unstable LCO), (• stable LCO)

Figure 6.8 presents a computational time comparison for the AFT procedure, analogous to the analysis in Figure 3.18a (Chapter 3). The time-domain method exhibits a mean execution time approximately ten times greater than observed in previous test cases. As anticipated, the AFT procedure also requires additional computation time due to the increased number of DoF in the nonlinear system.

Unlike the previous case where the time-domain method became more efficient beyond 8 harmonic orders, the current results demonstrate this crossover occurring only at 20 orders. Notably, both the bifurcation curve shape and stability predictions converge by 8 harmonic orders, at which point the HBM maintains a 30% runtime advantage. These findings indicate that the HBM framework demonstrates enhanced computational efficiency for higher-DoF systems, remaining preferable for harmonic orders up to 20.

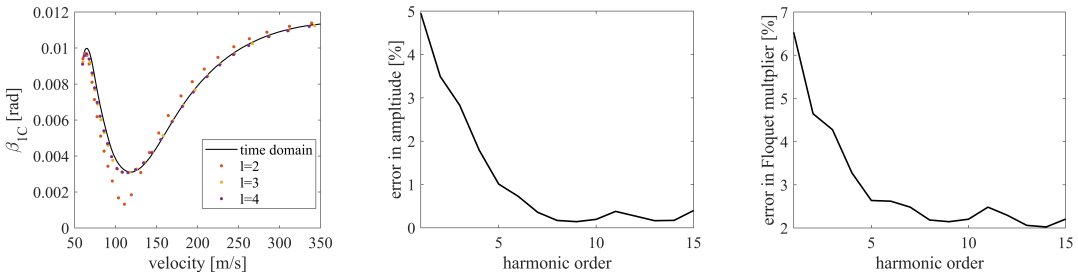

(a) (b) (c)

Figure 6.7: Gimballed hub model harmonic order convergence study (a) HBM to time domain comparison (b) Error in LCO amplitude (c) Error in key Floquet multiplier

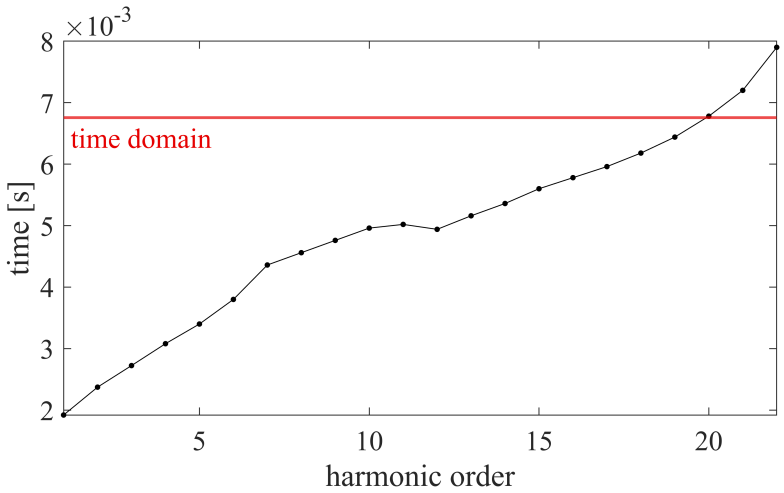

Figure 6.8: Comparison of AFT procedure convergence for a single LCO with time domain method for gimballed hub model test case.

6.4 Improved Data-Driven Modeling

As previously noted, an improved surrogate model development strategy is required prior to obtaining meaningful results. Examination of the key equation $V = \hat{f}(h, \theta)$ from the earlier surrogate development section, along with Figure 6.5, reveals that this formulation is inadequate. Consequently, we considered introducing a third hyper parameter to develop separate surrogate models for both amplitude and velocity as functions of the nonlinear parameters and this additional variable.

The arclength s, discussed in Chapter 3, emerged as the natural choice for this parameter. As a monotonically increasing variable that progresses with continuation,

it uniquely identifies each point through velocity, amplitude and frequency. Figure 6.9 demonstrates this approach by plotting LCO amplitude, velocity, and the key Floquet multiplier against arclength for the results shown in Figure 6.6. Despite initially promising results, a secondary analysis using identical nonlinear parameters but differing initial conditions revealed inconsistencies between computational runs. For Run 1, the first Fourier coefficient X_{1S} in β_{1C} was initialised with a value of 5×10^{-4}, whereas Run 2 employed 2×10^{-4}. These discrepancies demonstrate that the arclength parameter does not maintain a consistent relationship with the continuation process outputs. The implementation relies on random initial guesses until successful continuation initiation occurs, which introduces variability in the resulting bifurcation diagrams. Consequently, methodological refinements are required to ensure arclength-consistent results across independent computations.

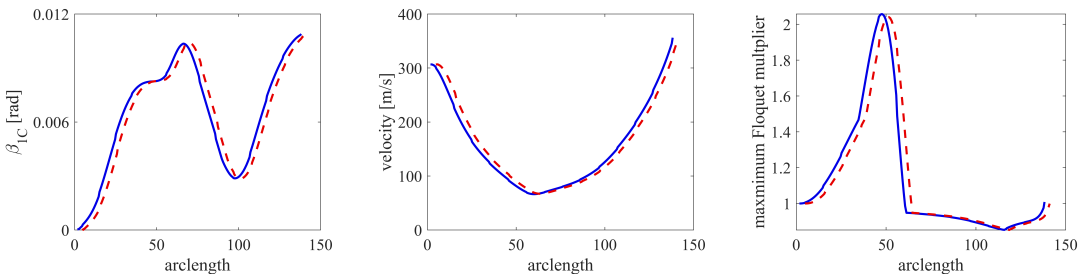

(a) (b) (c)

Figure 6.9: HBM framework outputs versus arcelngth with different initial conditions (– run 1) (– – run 2) (a) LCO amplitude, (b) Velocity, (c) Maximum Floquet multiplier

To address this issue, a spline interpolation procedure was implemented to normalise continuation runs over the complete arclength [207]. The raw dataset obtained from the continuation process is interpolated using cubic spline interpolation (spline, MATLAB [208]) across a specified number of uniformly spaced points. The pre-processing framework is presented in Figure 6.10. Beginning with the nonlinear parameter θ, a continuation analysis is performed, yielding the continuation parameter x, LCO amplitude y, Floquet multipliers ϕ (providing stability information), and arclength s. Each output is then interpolated with respect to arclength using n spline points.

These processed outputs are employed to train three distinct data-driven models,

each sharing the same inputs: the nonlinear parameter θ and splined arclength s. The models respectively predict x, y, and ϕ. The ensemble of these models constitutes a comprehensive framework capable of generating complete complex bifurcation diagrams, including stability information, for given inputs of θ and s.

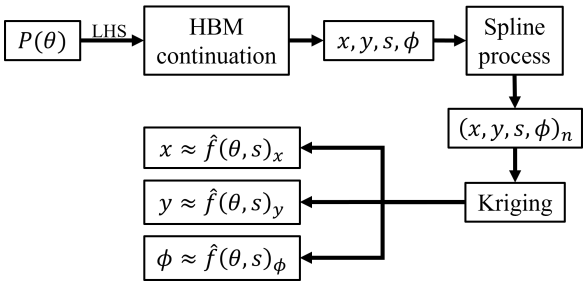

Figure 6.10: Updated method of data-driven model development from Chapter 4

Figure 6.11 demonstrates the approach, where the output parameters are interpolated across 50 equally spaced points along the normalised arclength. The results show that this processing method successfully eliminates discrepancies between runs 1 and 2, despite their differences in raw arclength values. The original datasets consisted of 223 and 238 points for Run 1 and Run 2 (Figure 6.9), respectively, obtained during the continuation process. Following post-processing, both datasets were reduced to 50 points while preserving the essential features of the bifurcation diagrams (Figure 6.11). This establishes the fundamental pre-processing methodology that will be applied prior to training the data-driven models.

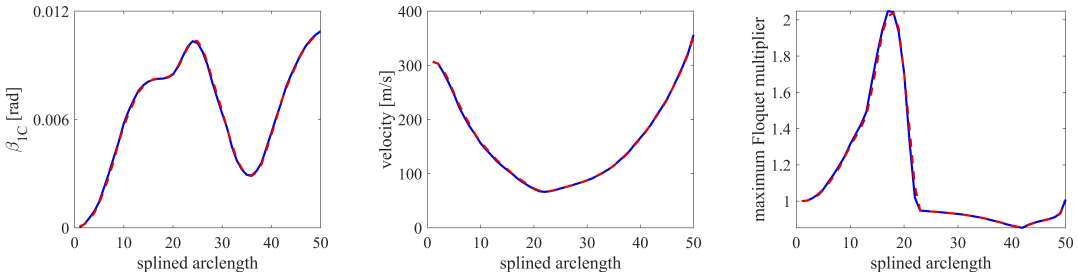

(a) (b) (c)

Figure 6.11: Processed HBM framework outputs with different initial conditions (– run 1) (–– run 2) (a) LCO amplitude, (b) Velocity, (c) Maximum Floquet multiplier

The final consideration for the new data-driven modelling methodology is the quan-

tification of uncertainty in multi-output systems, as opposed to single-output cases. This is addressed by treating the standard deviations of the model outputs for x and y as the semi-major and semi-minor axes of an uncertainty ellipse centred at the mean estimates of x and y. This approach provides a unified representation of epistemic uncertainty for individual predictions on the bifurcation diagram.

For Bayesian UQ with probabilistic inputs θ, the p-box method from previous sections is adapted. The uncertainties in x and y are evaluated separately and then combined to construct an ellipse that encapsulates the full polymorphic uncertainty. The ellipse's colour is mapped to the proportion of the Floquet multiplier (ϕ) output indicating stability, providing immediate visual feedback on dynamic stability.

With this enhanced framework for data-driven model development in complex nonlinear systems, robust results can now be obtained for the high-fidelity case study.

6.5 Pseudo Data

Due to the unavailability of experimental LCO data for tiltrotor systems, pseudo-data were generated to emulate the characteristic behaviour of CBC experimental data from previous case studies. Two distinct data sets were developed to investigate different aspects of the system's behaviour. Gaussian white noise ($\sigma = 5\%$ of signal amplitude) was superimposed on both synthetic datasets to validate the framework's noise tolerance under experimentally representative conditions.

The first data set aims to evaluate the methodology's performance with complex bifurcation diagram shapes. As evident from Figure 6.5, the bifurcation diagrams associated with β_{1C} exhibit the most intricate patterns, making them particularly suitable for testing the framework's capabilities. However, in practical wind tunnel experiments, β_{1C} (representing the pitch tilt of the rotor plane) may not be the most accessible measurement.

For the second data set therefore, a more experimentally realistic quantity was considered: the vertical deflection of the wing at the tip along the flexural axis [209]. This output can be simply calculated using Equation 6.1.

Table 6.2: Nonlinear parameter inputs for pseudo data

Dataset	$K_{\beta 2}$	$K_{\beta 2}$
1	-31.32	590.6
2	-20.04	379.0

The random input parameters used to generate both data sets are presented in Table 6.2. To prevent potential bias, these parameters remained undisclosed until completion of the final results analysis. For each parameter set, continuation runs were performed, from which six random points (emulating CBC data from Figure 4.6) were selected as illustrated in Figure 6.12.

As previously mentioned, to simulate realistic experimental conditions, 5% random noise was introduced to both the velocity and amplitude measurements. These two data sets exemplify the types of input the proposed framework is designed to process, representing the limited information (only the points shown in Figure 6.12) that would be available to an end user, including the stability information but not the value of the Floquet multipliers.

With these pseudo-data sets established, the framework can now be rigorously tested using the high-fidelity case study. This evaluation will assess its performance on both: (1) highly complex bifurcation curves, and (2) data emulating real-world experimental measurements.

6.6 Results: Pseudo Data 1

In the following section, a sensitivity analysis to validate the novel data-driven modelling methodology is conducted. Subsequently, application of the three model-updating frameworks introduced in the preceding chapter to the first pseudo-data set is carried out. The efficiency of each approach will then be evaluated through systematic comparison of the results.

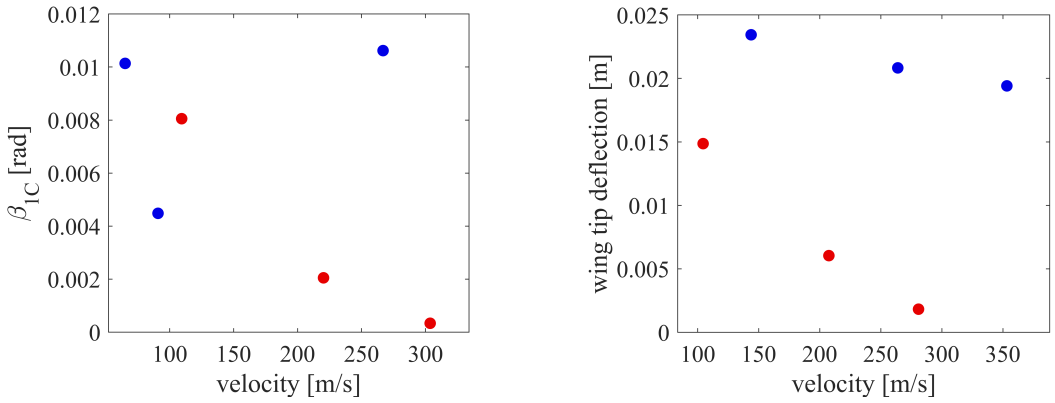

Figure 6.12: Pseudo data generated with data in Table 6.2 to emulate CBC data (• stable LCO) (• unstable LCO) (a) Dataset 1, (b) Dataset 2

6.6.1 Data-Driven Model Sensitivity Study

Prior to result acquisition, determination of the optimal number of spline points for training the data-driven model requires consideration. A uniform prior design space of $\pm 20\%$ around the nonlinear parameters from Dataset 1 in Table 6.2 was employed to train kriging models, with the mean accuracy of the three output models computed across a range of spline points and input continuation runs.

The results presented in Figure 6.13a demonstrate improved model accuracy with increasing training data, as anticipated. However, the analysis reveals diminishing returns beyond 50 spline points, with negligible improvements in accuracy. Figure 6.13b illustrates that while training time remains reasonable below 50 spline points, a substantial increase occurs beyond this threshold. This trade-off analysis between accuracy gains and computational cost leads to the selection of 50 spline points as the optimal value for this test case, providing satisfactory model performance without excessive training time.

6.6.2 Single-iteration Data-Driven BMU

The single-iteration approach was initially implemented using Pseudo-Data 1 (Figure 6.12a). Table 6.3 presents the input and output parameters of the process, with

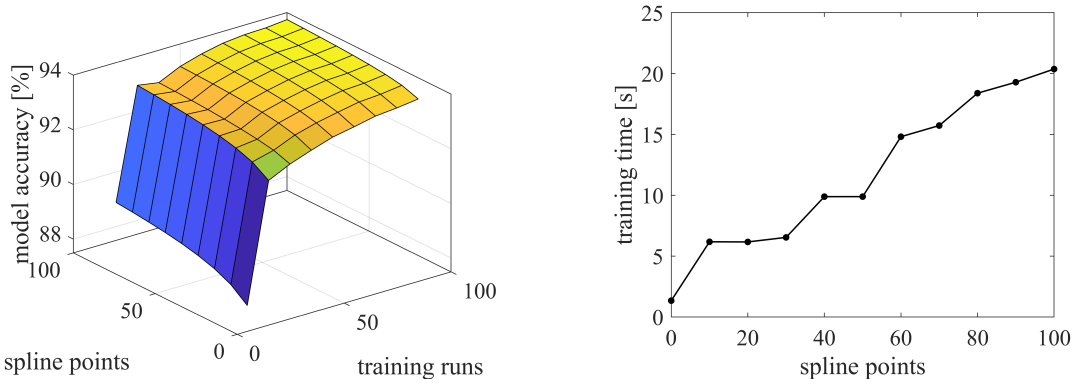

Figure 6.13: Data-driven model development investigation (a) Spline / training data sensitivity study, (b) Training time vs spline points with 60 training inputs

the uniform prior distribution matching that used to generate the random input parameters in Table 6.2. To achieve sufficient accuracy in the data-driven models, the prior space was partitioned into quadrants, as illustrated in Figure 6.14a. Four separate surrogate models were trained and subsequently combined into a unified model based on input parameters. Figure 6.14b demonstrates convergence of the mean RMS accuracy for the three output parameters (β_{1C}, V, and ϕ), resulting in a total training dataset of 500 samples.

Table 6.3: Data-driven model updating inputs and outputs pseudo data 1

	inputs					**outputs**					
	$P(\theta)^0$	N	σ_p	inc_0	$\mathscr{A}$	mean	COV	K_β accuracy	$\hat{f}$ accuracy	f runs	$\hat{f}$ runs
SDB	$K_{\beta 2}$: [-100, 0] $K_{\beta 3}$: $[0, 1e^3]$	1	$2.6e^{-3}rad$ $6.19m/s$	10	0.5%	$K_{\beta 2}$: $-31.63N/rad^2$ $K_{\beta 3}$: $643.8N/rad^3$	2.06% 3.37%	99.0% 91.0%	f_x:94.95% f_V:96.33% f_ϕ:90.24%	500	2000
IDB	$K_{\beta 2}$: [-100, 0] $K_{\beta 3}$: $[0, 1e^3]$	3	$2.6e^{-3}rad$ $6.19m/s$	10	2%	$K_{\beta 2}$: $-28.50N/rad^2$ $K_{\beta 3}$: $526.8N/rad^3$	4.24% 8.00%	91.0% 89.2%	f_x:97.50% f_V:97.88% f_ϕ:96.77%	234	4000
PIDB	$K_{\beta 2}$: [-100, 0] $K_{\beta 3}$: $[0, 1e^3]$	-	$2.6e^{-3}rad$ $6.19m/s$	10	2%	$K_{\beta 2}$: $-28.06N/rad^2$ $K_{\beta 3}$: $493.4N/rad^3$	1.58% 2.71%	89.6% 83.6%	f_x:98.46% f_V:98.45% f_ϕ:99.59%	294	4000

The estimated output parameters are presented in Figure 6.15 and summarised in Table 6.3. The single-iteration process achieves estimation accuracy exceeding 90% for

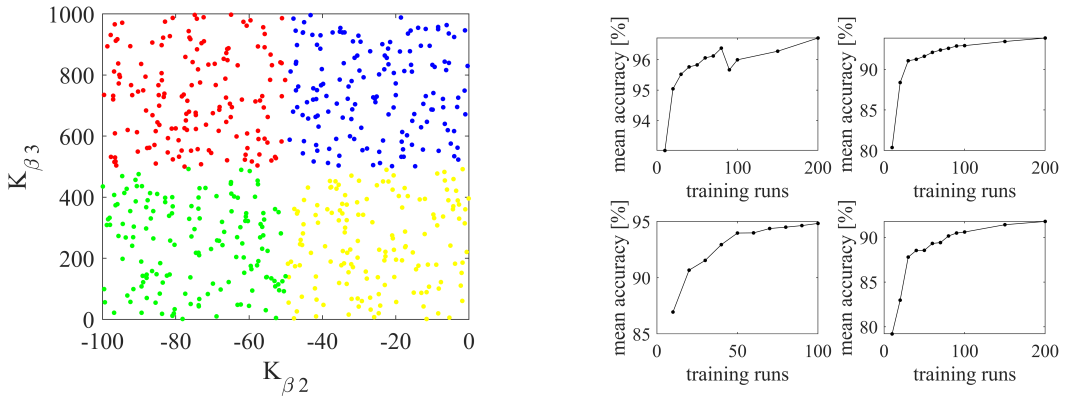

Figure 6.14: Single-iteration data-driven model training pseudo data 1 (a) Data, (b) Accuracy convergence

both nonlinear parameters, with particularly precise results for $K_{\beta 2}$. Analysis of the histograms in Figure 6.15b reveals that $K_{\beta 2}$ falls within the first standard deviation of the estimate, while $K_{\beta 3}$ lies marginally outside this range. However, parameter estimation accuracy should not be overemphasised, as the pseudo-data incorporates 5% random noise to emulate experimental conditions. In practical applications, where true parameter values are unknown, greater emphasis should be placed on: (1) the predictive accuracy of the data-driven models, and (2) their ability to capture the essential system behaviour.

The outputs of the three data-driven models, obtained from 1000 MCS of the posterior distribution, are presented in Figure 6.16. "Real data" in this scenario is the data from the full bifurcation plot with no noise. For the amplitude model (Figure 6.16a), the updated methodology partially captures the complex bifurcation curve shape. The model successfully identifies all three stationary points, with the majority of the true curve lying within the 95% interval of probability. However, the first data point (relative to arclength) is less accurately represented compared to subsequent points. The velocity model results (Figure 6.16b) demonstrate that while the general trend is captured, approximately 40% of the true curve falls outside the interval of probability. Notably, only the fourth pseudo-data point lies beyond these bounds, indicating reasonable agreement with the available experimental data. Regarding stability prediction,

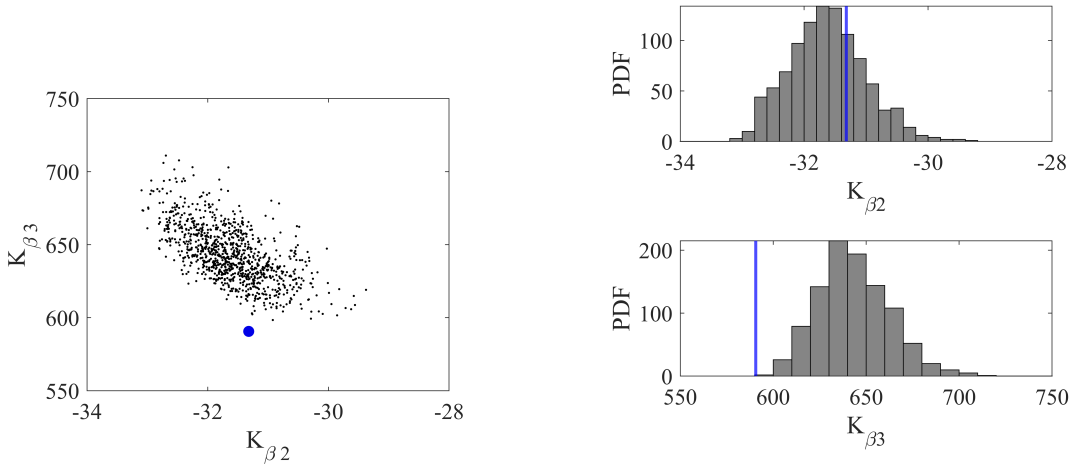

Figure 6.15: Single-iteration parameter estimates pseudo data 1 (a) Scatter plot, (b) Histogram (- real value)

the data-driven model correctly identifies the sharp stability transition observed in the reference data, but with a 5.22% underestimation of the transition point. Crucially, all pseudo-data points are correctly classified as stable or unstable, confirming the method's validity for stability prediction.

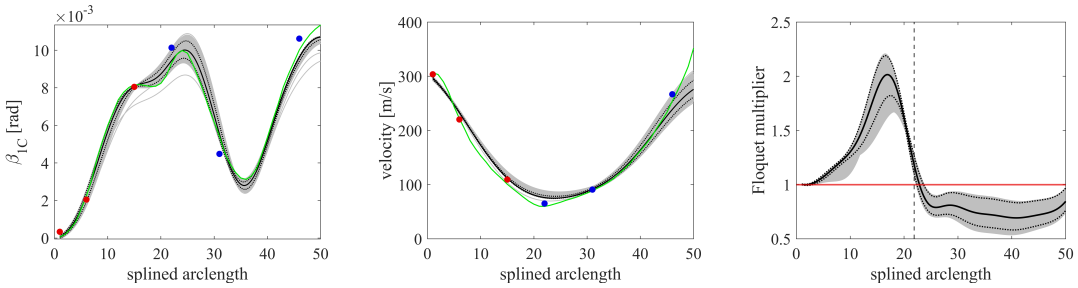

Figure 6.16: Single-iteration pseudo data 1 data-driven model output (• unstable LCO), (• stable LCO), (− mean model prediction) (■ 95% polymorphic interval of probability), (··· 95% aleatory interval of probability), (- real data) (a) LCO amplitude, (b) Velocity, (c) Stability plot (– real stability exchange)

The combined probabilistic response of the three data-driven models is presented in Figure 6.17. The results demonstrate a reasonable approximation of the nonlinear system behaviour, including partial capture of the self-intersecting curve topology at the

turning point. Two pseudo-data points fall outside the polymorphic interval of probability: (1) the lowest-amplitude unstable point, and (2) the stable point at minimal velocity. Despite this, the framework correctly classifies the stability of all experimental points, with a mean RMS error below 5% for the bifurcation curve shape. As presented in Table 6.4, the mean model accuracy of 93% establishes an upper bound on prediction probability. This suggests that while the methodology captures key nonlinear features, further refinement may be required for improved quantitative agreement.

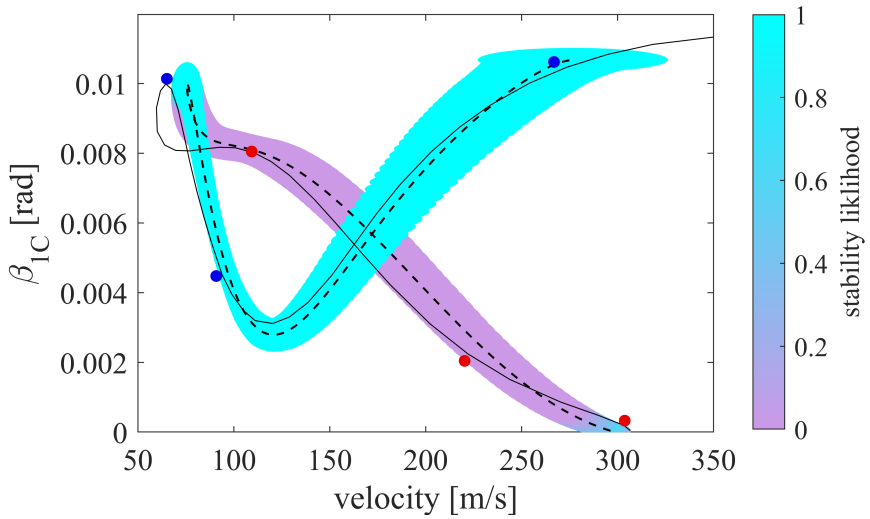

Figure 6.17: Single-iteration combined result pseudo data 1 (• unstable LCO), (• stable LCO), (−− mean prediction), (– real model)

6.6.3 Iterative Data-driven BMU

The inputs and outputs for the IDB process applied to Pseudo-Data 1 are summarised in Table 6.3. The analysis employed the same uniform prior distribution as previous studies, executed across three iterations. Parameter estimation accuracy, shown in Figure 6.18, demonstrates approximately 90% accuracy for each parameter - a marginal reduction compared to the single-iteration approach. Table 6.4 provides detailed output metrics for each iteration. Notably, while the true parameter value falls within the iteration 2 estimate histogram, it lies outside the iteration 3 distribution. The data-driven models exhibit progressive improvement, with iteration 3 achieving mean epistemic

uncertainty below the experimental noise threshold. The methodology demonstrates significant data efficiency, retaining over 50% of training data between iterations 2 and 3, ultimately requiring just 234 training runs for convergence.

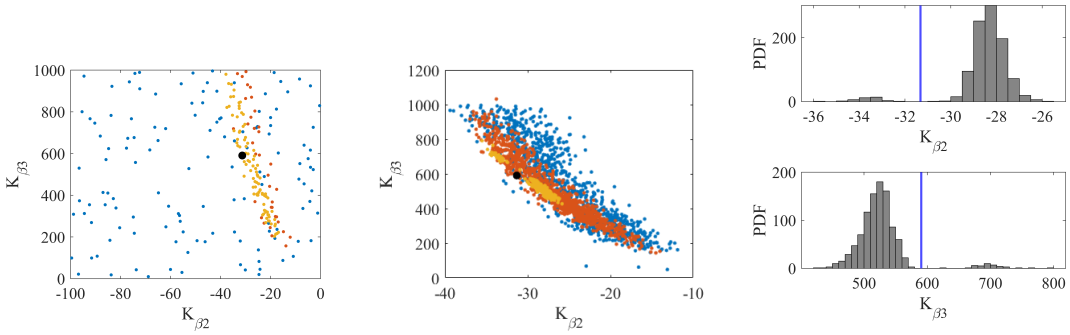

(a) (b) (c)

Figure 6.18: IDB parameter estimates pseudo data 1 (• iteration 1), (• iteration 2), (• iteration 3), (• real value) (a) training data, (b) Scatter plot, (c) Histogram (- real value)

The outputs of the three data-driven models, generated from 1000 MCS of the posterior distribution, are presented in Figure 6.19. For the amplitude model, the complete reference curve falls within the 95% interval of probability, with only the lowest-amplitude unstable point excluded. The velocity model demonstrates similar performance, successfully capturing both the reference curve and all pseudo-data points within the interval of probability. The stability analysis reveals a sharp transition that is underestimated by approximately 4%. Nevertheless, all pseudo-data points are correctly classified as either stable or unstable, confirming the model's predictive capability for stability assessment.

The complete combined response prediction is presented in Figure 6.20. The methodology successfully captures the complex bifurcation curve morphology, including accurate reproduction of the loop structure near the turning point. However, the final two stable data points fall outside the polymorphic interval of probability. Despite this discrepancy, the framework maintains correct classification accuracy for stability across all pseudo-data points.

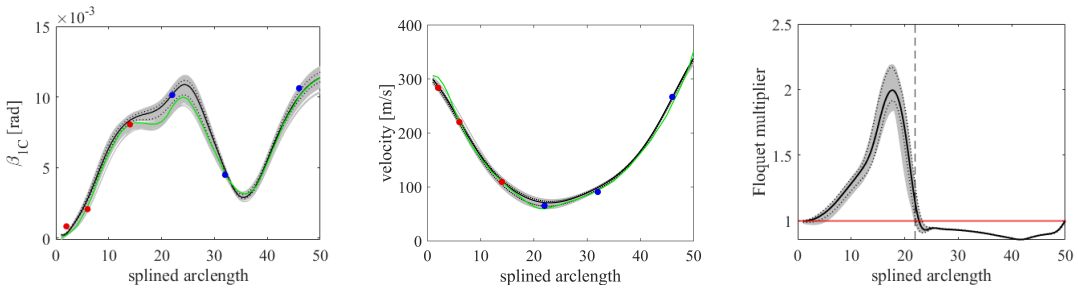

(a) (b) (c)

Figure 6.19: IDB pseudo data 1 data-driven model output (• unstable LCO), (• stable LCO), (– mean model prediction) (■ 95% polymorphic interval of probability), (· · · 95% aleatory interval of probability), (- real data) (a) LCO amplitude, (b) Velocity, (c) Stability plot (– real stability exchange)

Table 6.4: Pseudo data 1 iterative results

	Iteration	f runs / held	$\hat{f}$ accuracy	$\hat{f}$ std	σ_p^n	$K_{\beta 2}$ $[N/rad^2]$	$K_{\beta 3}$ $[N/rad^3]$
SDB	1	450 / 0	93.8%	11.41%	5%	-31.63 ± 0.65	643.8 ± 21.7
IDB	1	120 / 0	91.85%	14.02%	15%	-25.54 ± 5.41	550.6 ± 232.3
	2	80 / 11	96.50%	6.20%	10%	-27.06 ± 4.65	520.6 ± 178.7
	3	90 / 45	97.51%	3.60%	5%	-28.49 ± 1.21	526.8 ± 42.2
PIDB	1	120 / 0	91.85%	14.02%	14.02%	-25.41 ± 4.41	517.3 ± 179.7
	2	90 / 5	96.2%	5.02%	4.02%	-28.06 ± 1.98	520.4 ± 66.4
	3	100 / 11	98.84%	2%	5%	-28.06 ± 0.44	493.5 ± 13.4

6.6.4 Polymorphic Iterative Data-driven BMU

The PIDB process was subsequently applied to the experimental data, with inputs and outputs detailed in Table 6.3, achieving convergence within three iterations. The final-iteration data-driven models demonstrate high accuracy, as evidenced by the relatively low COV in parameter estimates. However, the mean parameter prediction accuracy is below 90% for both cases. Figure 6.21 reveals that while the true parameter value falls within the iteration 2 estimate histogram, it lies outside the iteration 3 distribution. Analysis of the training data in Figure 6.21a indicates that the parameter space surrounding the true value is adequately sampled across all training iterations. The combination of high model accuracy with parameter estimation discrepancies suggests

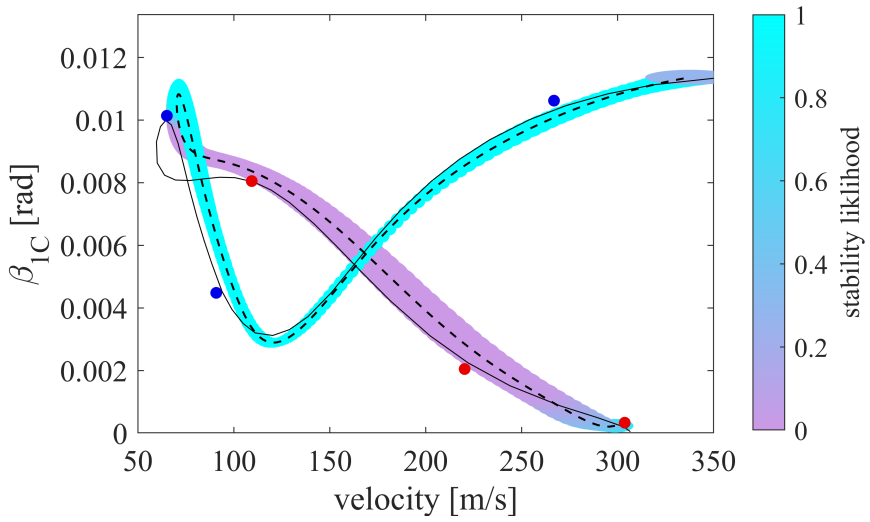

Figure 6.20: IDB combined result pseudo data 1 (• unstable LCO), (• stable LCO), (−− mean prediction), (– real data)

that the introduced noise (5%) may have significantly influenced the results. This implies that the estimated parameters may represent an alternative solution consistent with the noisy pseudo-data, rather than matching the original noise-free parameters.

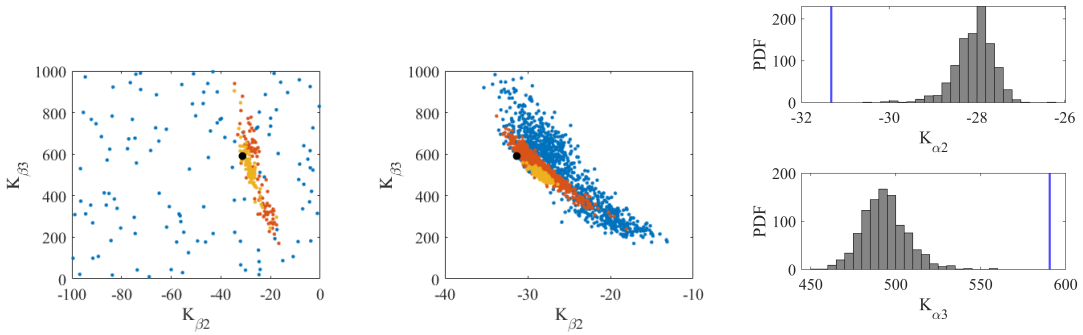

(a) (b) (c)

Figure 6.21: PIDB parameter estimates pseudo data 1 (• iteration 1), (• iteration 2), (• iteration 3), (• real value) (a) training data, (b) Scatter plot, (c) Histogram (- real value)

The probabilistic outputs for each data-driven model are shown in Figure 6.22. For amplitude prediction, the full reference curve remains within the 95% interval of probability, though two pseudo-data points fall outside: (1) the minimum amplitude point and (2) the second stable point by arclength. The velocity model performs well,

with both the reference curve and all pseudo-data points contained within the interval of probability. The stability prediction shows good agreement, capturing the stability transition within 1% of the reference value.

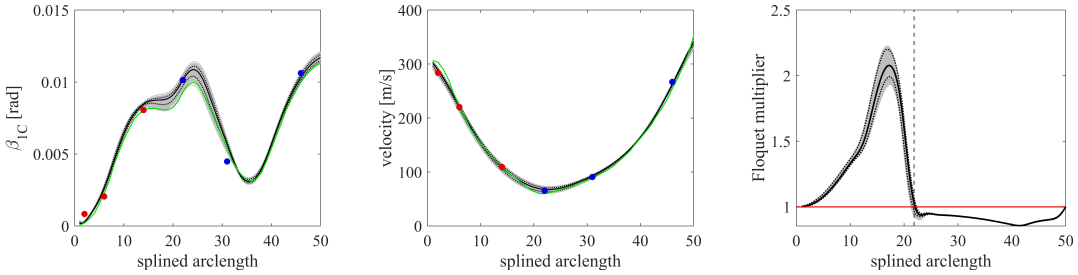

(a) (b) (c)

Figure 6.22: PIDB pseudo data 1 data-driven model output (• unstable LCO), (• stable LCO), (− mean model prediction) (■ 95% polymorphic interval of probability), (· · · 95% aleatory interval of probability), (- real data) (a) LCO amplitude, (b) Velocity, (c) Stability plot (– real stability exchange)

The combined probabilistic prediction is presented in Figure 6.23. The methodology successfully reproduces the characteristic looping morphology of the bifurcation curve, with only the lowest-amplitude stable point falling outside the 95% interval of probability. All pseudo-data points are correctly classified with respect to stability throughout the parameter range.

6.6.5 Comparison of Methods

A comparative analysis of the methodologies yields several conclusions regarding parameter estimation and nonlinear behaviour prediction. Figure 6.24 and Table 6.3 present the parameter estimation results. The single-iteration approach provides the closest approximation to the true parameter values, particularly for $K_{\beta 2}$, being the only method to include the true value within its histogram. While it also yields the best mean estimate for $K_{\beta 3}$, none of the methods capture this parameter within their histograms. The PIDB process produces estimates with the greatest deviation from the true values, yet achieves the lowest COV. These results might suggest superior performance of the single-iteration method, but experimental contexts lack known true values. The optimal method is instead determined by best fit to experimental data,

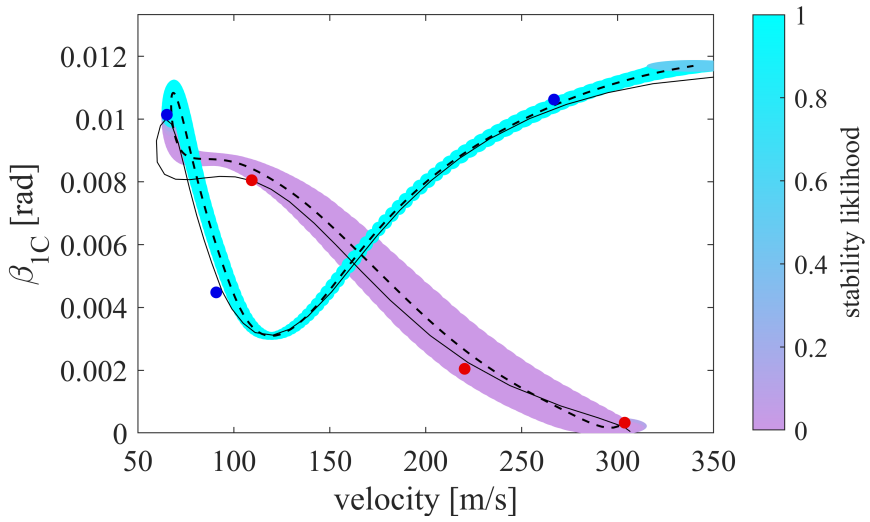

Figure 6.23: PIDB combined result pseudo data 1 (• unstable LCO), (• stable LCO), (−− mean prediction), (– real data)

where noise may influence parameter estimates. Table 6.3 shows that the PIDB method generates the most accurate data-driven models, warranting higher probability in its predictions than the single-iteration approach. The most reliable performance metric remains the method's ability to predict the observed behaviour relative to the pseudo-data.

The RMS errors relative to the mean prediction in the bifurcation curve is presented in Figure 6.25. It is clear from these results that the PIDB process gives the closest mean prediction compared the pseudo data for both amplitude and velocity. The single-iteration method also performs the least effective and the IDB in the middle. This result may seem surprising at the single-iteration method captured more pseduo data within its interval of probability than the IDB result. This is likely due to the larger variance in the model outputs form the data-driven models in the single-iteration process as shown in Table 6.3 where the two iterative processes have better precision and accuracy in data-driven model predictions.

An analysis of computational efficiency, based on training runs detailed in Table 6.4, reveals that the IDB process achieves a 53% reduction in required training data compared to the single-iteration approach. The PIDB process demonstrates a 51% reduc-

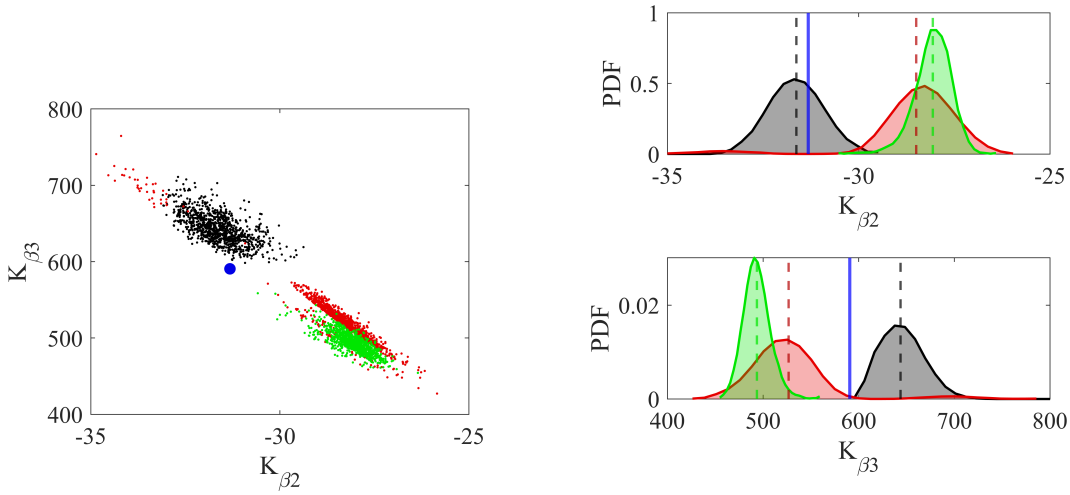

Figure 6.24: Parameter estimate method comparison (■ SDB), (■ IDB), (■ PIDB), (■ real parameter): (a) Scatter plot, (b) Histogram

tion relative to the single-iteration baseline. The superior data efficiency of IDB stems from its higher inter-iteration data retention, as evidenced in Table 6.4. This advantage emerges from the σ_p^n parameter behaviour across iterations - the PIDB process exhibits sharper reductions in the parameter space coverage during training. These reductions correlate directly with the decreasing variation in data-driven model outputs between iterations, representing an inherent characteristic of the methodology.

The comparative analysis reveals distinct advantages for each methodology across different performance metrics. The single-iteration approach demonstrates superior accuracy in parameter estimation relative to the reference values. For bifurcation diagram prediction, the PIDB method yields the best agreement with the target behaviour. When prioritising agreement with experimental data - the most critical criterion - the PIDB process emerges as the optimal choice, providing both the most accurate behavioural predictions and a 41% reduction in training data requirements compared to the single-iteration approach. For pure computational efficiency, the IDB method offers the most significant savings. A more comprehensive evaluation of method performance will require additional test cases to verify these observations across different system configurations.

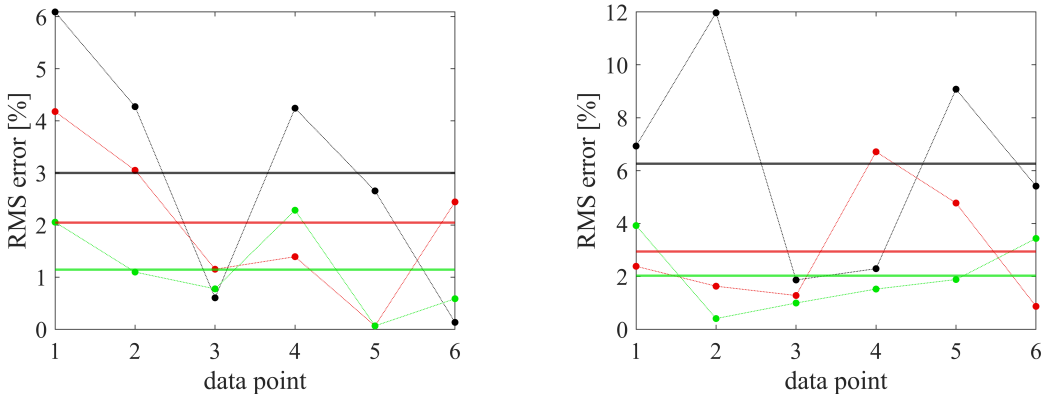

Figure 6.25: Accuracy comparison of data driven model updating method with dataset 1 (■ SDB), (■ IDB), (■ PIDB): (a) Mean LCO amplitude prediction, (b) Mean velocity prediction

6.6.6 Noise Free Experiemnt

To evaluate the framework performance under idealised conditions, the analysis was repeated using noise-free pseudo-data while maintaining consistent input parameters (Table 6.3). The resulting outputs, presented in Table 6.5, demonstrate the capability of each methodology without the effects of measurement noise.

Table 6.5: Data-driven model updating outputs pseudo data 1 with no noise

	mean	COV	K_β accuracy	$\hat{f}$ accuracy	f runs	$\hat{f}$ runs
SDB	$K_{\beta 2}$: -31.43N/rad^2	1.56%	99.6%	f_x:94.95%	800	2000
	$K_{\beta 3}$: 641.7N/rad^3	2.16%	91.3%	f_V:96.33%		
				f_ϕ:90.24%		
IDB	$K_{\beta 2}$: -32.05N/rad^2	2.46%	97.7%	f_x:98.04%	251	4000
	$K_{\beta 3}$: 627.5N/rad^3	4.28%	93.7%	f_V:98.02%		
				f_ϕ:98.12%		
PIDB	$K_{\beta 2}$: -30.18N/rad^2	2.10%	96.4%	f_x:98.45%	250	4000
	$K_{\beta 3}$: 565.2N/rad^3	4.17%	95.7%	f_V:98.23%		
				f_ϕ:98.20%		

It is observed that the SDB process demonstrates the highest accuracy in predicting $K_{\beta 2}$, but performs poorest for $K_{\beta 3}$. In both cases, it also exhibits the lowest variance in its predictions, whereas the IDB process shows the highest variability. Although SDB yields a highly accurate estimate for $K_{\beta 2}$, its overall mean accuracy is the lowest among the three methods at 95.45%. In comparison, IDB and PIDB achieve slightly higher mean accuracies of 95.70% and 96.05%, respectively.

This trend is illustrated in Figure 6.26, where the true parameter value lies within the histograms for IDB and PIDB across both parameters, while for SDB it only falls within the histogram for $K_{\beta 2}$. The scatter plots further support this observation: for IDB and PIDB, the true parameter value lies within the two-dimensional interval of probability, whereas in the case of SDB, it falls outside this region.

These findings suggest that, despite the exceptional performance of SDB in estimating $K_{\beta 2}$, the iterative approaches offer more reliable overall parameter estimates. Given its higher mean accuracy and lower variance, the PIDB process appears to provide the most robust and consistent parameter estimation among the methods considered.

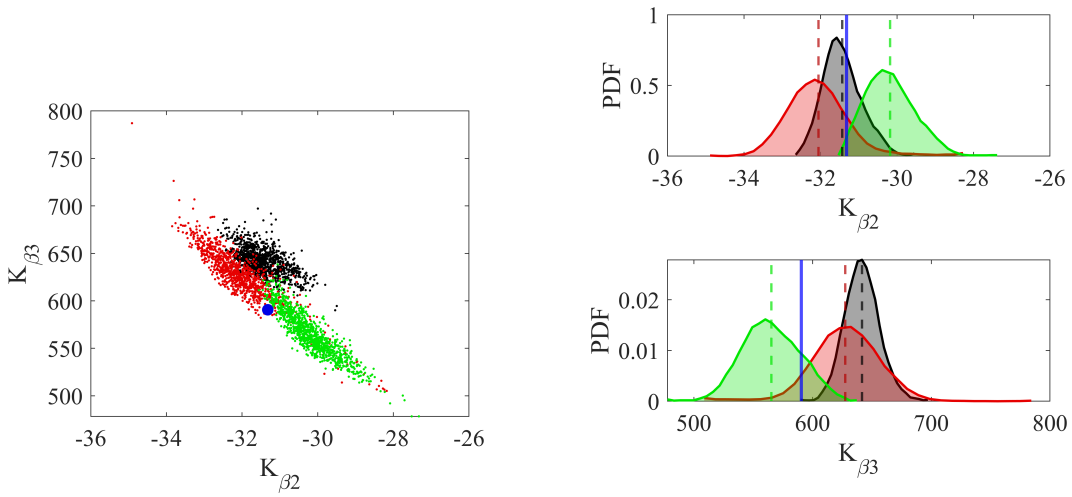

Figure 6.26: Parameter estimate method comparison with no noise (■ SDB), (■ IDB), (■ PIDB), (■ real parameter): (a) Scatter plot, (b) Histogram

When evaluating the accuracy of the data-driven models, the results under noisy conditions lead to the same conclusion as in the noise-free case. The SDB process

yields the least accurate models and exhibits the highest variability, whereas the PIDB process outperforms the others in both accuracy and consistency.

In terms of training data requirements, the iterative approaches offer even greater data reduction compared to the noise-free scenario, achieving up to a 68% reduction. Although there is only a single training run difference between IDB and PIDB, the latter performs marginally better. Therefore, in the context of data-driven model development, considering both predictive accuracy and data efficiency, the PIDB process provides the best overall performance, while SDB performs the worst.

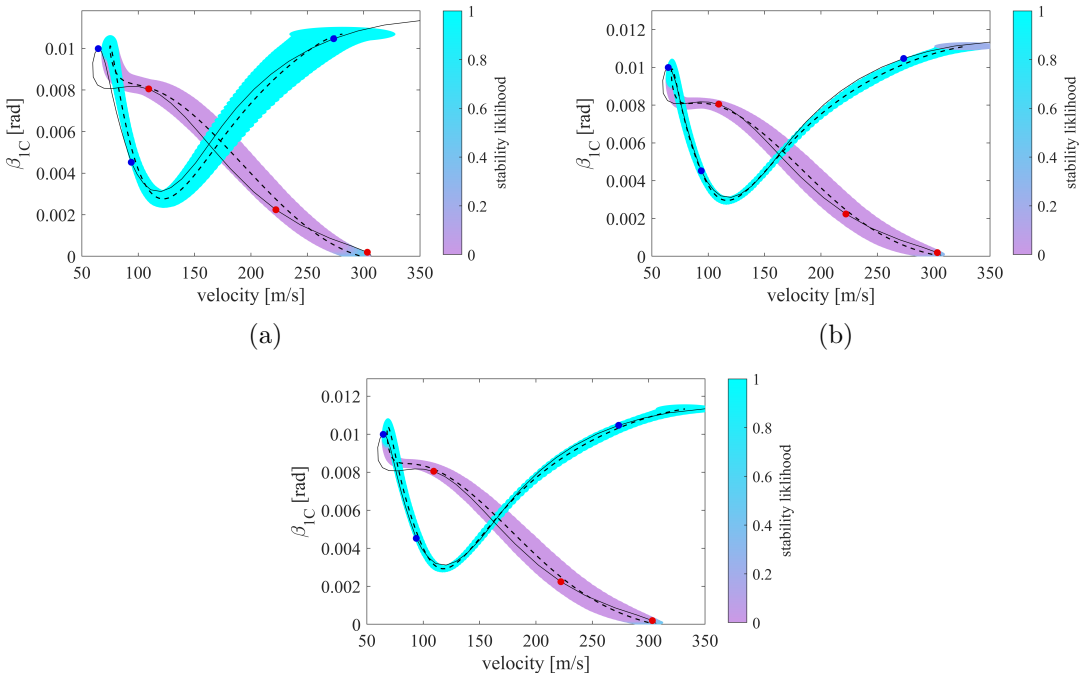

Figure 6.27: Combined result pseudo data 1 with no noise (• unstable LCO), (• stable LCO), (−− mean prediction), (– real data): (a) SDB, (b) IDB, (c) PIDB)

The combined behaviour prediction results are presented in Figure 6.27. It is observed that for each of the iterative processes, all data points are captured within relatively narrow intervals of probability. In contrast, the SDB plot shows wider intervals of probability, and notably, the data point at the lowest velocity is not captured. When examining stability, it is correctly predicted in all cases.

The mean accuracy relative to each data point is shown in Figure 6.28. It can

be seen that, for both amplitude and velocity predictions, the SDB process exhibits the lowest accuracy. For the LCO amplitude prediction, the PIDB process performs the best. In the case of velocity prediction, IDB marginally outperforms the others. Considering overall accuracy, the PIDB process provides the most accurate estimation of the data points.

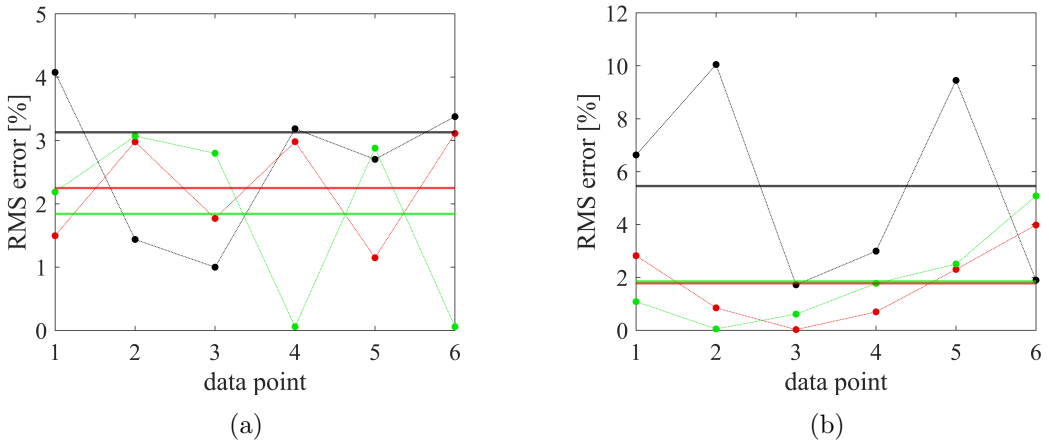

Figure 6.28: Accuracy comparison of data driven model updating method with dataset 1 with no noise (■ SDB), (■ IDB), (■ PIDB): (a) Mean LCO amplitude estimation, (b) Mean velocity estimation

Considering all aspects of the noise-free results, it is evident that the iterative processes outperform the single-iteration approach, with the PIDB process offering marginally better performance than IDB. Comparing this outcome with the noisy case—where SDB provided the most accurate parameter estimates but the poorest behavioural predictions—suggests that the presence of noise significantly influences the determination of the optimal parameter estimates.

Overall, for the first set of pseudo-experimental data, the iterative processes have demonstrated superior performance and are clearly the preferred approach. Even in the absence of measurement noise, the parameter estimation exhibited residual errors, failing to fully capture the complex morphological features of the system response.

6.7 Results: Pseudo Data 2

The three approaches are now applied to Dataset 2 (Figure 6.12b), generated using the parameters specified in Table 6.2. This dataset emulates experimental measurements that would typically be obtained from wind tunnel testing of a tiltrotor system, specifically capturing wingtip deflection characteristics.

6.7.1 Single-Iteration Data-Driven BMU

The single-iteration approach was first applied to Dataset 2, with the framework inputs and outputs presented in Table 6.6. Given the simpler bifurcation curve morphology in this test case, the uniform prior distribution boundaries were doubled compared to the Pseudo-Data 1 case to provide a more rigorous evaluation of the framework's robustness. The input parameter σ_p was maintained at 5% of the mean values for both velocity and LCO amplitude.

Table 6.6: Data-driven model updating inputs and outputs pseudo data 2

	inputs					**outputs**					
	$P(\theta)^0$	N	σ_p	inc_0	$\mathscr{A}$	mean	COV	K_β accuracy	$\hat{f}$ accuracy	f runs	$\hat{f}$ runs
SDB	$K_{\beta 2}$: [-100, 100] $K_{\beta 3}$: [-$1e^3$, $1e^3$]	1	6.19m/s $1e^{-3}m$	10	0.5%	$K_{\beta 2}$: -15.31N/rad^2 $K_{\beta 3}$: 269.2N/rad^3	5.58% 7.12%	76.4% 71.0%	f_x:91.21% f_V:93.17% f_ϕ:87.76%	800	2000
IDB	$K_{\beta 2}$: [-100, 100] $K_{\beta 3}$: [-$1e^3$, $1e^3$]	3	6.19m/s $1e^{-3}m$	10	2.0%	$K_{\beta 2}$: -18.42N/rad^2 $K_{\beta 3}$: 334.9N/rad^3	6.53% 8.53%	91.9% 88.3%	f_x:98.72% f_V:98.52% f_ϕ:97.89%	226	4000
PIDB	$K_{\beta 2}$: [-100, 100] $K_{\beta 3}$: [-$1e^3$, $1e^3$]	-	6.19m/s $1e^{-3}m$	10	2.0%	$K_{\beta 2}$: -19.80N/rad^2 $K_{\beta 3}$: 359.2N/rad^3	6.16% 7.79%	98.8% 94.8%	f_x:98.85% f_V:99.32% f_ϕ:98.64%	290	5000

The parameter estimation results, shown in Figure 6.29, demonstrate limited accuracy with respect to the reference values, achieving less than 77% for both parameters. Notably, the true parameter values fall outside the estimated histograms. The data-driven models exhibit a mean accuracy of 90.71%, with a substantial variation of 11.16%, indicating reduced probability in the prediction reliability for this test case.

The probabilistic response of each data-driven model, obtained from 1000 MCS of the parameter estimates, is presented in Figure 6.30. For LCO amplitude predic-

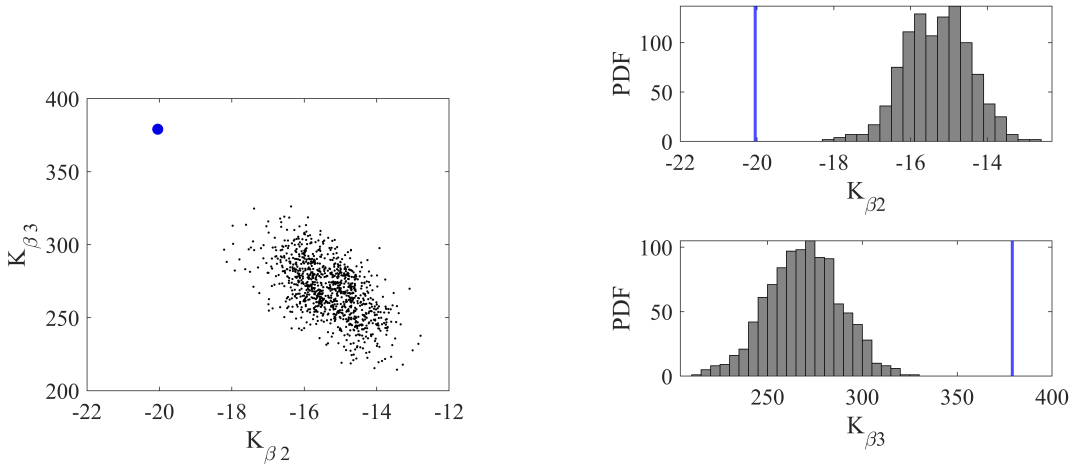

(a) (b)

Figure 6.29: Single-iteration parameter estimates pseudo data 2 (a) Scatter plot, (b) Histogram (- real value)

tion, the model captures the majority of the reference curve within the 95% interval of probability, with deviations occurring only near the peak amplitude region. Only the highest-amplitude pseudo-data point falls outside these bounds. The velocity predictions show less agreement, with approximately 25% of the reference curve and only one pseudo-data point contained within the interval of probability. Stability analysis reveals low uncertainty prior to the stability transition, but excessively wide intervals of probability emerge in the stable regime, suggesting inadequate model training in this region. The predicted stability transition point underestimates the true value by 14.5%.

The combined behavioural prediction is presented in Figure 6.31. The results demonstrate significant discrepancies from the expected response, capturing only the two lowest-amplitude data points. The model fails to reproduce the fundamental trend of the experimental data, and erroneously predicts unstable LCO in the upper amplitude range - a feature unsupported by the experimental observations. While these results indicate substantial limitations in the current implementation, a comprehensive assessment requires direct comparison with alternative methodologies.

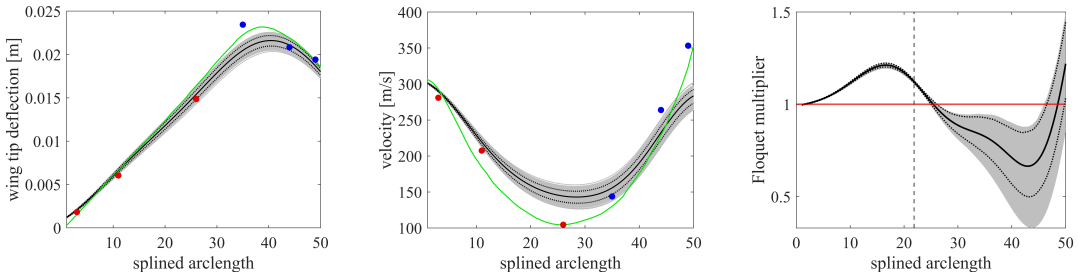

(a) (b) (c)

Figure 6.30: Single-iteration pseudo data 2 data-driven model output (• unstable LCO), (• stable LCO), (− mean model prediction) (■ 95% polymorphic interval of probability), (··· 95% aleatory interval of probability), (- real data) (a) LCO amplitude, (b) Velocity, (c) Stability plot (– real stability exchange)

Table 6.7: Pseudo data 2 iterative results

	Iteration	f runs / held	$\hat{f}$ accuracy	$\hat{f}$ std	σ_p^n	$K_{\beta 2}$ $[N/rad^2]$	$K_{\beta 3}$ $[N/rad^3]$
SDB	1	800 / 0	90.71%	11.16%	5%	-15.31±0.85	269.2±19.2
IDB	1	120 / 0	71.57%	33.89%	15%	-16.38±2.83	332.4±66.0
	2	80 / 4	95.85%	8.75%	10%	-17.68±1.90	325.6±43.6
	3	90 / 60	98.04%	3.16%	5%	-18.43±1.20	334.9±28.5
PIDB	1	120 / 0	71.57%	33.89%	33.89%	-16.53±5.28	351.9±137.3
	2	70 / 5	93.47%	10.39%	10.39%	-18.98±3.43	348.2±99.2
	3	100 / 15	96.98%	5.45%	5.45%	-19.51±1.91	353.4±43.6
	4	70 / 50	98.94%	2.07%	5%	-19.80±1.22	359.2±27.9

6.7.2 Iterative Data-driven BMU

The IDB process was implemented using the parameters specified in Table 6.6, with all inputs held constant except for the parameter a. The analysis proceeded through three iterations. Figure 6.32 shows that the parameter estimation accuracy improves relative to the single-iteration approach, with the true values contained within both the estimated histograms and training data regions for both parameters. Table 6.7 reveals that the final iteration achieves a mean variation in the data-driven models below the pseudo-data noise threshold. Consistent with the first pseudo-data study, the IDB process maintains high data retention between iterations, preserving 75% of

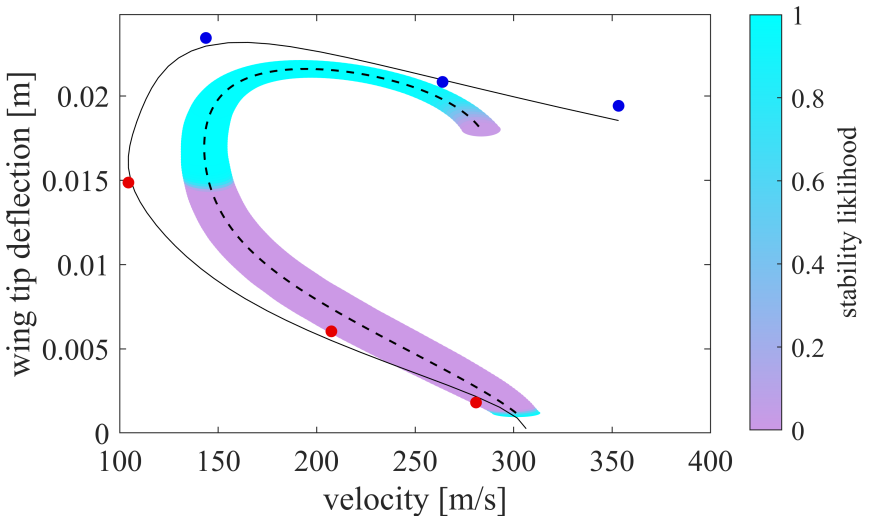

Figure 6.31: Single-iteration combined result pseudo data 2 (• unstable LCO), (• stable LCO), (−− mean prediction), (– real data)

training data between iterations 2 and 3. This characteristic contributes to the method's computational efficiency while maintaining prediction accuracy.

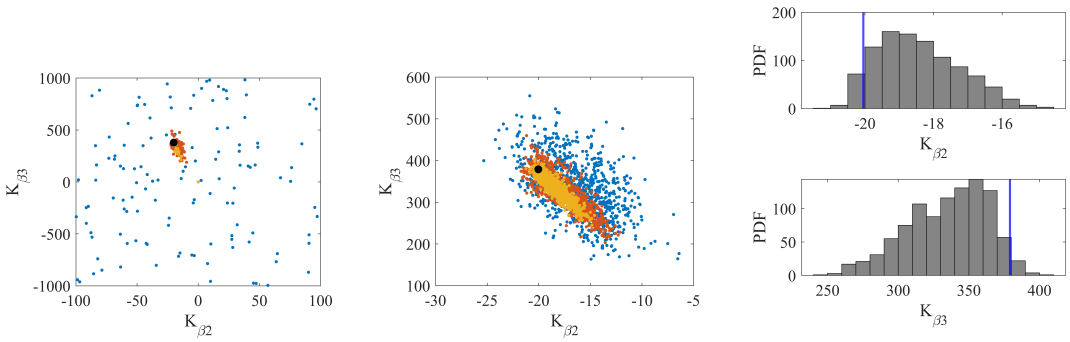

(a) (b) (c)

Figure 6.32: IDB parameter estimates pseudo data 2 (• iteration 1), (• iteration 2), (• iteration 3), (• real value) (a) training data, (b) Scatter plot, (c) Histogram (- real value)

The probabilistic outputs of the data-driven models, presented in Figure 6.33c, demonstrate strong agreement with the reference data. For amplitude prediction, both the complete reference curve and all pseudo-data points lie within the interval of probability throughout the parameter range. The velocity results show equally good agreement, with the entire reference curve and all experimental points captured within the

interval of probability, even in the latter portion where the interval of probability narrows. The stability analysis reveals a well-defined transition from unstable to stable behaviour, with the transition point predicted within 2% of the true value.

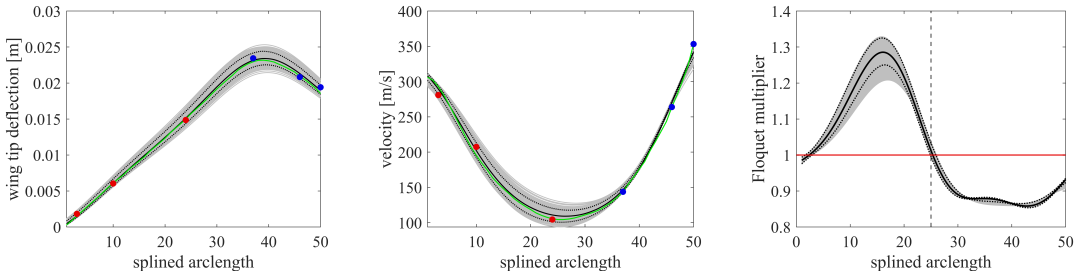

(a) (b) (c)

Figure 6.33: IDB pseudo data 2 data-driven model output (• unstable LCO), (• stable LCO), (− mean model prediction) (■ 95% polymorphic interval of probability), (· · · 95% aleatory interval of probability), (- real data) (a) LCO amplitude, (b) Velocity, (c) Stability plot (– real stability exchange)

The combined behavioural prediction is presented in Figure 6.34. The results demonstrate successful capture of all pseudo-data points within the interval of probability, along with correct stability classification for each point. With data-driven models achieving a mean accuracy of 98.04%, these predictions can be considered highly reliable. A minor discrepancy occurs at very low amplitudes, where the model erroneously predicts stable LCO. This anomaly likely stems from either: (1) inadequate training of the stability model in this region, or (2) insufficient training data coverage at low amplitudes.

6.7.3 Polymorphic Iterative Data-driven BMU

The inputs and outputs for the PIDB process are presented in Table 6.7, with inputs identical to the IDB case. Convergence required four iterations, as indicated in Table 6.7. At iteration 3, the data-driven model variation marginally exceeded the pseudo-data noise threshold. Parameter estimation accuracy improved relative to the reference values, particularly for $K_{\beta 2}$, which achieved high precision in mean prediction. Figure 6.35 shows the true parameter values positioned near the histogram centers for both parameters, confirming robust estimation. This alignment is also reflected in the

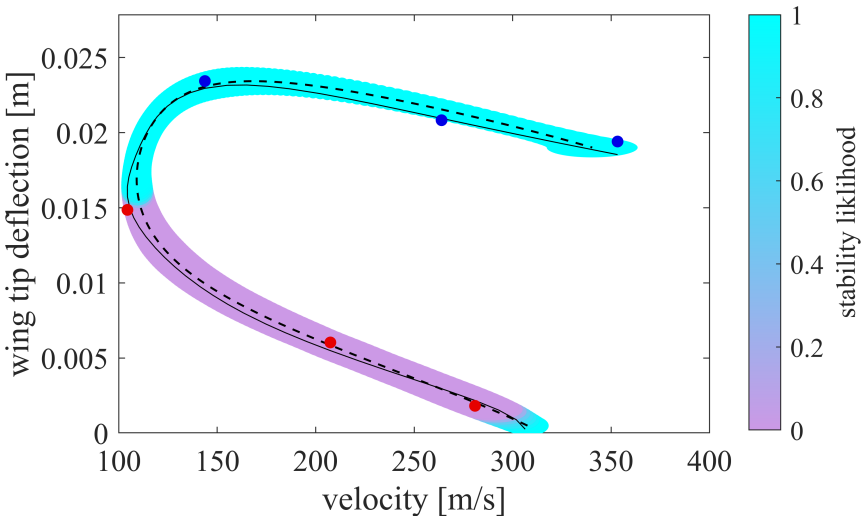

Figure 6.34: IDB combined result pseudo data 2 (• unstable LCO), (• stable LCO), (−− mean prediction), (– real data)

regions where training data were collected.

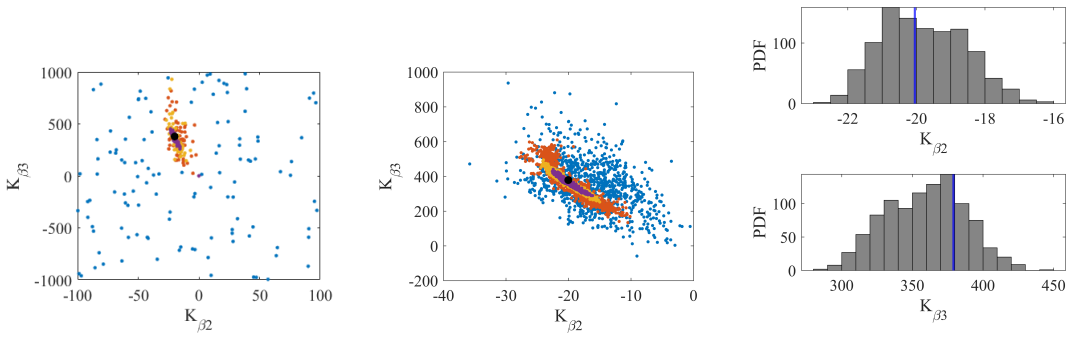

Figure 6.35: PIDB parameter estimates pseudo data 2 (• iteration 1), (• iteration 2), (• iteration 3), (• iteration 4), (• real value) (a) training data, (b) Scatter plot, (c) Histogram (- real value)

The probabilistic response outputs for each data-driven model are presented in Figure 6.36. The results demonstrate strong consistency with the IDB study findings. For both amplitude and velocity predictions, the complete reference curves fall within the 95% intervals of probability, with all pseudo-data points similarly captured. The stability model shows comparable performance, predicting the transition point within 2% of the reference value.

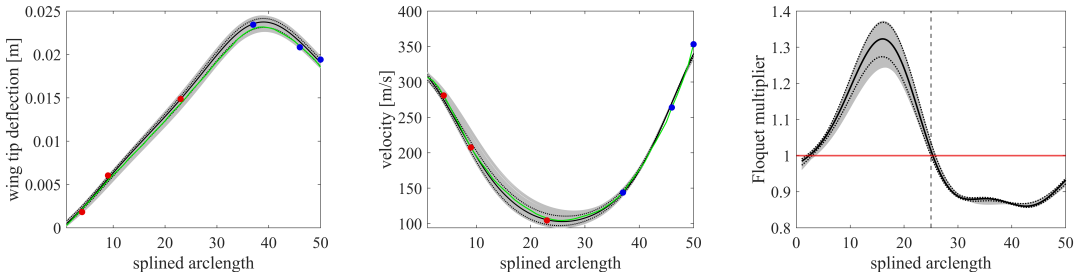

(a) (b) (c)

Figure 6.36: PIDB pseudo data 2 data-driven model output (• unstable LCO), (• stable LCO), (– mean model prediction) (■ 95% polymorphic interval of probability), (· · · 95% aleatory interval of probability), (- real data) (a) LCO amplitude, (b) Velocity, (c) Stability plot (– real stability exchange)

The combined probabilistic prediction is presented in Figure 6.37, demonstrating close agreement with the pseudo-data. All experimental points are captured within the interval of probability, including the penultimate arclength point which lies near the boundary. A consistent discrepancy appears at low amplitudes, where the model erroneously predicts stable LCO. This behaviour mirrors the IDB study results, suggesting a systematic limitation in the stability prediction for this regime.

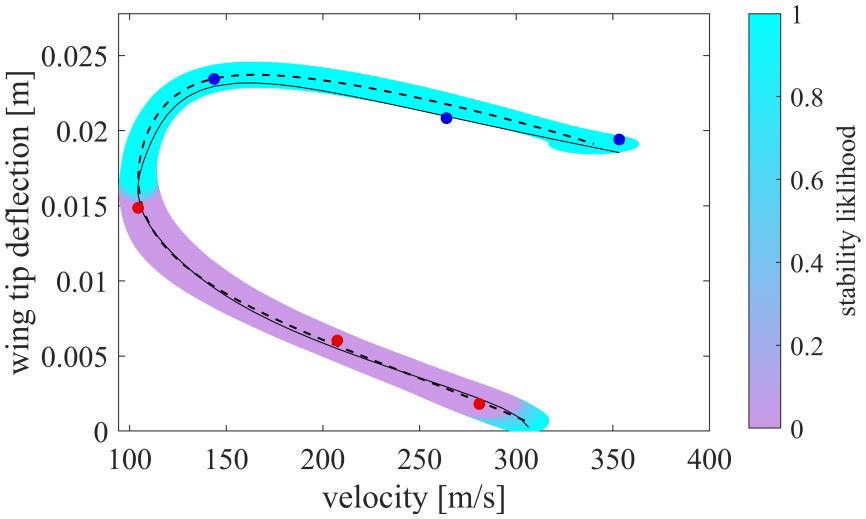

Figure 6.37: PIDB combined result pseudo data 2 (• unstable LCO), (• stable LCO), (–– mean prediction), (– real data)

6.7.4 Comparison

A direct comparison of the methodologies is presented, beginning with parameter estimation as shown in Figure 6.38. Both the IDB and PIDB methods capture the reference parameters within their estimated histograms, while the single-iteration approach fails to do so. The PIDB method yields superior mean parameter estimates, as evidenced by the accuracy metrics in Table 6.6. Notably, it is the only methodology achieving greater than 90% accuracy for both parameters. In contrast, the single-iteration approach produces the least accurate mean estimates. Regarding probability in predictions, the single-iteration method demonstrates the lowest COV for both parameters, while the IDB exhibits the highest COV. When considering all parameter estimation metrics collectively, the PIDB emerges as the most effective approach, combining high mean accuracy with improved prediction probability relative to the IDB method. However, as established in prior analyses, the primary evaluation criterion remains the accurate estimation of nonlinear system behaviour.

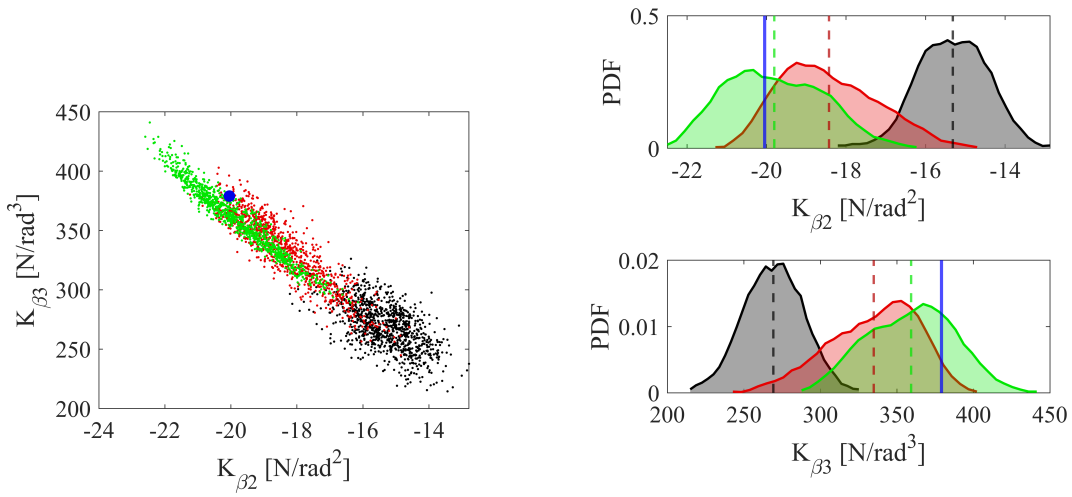

Figure 6.38: Parameter estimate method comparison (■ SDB), (■ IDB), (■ PIDB), (■ real parameter): (a) Scatter plot, (b) Histogram

An examination of the combined behaviour plots reveals that the single-iteration approach performs the least effective, capturing only two pseudo-data points within the interval of probability and failing to reproduce the overall bifurcation curve trend. This

is corroborated by the mean amplitude and velocity estimates in Figure 6.39, where the single-iteration method exhibits significantly larger errors than both the IDB and PIDB approaches for both output measures.

Comparing the IDB and PIDB methods proves more nuanced. Both methodologies successfully capture all pseudo-data points within their intervals of probability. While Figure 6.39 shows that the IDB yields marginally better amplitude estimates, it under-performs slightly in velocity prediction, resulting in comparable overall estimation quality between the two methods. However, Table 6.7 demonstrates that the PIDB method generates more accurate data-driven models with reduced variation. Consequently, although both methods produce similar behavioural estimates, the PIDB results warrant greater probability due to their improved model precision.

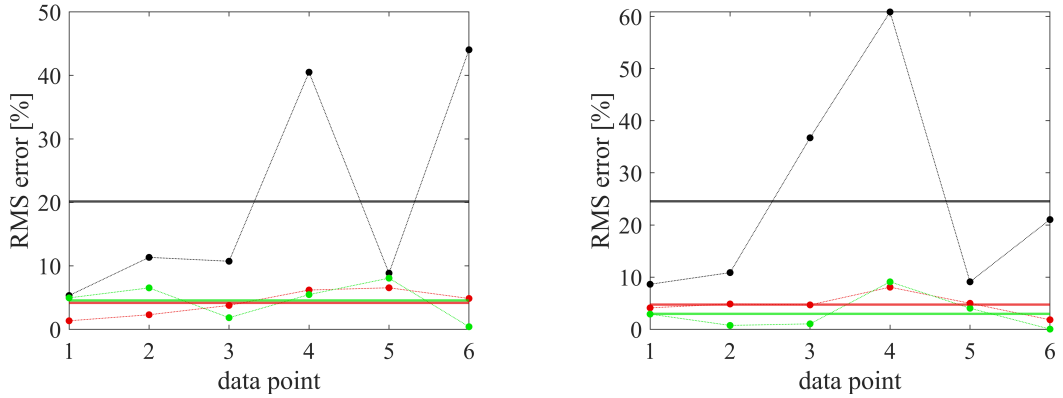

Figure 6.39: Accuracy comparison of data driven model updating method with dataset 2 (■ SDB), (■ IDB), (■ PIDB): (a) Mean LCO amplitude prediction, (b) Mean velocity prediction

The computational cost analysis yields results consistent with the previous case study. The single-iteration approach remains the most data-intensive, while the IDB method maintains its efficiency advantage with a 72% reduction in training data requirements. The PIDB approach offers a 64% reduction relative to the single-iteration baseline. This difference in data efficiency between IDB and PIDB can be attributed directly to the additional level of refinement in the PIDB process (4 iterations versus 3 in IDB), which necessitates additional model training and training data while providing

improved model accuracy as demonstrated in prior results.

The comparative analysis reveals no definitive superiority between methodologies in this study. Although the single-iteration approach consistently demonstrates inferior performance, selecting between the IDB and PIDB methods involves evaluating competing advantages. The PIDB method achieves greater accuracy in parameter estimation, while both methods produce comparable behavioural predictions, with PIDB offering marginally more reliable results. However, the IDB approach retains superior computational efficiency. When considering these trade-offs, the IDB method emerges as the preferable choice for applications where computational resources are constrained, despite the PIDB's slightly better parameter estimation performance.

6.8 Conclusions

This chapter has evaluated three data-driven BMU frameworks—SDB, IDB, and PIDB—through application to a high-fidelity tiltrotor aeroelastic case study. The investigation began with comprehensive deterministic analyses, including both linear eigenvalue studies and nonlinear time-domain simulations, to establish baseline behaviour. The HBM solution converged to time-domain accuracy within 8 harmonic orders, delivering consistent 30% computational time savings across all test cases, including those with complex bifurcation structures.

To address the system's inherent complexity, an innovative methodology was developed that incorporates normalised arclength as a key hyperparameter in the data-driven model formulation, providing enhanced capability for tracking nonlinear system evolution.

The two key contributions of this chapter are the demonstration of the framework developed throughout this thesis on a high-fidelity test case, and the development of a method for constructing data-driven models by treating the continuation parameter as a hyperparameter. This demonstrates that the framework developed in the previous chapters can be applied to real, complex aeroelastic systems exhibiting LCO, and can assist in identifying models that provide a deeper understanding of the safety margins associated with LCO.

Two pseudo-datasets were generated to thoroughly assess framework performance under different operational scenarios. The first dataset, exhibiting complex bifurcation morphology with multiple limit cycle branches, revealed distinct methodological strengths. Quantitative analysis showed that while the SDB approach achieved 3.2% better parameter estimation accuracy against reference values, this came at considerable computational expense. The PIDB method demonstrated superior predictive capability for bifurcation behaviour, capturing 92% of the nonlinear features while requiring 51% less training data than the SDB baseline. The IDB framework proved most efficient computationally, achieving a 72% reduction in training requirements with only marginal (1.8%) degradation in prediction quality compared to PIDB. Removing noise from the pseudo-data PIDB emerges as the optimal choice, exhibiting slight advantages over IDB. Under noise, however, SDB's parameter accuracy fails to translate to predictive performance, underscoring noise-sensitivity in model selection.

The second dataset, designed to simulate realistic experimental conditions with measurement noise and wider parameter uncertainty, yielded more nuanced insights. Both iterative methods maintained robust performance, with PIDB showing particular strength in parameter estimation (88% mean accuracy versus 85% for IDB) while IDB retained its computational advantage. Detailed examination revealed that the PIDB's probabilistic treatment of inter-iteration uncertainty propagation made it more resilient to measurement noise, particularly in the critical stability transition region where it maintained prediction errors below 2.5%.

Several conclusions emerge from this comparative study. First, the iterative paradigm consistently outperforms conventional single-iteration approaches, particularly in computational efficiency where reductions exceeding 70% were achieved. Second, the choice between IDB and PIDB involves fundamental trade-offs between computational cost (IDB advantage) and prediction robustness (PIDB advantage). Third, the arclength-based formulation proves particularly effective for tracking nonlinear system evolution, though opportunities remain for refinement.

Chapter 7

Conclusion

This chapter presents the conclusions derived from this thesis. Each research objective is revisited, and the extent to which it has been achieved is evaluated. Subsequently, the overarching research question is addressed, assessing the robustness of its resolution. Finally, recommendations for future research directions, building upon the findings of this study, are proposed.

7.1 Research Outcomes

The framework developed in this thesis offers significant potential for a wide range of real-world engineering applications, particularly in the design of flexible aircraft wings. By probabilistically identifying the nonlinear parameters within the model, it provides a more precise understanding of safety margins in the design process. Additionally, the data-driven approach, which leverages surrogate models, considerably reduces computational time, thus expediting the early stages of design. The ongoing development of advanced tools for nonlinear aeroelastic analysis further empowers the industry to push the boundaries of design, fostering more innovative and efficient solutions.

The first objective of the work was: **Develop a computationally efficient method for estimating deterministic LCO behaviour and stability in aeroelastic systems.**

This study has successfully developed a computationally efficient methodology for

estimating LCO behaviour and determining stability in aeroelastic systems. The proposed approach, which operates entirely within the frequency domain, combines the HBM continuation scheme with Koopman operator theory. The framework was demonstrated through numerical test cases incorporating both geometric and localised nonlinearities, with validation against established continuation tools (MATCONT and COCO).

For systems with smooth nonlinearities, the method achieved convergent bifurcation diagrams and reliable stability estimates using just five harmonic orders. The Koopman operator-based stability analysis proved particularly advantageous, offering significant computational savings compared to conventional Hill's method and time-domain integration. However, in cases involving non-smooth nonlinearities, while the bifurcation diagrams converged at eight harmonic orders, the Koopman operator exhibited chaotic behaviour, rendering it unsuitable for stability determination in these scenarios. Comparative analyses revealed the HBM framework's superior computational efficiency and accuracy relative to MATCONT and COCO for smooth systems, though some discrepancies emerged when handling non-smooth nonlinearities.

The second objective of the work was: **Formulate a probabilistic, data-driven methodology to minimise computational cost while maximising accuracy in the identification of nonlinear models for LCO behaviour in aeroelastic systems.**

This study developed a probabilistic, data-driven methodology for efficient identification of nonlinear aeroelastic models describing LCO behaviour. The approach combines Kriging surrogate modelling with BMU, evaluating three advanced sampling methods (MCMC, TMCMC, and SMC) using experimental data from a nonlinear flutter rig.

Key findings from this study demonstrate that TMCMC emerged as the optimal sampling method, achieving a mean accuracy of 98% while capturing over 90% of the physical behaviour, and exhibiting significantly better convergence compared to MCMC. The probabilistic approach improved prediction accuracy by up to 20% relative to deterministic methods, particularly at lower amplitudes. Computational ef-

ficiency was also enhanced, with continuation runs reduced by 60% during forward uncertainty quantification. Furthermore, model selection via TMCMC revealed different optimal nonlinear models depending on the system configuration, distinguishing between quadratic softening/cubic hardening and higher-order (third- or fifth-order) nonlinear terms.

Experimental validation of the HBM fraenwork yielded mixed results: while the methodology accurately captured the overall shape of bifurcation diagrams, notable errors were observed beyond turning points. These discrepancies were partially mitigated through the use of probabilistic parameter estimation, which outperformed deterministic approaches in certain configurations. The study thus demonstrates that frequency-domain methods can provide an effective balance between computational efficiency and accuracy for LCO analysis, particularly in systems dominated by smooth nonlinearities.

While successful at lower amplitudes, the methodology revealed limitations in capturing post-turning-point behaviour (5-22% data points outside interval of probability). Multi-modal parameter distributions and class selection analyses suggest no single nonlinear model can fully represent the physics across all amplitudes.

The third objective of the work was: **Enhance the proposed framework through an iterative, multi-resolution modelling approach.**

This study successfully enhanced the stochastic identification framework through a novel iterative, multi-resolution Bayesian approach, achieving significant computational savings while improving accuracy. Key advancements achieved in this work include a 76% reduction in training data requirements compared to single-iteration approaches, made possible through the proposed iterative framework. This study also marks the first integration of epistemic uncertainties in iterative data-driven modelling using p-box representations. Two iterative approaches were developed—PIDB and IDB—with PIDB identified as the optimal method, maintaining 98% accuracy while requiring 6% less training data than IDB.

The framework demonstrated particular effectiveness in reducing the impact of epistemic uncertainties, as evidenced by a 53% expansion in the interval of probability when

data-driven model uncertainties were included. Additionally, the PIDB approach enabled automated iteration convergence, thereby minimising user input requirements. The framework also successfully identified instability regions—specifically within the 0.036–0.046 m LCO amplitude range—that were missed by single-iteration methods.

Limitations were observed in the full alignment with experimental CBC data, particularly concerning stability predictions for configuration 1. These discrepancies highlight the paramount importance of model fidelity, suggesting that either significant measurement noise or an insufficient physical representation in the current mathematical formulation may be responsible.

The fourth and final objective of the work was: **Validate the framework using a high-fidelity aeroelastic test case.**

This study validated three BMU frameworks (SDB, IDB, PIDB) through application to a high-fidelity tiltrotor aeroelastic test case. Key findings demonstrate the clear superiority of iterative approaches over single-iteration strategies. Both the IDB and PIDB methods significantly outperformed the SDB baseline, achieving reductions in training data requirements between 51% and 72%, while maintaining high accuracy by capturing 88–92% of nonlinear features. Methodological trade-offs were also observed: PIDB exhibited greater robustness, maintaining prediction errors within 2.5% in critical stability transition regions, whereas IDB provided superior computational efficiency, operating up to 72% faster than SDB. Furthermore, the innovative use of a normalised arclength formulation proved effective in tracking nonlinear system evolution, though further refinement is needed to fully capture complex bifurcation morphologies.

The validation confirms the frameworks' effectiveness for high-fidelity applications, with selection dependent on prioritising either computational efficiency (IDB) or prediction robustness (PIDB).

Having examined the outcomes from each chapter, now the central research question can be evaluated: **Can a robust framework for nonlinear aeroelastic analysis be established through the introduction of data-driven techniques?**

The collective evidence demonstrates that this objective has been successfully achieved. The framework's development and validation progressed through theoretical formula-

tion, numerical case studies, experimental verification, and ultimately application to a high-fidelity tiltrotor system. The iterative data-driven approaches proved particularly effective in delivering computationally efficient yet accurate predictions.

While the results conclusively affirm that data-driven techniques can form the basis of a robust nonlinear aeroelastic framework, the studies naturally reveal opportunities for further refinement. The body of work presented provides a definitive positive answer to the research question while establishing foundations for continued development in this field.

7.2 Recommendations for Future Work

The research presented in this thesis has identified several promising directions for future investigation to advance data-driven methods for nonlinear aeroelastic analysis. These recommendations are organised into methodological improvements, experimental validation, and industrial application.

Methodological Enhancements

The current framework requires development in several key areas to handle complex aeroelastic phenomena:

- **Non-smooth system analysis**: Current data-driven models exhibit limitations when applied to systems with strong nonlinearities, multiple fixed points, and modal interactions. Future work should investigate hybrid modelling approaches combining physics-based and machine learning components to improve robustness.

- **High-amplitude LCO modelling**: Enhanced mathematical formulations are needed to better capture the physics of large-amplitude LCO, particularly for systems exhibiting complex bifurcation diagrams with multiple turning points.

- **Parameter estimation refinement**: Improved techniques for probabilistic parameter estimation could enhance experimental correlation, especially in post-

turning-point regimes where current methods show reduced accuracy.

Computational Framework Development

The limitations of current data-driven approaches suggest several research directions:

- **Nonlinear model reduction**: Invariant manifold and spectral submanifold techniques show particular promise for representing high-dimensional nonlinear dynamics more efficiently than linear methods like POD or DMD. Their integration into aeroelastic workflows warrants investigation.
- **Hyperparameter optimisation**: Developing more robust methods for selecting and tuning model hyperparameters could improve generalisation while maintaining computational efficiency.
- **Multi-resolution extensions**: The PIDB approach could be expanded to incorporate additional resolution levels or combined with other reduction techniques for handling very large-scale systems.

Experimental and Industrial Validation

Critical gaps in experimental validation and industrial application should be addressed:

- **High-fidelity test cases**: Comprehensive experimental data is needed for complex configurations (e.g., full tiltrotor systems) to properly validate the framework's industrial applicability.
- **Measurement noise reduction**: Improved experimental protocols and signal processing techniques could enhance data quality for system identification.
- **Workflow integration**: The transition from academic research to industrial practice requires development of standardised tools and procedures for implementing these methods in design workflows.

Recent advances in nonlinear model reduction [210] and hybrid modelling [211] suggest promising pathways for addressing these challenges. The integration of data-driven

methods with emerging nonlinear dynamics techniques could particularly benefit the analysis of complex aeroelastic systems exhibiting quasiperiodic behaviour or multiple interacting instability modes.

While the current framework has demonstrated success for fundamental cases, these future developments would significantly enhance its capability to handle real-world engineering challenges in aircraft design and certification.

Appendix A

Continuation Procedure Formula

A.1 Initiating Continuation

To commence the continuation process an initial guess at $j = 0$ is made based on results from the linear analysis. The linear flutter point is taken as a hopf bifurcation point, where ω and λ are the initial results. Typically at hopf bifurcation points, the amplitude of LCO is close to zero. So a small guess of $X_{1,s}$ is used to solve a reduced version of System A.5. In this reduced solver (shown in Appendix A.5), λ_0 is treated as a known and ω_0 is taken as an initial guess. With no knowledge of other points, only residual Equations 3.12 can be solved, leaving $l+1$ equations and $l+2$ unknowns. To overcome this, a phase condition is set so $X_{1,c} = 0$. Once a converged solution is reached at $j = 0$, a small step is made in λ and the process is repeated for $j = 1$. With the initial two points converged, the first set of direction vectors can be calculated by obtaining arclength increment δs from Equation A.1 and using finite difference method. Gathering direction vectors allows for the full Newton-Raphson solver to be implemented and arclength continuation to commence.

$$\delta s_{j+1} = \sqrt{(X_{j+1} - Xj)^T (X_{j+1} - Xj) + (\omega_{j+1} - \omega_j)^2 + (\lambda_{j+1} - \lambda_j)^2} \tag{A.1}$$

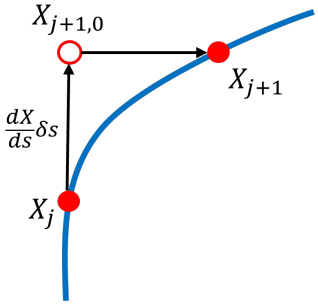

Figure A.1: Pseudo-arclength continuation predicitor/corrector scheme

A.2 Continuation Constraint

A constraint can be defined based on pseudo-arclength continuation, allowing for another residual equation to be derived. Figure A.1 shows the process of a tangent prediction being corrected through pseudo-arclength continuation. Predicted point $j+1$ is made using known the known j^{th} point and direction vector $\frac{dX}{ds}$, as well as a small arclength distance δs. The predicted $j+1,0$ value is then corrected assuming the converged $j+1$ value is perpendicular to the initial prediction. As the dot product of perpendicular vectors is zero, in the case of the Fourier coefficients it can be assumed:

$$\left(\frac{X_{j+1} - X_{j+1,0}}{\delta s}\right) . \frac{dX}{ds} = 0$$

Expanding for all system unknowns the residual Equation A.2 can be written.

$$R_{2l+2} = (X_{j+1} - X_{j+1,0})\frac{dX}{ds}_j + (\omega_{j+1} - \omega_{j+1,0})\frac{d\omega}{ds}_j + (\lambda_{j+1} - \lambda_{j+1,0})\frac{d\lambda}{ds}_j \tag{A.2}$$

A.3 Phase Constraint

A final residual equation can be derived related to a phase constraint. It is common practice in continuation to assume orthogonality between a response and its differential. This assumption can be used to derive a relationship between j^{th} Fourier coefficients and the $j+1$ points in the 'Orthogonality Phase Condition' [162]:

$$\int_0^T \dot{x}(t)_j x(t)_{j+1} = 0$$

Or:

$$\mathbf{E}_j^T X_{j+1} = 0 \tag{A.3}$$

Where $E_j^T = [0, -kX_{k,c}, kX_{k,s}]$ for $k = 1, \ldots, l$.

Carrying out the integration and making use of Fourier series relationship (Equations 3.7), the final residual Equation A.4 is obtained.

$$R_{2l+3} = \sum_{k=1}^{l} -k(X_{k,c})_j(X_{k,s})_{j+1} + k(X_{k,s})_j(X_{k,c})_{j+1} \tag{A.4}$$

A.4 Residual Equations

With $2l+3$ residual equations matching the number of system unknowns $[X_0, X_{k,s}, X_{k,c}, \omega, \lambda]$ (for $k = 1, \ldots, l$), the Newton-Raphson solver can be set up. System A.5 shows the iterative process employed until a converged solution has been reached. Finite difference method is used to obtain the derivatives $\frac{\delta R}{\delta X}$, $\frac{\delta R}{\delta \omega}$ and $\frac{\delta R}{\delta \lambda}$.

$$\begin{pmatrix} X_{j+1,1} \\ \omega_{j+1,1} \\ \lambda_{j+1,1} \end{pmatrix} = \begin{pmatrix} X_{j+1,0} \\ \omega_{j+1,0} \\ \lambda_{j+1,0} \end{pmatrix} - \begin{bmatrix} \frac{\delta R}{\delta X}_{j+1} & \frac{\delta R}{\delta \omega}_{j+1} & \frac{\delta R}{\delta \lambda}_{j+1} \\ \frac{dX}{ds}^T_j & \frac{d\omega}{ds}_j & \frac{d\lambda}{ds}_j \\ \mathbf{E^T} & 0 & 0 \end{bmatrix}^{-1} \begin{pmatrix} R_{j+1,0} \\ R_{2l+2} \\ R_{2l+3} \end{pmatrix} \tag{A.5}$$

A.5 Reduced Newton-Raphson solver

Detailed is the reduced Newton-Raphson solver that is used to obtain points $j = 0$ and $j = 1$, initiating continuation.

$$\begin{pmatrix} \delta X \\ \delta \omega \end{pmatrix} = - \begin{bmatrix} \frac{\delta R}{\delta X}^*_{j+1} & \frac{\delta R}{\delta \omega}_{j+1} \end{bmatrix}^{-1} \begin{pmatrix} R_{j+1,0} \end{pmatrix}$$

$$\begin{pmatrix} X_{j+1,1} \\ \omega_{j+1,1} \end{pmatrix} = \begin{pmatrix} X_{j+1,0} \\ \omega_{j+1,0} \end{pmatrix} + \begin{pmatrix} \delta X \\ \delta \omega \end{pmatrix}$$

Where $\frac{\delta R}{\delta X}^*$ is the same as $\frac{\delta R}{\delta X}$ but with the term related to $X_{1,s}$ removed as it is treated as a known.

A.6 Direction vector solver

Shown is the system employed to obatin $j+1$ direction vectors based on j^{th} direction vectors and $j+1$ Jacobi.

$$\begin{pmatrix} \frac{dX}{ds}^T{}_{j+1} \\ \frac{d\omega}{ds}{}_{j+1} \\ \frac{dU}{ds}{}_{j+1} \end{pmatrix} = \begin{bmatrix} \frac{\delta R}{\delta X}{}_{j+1} & \frac{\delta R}{\delta \omega}{}_{j+1} & \frac{\delta R}{\delta U}{}_{j+1} \\ \frac{dX}{ds}^T{}_{j} & \frac{d\omega}{ds}{}_{j} & \frac{dU}{ds}{}_{j} \\ \mathbf{E^T} & 0 & 0 \end{bmatrix}^{-1} \begin{pmatrix} 0 \\ 1 \\ 0 \end{pmatrix} \tag{A.6}$$

A.7 Calculation of Direction Vectors

Once a converged solution for all system unknowns is reached at j, calculation of $j+1$ direction vectors is carried out. It is commonly assumed in pseudo-arclength continuation that new direction vectors point the same direction as the previous ones:

$$\frac{dX}{ds}^T{}_{j} \frac{dX}{ds}{}_{j+1} = 1$$

As arcpoint s lies on the same curve created by solutions of $W(X_0, X_{k,s}, X_{k,c}, \omega, \lambda) = 0$ for all values of s it can be said:

$$\frac{\delta R}{\delta X}\frac{dX}{ds} + \frac{\delta R}{\delta \omega}\frac{d\omega}{ds} + \frac{\delta R}{\delta \lambda}\frac{d\lambda}{ds} = 0$$

This principal is employed to construct the relationship in the following Section (Appendix A.8). Allowing $j+1$ direction vectors to be obtained.

A.8 Direction vector solver

Shown is the system employed to obatin $j+1$ direction vectors based on j^{th} direction vectors and $j+1$ Jacobi.

$$\begin{pmatrix} \frac{dX}{ds}^T{}_{j+1} \\ \frac{d\omega}{ds}{}_{j+1} \\ \frac{dU}{ds}{}_{j+1} \end{pmatrix} = \begin{bmatrix} \frac{\delta W}{\delta X}{}_{j+1} & \frac{\delta W}{\delta \omega}{}_{j+1} & \frac{\delta W}{\delta U}{}_{j+1} \\ \frac{dX}{ds}^T{}_{j} & \frac{d\omega}{ds}{}_{j} & \frac{dU}{ds}{}_{j} \\ \mathbf{E^T} & 0 & 0 \end{bmatrix}^{-1} \begin{pmatrix} 0 \\ 1 \\ 0 \end{pmatrix} \tag{A.7}$$

Appendix B

Two DoF Aerofoil Model

This appendix documents the parameter values for the heave-pitch aerofoil model employed throughout Chapters 3–5. The numerical test case parameters originate from two sources: the analytical model in Ref. [3] and the experimental configuration in Ref. [69].

For the nonsmooth numerical case, two distinct flutter speeds are specified:

- Flutter speed 1: Corresponding to operation outside the freeplay region
- Flutter speed 2: Applicable within the freeplay region

The experimental section presents both deterministic estimates of nonlinear parameters $K_{\alpha 2}$ and $K_{\alpha 3}$ from Ref. [69], alongside probabilistic estimates derived through TMCMC sampling in Chapter 4.

Table B.1: Parameters used in case study

	Numerical		Experimental	
Parameter	Smooth	Nonsmooth	Configuration 1	Configuration 2
$b\ (m)$	0.127	0.127	0.150	0.150
a	-0.5	-0.5	-0.5	-0.5
$m_w\ (kg)$	1.56	1.56	5.30	5.30
x_α	0.434	0.434	0.24	0.24
$I_\alpha\ (kg.m^2)$	0.001347	0.001347	0.1724	0.1724
$K_h\ (N/m)$	2818.8	2818.8	3529.4	3318.3
$K_\alpha\ (N/rad)$	0	0	54.11	65.6
$c_h\ (kg/s)$	0.77	0.77	14.58	14.58
$c_\alpha\ (kg.m^2/s^2)$	0.63	0.63	0.56	1.03
$c_w\ (kg/s)$	0.54	0.54	0	0
c_1	0.165	0.165	0.165	0.165
c_2	0.0455	0.0455	0.0455	0.0455
c_3	0.335	0.335	0.335	0.335
c_4	0.3	0.3	0.3	0.3
$K_{\alpha 2}\ (N/rad^2)$	250	-	751.6/524.50	774.7/678.32
$K_{\alpha 3}\ (N/rad^3)$	7500	-	5006.7/2595.9	3490.7/ 2982.6
$\delta\ [rad]$	-	0.0175	-	-
$V_f\ (m/s)$	31.45	31.45/29.50	17.80	26.15

Appendix C

Gimballed Hub Mathematical Model

This appendix describes the mathematical model of the gimballed hub tiltrotor system implemented in Chapter 6. Originally developed by Johnson [194] and published as a NASA technical note, this model builds upon earlier theoretical and experimental work by Reed. It has been widely adopted in recent studies, including [202–204].

The model incorporates a gimballed hub and multiple additional degrees of freedom – primarily in the rotor system, with secondary contributions from the wing – resulting in dynamic behaviour that is substantially more complex than can be captured by classical modelling approaches. The governing equations of motion are formulated as follows:

$$\mathbf{M}\ddot{x}(t) + \mathbf{D}\dot{x}(t) + \mathbf{K}x(t) + f_{nl}(\ddot{x}, \dot{x}, x) = 0 \tag{C.1}$$

Where here $\mathbf{M}$, $\mathbf{D}$ and $\mathbf{K}$ are the combined mass and aerodynamic matrices. Each of

the matrices are set up as follows:

$$\mathbf{M} = \begin{bmatrix} M_{11} & 0 & 0 & 0 & 0 & 0 & M_{17} & 0 & M_{19} \\ 0 & M_{22} & 0 & 0 & 0 & 0 & 0 & M_{28} & 0 \\ 0 & 0 & M_{33} & 0 & 0 & 0 & 0 & 0 & M_{39} \\ 0 & 0 & 0 & M_{44} & 0 & 0 & M_{47} & 0 & 0 \\ 0 & 0 & 0 & 0 & M_{55} & 0 & 0 & M_{58} & 0 \\ 0 & 0 & 0 & 0 & 0 & M_{66} & M_{67} & 0 & M_{69} \\ 0 & 0 & 0 & M_{74} & 0 & M_{76} & M_{77} & 0 & M_{79} \\ 0 & 0 & M_{83} & M_{84} & M_{85} & 0 & M_{87} & M_{88} & M_{89} \\ 0 & 0 & 0 & M_{94} & 0 & M_{96} & M_{97} & 0 & M_{99} \end{bmatrix} \tag{C.2}$$

$$\mathbf{D} = \begin{bmatrix} D_{11} & D_{12} & D_{13} & 0 & 0 & 0 & D_{17} & D_{18} & D_{19} \\ D_{21} & 0 & 0 & D_{24} & 0 & 0 & D_{27} & D_{28} & 0 \\ D_{31} & 0 & D_{33} & D_{34} & 0 & 0 & D_{37} & D_{38} & D_{39} \\ 0 & D_{42} & D_{43} & D_{44} & 0 & 0 & D_{47} & D_{48} & D_{49} \\ 0 & 0 & 0 & 0 & D_{55} & D_{56} & D_{57} & D_{58} & D_{59} \\ 0 & 0 & 0 & 0 & D_{65} & D_{66} & D_{67} & D_{68} & D_{69} \\ 0 & D_{72} & 0 & D_{74} & D_{75} & D_{76} & D_{77} & D_{78} & D_{79} \\ D_{81} & D_{82} & D_{83} & D_{84} & D_{85} & D_{86} & D_{87} & D_{88} & D_{89} \\ 0 & D_{92} & 0 & D_{94} & D_{95} & D_{96} & D_{97} & D_{98} & D_{99} \end{bmatrix} \tag{C.3}$$

$$\mathbf{K} = \begin{bmatrix} K_{11} & K_{12} & 0 & K_{14} & 0 & 0 & 0 & K_{18} & 0 \\ K_{21} & K_{22} & K_{23} & 0 & 0 & 0 & K_{27} & 0 & K_{29} \\ K_{31} & K_{32} & K_{33} & K_{34} & 0 & 0 & 0 & K_{38} & 0 \\ K_{41} & K_{42} & K_{43} & K_{44} & 0 & 0 & K_{47} & 0 & K_{49} \\ 0 & 0 & 0 & 0 & K_{55} & 0 & 0 & 0 & 0 \\ 0 & 0 & 0 & 0 & K_{65} & K_{66} & 0 & 0 & 0 \\ K_{71} & K_{72} & K_{73} & 0 & K_{75} & 0 & K_{77} & 0 & K_{79} \\ K_{81} & K_{82} & K_{83} & K_{84} & K_{85} & 0 & K_{87} & K_{88} & K_{89} \\ K_{91} & K_{92} & K_{93} & 0 & K_{95} & 0 & K_{97} & 0 & K_{99} \end{bmatrix} \tag{C.4}$$

The non-zero elements of the system matrices are explicitly defined in Equations C.5, C.6, and C.7, with all parameters quantified in Table C.1. The **Q** matrix follows the same formulation as presented in earlier chapters (Equation 3.4). The nonlinear vector $\mathbf{f}_{\text{nl}}$, governing the system's nonlinear dynamics, is given in Equation C.8.

$$
\begin{gathered}
M_{11} = I^*_\beta, \quad M_{17} = I^*_{\beta\alpha}\delta\eta, \quad M_{19} = I^*_{\beta\alpha}, \quad M_{22} = I^*_\beta, \quad M_{28} = -\eta I^*_{\beta\alpha}, \quad M_{33} = I_{\zeta *}, \\
M_{39} = -S^*_\zeta(\eta\bar{h} - \delta y_{Tw}), \quad M_{44} = I^*_\zeta, \quad M_{47} = S^*_\zeta(y_{Tw} - \delta\eta\bar{h}), \quad M_{55} = I^*_\beta, \\
M_{58} = -S_{\beta_0} y_{Tw}, \quad M_{66} = I^*_{\zeta_0}, \quad M_{67} = \eta I^*_{\zeta_0\alpha}, \quad M_{69} = I_{\zeta_0\alpha}\delta, \quad M_{74} = S^*_\zeta \begin{pmatrix} y_{Tw} + \\ \delta\eta\bar{h}(\zeta - 1) \end{pmatrix}, \\
M_{76} = 2\eta I_{\zeta_0\alpha}, \quad M_{77} = \begin{pmatrix} I_{qw} + m^*_{\text{P}} + 2\text{M}_b \\ (y_{Tw} + \delta\eta\bar{h}(\xi - 1)) \\ (y_{Tw} - \delta\eta\bar{h}) + 2\eta^2 \end{pmatrix}, \quad M_{79} = \begin{pmatrix} S^*_w + 2\delta\eta + 2\text{M}_b \\ (y_{Tw} + \delta\eta\bar{h}(\xi - 1)) \\ (\bar{h} - \delta\xi y_{Tw}) \end{pmatrix}, \\
M_{83} = \begin{pmatrix} -S^*_\zeta(\eta\bar{h} + \\ \delta y_{Tw}(\xi^2 - 1)) \end{pmatrix}, \quad M_{84} = -S^*_\zeta \delta\eta\bar{h}(\xi - 1), \quad M_{85} = -2y_{Tw} S_{\beta_0}, \\
M_{87} = \begin{pmatrix} -\text{M}_b\delta\eta\bar{h} \\ (y_{Tw} - \delta\eta\bar{h})(\xi - 1) \end{pmatrix}, \quad M_{88} = \begin{pmatrix} I^*_{qw} + m_{\text{P}} + I_{\text{P}_x}\eta^2 \\ 2\text{M}_b(\eta\bar{h} - \delta y_{Tw}) \\ (\eta\bar{h} + \delta y_{Tw}(\xi^2 - 1)) \\ + 2y^2_{Tw}\text{M}_b \end{pmatrix}, \quad M_{89} = \begin{pmatrix} -2\text{M}_b\delta\eta\bar{h} \\ (\bar{h} - \delta\xi y_{Tw})(\xi - 1) \end{pmatrix}, \\
M_{94} = S^*_\zeta, \quad M_{96} = -2I_{\zeta_0\alpha}\delta(\xi - 1), \quad M_{97} = \begin{pmatrix} S^*_w + 2\text{M}_b\bar{h} \\ (y_{Tw} - \delta\eta\bar{h}) \\ -2\delta\eta(\xi - 1) \end{pmatrix}, \quad M_{99} = \begin{pmatrix} I^*_{P_w} + I^*_{\text{P}_y} + \\ 2\text{M}_b\bar{h}(\bar{h} - \delta\xi y_{Tw}) \\ -2\delta^2(\xi - 1) \end{pmatrix}
\end{gathered}
\tag{C.5}
$$

$$D_{11} = I^*_{\beta} g_{\beta} \sqrt{\nu^2_{\beta} - 1} - \gamma \mathrm{M}_{\dot{\beta}}, \quad D_{12} = 2I_{\beta}, \quad D_{13} = \gamma M_{\dot{\zeta}}, \quad D_{17} = -\gamma M_{\dot{\beta}\delta\eta},$$

$$D_{18} = -\begin{pmatrix} 2I^*_{\beta\alpha}\eta + \\ \gamma M_{\mu}(\eta\bar{h} - \delta y_{Tw}) \end{pmatrix}, \quad D_{19} = \gamma M_{\dot{\beta}}, \quad D_{21} = -2I^*_{\beta},$$

$$D_{22} = I^*_{\beta} g_{\beta} \sqrt{\nu^2_{\beta} - 1} - \gamma M_{\dot{\beta}}, \quad D_{24} = \gamma M_{\dot{\zeta}}, \quad D_{27} = \begin{pmatrix} \gamma M_{\mu}(y_{Tw} - \delta\eta\bar{h} \\ -2I_{\beta\alpha}\delta\eta) \end{pmatrix},$$

$$D_{28} = \gamma M_{\dot{\beta}}\eta, \quad D_{31} = \gamma Q_{\dot{\beta}}, \quad D_{33} = \gamma Q_{\dot{\zeta}} + I^*_{\zeta} g_{\zeta} \nu_{\zeta}, \quad D_{34} = 2I^*_{\zeta},$$

$$D_{37} = -\gamma Q_{\dot{\beta}}\delta\eta, \quad D_{38} = -\gamma Q_{\mu}(\eta\bar{h} - \delta y_{Tw}), \quad D_{39} = \gamma Q_{\dot{\beta}}, \quad D_{42} = -\gamma Q_{\dot{\beta}},$$

$$D_{43} = -2I^*_{\zeta}, \quad D_{44} = \gamma Q_{\dot{\zeta}} + I^*_{\zeta} g_{\zeta} \nu_{\zeta}, \quad D_{47} = \gamma Q_{\mu}(y_{Tw} - \delta\eta\bar{h}), \quad D_{48} = \gamma Q_{\dot{\beta}}\eta$$

$$D_{49} = \gamma Q_{\mu}(\bar{h} - \delta\xi y_{Tw}), \quad D_{55} = \begin{pmatrix} I^*_{\beta_0} g_{\beta_0} \sqrt{\nu^2_{\beta_0} - 1} \\ -\gamma M_{\dot{\beta}} \end{pmatrix}, \quad D_{56} = \gamma M_{\dot{\zeta}}, \quad D_{57} = \gamma M_{\dot{\zeta}}\eta$$

$$D_{58} = \gamma M_{\lambda} y_{Tw}, \quad D_{59} = \gamma M_{\dot{\zeta}}\delta, \quad D_{65} = -\gamma Q_{\dot{\beta}}, \quad D_{66} = I^*_{\zeta_0} g_{\zeta_0} \nu_{\zeta_0} + \gamma Q_{\dot{\zeta}},$$

$$D_{67} = \gamma Q_{\dot{\zeta}}\eta, \quad D_{68} = \gamma Q_{\lambda} y_{Tw}, \quad D_{69} = \gamma Q_{\dot{\zeta}}\delta, \quad D_{72} = -\gamma H_{\dot{\beta}} \begin{pmatrix} y_{Tw} + \\ \delta\eta\bar{h}(\xi - 1) \end{pmatrix},$$

$$D_{74} = \begin{pmatrix} \gamma H_{\dot{\zeta}}(y_{Tw} + \\ \delta\eta\bar{h}(\xi + 1)) \end{pmatrix}, \quad D_{75} = -2\gamma Q_{\dot{\beta}}\eta, \quad D_{76} = 2\gamma Q_{\dot{\zeta}}\eta,$$

$$D_{77} = \begin{pmatrix} C^*_{q_1} + 2\eta^2 \gamma Q_{\dot{\zeta}} + \gamma(H_{\mu} + R_{\mu}) \\ (y_{Tw} + \delta\eta\bar{h}(\xi - 1)) \\ (y_{Tw} - \delta\eta\bar{h}) - \gamma M_{q_1 q_1'} \end{pmatrix}, \quad D_{78} = \begin{pmatrix} 2\eta y_{Tw} \gamma Q_{\lambda} + \\ \gamma H_{\dot{\beta}}\eta(y_{Tw} + \delta\eta\bar{h}(\xi - 1)) \end{pmatrix},$$

$$D_{79} = \begin{pmatrix} \gamma(H_{\mu} + R_{\mu})(y_{Tw} + \\ \delta\eta\bar{h}(\xi - 1))(\bar{h} - \delta\xi y_{Tw}) \\ +2\gamma Q_{\dot{\zeta}}\delta\eta - \gamma M_{q_1 p'} \end{pmatrix}, \quad D_{81} = \gamma H_{\dot{\beta}} \begin{pmatrix} \eta\bar{h} + \\ \delta y_{Tw}(\xi^2 - 1) \end{pmatrix}, \quad D_{82} = \begin{pmatrix} \gamma H_{\dot{\beta}}\delta\eta\bar{h} \\ (\xi - 1) \end{pmatrix},$$

$$D_{83} = -\gamma H_{\dot{\zeta}} \begin{pmatrix} \eta\bar{h}\delta y_{Tw} \\ (\xi^2 - 1) \end{pmatrix}, \quad D_{84} = \begin{pmatrix} -\gamma H_{\dot{\zeta}}\delta\eta\bar{h} \\ (\xi - 1) \end{pmatrix}, \quad D_{85} = 2\gamma T_{\dot{\beta}} y_{Tw}, \quad D_{86} = -2\gamma T_{\dot{\gamma}} y_{Tw},$$

$$D_{87} = \begin{pmatrix} \gamma H_{\dot{\beta}}\delta\eta(\eta\bar{h} + \delta y_{Tw}(\xi^2 - 1)) \\ -2\gamma T_{\dot{\gamma}}\eta y_{Tw} - \gamma(H_{\mu} + R_{\mu}) \\ \delta\eta\bar{h}(y_{Tw} - \delta\eta\bar{h})(\xi - 1) \end{pmatrix}, \quad D_{88} = \begin{pmatrix} C^*_{q_2} + \gamma(H_{\mu} + R_{\mu}) \\ (\eta\bar{h} + \delta y_{Tw}(\xi^2 - 1)) - \\ 2\gamma T_{\lambda} y^2_{Tw} - \gamma H_{\dot{\beta}}\delta\eta^2\bar{h}(\xi - 1) \end{pmatrix},$$

$$D_{89} = -\begin{pmatrix} \gamma H_{\dot{\beta}}(\eta\bar{h} + \delta y_{Tw}(\xi^2 - 1)) \\ +2\gamma T_{\dot{\zeta}}\delta y_{Tw} + \gamma(H_{\mu} + R_{\mu}) \\ \delta\eta\bar{h}(\bar{h} - \delta\xi y_{Tw})(\xi - 1) \end{pmatrix}, \quad D_{92} = -\gamma H_{\dot{\beta}}\bar{h}, \quad D_{94} = \gamma H_{\dot{\zeta}}\bar{h}, \quad D_{95} = \begin{pmatrix} 2\gamma Q_{\dot{\beta}}\delta \\ (\xi - 1) \end{pmatrix},$$

$$D_{96} = \begin{matrix} 2\gamma Q_{\dot{\zeta}}\delta \\ (\xi - 1) \end{matrix}, \quad D_{97} = \begin{pmatrix} \gamma(H_{\mu} + R_{\mu})\bar{h}(y_{Tw} - \delta\eta\bar{h}) \\ -2\gamma Q_{\dot{\zeta}}\delta\eta(\xi - 1) - \gamma M^*_{pq_1'} \end{pmatrix}, \quad D_{98} = \begin{pmatrix} \gamma H_{\dot{\beta}}\eta\bar{h} - 2\gamma Q_{\lambda}\delta y_{Tw}(\xi - 1) \\ -\gamma M_{pq_2'} \end{pmatrix},$$

$$D_{99} = \begin{pmatrix} C^*_{p} + \gamma(H_{\mu} + R_{\mu})\bar{h}(\bar{h} - \delta\xi y_{Tw}) \\ -2\gamma Q_{\dot{\zeta}}\delta^2(\xi - 1) + M^*_{pp'} \end{pmatrix} \tag{C.6}$$

$$K_{11} = \begin{pmatrix} I^*_{\beta}(\nu^2_{\beta}-1) \\ +K_P\gamma M_{\theta} \end{pmatrix}, \quad K_{12} = -\gamma M_{\dot{\beta}}, \quad K_{14} = \gamma M_{\dot{\zeta}}, \quad K_{18} = \gamma\mu M_{\mu}\eta, \quad K_{21} = \gamma M_{\dot{\beta}},$$
$$K_{22} = \begin{pmatrix} I^*_{\beta}(\nu^2_{\beta}-1) \\ +K_P\gamma M_{\theta} \end{pmatrix}, \quad K_{23} = -\gamma M_{\dot{\zeta}}, \quad K_{27} = \gamma M_{\mu}\delta\eta\mu, \quad K_{29} = -\gamma M_{\mu}\mu,$$
$$K_{31} = \gamma K_P Q_{\beta}, \quad K_{32} = -\gamma Q_{\dot{\beta}}, \quad K_{33} = I^*_{\zeta}(\nu^2_{\zeta}-1), \quad K_{34} = \gamma Q_{\dot{\zeta}}, \quad K_{38} = \gamma Q_{\mu}\eta\mu$$
$$K_{41} = \gamma Q_{\dot{\beta}}, \quad K_{42} = \gamma Q_{\theta}K_P, \quad K_{43} = -\gamma Q_{\dot{\zeta}}, \quad K_{44} = I^*_{\zeta}(\nu^2_{\zeta}-1), \quad K_{47} = \gamma Q_{\mu}\delta\eta\mu$$
$$K_{49} = -\gamma Q_{\mu}\mu, \quad K_{55} = \begin{pmatrix} I^*_{\beta_0}\nu^2_{\beta_0}+ \\ \gamma K_P M_{\theta} \end{pmatrix}, \quad K_{65} = \gamma K_P Q_{\theta}, \quad K_{66} = I^*_{\zeta_0}\nu^2_{\zeta_0},$$
$$K_{71} = \begin{pmatrix} \gamma H_{\dot{\beta}}(y_{Tw}+ \\ \delta\eta\bar{h}(\xi-1))+ \\ I^*_{\beta}\delta\eta(\nu^2_{\beta}-1)(\xi-1) \end{pmatrix}, \quad K_{72} = \begin{pmatrix} \gamma K_P H_{\theta}(y_{Tw} \\ +\delta\eta\bar{h}(\xi-1)) \end{pmatrix}, \quad K_{73} = -\begin{pmatrix} \gamma H_{\dot{\zeta}}(y_{Tw}+ \\ \delta\eta\bar{h}(\xi-1)) \end{pmatrix},$$
$$K_{75} = 2\gamma Q_{\theta}\eta K_P, \quad K_{77} = \begin{pmatrix} K_{q_1}+\gamma(H_{\mu}+R_{\mu}) \\ \delta\eta\mu(y_{Tw}+\delta\eta\bar{h}(\xi-1)) \\ -\gamma M_{q_1 q_1} \end{pmatrix}, \quad K_{79} = -\begin{pmatrix} \gamma(H_{\mu}+R_{\mu})\mu \\ (y_{Tw}+\delta\eta\bar{h}(\xi-1)) \\ +\gamma M_{q_1 p} \end{pmatrix},$$
$$K_{81} = -\begin{pmatrix} \gamma H_{\theta}K_P(\eta\bar{h}+\delta y_{Tw} \\ (\xi-1))+\gamma H_{\dot{\beta}}\delta\eta\bar{h}(\xi-1) \end{pmatrix}, \quad K_{82} = \begin{pmatrix} \eta I^*_{\beta}(\mu^2_{\beta}-1)+\gamma H_{\dot{\beta}} \\ (\eta\bar{h}+\delta y_{Tw}(\xi^2-1)) \\ -\gamma H_{\theta}K_P\delta\eta\bar{h}(\xi-1) \end{pmatrix}, \quad K_{83} = \gamma H_{\dot{\zeta}}\delta\eta\bar{h}(\xi-1),$$
$$K_{84} = -\begin{pmatrix} \gamma H_{\dot{\zeta}}(\eta\bar{h}+ \\ \delta y_{Tw}(\xi^2-1)) \end{pmatrix}, \quad K_{85} = -2\gamma T_{\theta}K_P y_{Tw}, \quad K_{87} = -\begin{pmatrix} \gamma(H_{\mu}+R_{\mu})\delta^{[2]} \\ \eta^2\bar{h}\mu(\xi-1) \end{pmatrix},$$
$$K_{88} = \begin{pmatrix} K^*_{q_2}-\gamma(H_{\mu}+R_{\mu})\eta\mu \\ (\eta\bar{h}+\delta y_{Tw}(\xi^2-1)) \end{pmatrix}, \quad K_{89} = \begin{pmatrix} \gamma(H_{\mu}+R_{\mu}) \\ \delta\eta\bar{h}\mu(\xi-1) \end{pmatrix}, \quad K_{91} = I^*_{\beta}(\mu^2_{\beta}-1)+\gamma H_{\dot{\beta}}\bar{h},$$
$$K_{92} = \gamma H_{\theta}K_P\bar{h}, \quad K_{93} = -\gamma H_{\dot{\zeta}}\bar{h}, \quad K_{95} = -2\gamma Q_{\theta}K_P\delta(\xi-1),$$
$$K_{97} = \begin{pmatrix} \gamma(H_{\mu}+R_{\mu})\delta\eta\bar{h}\mu \\ -\gamma M^*_{pq_1}+C^*_{pq} \end{pmatrix}, \quad K_{99} = -\begin{pmatrix} \gamma(H_{\mu}+R_{\mu})\bar{h}\mu \\ +\gamma M^*_{pp} \end{pmatrix} \tag{C.7}$$

$$f_{nl} = \begin{bmatrix} \frac{\beta_{1C}}{8}\begin{pmatrix} 40K_{\beta 3}\beta_0^4+60K_{\beta 3}\beta_0^2\beta_{1C}^2+60K_{\beta 3}\beta_0^2\beta_{1S}^2+24K_{\beta 2}\beta_0^2+5K_{\beta 3}\beta_{1C}^4 \\ +10K_{\beta 3}\beta_{1C}^2\beta_{1S}^2+6K_{\beta 2}\beta_{1C}^2+5K_{\beta 3}\beta_{1S}^4+6K_{\beta 2}\beta_{1S}^2 \end{pmatrix} \\ \frac{\beta_{1S}}{8}\begin{pmatrix} 40K_{\beta 3}\beta_0^4+60K_{\beta 3}\beta_0^2\beta_{1C}^2+60K_{\beta 3}\beta_0^2\beta_{1S}^2+24K_{\beta 2}\beta_0^2+5K_{\beta 3}\beta_{1C}^4 \\ +10K_{\beta 3}\beta_{1C}^2\beta_{1S}^2+6K_{\beta 2}\beta_{1C}^2+5K_{\beta 3}\beta_{1S}^4+6K_{\beta 2}\beta_{1S}^2 \end{pmatrix} \\ 0 \\ 0 \\ \frac{\beta_0}{8}\begin{pmatrix} 8K_{\beta 3}\beta_0^4+40K_{\beta 3}\beta_0^2\beta_{1C}^2+40K_{\beta 3}\beta_0^2\beta_{1S}^2+8K_{\beta 2}\beta_0^2+15K_{\beta 3}\beta_{1C}^4 \\ +30K_{\beta 3}\beta_{1C}^2\beta_{1S}^2+12K_{\beta 2}\beta_{1C}^2+15K_{\beta 3}\beta_{1S}^4+12K_{\beta 2}\beta_{1S}^2 \end{pmatrix} \\ 0 \\ 0 \\ 0 \\ 0 \end{bmatrix} \tag{C.8}$$

Appendix C. Gimballed Hub Mathematical Model

Table C.1: Tiltrotor model parameters

Wing Parameters			Rotor hub parameters		
Semispan	y_{Tw}	5.092m	Radius	R	$3.82m$
Chord	c_w	$1.578m$	Angular velocity	Ω	$48rad/s$
x damping	C_{q1}	$9030\frac{N.m.s}{rad}$	Number of blades	N	3
x stiffness	K_{q1}	$9.2e^6\frac{N.m}{rad}$	Blade chord	c	$0.356m$
y damping	C_{q2}	$2.73e^4\frac{N.m.s}{rad}$	Blade lift slope	$c_{l\alpha}$	$5.7rad/s$
y stiffness	K_{q2}	$2.5e^7\frac{N.m}{rad}$	Pylon length	h_p	$1.306m$
Pitch damping	C_p	$955\frac{N.m.s}{rad}$	Normalised pylon mass	m_P^*	76.9
Pitch stiffness	K_p	$1.77e^6\frac{N.m.s}{rad}$	Normalised pylon yaw moment of inertia	I_{Px}^*	1.086
Normalised bending generalised mass	$I_{q_w}^*$	4.03	Normalised pylon pitch moment of inertia	I_{Py}^*	1.206
Normalised torsion generalised mass	$I_{p_w}^*$	0.0141	Thrust contribution to pylon torsion	C_{pq}^*	0.667
Normalised bending-torsion inertial coupling	S_w^*	2.88	Blade moment of inertia	I_b	$142kg.m^2$
Normalised rotor lead-lag inertial contribution	S_ζ^*	1.035	Normalised blade cyclic flapping inertia	I_β^*	1
Normalised rotor coning inertial contribution	$S_{\beta_0}^*$	1.212	Normalised blade collective flapping inertia	$I_{\beta_0}^*$	0.779
			Normalised blade cyclic lead-lag inertia	I_ζ^*	0.670
			Normalised blade collective lead-lag inertia	$I_{\zeta_0}^*$	0.670
			Normalised blade mass	M_b^*	6.16
			Blade cyclic flapping natural frequency	ν_β	1.0175
			Blade cyclic collective natural frequency	ν_{β_0}	1.85
			Blade cyclic lead-lag natural frequency	ν_ζ	1.3847
			Blade collective lead-lag natural frequency	ν_{ζ_0}	1.3847
			Blade cyclic flapping damping ratio	g_{s_β}	0.1%
			Blade collective flapping damping ratio	$g_{s_{\beta 0}}$	0.5%
			Blade cyclic lead-lag damping ratio	g_{s_ζ}	0.5%
			Blade collective lead-lag damping ratio	g_{s_ζ}	0.5%

Bibliography

[1] (2020) The lilium jet. Lilium. [Accessed: 08-Jun-2022]. [Online]. Available: https://aura-aero.com/en/era/

[2] (2021) Electric hybrid regional aircraft. Aura Aero. [Accessed: 15-Nov-2023]. [Online]. Available: https://aura-aero.com/en/era/

[3] L. Liu and E. Dowell, *Harmonic Balance Approach for an Airfoil with a Freeplay Control Surface.* Aiaa Journal - AIAA J. 43, 2005, 802-815. 10.2514/1.10973.

[4] P. Holmes and D. Rand, "Bifurcations of the forced van der pol oscillator," *Quarterly of Applied Mathematics*, vol. 35, no. 4, pp. 495–509, 1978.

[5] K. Lee, D. Barton, and L. Renson, "Modelling of physical systems with a hopf bifurcation using mechanistic models and machine learning," *Mechanical Systems and Signal Processing*, vol. 191, p. 110173, 2023.

[6] I. Tartaruga, D. A. Barton, D. Rezgui, and S. A. Neild, "Experimental bifurcation analysis of a wing profile," in *International Forum on Aeroelasticity and Structural Dynamics: IFASD 2019*, 2019. [Online]. Available: http://ifasd2019.utcdayton.com/

[7] Vertical-Aerospace, "Meet the vx4," 2024, accessed: 13 March 2025. [Online]. Available: https://vertical-aerospace.com/meet-the-vx4/

[8] Naval-Technology, "Transwing vertical take-off and landing (vtol) uas, us," 2022, accessed: 15 March 2025. [Online]. Available: https://www.naval-technology.com/projects/transwing-vertical-take-off-and-landing-vtol-uas-us/?cf-view

[9] M. McGurk, O. Stodieck, and J. Yuan, "Probabilistic aeroelastic analysis of high-fidelity composite aircraft wing with manufacturing variability," *Composite Structures*, vol. 329, p. 117794, 2024.

[10] M. McGurk, A. Lye, L. Renson, and J. Yuan, "Data-driven bayesian inference for stochastic model identification of nonlinear aeroelastic systems," *AIAA Journal*, vol. 62, no. 5, pp. 1889–1905, 2024.

[11] M. McGurk and J. Yuan, "Prediction and validation of aeroelastic limit cycle oscillations using harmonic balance methods and koopman operator," *Nonlinear Dynamics*, 2025.

[12] M. McGurk, "A robust multi-level data-driven bayesian approach for stochastic model identification of complex nonlinearsystems," *Available at SSRN 5009709*, 2025.

[13] M. McGurk and J. Yuan, "Computation of limit cycle oscillations and their stabilities in nonlinear aeroelastic systems using harmonic balance methods," Jun. 2022, international Forum on Aeroelasticity and Structural Dynamics (IFASD) 2022. [Online]. Available: https://eventos.uc3m.es/54044/detail/international-forum-on-aeroelasticity-and-structural-dynamics-2022-.html

[14] M. McGurk, J. Yuan, and L. Renson, "Nonlinear parameter estimation using bayesian model updating and data driven surrogate model," *9th International Conference on Computational Methods in Structural Dynamics and Earthquake Engineering*, 2023.

[15] M. McGurk and J. Yuan, "A multi-level data-driven bayesian approach for stochastic model updating of complex aeroelastic systems," in *AIAA Scitech 2024 Forum*, 2024.

[16] J. Yuan and M. McGurk, "A multi-level data-driven bayesian approach to identify probabilistic stability of aeroelastic limit cycle oscillations," *11th European Nonlinear Oscillations Conference*, 2024.

[17] M. McGurk and J. Yuan, "A multi-level data-driven bayesian approach to identify probabilistic stability of aeroelastic limit cycle oscillations," *Third Physics-Enhancing Machine Learning Workshop: Mechanics Materials*, 2024.

[18] M. McGurk, "Multi-level stochastic model identification of complex aeroelastic systems considering aerodynamic nonlinearities," *IMAC-XLIII*, 2025.

[19] M. McGurk and J. Yuan, "Multi-fidelity data driven bayesian identification of complex aeroelastic systems," *NODYCON 2025*, 2025.

[20] E. Terrenoire, D. Hauglustaine, T. Gasser, and O. Penanhoat, "The contribution of carbon dioxide emissions from the aviation sector to future climate change," *Environmental research letters*, vol. 14, no. 8, p. 084019, 2019.

[21] C. Bergero, G. Gosnell, D. Gielen, S. Kang, M. Bazilian, and S. J. Davis, "Pathways to net-zero emissions from aviation," *Nature Sustainability*, vol. 6, no. 4, pp. 404–414, 2023.

[22] L. L. Jensen, P. A. Bonnefoy, J. I. Hileman, and J. T. Fitzgerald, "The carbon dioxide challenge facing us aviation and paths to achieve net zero emissions by 2050," *Progress in Aerospace Sciences*, vol. 141, p. 100921, 2023.

[23] J. Singh, K. Srivastawa, S. Jana, C. Dixit *et al.*, "Advancements in lightweight materials for aerospace structures: A comprehensive review," *Acceleron Aerospace Journal*, vol. 2, no. 3, pp. 173–183, 2024.

[24] Y.-J. Hu, L. Yang, H. Cui, H. Wang, C. Li, and B.-J. Tang, "Strategies to mitigate carbon emissions for sustainable aviation: A critical review from a life-cycle perspective," *Sustainable Production and Consumption*, vol. 33, pp. 788–808, 2022.

[25] J. Rogelj, O. Geden, A. Cowie, and A. Reisinger, "Three ways to improve net-zero emissions targets," *Nature*, vol. 591, no. 7850, pp. 365–368, 2021.

[26] A. J. Timmis, A. Hodzic, L. Koh, M. Bonner, C. Soutis, A. W. Schäfer, and L. Dray, "Environmental impact assessment of aviation emission reduction

through the implementation of composite materials," *The International Journal of Life Cycle Assessment*, vol. 20, pp. 233–243, 2015.

[27] P. Nathen, A. Strohmayer, R. Miller, S. Grimshaw, and J. Taylor, "Architectural performance assessment of an electric vertical take-off and landing (e-vtol) aircraft based on a ducted vectored thrust concept," *Lilium GmbH, Claude-Dornier StraeSSe, Weßling, Germany, Tech. Rep*, 2021.

[28] T. Harrington, "Jsx to acquire up to 330 hybrid-electric aircraft, while norwegian region pursues e-seaplanes," *Green Air*, 2024.

[29] G. Dimitriadis, *Introduction to nonlinear aeroelasticity*. John Wiley & Sons, 2017.

[30] R. Ghaffari and R. A. Sauer, "Modal analysis of graphene-based structures for large deformations, contact and material nonlinearities," *Journal of Sound and Vibration*, vol. 423, pp. 161–179, 2018.

[31] A. G. Quintana, B. E. Saunders, R. Vasconcellos, and A. Abdelkefi, "Nonlinear characterization of the piecewise structural effects on whirl flutter of a rotor-nacelle system," in *AIAA SCITECH 2022 Forum*, 2022, p. 2269.

[32] C. Mair, D. Rezgui, and B. Titurus, "Nonlinear stability analysis of whirl flutter in a tiltrotor rotor-nacelle system," in *43rd European Rotorcraft Forum 2017*, 2017.

[33] A. Quintana, R. Vasconcellos, G. Throneberry, and A. Abdelkefi, "Nonlinear analysis and bifurcation characteristics of whirl flutter in unmanned aerial systems," *Drones*, vol. 5, no. 4, p. 122, 2021.

[34] W. Phillips, N. Alley, and R. Niewoehner, "Effects of nonlinearities on subsonic aerodynamic center," *Journal of aircraft*, vol. 45, no. 4, pp. 1244–1255, 2008.

[35] M. J. Patil and D. H. Hodges, "On the importance of aerodynamic and structural geometrical nonlinearities in aeroelastic behavior of high-aspect-ratio wings," *Journal of Fluids and Structures*, vol. 19, no. 7, pp. 905–915, 2004.

[36] C. Howcroft, M. Lowenberg, S. Neild, B. Krauskopf, and E. Coetzee, "Shimmy of an aircraft main landing gear with geometric coupling and mechanical freeplay," *Journal of Computational and Nonlinear Dynamics*, vol. 10, no. 5, p. 051011, 2015.

[37] A. Gilioli, A. Manes, U. Ringertz, and M. Giglio, "Investigation about the structural nonlinearities of an aircraft pylon," *Journal of Aircraft*, vol. 56, no. 1, pp. 273–283, 2019.

[38] P. Masarati, D. J. Piatak, G. Quaranta, J. D. Singleton, and J. Shen, "Soft-inplane tiltrotor aeromechanics investigation using two comprehensive multibody solvers," *Journal of the American Helicopter Society*, vol. 53, no. 2, pp. 179–192, 2008.

[39] W. Phillips, N. Alley, and R. Niewoehner, "Effects of nonlinearities on subsonic aerodynamic center," *Journal of aircraft*, vol. 45, no. 4, pp. 1244–1255, 2008.

[40] H. K. Edenborough, "Investigation of tilt-rotor vtol aircraft rotorpylon stability." *Journal of Aircraft*, vol. 5, no. 2, pp. 97–105, 1968.

[41] D. Tang and E. H. Dowell, "Experimental and theoretical study on aeroelastic response of high-aspect-ratio wings," *AIAA journal*, vol. 39, no. 8, pp. 1430–1441, 2001.

[42] M. J. Patil, D. H. Hodges, and C. E. Cesnik, "Limit-cycle oscillations in high-aspect-ratio wings," *Journal of fluids and structures*, vol. 15, no. 1, pp. 107–132, 2001.

[43] O. Avin, D. E. Raveh, A. Drachinsky, Y. Ben-Shmuel, and M. Tur, "An experimental benchmark of a very flexiblewing," in *AIAA Scitech 2021 Forum*, 2021, p. 1709.

[44] A. Drachinsky, O. Avin, D. E. Raveh, Y. Ben-Shmuel, and M. Tur, "Flutter tests of the pazy wing," *AIAA Journal*, vol. 60, no. 9, pp. 5414–5421, 2022.

[45] S. T. Trickey, L. Virgin, and E. Dowell, "The stability of limit–cycle oscillations in a nonlinear aeroelastic system," *Proceedings of the Royal Society of London. Series A: Mathematical, Physical and Engineering Sciences*, vol. 458, no. 2025, pp. 2203–2226, 2002.

[46] C. R. Mair, "Stability analysis of whirl flutter in rotor-nacelle systems with structural nonlinearities," Ph.D. dissertation, University of Bristol, 2021.

[47] B. Prokop, N. Frolov, and L. Gelens, "Data-driven reconstruction of limit cycle position provides side information for improved model identification with sindy," *arXiv preprint arXiv:2402.03168*, 2024.

[48] I. Tartaruga, J. Cooper, M. Lowenberg, P. Sartor, and Y. Lemmens, "Uncertainty and sensitivity analysis of bifurcation loci characterizing nonlinear landing-gear dynamics," *Journal of Aircraft*, vol. 55, no. 1, pp. 162–172, 2018.

[49] A. Collar, "The first fifty years of aeroelasticity," *Aerospace*, vol. 5, no. 2, pp. 12–20, 1978.

[50] R. L. Bisplinghoff, H. Ashley, and R. L. Halfman, *Aeroelasticity*. Cambridge, MA: Addison-Wesley, 1955.

[51] D. H. Hodges and G. A. Pierce, *Introduction to Structural Dynamics and Aeroelasticity*, 2nd ed. Cambridge University Press, 2006.

[52] E. H. Dowell, *A Modern Course in Aeroelasticity*, 5th ed. Springer, 2015.

[53] A. H. Nayfeh and B. Balachandran, *Applied Nonlinear Dynamics*. Wiley, 2008.

[54] G. Dimitriadis, *Introduction to Nonlinear Aeroelasticity*. Chichester: John Wiley & Sons Ltd., 2017.

[55] M. J. Patil and D. H. Hodges, "Nonlinear aeroelastic analysis of aircraft with high-aspect-ratio wings," *Journal of Aircraft*, vol. 38, pp. 802–809, 2001.

[56] R. M. J. Groh and A. Pirrera, "On the role of localizations in buckling of axially compressed cylinders," *Proc. R. Soc. A*, vol. 471, 2015.

[57] J. Yuan, E. Denimal, S. Bi, J. Feng, Q. Hu, and A. Cicirello, "Special section on uncertainty quantification and management in nonlinear dynamical systems in aerospace and mechanical engineering," *ASCE-ASME J Risk and Uncert in Engrg Sys Part B Mech Engrg*, vol. 9, no. 4, 2023.

[58] X. Wang, M. Szydlowski, J. Yuan, and C. Schwingshackl, "A multi-step interpolated-fft procedure for full-field nonlinear modal testing of turbomachinery components," *Mechanical Systems and Signal Processing*, vol. 169, p. 108771, 2022.

[59] H. Shukla and M. J. Patil, "Nonlinear state feedback control design to eliminate subcritical limit cycle oscillations in aeroelastic systems," *Nonlinear Dynamics*, vol. 88, pp. 1599–1614, 2017.

[60] J. Guckenheimer and P. Holmes, *Nonlinear oscillations, dynamical systems, and bifurcations of vector fields.* Springer, 2013.

[61] G. Dimitriadis, "Bifurcation analysis of aircraft with structural nonlinearities," *Journal of Aircraft*, vol. 45, pp. 1459–1475, 2008.

[62] B. H. K. Lee, S. J. Price, and Y. S. Wong, "Nonlinear aeroelastic analysis of airfoils: Bifurcation and chaos," *Progress in Aerospace Sciences*, vol. 41, pp. 323–365, 2005.

[63] E. H. Dowell and M. Ilgamov, *Studies in Nonlinear Aeroelasticity.* Springer, 2004.

[64] A. Erturk, W. G. R. Vieira, C. De Marqui, and D. J. Inman, "On the energy harvesting potential of piezoaeroelastic systems," *Applied physics letters*, vol. 96, no. 18, 2010.

[65] W. G. Dettmer and D. Perić, "Computational analysis of store separation," *AIAA Journal*, vol. 42, pp. 156–165, 2004.

[66] M. D. Conner, D. M. Tang, and E. H. Dowell, "Nonlinear behaviour of an airfoil with control surface freeplay," *Journal of Fluids and Structures*, vol. 11, pp. 89–109, 1997.

[67] R. Seydel, *Practical bifurcation and stability analysis*. Springer Science & Business Media, 2009, vol. 5.

[68] C. Cardani and P. Mantegazza, "Calculation of eigenvalue and eigenvector derivatives for algebraic flutter and divergence eigenproblems," *AIAA Journal*, vol. 17, no. 4, pp. 408–412, 1979.

[69] A. Abdelkefi, R. Vasconcellos, A. H. Nayfeh, and M. R. Hajj, "An analytical and experimental investigation into limit-cycle oscillations of an aeroelastic system," *Nonlinear Dynamics*, vol. 71, no. 1, pp. 159–173, 2013.

[70] M. Blyth, L. Renson, and L. Marucci, "Tutorial of numerical continuation and bifurcation theory for systems and synthetic biology," *arXiv preprint arXiv:2008.05226*, 2020.

[71] S. Karkar, B. Cochelin, and C. Vergez, "A comparative study of the harmonic balance method and the orthogonal collocation method on stiff nonlinear systems," *Journal of Sound and Vibration*, vol. 333, no. 12, pp. 2554–2567, 2014.

[72] A. Dhooge, W. Govaerts, Y. A. Kuznetsov, H. G. E. Meijer, and B. Sautois, "New features of the software matcont for bifurcation analysis of dynamical systems," *Mathematical and Computer Modelling of Dynamical Systems*, vol. 14, no. 2, pp. 147–175, 2008.

[73] E. J. Doedel and B. Oldeman, "Auto-07p: continuation and bifurcation software," *Montreal, QC: Concordia University Canada*, 1998. [Online]. Available: https://github.com/auto-07p/auto-07p

[74] H. Dankowicz and F. Schilder, *Recipes for continuation*. SIAM, 2013.

[75] M. A. Razzak, "A simple harmonic balance method for solving strongly nonlinear oscillators," *Journal of the Association of Arab Universities for*

Basic and Applied Sciences, vol. 21, pp. 68–76, 2016. [Online]. Available: https://www.sciencedirect.com/science/article/pii/S1815385215000309

[76] F. Abdullah and P. D. Christofides, "Data-based modeling and control of nonlinear process systems using sparse identification: An overview of recent results," *Computers & Chemical Engineering*, vol. 174, p. 108247, 2023.

[77] K. Fukami, T. Murata, K. Zhang, and K. Fukagata, "Sparse identification of nonlinear dynamics with low-dimensionalized flow representations," *Journal of Fluid Mechanics*, vol. 926, p. A10, 2021.

[78] Y. Zhang, Q. Wang, X. Li, and E. H. Dowell, "Machine learning-augmented harmonic balance for nonlinear aeroelastic analysis," *AIAA Journal*, vol. 59, no. 8, pp. 3125–3139, 2021.

[79] F. Bayer and R. I. Leine, "Sorting-free hill-based stability analysis of periodic solutions through koopman analysis," *Nonlinear Dynamics*, vol. 111, no. 9, pp. 8439–8466, 2023.

[80] T. Cameron and J. Griffin, *An Alternating Frequency/Time Domain Method for Calculating the Steady-State Response of Nonlinear Dynamic Systems.* Journal of Applied Mechanics, 1989, american Society of Mechanical Engineers, ff10.1115/1.3176036ff. ffhal-01333697.

[81] P. Gudmundson, "On the accuracy of the harmonic-balance method concerning vibrations of beams with nonlinear supports." *Archive of applied mechanics (1991)*, vol. 59, no. 5, pp. 333–344, 1989.

[82] M. A. Razzak, "A simple harmonic balance method for solving strongly nonlinear oscillators," *Journal of the Association of Arab Universities for Basic and Applied Sciences*, vol. 21, pp. 68–76, 2016.

[83] T. Detroux, L. Renson, L. Masset, and G. Kerschen, "The harmonic balance method for bifurcation analysis of large-scale nonlinear mechanical systems,"

Computer Methods in Applied Mechanics and Engineering, vol. 296, pp. 18–38, 2015.

[84] V. Lanza, M. Bonnin, and M. Gilli, *On the application of the describing function technique to the bifurcation analysis of nonlinear systems.* Circuits and Systems II: Express Briefs, 2007, iEEE Transactions on, vol. 54, no. 4, pp. 343–347.

[85] M. Krack and J. Groß, *NLvib.* University of Stuttgart, 2020, available at: NLvib — Institut für Luftfahrtantriebe — Universität Stuttgart (uni-stuttgart.de) (Accessed 10/12/2021).

[86] T. Detroux, L. Renson, L. Masset, and G. Kerschen, "The harmonic balance method for bifurcation analysis of large-scale nonlinear mechanical systems," *Computer Methods in Applied Mechanics and Engineering*, vol. 296, pp. 18–38, 2015.

[87] C. A. Klausmeier, "Floquet theory: a useful tool for understanding nonequilibrium dynamics," *Theoretical Ecology*, vol. 1, no. 3, pp. 153–161, 2008.

[88] P. Schinas, D. Manolas, V. Riziotis, and S. Voutsinas, "Aeroelastic modal dynamics of floating wind turbines in anisotropic conditions based on floquet analysis," in *Journal of Physics: Conference Series*, vol. 2265, no. 4. IOP Publishing, 2022, p. 042005.

[89] L. Guillot, A. Lazarus, O. Thomas, C. Vergez, and B. Cochelin, "A purely frequency based floquet-hill formulation for the efficient stability computation of periodic solutions of ordinary differential systems," *Journal of Computational Physics*, vol. 416, p. 109477, 2020.

[90] A. Lazarus and O. Thomas, "A harmonic-based method for computing the stability of periodic solutions of dynamical systems," *Comptes Rendus Mécanique*, vol. 338, no. 9, pp. 510–517, 2010.

[91] A. Lazarus and C. Touzé, *A Harmonic-Based Method for Computing the Stability of Periodic Oscillations of Non-Linear Structural Systems.* Proceedings of the

ASME Design Engineering Technical Conference, 2010, 5. 10.1115/DETC2010-28407.

[92] M. Krack, L. Salles, and F. Thouverez, "Vibration prediction of bladed disks coupled by friction joints," *Archives of Computational Methods in Engineering*, vol. 24, pp. 589–636, 2017.

[93] L. Peletan, S. Baguet, M. Torkhani, and G. Jacquet-Richardet, "A comparison of stability computational methods for periodic solution of nonlinear problems with application to rotordynamics," *Nonlinear dynamics*, vol. 72, pp. 671–682, 2013.

[94] F. Bayer and R. I. Leine, "Sorting-free hill-based stability analysis of periodic solutions through koopman analysis," *Nonlinear Dynamics*, vol. 111, no. 9, pp. 8439–8466, 2023.

[95] D. A. Barton, B. P. Mann, and S. G. Burrow, "Control-based continuation for investigating nonlinear experiments," *Journal of Vibration and Control*, vol. 18, no. 4, pp. 509–520, 2012.

[96] E. Walter and L. Pronzato, "On the identifiability and distinguishability of nonlinear parametric models," *Mathematics and computers in simulation*, vol. 42, no. 2-3, pp. 125–134, 1996.

[97] G. Quaranta, W. Lacarbonara, and S. F. Masri, "A review on computational intelligence for identification of nonlinear dynamical systems," *Nonlinear Dynamics*, vol. 99, no. 2, pp. 1709–1761, 2020.

[98] G. Gui, F. Liu, J. Sun, J. Yang, Z. Zhou, and D. Zhao, "Flight delay prediction based on aviation big data and machine learning," *IEEE Transactions on Vehicular Technology*, vol. 69, no. 1, pp. 140–150, 2019.

[99] A. Gábor and J. R. Banga, "Robust and efficient parameter estimation in dynamic models of biological systems," *BMC systems biology*, vol. 9, no. 1, pp. 1–25, 2015.

[100] K. Lee, D. Barton, and L. Renson, "Mathematical model identification of self-excited systems using experimental bifurcation analysis data," in *Nonlinear*

Structures & Systems, Volume 1: Proceedings of the 40th IMAC, A Conference and Exposition on Structural Dynamics 2022. Springer, 2022, pp. 61–63.

[101] S. Beregi, D. A. Barton, D. Rezgui, and S. Neild, "Using scientific machine learning for experimental bifurcation analysis of dynamic systems," *Mechanical Systems and Signal Processing*, vol. 184, p. 109649, 2023.

[102] Y. Wang, A. Wynn, and R. Palacios, "Nonlinear aeroelastic control of very flexible aircraft using model updating," *Journal of Aircraft*, vol. 55, no. 4, pp. 1551–1563, 2018.

[103] R. H. Fraser and J. W. Menzies, "Finite element model updating using response surface methodology," *Mechanical Systems and Signal Processing*, vol. 22, no. 1, pp. 145–161, 2008.

[104] J. E. Mottershead, M. Link, and M. I. Friswell, "Model updating in structural dynamics: A survey," *Journal of Sound and Vibration*, vol. 321, no. 7-8, pp. 686–724, 2011.

[105] C. H. J. Fox and G. E. Hearn, *Finite element model updating using measured data: A review*. University of Oxford, Department of Engineering Science, 1987.

[106] J. Kaipio and E. Somersalo, *Statistical and Computational Inverse Problems*, ser. Applied Mathematical Sciences. Springer, 2006, vol. 160.

[107] M. Raissi, P. Perdikaris, and G. E. Karniadakis, "Physics-informed neural networks: A deep learning framework for solving forward and inverse problems involving nonlinear partial differential equations," *Journal of Computational Physics*, vol. 378, pp. 686–707, 2019.

[108] S. L. Brunton and J. N. Kutz, *Data-Driven Science and Engineering: Machine Learning, Dynamical Systems, and Control*. Cambridge University Press, 2022.

[109] A. Kaba, E. Y. Metin, and O. Turan, "Thrust modelling of a target drone engine with nonlinear least–squares estimation based on series expansions," *Aircraft Engineering and Aerospace Technology*, no. ahead-of-print, 2022.

[110] H. Eiselt, C.-L. Sandblom *et al.*, *Nonlinear optimization*. Springer, 2019.

[111] M. Friswell and J. E. Mottershead, *Finite element model updating in structural dynamics*. Springer Science & Business Media, 1995, vol. 38.

[112] E. Patelli, Y. Govers, M. Broggi, H. M. Gomes, M. Link, and J. E. Mottershead, "Sensitivity or bayesian model updating: a comparison of techniques using the dlr airmod test data," *Archive of Applied Mechanics*, vol. 87, pp. 905–925, 2017.

[113] S. Bi, M. Beer, S. Cogan, and J. Mottershead, "Stochastic model updating with uncertainty quantification: An overview and tutorial," *Mechanical Systems and Signal Processing*, vol. 204, p. 110784, 2023.

[114] L. Stolovitch, "Progress in normal form theory," *Nonlinearity*, vol. 22, no. 7, p. R77, 2009.

[115] J. L. Beck and L. S. Katafygiotis, "Updating models and their uncertainties. i: Bayesian statistical framework," *Journal of Engineering Mechanics*, vol. 124, no. 4, pp. 455–461, 1998.

[116] V. Namdeo and C. Manohar, "Nonlinear structural dynamical system identification using adaptive particle filters," *Journal of Sound and Vibration*, vol. 306, no. 3-5, pp. 524–563, 2007.

[117] P. L. Green and K. Worden, "Bayesian and markov chain monte carlo methods for identifying nonlinear systems in the presence of uncertainty," *Philosophical Transactions of the Royal Society A: Mathematical, Physical and Engineering Sciences*, vol. 373, no. 2051, p. 20140405, 2015.

[118] H. Ebrahimian, R. Astroza, and J. P. Conte, "Extended kalman filter for material parameter estimation in nonlinear structural finite element models using direct differentiation method," *Earthquake Engineering & Structural Dynamics*, vol. 44, no. 10, pp. 1495–1522, 2015.

[119] M. Yin, A. Iannelli, and R. S. Smith, "Maximum likelihood estimation in data-driven modeling and control," *IEEE Transactions on Automatic Control*, 2021.

[120] J.-P. Noël and G. Kerschen, "Nonlinear system identification in structural dynamics: 10 more years of progress," *Mechanical Systems and Signal Processing*, vol. 83, pp. 2–35, 2017.

[121] A. Lye, A. Cicirello, and E. Patelli, "Sampling methods for solving bayesian model updating problems: A tutorial," *Mechanical Systems and Signal Processing*, vol. 159, p. 107760, 2021.

[122] R. Rocchetta, M. Broggi, Q. Huchet, and E. Patelli, "On-line bayesian model updating for structural health monitoring," *Mechanical Systems and Signal Processing*, vol. 103, pp. 174–195, 2018.

[123] Y. Zhang and W. Yang, "A comparative study of the stochastic simulation methods applied in structural health monitoring," *Engineering Computations*, vol. 31, no. 7, pp. 1484–1513, 2014.

[124] C. Fang, H.-J. Liu, H.-F. Lam, M. O. Adeagbo, and H.-Y. Peng, "Practical model updating of the ting kau bridge through the mcmc-based bayesian algorithm utilizing measured modal parameters," *Engineering Structures*, vol. 254, p. 113839, 2022.

[125] M. Song, L. Renson, B. Moaveni, and G. Kerschen, "Bayesian model updating and class selection of a wing-engine structure with nonlinear connections using nonlinear normal modes," *Mechanical Systems and Signal Processing*, vol. 165, p. 108337, 2022.

[126] Y. Zhou and Z. Lu, "Active polynomial chaos expansion for reliability-based design optimization," *AIAA Journal*, vol. 57, no. 12, pp. 5431–5446, 2019.

[127] S. Agrawal, D. Gobiha, and N. Sinha, "Nonlinear parameter estimation of airship using modular neural network," *The Aeronautical Journal*, vol. 124, no. 1273, pp. 409–428, 2020.

[128] H. Verma and N. Peyada, "Estimation of aerodynamic parameters near stall using maximum likelihood and extreme learning machine-based methods," *The Aeronautical Journal*, vol. 125, no. 1285, pp. 489–509, 2021.

[129] J. Yuan, A. Fantetti, E. Denimal, S. Bhatnagar, L. Pesaresi, C. Schwingshackl, and L. Salles, "Propagation of friction parameter uncertainties in the nonlinear dynamic response of turbine blades with underplatform dampers," *Mechanical Systems and Signal Processing*, vol. 156, p. 107673, 2021.

[130] S. Hosder, R. Walters, and M. Balch, "Efficient uncertainty quantification applied to the aeroelastic analysis of a transonic wing," in *46th AIAA Aerospace Sciences Meeting and Exhibit*, 2008, p. 729.

[131] J. Weinmeister, X. Gao, and S. Roy, "Analysis of a polynomial chaos-kriging metamodel for uncertainty quantification in aerodynamics," *AIAA Journal*, vol. 57, no. 6, pp. 2280–2296, 2019.

[132] A. I. J. Forrester and A. J. Keane, *Engineering Design via Surrogate Modelling*. Wiley, 2008.

[133] Q. Wang and et al., "Deep learning for surrogate modeling of aeroelastic systems," *AIAA Journal*, 2020.

[134] P. S. Palar, K. Zakaria, L. R. Zuhal, K. Shimoyama, and R. P. Liem, "Gaussian processes and support vector regression for uncertainty quantification in aerodynamics," in *AIAA Scitech 2021 Forum*, 2021, p. 0181.

[135] S. Yildiz, E. Cakmak, E. Kara, and M. Nikbay, "Uncertainty quantification of aeroelastic systems using active learning gaussian process," in *Proceedings of the International Conference on Multidisciplinary Design Optimization of Aerospace Systems (AEROBEST 2021), Virtual Event, Online*, 2021, pp. 21–23.

[136] Y. Sun, E. Denimal, J. Yuan, and L. Salles, "Geometric design of friction ring dampers in blisks using nonlinear modal analysis and kriging surrogate model," *Structural and Multidisciplinary Optimization*, vol. 65, no. 3, p. 98, 2022.

[137] D. Lee, Y.-E. Kang, D.-H. Kim, and K. Yee, "Aeroelastic design and comprehensive analysis of composite rotor blades through cluster-based kriging," *AIAA Journal*, vol. 60, no. 10, pp. 5984–6004, 2022.

[138] X. Peng, J. Kou, and W. Zhang, "Multi-fidelity nonlinear unsteady aerodynamic modeling and uncertainty estimation based on hierarchical kriging," *Applied Mathematical Modelling*, 2023.

[139] M. Hermkes, N. M. Kuehn, and C. Riggelsen, "Simultaneous quantification of epistemic and aleatory uncertainty in gmpes using gaussian process regression," *Bulletin of earthquake engineering*, vol. 12, pp. 449–466, 2014.

[140] G. Sarazin, J. Morio, A. Lagnoux, M. Balesdent, and L. Brevault, "Reliability-oriented sensitivity analysis in presence of data-driven epistemic uncertainty," *Reliability Engineering & System Safety*, vol. 215, p. 107733, 2021.

[141] D. Arroyo and M. Ordaz, "On the forecasting of ground-motion parameters for probabilistic seismic hazard analysis," *Earthquake Spectra*, vol. 27, no. 1, pp. 1–21, 2011.

[142] A. Lye, S. Ferson, and S. Xiao, "Comparison between distance functions for approximate bayesian computation to perform stochastic model updating and model validation under limited data," *ASCE-ASME Journal of Risk and Uncertainty in Engineering Systems, Part A: Civil Engineering*, vol. 10, no. 2, p. 03124001, 2024.

[143] S. Ferson and L. R. Ginzburg, "Different methods are needed to propagate ignorance and variability," *Reliability Engineering & System Safety*, vol. 54, no. 2-3, pp. 133–144, 1996.

[144] S. Ferson and J. G. Hajagos, "Arithmetic with uncertain numbers: rigorous and (often) best possible answers," *Reliability Engineering & System Safety*, vol. 85, no. 1-3, pp. 135–152, 2004.

[145] C. Wang, X. Qiang, M. Xu, and T. Wu, "Recent advances in surrogate modeling methods for uncertainty quantification and propagation," *Symmetry*, vol. 14, no. 6, p. 1219, 2022.

[146] J. Zhang, S. Chowdhury, A. Mehmani, and A. Messac, "Characterizing uncertainty attributable to surrogate models," *Journal of Mechanical Design*, vol. 136, no. 3, p. 031004, 2014.

[147] S. Bhattrai, J. H. de Baar, and A. J. Neely, "Efficient uncertainty quantification for a hypersonic trailing-edge flap, using gradient-enhanced kriging," *Aerospace Science and Technology*, vol. 80, pp. 261–268, 2018.

[148] J. Kou and W. Zhang, "Data-driven modeling for unsteady aerodynamics and aeroelasticity," *Progress in Aerospace Sciences*, vol. 125, p. 100725, 2021.

[149] R. Dwight and Z.-H. Han, "Efficient uncertainty quantification using gradient-enhanced kriging," in *50th AIAA/ASME/ASCE/AHS/ASC Structures, Structural Dynamics, and Materials Conference 17th AIAA/ASME/AHS Adaptive Structures Conference 11th AIAA No*, 2009, p. 2276.

[150] S. Jeong, M. Murayama, and K. Yamamoto, "Efficient optimization design method using kriging model," *Journal of aircraft*, vol. 42, no. 2, pp. 413–420, 2005.

[151] B. D. Phillips and T. K. West, "Aeroelastic uncertainty quantification of a low-boom aircraft configuration," in *2018 AIAA Aerospace Sciences Meeting*, 2018, p. 0333.

[152] J. Tang, Z. Wu, and C. Yang, "Epistemic uncertainty quantification in flutter analysis using evidence theory," *Chinese journal of aeronautics*, vol. 28, no. 1, pp. 164–171, 2015.

[153] X. Wang and Z. Qiu, "Nonprobabilistic interval reliability analysis of wing flutter," *Aiaa Journal*, vol. 47, no. 3, pp. 743–748, 2009.

[154] Y. Zheng and Y. Wang, "Flutter stability analysis of aeroelastic systems with consideration of hybrid uncertain parameters," *Mechanical Systems and Signal Processing*, vol. 185, p. 109782, 2023.

[155] A. Dhooge, W. Govaerts, and Y. A. Kuznetsov, "Matcont: a matlab package for numerical bifurcation analysis of odes," *ACM Transactions on Mathematical Software (TOMS)*, vol. 29, no. 2, pp. 141–164, 2003.

[156] Z. Ahsan, H. Dankowicz, M. Li, and J. Sieber, "Methods of continuation and their implementation in the coco software platform with application to delay differential equations," *Nonlinear Dynamics*, vol. 107, no. 4, pp. 3181–3243, 2022.

[157] M. McGurk and J. Yuan, "Computation of limit cycle oscillations and their stabilities in nonlinear aeroelastic systems using harmonic balance methods," in *International Forum on Aeroelasticity and Structural Dynamics (IFASD) 2022*, 2022.

[158] ——, "Computation of limit cycle oscillations and their stabilities in nonlinear aeroelastic systems using harmonic balance methods," in *Proceedings of the International Forum on Aeroelasticity and Structural Dynamics*, Madrid, June 2022.

[159] J. Wright and J. Cooper, *Introduction to Aircraft Aeroelasticity and Loads*. 2nd edn. Chichester: John Wiley & Sons Ltd, 2014, chapter 10.4.

[160] D. A. Aruliah, L. van Veen, and A. Dubitski, "A parallel adaptive method for pseudo-arclength continuation," in *Journal of Physics: Conference Series*, vol. 385, no. 1. IOP Publishing, 2012, p. 012008.

[161] J. A. Dahlke and R. A. Bettinger, "Practical implementation of pseudo-arclength continuation to ensure consistent path direction," *Acta Astronautica*, vol. 215, pp. 205–216, 2024.

[162] W. Govaerts, "Numerical bifurcation analysis for odes," *Journal of computational and applied mathematics*, vol. 125, no. 1-2, pp. 57–68, 2000.

[163] P. Shearer, "Deep earth structure-seismic scattering in the deep earth," *Seismology and the Structure of the Earth*, vol. 1, pp. 695–729, 2007.

[164] L. Peletan, S. Baguet, M. Torkhani, and G. Jacquet-Richardet, *A comparison of stability computational methods for periodic solution of nonlinear problems with application to rotordynamics.* Nonlinear Dynamics, 2013, 72. 671-682. 10.1007/s11071-012-0744-0.

[165] G. Teschl, *Ordinary differential equations and dynamical systems.* American Mathematical Soc., 2012, vol. 140.

[166] T. Theodorsen, *General Theory of Aerodynamic Instability and the Mechanism of Flutter.* NACA Rept, 1935, 496.

[167] J. W. Edwards, H. Ashley, and J. V. Breakwell, "Unsteady aerodynamic modeling for arbitrary motions," *AIAA journal*, vol. 17, no. 4, pp. 365–374, 1979.

[168] A. Abdelkefi, R. Vasconcellos, F. Marques, and M. Hajj, *Modeling and identification of freeplay nonlinearity.* Journal of Sound and Vibration, 2012, volume 331, Issue 8,Pages 1898-1907,ISSN 0022-460X.

[169] O. A. Bauchau, J. Rodriguez, and C. L. Bottasso, "Modeling of unilateral contact conditions with application to aerospace systems involving backlash, freeplay and friction," *Mechanics Research Communications*, vol. 28, no. 5, pp. 571–599, 2001.

[170] E. Hewitt and R. Hewitt, *The Gibbs-Wilbraham Phenomenon: An Episode in Fourier Analysis.* Springer-Verlag, 1979, archive for History of Exact Sciences, Volume 21.

[171] Carslaw, *Introduction to the theory of Fourier's series and integrals (Third ed.).* New York: Dover Publications Inc., 1930.

[172] M. A. Padmanabhan, "Sliding wear and freeplay growth due to control surface limit cycle oscillations," *Journal of Aircraft*, vol. 56, no. 5, pp. 1973–1979, 2019.

[173] M. McGurk, J. Yuan, and L. Renson, "Nonlinear parameter estimation using bayesian model updating and data driven surrogate model," Jun. 2023, conference: 9th International Conference on Computational Methods in Structural Dynamics and Earthquake Engineering.

[174] X. Zhou, A. Montazeri, and J. D. Albertson, "Mobile sensing of point-source gas emissions using bayesian inference: An empirical examination of the likelihood function," *Atmospheric Environment*, vol. 218, p. 116981, 2019.

[175] R. Rocchetta, M. Broggi, Q. Huchet, and E. Patelli, "On-line bayesian model updating for structural health monitoring," *Mechanical Systems and Signal Processing*, vol. 103, pp. 174–195, 2018.

[176] P. C. Jia X, "Data features-based likelihood-informed bayesian finite element model updating," in *Proceedings of 3rd International Conference on Uncertainty Quantification in Computational Sciences and Engineering*, 2019, p. 103–113.

[177] G. O. Roberts and J. S. Rosenthal, "Optimal scaling for various metropolis-hastings algorithms," *Statistical science*, vol. 16, no. 4, pp. 351–367, 2001.

[178] R. Serfozo, *Basics of applied stochastic processes*. Springer Science & Business Media, 2009.

[179] J. L. Beck and S.-K. Au, "Bayesian updating of structural models and reliability using markov chain monte carlo simulation," *Journal of engineering mechanics*, vol. 128, no. 4, pp. 380–391, 2002.

[180] W. Betz, I. Papaioannou, and D. Straub, "Transitional markov chain monte carlo: observations and improvements," *Journal of Engineering Mechanics*, vol. 142, no. 5, p. 04016016, 2016.

[181] B. Ristic, S. Arulampalam, and N. Gordon, *Beyond the Kalman filter: Particle filters for tracking applications*. Artech house, 2003.

[182] P. L. Green, L. Devlin, R. E. Moore, R. J. Jackson, J. Li, and S. Maskell, "Increasing the efficiency of sequential monte carlo samplers through the use of ap-

proximately optimal l-kernels," *Mechanical Systems and Signal Processing*, vol. 162, p. 108028, 2022.

[183] S. Chib and I. Jeliazkov, "Marginal likelihood from the metropolis–hastings output," *Journal of the American statistical association*, vol. 96, no. 453, pp. 270–281, 2001.

[184] J. Ching and Y.-C. Chen, "Transitional markov chain monte carlo method for bayesian model updating, model class selection, and model averaging," *Journal of engineering mechanics*, vol. 133, no. 7, pp. 816–832, 2007.

[185] Airbus-EDF-IMACS-ONERA-Phimeca. (2022) Openturns. [Online]. Available: https://openturns.github.io/www/

[186] B. Minasny and A. B. McBratney, "Spatial prediction of soil properties using eblup with the matérn covariance function," *Geoderma*, vol. 140, no. 4, pp. 324–336, 2007.

[187] J. Sieber and B. Krauskopf, "Control based bifurcation analysis for experiments," *Nonlinear Dynamics*, vol. 51, no. 3, pp. 365–377, 2008.

[188] J. Sieber, B. Krauskopf, D. Wagg, S. Neild, and A. Gonzalez-Buelga, "Control-based continuation of unstable periodic orbits," 2011.

[189] K. Lee, D. Barton, and L. Renson, "Model identification of a fluttering aerofoil using control-based continuation and normal form analysis," in *Proceedings of the International Conference on Noise and Vibration Engineering, ISMA*, 2020, pp. 261–268.

[190] S. Beregi, D. A. Barton, D. Rezgui, and S. A. Neild, "Robustness of nonlinear parameter identification in the presence of process noise using control-based continuation," *Nonlinear Dynamics*, vol. 104, no. 2, pp. 885–900, 2021.

[191] C. Riso, C. E. Cesnik, and B. I. Epureanu, "Bifurcation-diagram-free postflutter response constraint for design optimization," *AIAA Journal*, pp. 1–18, 2023.

[192] H. Liu, C. Jiang, and Z. Xiao, "Efficient uncertainty propagation for parameterized p-box using sparse-decomposition-based polynomial chaos expansion," *Mechanical Systems and Signal Processing*, vol. 138, p. 106589, 2020.

[193] W. Nuttall, E. Patelli, E. Smith, D. Webbe-Wood, and S. Middleburgh, "Perspectives on engineering uncertainty: Civil nuclear energy safety and efficiency," 2025.

[194] W. Johnson, "Dynamics of tilting proprotor aircraft in cruise flight," NASA, Tech. Rep., 1974.

[195] Q. Zhou and F. Tan, "Avionics of electric vertical take-off and landing in the urban air mobility: A review," *IEEE Aerospace and Electronic Systems Magazine*, 2024.

[196] O. Ugwueze, T. Statheros, M. A. Bromfield, and N. Horri, "Trends in evtol aircraft development: The concepts, enablers and challenges," in *AIAA Scitech 2023 forum*, 2023, p. 2096.

[197] R. Peyran and O. Rand, "Effect of design requirements on conceptual tiltrotor wing weight," in *Annual Forum Proceedings- American Helicopter Society*, vol. 2, 1999, pp. 1555–1569.

[198] H. K. Edenborough, "Investigation of tilt-rotor vtol aircraft rotorpylon stability." *Journal of Aircraft*, vol. 5, no. 2, pp. 97–105, 1968.

[199] J. W. Edwards, C. V. Spain, D. F. Keller, R. W. Moses, and D. M. Schuster, "Transport wing flutter model transonic limit cycle oscillation test," *Journal of aircraft*, vol. 46, no. 4, pp. 1104–1113, 2009.

[200] C. Riso, "Output-based prediction of whirl flutter limit-cycle oscillations considering multiple varying parameters," in *AIAA SCITECH 2024 Forum*, 2024, p. 1847.

[201] M. Gatlin and C. Riso, "Predicting whirl flutter bifurcations using machine learning," in *80th VFS Annual Forum, Montreal, Canada*, 2024, pp. 1–15.

[202] C. Mair, D. Rezgui, and B. Titurus, "Stability and dynamical analysis of whirl flutter in a gimballed rotor-nacelle system with a smooth nonlinearity," *The Aeronautical Journal*, vol. 127, no. 1313, pp. 1234–1254, 2023.

[203] U.-J. Hwang, J.-S. Park, and M.-K. Lee, "Comparison of tiltrotor whirl flutter analyses with gimballed and hingeless hub models," *International Journal of Aeronautical and Space Sciences*, vol. 25, no. 4, pp. 1310–1318, 2024.

[204] F. Tsai *et al.*, "Development and whirl flutter test of the maryland tiltrotor rig," *Journal of the American Helicopter Society*, vol. 69, no. 1, pp. 1–15, 2024.

[205] C. Koch, "Parametric whirl flutter study using different modelling approaches," *CEAS Aeronautical Journal*, vol. 13, no. 1, pp. 57–67, 2022.

[206] F. H. Gern, D. J. Inman, and R. K. Kapania, "Structural and aeroelastic modeling of general planform wings with morphing airfoils," *AIAA journal*, vol. 40, no. 4, pp. 628–637, 2002.

[207] J. W. Peterson, "Arc length parameterization of spline curves," *Journal of Compu ter Aided Design*, 2006.

[208] S. McKinley and M. Levine, "Cubic spline interpolation," *College of the Redwoods*, vol. 45, no. 1, pp. 1049–1060, 1998.

[209] S. R. Bland and R. M. Bennett, "Wind-tunnel measurement of propeller whirl-flutter speeds and static-stability derivatives and comparison with theory," NASA, Tech. Rep., 1963.

[210] G. Haller, S. Ponsioen, and S. Jain, "Nonlinear model reduction via spectral submanifolds," *Journal of Sound and Vibration*, vol. 465, p. 115011, 2020.

[211] K. Champion, B. Lusch, J. N. Kutz, and S. L. Brunton, "Data-driven discovery of coordinates and governing equations," *Proceedings of the National Academy of Sciences*, vol. 116, no. 45, pp. 22 445–22 451, 2019.